Volume 51
Number 16
21 August 2022
Pages 6867–7306

Chem Soc Rev

Chemical Society Reviews

rsc.li/chem-soc-rev

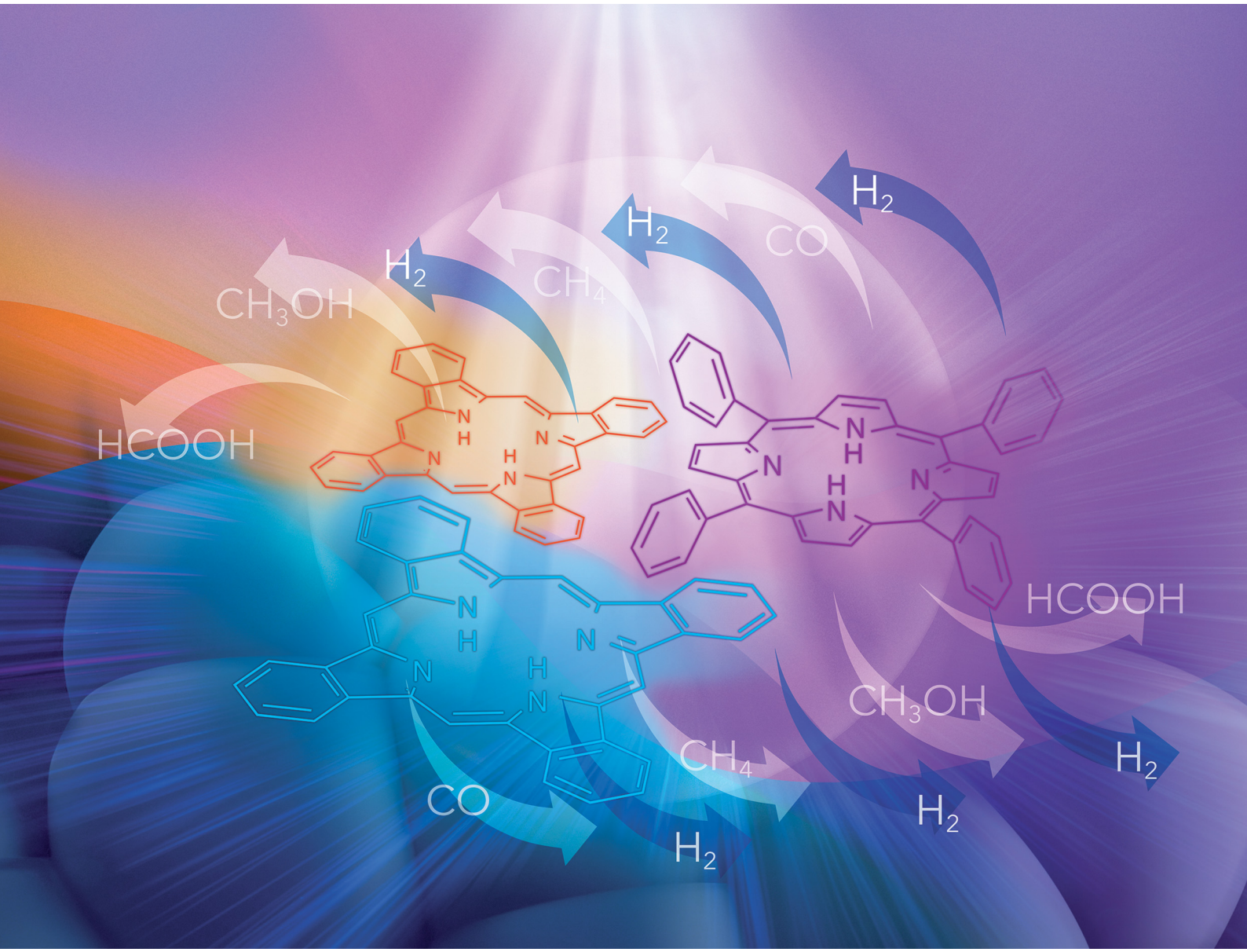

ISSN 0306-0012

ROYAL SOCIETY OF CHEMISTRY

REVIEW ARTICLE

Georgios Charalambidis, Kalliopi Ladomenou, Mine Ince, Athanassios G. Coutsolelos *et al.*

Porphyrins and phthalocyanines as biomimetic tools for photocatalytic H_2 production and CO_2 reduction

Chem Soc Rev

REVIEW ARTICLE

View Article Online
View Journal | View Issue

Cite this: *Chem. Soc. Rev.*, 2022, **51**, 6965

Porphyrins and phthalocyanines as biomimetic tools for photocatalytic H_2 production and CO_2 reduction

Emmanouil Nikoloudakis, [a] Ismael López-Duarte, [b] Georgios Charalambidis, *[a] Kalliopi Ladomenou, *[c] Mine Ince *[d] and Athanassios G. Coutsolelos *[ae]

The increasing energy demand and environmental issues caused by the over-exploitation of fossil fuels render the need for renewable, clean, and environmentally benign energy sources unquestionably urgent. The zero-emission energy carrier, H_2 is an ideal alternative to carbon-based fuels especially when it is generated photocatalytically from water. Additionally, the photocatalytic conversion of CO_2 into chemical fuels can reduce the CO_2 emissions and have a positive environmental and economic impact. Inspired by natural photosynthesis, plenty of artificial photocatalytic schemes based on porphyrinoids have been investigated. This review covers the recent advances in photocatalytic H_2 production and CO_2 reduction systems containing porphyrin or phthalocyanine derivatives. The unique properties of porphyrinoids enable their utilization both as chromophores and as catalysts. The homogeneous photocatalytic systems are initially described, presenting the various approaches for the improvement of photosensitizing activity and the enhancement of catalytic performance at the molecular level. On the other hand, for the development of the heterogeneous systems, numerous methods were employed such as self-assembled supramolecular porphyrinoid nanostructures, construction of organic frameworks, combination with 2D materials and adsorption onto semiconductors. The dye sensitization on semiconductors opened the way for molecular-based dye-sensitized photoelectrochemical cells (DSPECs) devices based on porphyrins and phthalocyanines. The research in photocatalytic systems as discussed herein remains challenging since there are still many limitations making them unfeasible to be used at a large scale application before finding a large-scale application.

Received 4th March 2022

DOI: 10.1039/d2cs00183g

rsc.li/chem-soc-rev

1. Introduction

The use of fossil fuels for the increasing energy demand indicates that the global sources will be depleted in the near future. The relentless use of fossil fuels as the primary energy source at this pace will force us to face two major global challenges: increasing energy costs due to limited fossil fuel resources and climate change caused by greenhouse gas emissions. Solar energy is an inexhaustible source of energy and the sunlight reaching the earth daily is enough to meet all the energy needs of humanity. Of all the renewable energy sources, solar power has the highest potential to become the energy source of the future.[1] However, the major problem is related to the storage of sunlight which remains an important scientific and technological challenge. In fact, photovoltaic technologies that produce electrical energy from solar light have shown great development in the last decades compared to other renewable energy sources and generate electricity at a considerable scale.[2] Though the widespread use of photovoltaic technology is a promising approach to curb the demand for fossil fuels. Today's photovoltaic technologies, especially for the transport sector, are not able to fulfil societal needs. Considering that currently, transportation is one of the sectors with the highest energy supply, the conversion of solar energy into storable energy carriers and solar fuels appears as a promising solution to produce cost-effective fuels and ensure the sustainability of

[a] *University of Crete, Department of Chemistry, Laboratory of Bioinorganic Chemistry, Voutes Campus, Heraklion, Crete, Greece. E-mail: acoutsol@uoc.gr, gcharal@uoc.gr*
[b] *Departamento de Química en Ciencias Farmacéuticas, Universidad Complutense de Madrid, 28040 Madrid, Spain*
[c] *International Hellenic University, Department of Chemistry, Laboratory of Inorganic Chemistry, Agios Loucas, 65404, Kavala Campus, Greece. E-mail: kladomenou@chem.ihu.gr*
[d] *Department of Natural and Mathematical Sciences, Faculty of Engineering, Tarsus University, Mersin, Turkey. E-mail: mine.ince@tarsus.edu.tr*
[e] *Institute of Electronic Structure and Laser (IESL) Foundation for Research and Technology - Hellas (FORTH), Vassilika Vouton, Heraklion, Crete, Greece*

the energy supply. As previously mentioned, one additional problem arising from the use of fossil fuels is global warming which causes many uncontrollable problems such as climate change, depletion of biodiversity, and change of the water cycle. CO_2 is the main greenhouse gas causing global warming.[3] In this sense, technologies for converting CO_2 and water into sustainable fuels and/or high value-added chemicals are of particular interest as they have the potential to address challenges of the dependency on fossil fuels and greenhouse emissions. Undoubtedly, the conversion of CO_2 into chemical fuel and raw materials will not only contribute to the CO_2 emission balance but will also have a significant environmental and economic impact.[4]

On the other hand, as a zero-emission energy carrier, H_2 is an ideal alternative to carbon-based fossil fuels that can be used to produce both fuel and electricity as well as value-added feedstock such as methanol, methane, *etc.*[5] However, most of the H_2 production is currently based on the conventional reform of fossil fuel that has been causing greenhouse gas emissions. The contradiction of using fossil fuels to produce hydrogen has been addressed over the last decades by the development of low-cost and environmentally friendly alternative methods such as photocatalytic H_2 production.[6] As a consequence, from an environmental, economic, and social point of view, the generation of H_2 from water and reduction of CO_2 to solar fuels by using sunlight could be an optimal solution for the sustainability of energy supply and fuel sources.

Sunlight can be converted into storable chemicals and fuels with three main processes: natural photosynthesis, artificial photosynthesis and thermochemical method.[7,8] Photosynthesis

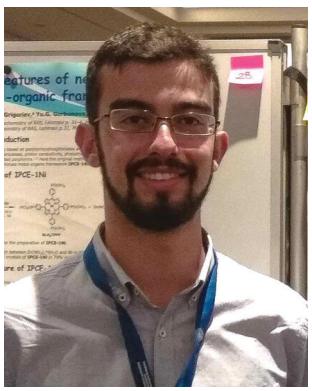

Emmanouil Nikoloudakis

Emmanouil Nikoloudakis has recently finished his PhD degree in the Laboratory of Bio-Inorganic Chemistry, in the Department of Chemistry at the University of Crete. He got his Bachelor and his Master's degrees from the Department of Chemistry at the University of Crete in 2017 and 2019, respectively. In 2017 and 2020 he visited collaborating laboratories in France, in Grenoble and Nantes respectively, as a post-graduate student. In 2021, he visited the University of North Texas, in Denton in USA, under the Fulbright program as a visiting research student where he worked for 4 months.

Ismael López-Duarte

Ismael López-Duarte received his PhD (2010) from the Universidad Autónoma de Madrid under the supervision of Profs. T. Torres and M. V. Martínez-Díaz. He carried out postdoctoral work at the University of Oxford as Marie Curie Fellow (Prof. H. L. Anderson FRS), the Imperial College London (Prof. M. K. Kuimova) and the Queen Mary University of London (Prof. L. Milanesi). Currently, he is Assistant Professor in the Department of Chemistry in Pharmaceutical Sciences at Universidad Complutense de Madrid. His research interests include the design and synthesis of porphyrinoid chromophores for energy and biomedical applications.

Georgios Charalambidis

Georgios Charalambidis received his Bachelor's (2002), Master's (2005), and PhD (2007) degrees from the University of Crete. Currently his is the Principal Investigator in the project entitled "Development of Bio-Inspired Photocatalytic Systems for H_2 Production and CO_2 Reduction" funded from the Hellenic Foundation for Research (HFRI), at the Chemistry Department of the University of Crete. His current research interests include the synthesis of porphyrin-related compounds for their application in solar cells, photocatalytic hydrogen production and CO_2 reduction, artificial photosynthesis molecular materials and self-assembling nanostructures.

Kalliopi Ladomenou

Assistant Professor Kalliopi Ladomenou received her BSc (1998) and MSc from the University of Crete. She obtained her PhD (2002) from the University of Liverpool and worked as a Post-Doctoral Researcher at the University of Edinburgh (2002–2004). Then she joined the University of Crete as a Researcher. In 2022 she was elected as an Assistant Professor at the Chemistry Department of the International Hellenic University. During her research activity she has been involved in several national and European projects. Her research interests include the synthesis of chromophores and catalysts for applications in solar cells, H_2 production, CO_2 reduction, artificial photosynthesis and biomimetic catalysis.

is the process in which plants and living organisms convert energy from sunlight into chemical energy in the form of sugar, which acts as an energy source. In this process, the sunlight absorbed by the light-harvesting pigments, *i.e.*, antenna molecules, is transformed into chemical energy in the reaction center by cascades of energy and electron transfer between organic pigments. Artificial photosynthesis aims to mimic the photochemical process of natural photosynthesis and consists of light absorption and charge-transfer processes together with catalytic oxidation and reduction of H_2O and catalytic reduction of CO_2.[9] Artificial photosynthesis can play a crucial role, without a doubt, in tackling global energy and environmental problems, not only in producing renewable fuels such as H_2 but also in reducing atmospheric CO_2 emissions by converting CO_2 into valuable chemicals. In the thermochemical method, water and CO_2 can be converted into solar fuels including H_2 by using sunlight as the heat source to drive endothermic chemical reactions.

CO_2 is a thermodynamically extremely stable molecule and breaking the C=O bonds (750 kJ mol^{-1}) requires high energy. Consequently, CO_2 reduction is a notably challenging process due to the large conversion energy barrier, since any reduction process demands high energy input.[10] An encouraging approach to overcome the energy sufferings of CO_2 conversion has been the direct use of solar energy by mimicking natural photosynthetic systems. Indeed, compared to the CO_2 reduction methods such as thermochemical conversion,[11] electrochemical reduction[12–15] or biochemical technology,[16] the photocatalytic conversion of CO_2 based on artificial photosynthesis is the most attractive route in terms of using direct solar energy and water at room temperature and atmospheric pressure.[17]

Photocatalytic conversion is the process in which a certain photocatalyst, *i.e.*, semiconductors or molecular chromophores, uses the energy from sunlight to drive the reduction reactions of CO_2 into carbon-based products and the splitting of water into H_2 and O_2. The photocatalytic process can be divided into homogenous and heterogeneous systems depending on the reaction phase. In a photochemical system three components are essential (i) a photosensitizer (PS) able to absorb visible light generating excited species $PS^{\bullet}$ with useful redox properties (ii) a sacrificial electron donor (SED) that can be reduced or oxidized by quenching of the excited species $PS^{\bullet}$ in electron transfer reactions and (iii) a catalyst, able to collect several electrons facilitating the exchange of two or four electrons with water. All the above components can be in the same (homogenous) or in different phases (heterogeneous).

Each system has its own set of benefits and drawbacks. In homogeneous photocatalysis, the molecular structure of the components is usually well-defined, and this enables the determination of the corresponding catalytic mechanism. The chemical versatility of the molecular catalysts provides control of the physical, optical, and electronic properties by chemical modifications. Furthermore, these systems present higher selectivity and the identification of the structural characteristics that impact catalytic activity is easier. However, homogeneous catalysts suffer from high costs, difficult recovery/separation process from the reaction, and lack of long-term use. Although heterogeneous systems have the advantage of efficient recovery and recyclability of photocatalysts, other factors such as low light-harvesting capacity and low reactivity limit the overall efficiency. A hybrid catalyst, on the other hand, is a potential way to combine the advantages of homogeneous and heterogeneous catalysts by immobilizing a homogeneous molecular catalyst on solids.

The operating principle of the photocatalytic systems based on a single semiconductor or a molecular PS for water splitting and CO_2 reduction are very similar as shown in Fig. 1.

There are four critical processes in the operation of photocatalytic reduction including, light-harvesting, charge separation, redox reactions, and product desorption. In this process, the absorption of light by the photosensitizer generates electron–hole pairs which can either undergo the desired charge or turn

Mine Ince

Prof. Mine Ince received her PhD (2012) from the Universidad Autónoma de Madrid (UAM) under the supervision of Profs. T. Torres and M.V. Martínez-Díaz. She, then, joined the group of Prof. Michael Grätzel at EPFL (Switzerland) as a postdoctoral researcher (2013). She is currently a full professor in the Department of Natural and Mathematical Sciences at Tarsus University (Turkey). Her current research interests include the preparation of novel phthalocyanine-based materials for their application in organic photovoltaic devices and in photocatalysis (CO_2 reduction and water splitting).

Athanassios G. Coutsolelos

Professor Athanassios G. Coutsolelos received his PhD from the University of Dijon in France (1985) with Prof. R. Guilard. After postdoctoral research (1985–1986), at the University of Texas in Houston with Prof. K. M. Kadish, he joined the University of Crete where he obtained a full Professor position in 1999. He was invited as a Visiting Professor at the University of Notre Dame (USA) in 1996, as well as in Orsay (1994, 2000 and 2016) and in Strasbourg (2010), France. He is the director of the Laboratory of Bioinorganic Chemistry and his primary research interests focuses on the development of new materials based on porphyrin derivatives for artificial photosynthesis.

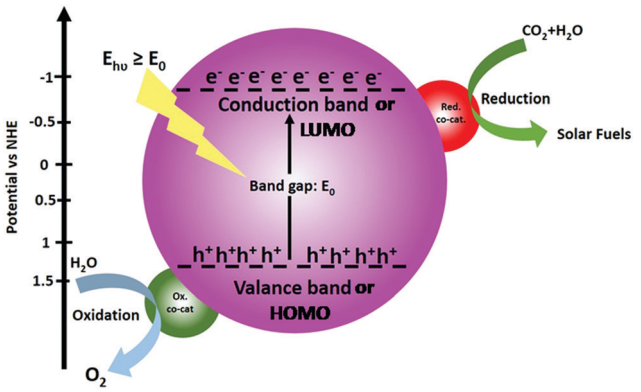

Fig. 1 Schematic energy diagram of photocatalytic water splitting and CO_2 reduction reactions.

back to the ground state by the radiative or non-radiative process (recombination). The photo-excited electron is used in H_2O and CO_2 reduction reactions, meanwhile, the holes in the valence band are consumed by oxidation of H_2O to produce O_2.[18] For both photocatalytic H_2 production from H_2O and CO_2 reduction, the CB level/LUMO orbital must be more negative than the H_2 evolution potential and the reduction potential of the desired CO_2 conversion products (Fig. 1). In addition, the VB level/HOMO orbital in both systems should be more positive than the oxygen generation potential.

As far as the reduction products are concerned, CO_2 can be converted to a variety of chemicals such as formic acid, carbon monoxide, methanol, C2+ alcohols, methane *etc.* (Table 1). The product diversity of CO_2 reductions largely depends on the reaction conditions, types of catalyst and the number of electron and proton transfers. Since the selectivity problem of the CO_2 reduction product is much more pronounced due to the diversity of CO_2 reduction products compared to H_2O reduction, photocatalysts with high selectivity are required for photocatalytic CO_2 reduction. One of the most important aspects governing catalytic efficiency and product selectivity is the rational design of catalysts with a proper structure since the optimum CB band edge position/HOMO–LUMO gap provide sufficient driving force for photo-driven redox processes. However, the product selectivity and inhibition of H_2 formation are governed by several factors such as active sites of catalysts, adsorption of the reactants, desorption/dissociation of the products *etc.* Meanwhile, the splitting of water consists of two steps of reactions namely oxidation and reduction of water to produce O_2 and H_2, respectively. Hydrogen and oxygen production from water by visible light requires one or several intermediates able to absorb visible light, to convert the excitation energy to redox energy (charges) and to transfer several electrons to water leading to the formation of H_2 and O_2. The reaction is a multi-electron transfer process, where the hydrogen requires two electrons reaction (g), Table 1) while oxygen provides four electrons (reaction (f), Table 1).

Table 1 Some possible reactions related to the photocatalytic conversion of CO_2 reduction and water splitting (E^0 *vs.* NHE at pH 7)

$CO_2 + 2e^- + 2H^+ \rightarrow CO + H_2O \quad E^0 = -0.53$ V	(a)
$CO_2 + 2e^- + 2H^+ \rightarrow HCOOH \quad E^0 = -0.61$ V	(b)
$CO_2 + 4e^- + 4H^+ \rightarrow CH_2O + H_2O \quad E^0 = -0.48$ V	(c)
$CO_2 + 6e^- + 6H^+ \rightarrow CH_3OH + H_2O \quad E^0 = -0.38$ V	(d)
$CO_2 + 8e^- + 8H^+ \rightarrow CH_4 + 2H_2O \quad E^0 = -0.24$ V	(e)
$2H_2O + 4h^+ \rightarrow O_2 + 4H^+ \quad E^0 = 0.81$ V	(f)
$2H^+ + 2e^- \rightarrow H_2 \quad E^0 = -0.42$ V	(g)

Homogeneous photocatalysis is used to convert solar energy into accessible and clean fuel in a molecular accessible form. The difficulty in this type of catalysis is the separation of the catalyst after the completion of the reaction and the low stability of molecular catalysts. The first homogeneous photocatalytic H_2 production was reported by Lehn *et al.*[19] In this review, we will only present the most recent reports of this category. In typical examples of photocatalytic H_2 production, an organometallic complex is a catalyst and an organic or organometallic compound is the PS. In order to achieve effective H_2 production, the PS must be able to absorb photons from a light source to reach an excited state. Then the excited state is quenched by electrons from an electron donor. This procedure can be achieved in two different ways, a reductive or an oxidative path. During the reductive quenching, an electron is transferred from the SED to the PS. The photosensitizer is reduced and an electron is transferred to the catalyst. In the case of oxidative quenching, an electron from the excited PS is transferred to the catalyst and the oxidized form of the PS oxidizes the SED. Then the catalyst reduces the protons, resulting to H_2 production.

Heterogeneous photocatalysis usually use photocatalytic system with fulfilling fundamental requirements: (1) high light-harvesting efficiency; (2) fast charge separation; (3) slow charge recombination rate, could have the potential to address these challenges. Since the first breakthroughs came with a photoreduction of CO_2 in an aqueous suspension catalyzed by diverse semiconductors[20] and an evolution of H_2 *via* photoelectrochemical water splitting on TiO_2,[21] researchers have concentrated their efforts on developing effective photocatalysts. Most common photocatalysts are based on transition metals or semiconductors such as TiO_2, ZnO, $BiVO_4$, ZrO_2, WO_3, ZnS, CdS, *etc.*[22,23] However, the photocatalytic performance of these semiconductors in their pristine form is substantially limited by insufficient absorption of visible light with wide bandgap, poor charge separation and concomitant low conversion efficiency. An ideal photocatalyst should match key requirements such as a suitable energy band structure that efficiently absorbs light throughout a large portion of the solar emission spectrum and efficient charge transfer. Reports have indicated that structural and chemical modifications of photocatalyst including metal/ion doping, semiconductor/co-catalyst coupling, dye-sensitization, creating surface disordering, and defects, controlled morphology, *etc.*, are effective ways to increase the photocatalytic performance of photocatalysts and to tune the photocatalytic selectivity.[24,25]

Among them, heterojunction-based system (p–n junction), Z scheme configuration and dye sensitization of semiconductors are of particular interest in the point of having the potential to

address the challenge of the charge recombination rate, solar light harvesting, and selectivity and stability towards the desired products.[18] The additional benefit of these structures is to provide an extra photoexcited electron which is advantageous in terms of yield of reduction product. Similar to those proposed these structure modifications, the incorporation of co-catalyst (generally noble metal nanoparticles) which serve as active catalytic centers play an important role in reducing recombination by extracting excited electrons.[23]

Artificial antenna systems based on organic sensitizers have attracted much attention as light-harvesting photosensitizers (PSs) in artificial energy conversion systems, such as dye-sensitized solar cells (DSSCs).[26] Attachment of the photosensitizers on the semiconductor surface increases the light-harvesting ability and facilitates the charge transport properties without altering the catalytic activity of the semiconductor. Since the key process of this system is photo-induced charge separation and transfer, the dye is the pivotal component in artificial photosynthetic devices. The role of dye is multiple as it absorbs light and then directs the charge transfer kinetics and the dye regeneration. The dyes must, therefore, fulfil some essential requirements such as high LUMO energy level than CB of semiconductor, more positive oxidation potential than SED, broad absorption spectrum cover the whole visible region and even the part of near-infrared (NIR) and an anchoring group to bind strongly onto a semiconductor.[27]

In order to maximize the productivity of the photocatalyst, particularly in the function of solar irradiation, the utilization of photosensitizer to form dye-sensitized photocatalyst (DSP) is an alternative strategy to increase the yield of solar to fuel conversion.[27] Considering that nearly 50% of the solar energy lies in the visible-NIR region, a light-harvesting system capable of absorbing in this region is required not only to avoid loss of photons but also to increase charge transfer rates without altering the catalytic activity of the semiconductor. Using a dye sensitizer to enhance the functionality of a photocatalyst has proven to be a highly successful approach to panchromatic sensitization of semiconductors, and it is widely utilized in artificial energy conversion systems such as DSSCs.[26] The operating mechanism of DSP is very similar to DSSCs, that is, the excitation of the dye upon visible-light irradiation is followed by charge separation by electron injection from excited dye to the CB of semiconductor and leaving the photogenerated holes in dye sensitizer (Fig. 2). In contrast to DSSCs, the excited electron is used to reduce CO_2 or H_2O on the semiconductor surface while the oxidized dye sensitizer is regenerated by electron transfer from the SED component.[28]

Apart from the desired pathway of electron transfer (injection and dye regeneration) processes, there are also undesirable competing processes, namely the recombination of injected electrons with oxidized dye and/or the relaxation of excited electrons in the ground state which are critical for the function of the DSP.[25] In this electron-transfer process, SED plays an important role, not only restricting the recombination between the injected electrons and dye cation but also suppressing the photocatalytic O_2 production half-reaction. Similarly, the incorporation of co-catalyst on the semiconductor appears as a

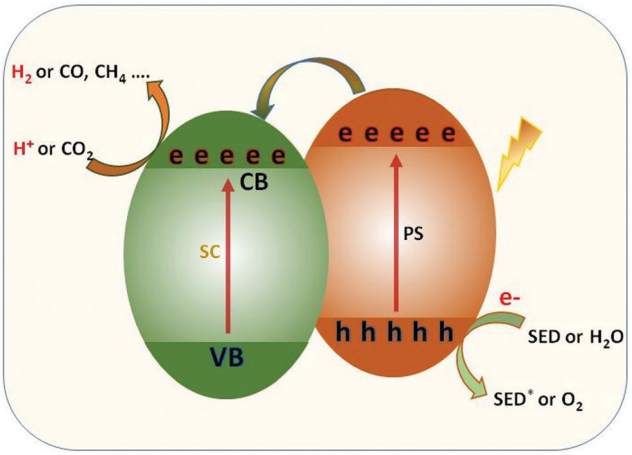

Fig. 2 Dye-sensitized photocatalyst, SC: semiconductor, PS: photosensitizer.

possible way to improve the photocatalytic activity by increasing charge separation and suppressing the charge recombination.[27] From the H_2 production performance point of view, the loading of semiconductors with a noble metal-based co-catalyst, which serves as an active centre, such as Pt, Au, Pd, Rh *etc.* is required to increase the photocatalytic H_2 production efficiencies. The large work functions and better conductivity of noble metals accelerate photocatalytic reduction reactions by extracting photoinduced electrons from the semiconductor surface.[29]

Dye-sensitized photoelectrochemical cells (DSPECs) towards proton as well as CO_2 reduction have attracted extensive scientific attention.[30–33] The development of molecular-based DSPECs opened the way to the utilization of porphyrins and phthalocyanines in this field. These systems are designed to perform a reduction catalytic reaction at the cathode like H_2 production or CO_2 conversion while an oxidation process like O_2 production is performed at the anode. One target of such systems is to create water-splitting devices with the benefit of separately H_2 and O_2 production.[34,35] Moreover, the big advantage of DSPEC schemes is that no sacrificial agent is needed since the necessary electrons for the reduction are provided from the oxidation process through the external circuit. On the other hand, a common drawback of these systems is the need to apply external electrical bias to accomplish the desired conversions, however, there are examples where this issue was overwhelmed and only the energy input from sunlight was necessary. Noteworthy, the nature of the dye sensitizer in all the aforementioned systems strongly affects the activity of the catalysts.

Porphyrins and related compounds occur in nature and are essential for life on Earth as they play a crucial role in relevant biological processes. In natural photosynthesis, chlorophylls are primary components of the light-harvesting antenna systems which mission is to collect most of the sunlight and then efficiently transfer the resulting singlet excitation energy to the reaction centers. Porphyrins (Pors) are macrocycles composed of four pyrrole units interconnected by methine bridges, presenting a highly conjugated 18-π electron aromatic system that accounts for their unique optical and physicochemical properties. Phthalocyanines (Pcs) are synthetic analogous of porphyrins and are

both a family of pigments that present similarities between their structures. Pcs are composed of four isoindole units linked by four aza-nitrogen bridges. The Pc macrocycle is also a fully aromatic 18-π electron system. Because of their extraordinary properties, it is not surprising that porphyrins, phthalocyanines and other porphyrinoid derivatives have been the candidate of choice for constructing artificial molecule-based reaction centers that mimic the light-harvesting and charge-separation functions in the photosynthetic reaction center, with the aim to shed light on the basic principles that govern photoinduced charge separation and electron transfer processes.[36] Pors and Pcs are thermally and photochemically stable chromophores whose optical and electronic properties can be easily tailored by systematic modification of the peripheral and non-peripheral substituents and the metal centre. Pors and Pcs possess efficient light absorption features in the visible and NIR regions of the solar spectrum, which makes them ideal components of light-harvesting systems in artificial photosynthesis and photovoltaics. In particular, Pors have a very intense absorption in the visible region centered around 400–450 nm (Soret band) and moderate absorption around 500–650 nm (Q band). While Pcs possess a very strong absorption at 300–400 nm (Soret band) and 700 nm (Q band). The possibilities of engineering novel functional materials based on Pcs and Pors macrocycles for applications in artificial photosynthesis are almost endless because of the extraordinary synthetic versatility and robustness of these macrocycles. Over the years, a myriad of porphyrins and analogues have been extensively studied as model compounds that mimic the light-harvesting and charge-separation functions in the photosynthetic reaction center and relevant results have been summarised in excellent reviews.[37–40]

This review highlights recent advances in the development of porphyrinoid-based photocatalytic H_2 production and CO_2 reduction schemes. In particular, the roles of porphyrin and phthalocyanine derivatives as dye sensitizers, catalysts and co-catalysts and the influence of their structural aspects on the photocatalytic H_2 production and CO_2 reduction activity are systematically discussed. A section of this review will also pay particular attention to the use of supramolecular assemblies based on phthalocyanines or porphyrins to promote the visible-light-driven photocatalytic CO_2/H_2O conversion. The recent advances in the effects of the integration of Pc and Pors as catalytically active building blocks and/or photosensitizers in both homogeneous and heterogeneous photocatalytic systems on CO_2 conversion and H_2 production efficiency will be highlighted.

2. Porphyrins for photocatalytic H_2 production

2.1 Homogeneous systems

In these homogeneous systems all components, the reactants and the catalyst are in the same phase (solution) and are uniformly distributed. In this section, recent examples of homogeneous photocatalytic H_2 production will be discussed, based on porphyrin molecules that have been used either as PSs or as catalysts. In the first photocatalytic systems, different porphyrins are utilized as PS and cobalt-based complexes are mainly employed as catalysts. There are also a few examples where the PS and the catalyst are covalently linked. The porphyrins that are used as catalysts are water-soluble cobalt-based molecules.

2.1.1 Porphyrins as chromophores in homogeneous H_2 production systems. In this section, examples of homogenous catalysis will be discussed using a porphyrin as PS and an appropriate molecular catalyst in the presence of a SED. The main drawback of all these examples is the stability of either the photosensitizer or the molecular catalyst. However, these systems are usually composed of noble metal-free molecules with facile and low-cost synthetic methods and most of them are able to produce H_2 in aqueous media. One common photosensitizer that is used in this section is the tetracationic water soluble porphyrin, the *meso*-tetrakis(1-methyl-pyridinium-4-yl)porphyrin chloride H_2TMPyP, varying the metal in the center of the porphyrin ring (Fig. 3).

Coutsolelos and co-workers used the Zn porphyrin, ZnTMPyP as photosensitizer and a cobaloxime complex [CoIII(dmgH)$_2$(py)Cl] Cat1 as a catalyst (Fig. 4).[41] This system upon visible photo-irradiation ($\lambda > 400$ nm) of light produced H_2 in MeCN–H_2O (1 : 1) with 10% triethanolamine (TEOA) as SED. A maximum of 280 turn over numbers (TONs) was obtained after 25 h of irradiation. Next, the same research group used the same water-soluble porphyrin as PS, ZnTMPyP and a series of cobaloxime catalysts bearing different axial groups Cat1-10 (Fig. 4).[42]

The catalysts were synthesized altering the pyridine and imidazole axial ligands. All photocatalytic experiments were

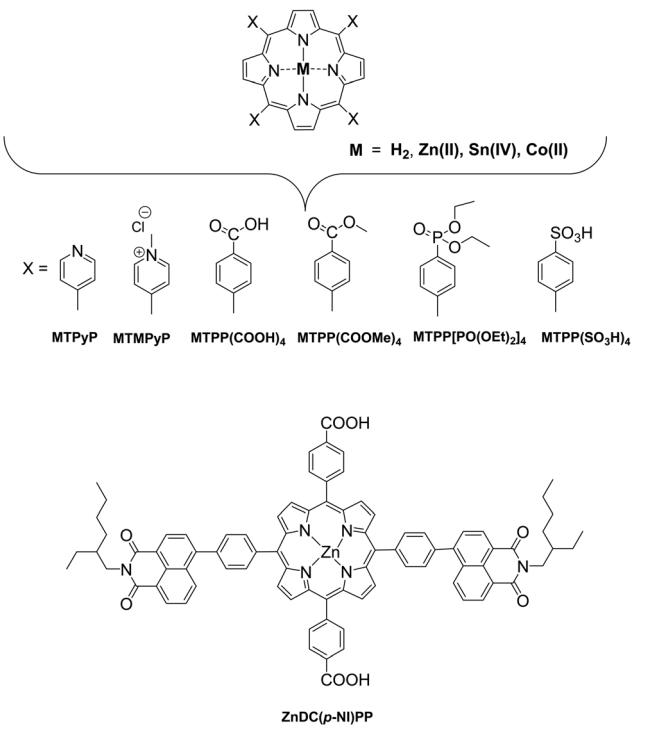

Fig. 3 Chemical structures of porphyrins used as photosensitizers.

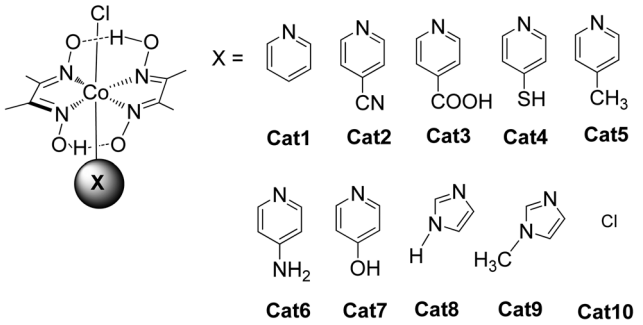

Fig. 4 Chemical structures of various cobaloxime-based catalysts.

done under similar experimental conditions with their previous work as shown in (Table 2, entries 1a, b–11). More specifically, *N*-methyl imidazole Cat9 achieved 1135 TONs for H_2 production upon 50 h of irradiation, while Cat8 with an imidazole as axial ligand reached 565 TONs. In the case of the catalysts that have pyridine as an axial ligand, the ones with an electron-donating group were proved to be more effective towards H_2 production (Table 2, entries 9 and 10). Moreover, upon addition of TiO_2 nanoparticles to the less active catalyst Cat3 (40 TON) the activity of the system increased to 223 TONs (Table 2, entry 4). This enhanced activity in the presence of TiO_2 may be attributed to the lower electron-withdrawing properties of the new complex or due to the role of TiO_2 as an electron reservoir. In a similar work, Bodedla *et al.* synthesized a *meso*-substituted porphyrin conjugated with two naphthalimide (NI) moieties (ZnDC(*p*-NI)PP, Fig. 3) and utilized as photosensitizer in combination with cobaloxime catalyst Cat1.[43] ZnDC(*p*-NI)PP exhibited a H_2 evolution rate of 35.70 mmol g^{-1} h^{-1} and reached a TON of 5958 (Table 2, entry 11), outperforming the reference systems lacking the NI moieties. The enhanced activity of this system was attributed to the intramolecular energy transfer from the NI donor to the porphyrin acceptor that would promote long-lived photoexcitation states. In addition, Coutsolelos and coworkers extended their research and used Sn metallated water-soluble porphyrin, SnTMPyP as photosensitizer with different cobaloximes as catalysts Cat1, Cat3, Cat7 in a mixture of 1 : 1 (v/v) MeCN and aqueous TEOA (10%) solution (Fig. 3 and 4).[44] The samples were irradiated with a 500 W Xenon lamp at $\lambda >$ 440 nm and H_2 production occurred. The best result obtained with Cat 1 that reached a TON of 150 at pH = 7 after 100 h of irradiation, while when Cat3 was used 53 TON was obtained. Also, when TiO_2 was added at the catalyst Cat3 the hydrogen production was increased to 131 TON. In the case of Cat7, no H_2 was produced under the same experimental conditions (Table 2, entries 12–15). Exploring more cobalt-based water soluble catalysts Chavarot-Kerlidou and Coutsolelos studied the H_2 production of a novel polypyridyl cobalt catalyst $CoCatBF_4$, with the water-soluble photosensitizer ZnTMPyP (Fig. 5).[45] The system was able to evolve H_2 (443 TONs) under visible light irradiation at pH 4.5 and in the presence of ascorbic acid (AA)/tris-(2-carboxyethyl)phosphine (TCEP) 0.1 M each, as sacrificial electron donor system (Table 2, entry 16).

All the previous work that was conducted in our group, inspired us to explore further positively, negatively charged and neutral zinc and tin porphyrins as photosensitizers with cobaloximes as catalysts Cat1 and Cat9 for H_2 evolution (Fig. 3 and 4).[46] We wanted to investigate if different charges on the photosensitizer can influence its ability to produce H_2. The optimum conditions of this type of system were found and the positively charged ZnTMPyP reached 1135 TON, where the neutral tin porphyrins SnTMPyP, $SnTPP(COOMe)_4$ and $SnTPP[PO(OEt)_2]_4$ reached maximum TONs of 303, 128 and 48, respectively. In all cases, the catalyst that gave the best results was Cat9 at pH 7 in 1 : 1 MeCN/H_2O and TEOA [5% (v/v)] (Table 2, entries 17–19). Moreover, after photophysical and electrochemical studies it was found that the photocatalysis was proceeding mostly *via* oxidative quenching of the PS. In another report, a water soluble Sn(IV) porphyrin SnTCPP was used as photosensitizer and as catalyst a cobalt-based molecule Cat1.[47] The system was able to produce H_2 with 1.3 TON under visible light irradiation at pH 8.5 and with TEOA as SED (Table 2, entry 20). Additionally, a single water-soluble porphyrin $ZnTPP(SO_3)^{4-}$ was reported to produce H_2 in the presence of different sacrificial electron donors and in the absence of a catalyst.[48] The photocatalytic system produced H_2 with 0.03 TON in TEOA at pH 7, in the presence of an inorganic salt Na_2SO_3 with 0.11 TON. The best result was obtained upon visible light irradiation in the presence of triethylamine (TEA) with 1.15 TON (Table 2, entries 21–23). In this case, the water-soluble porphyrin had a dual role; it could act as a light-harvesting chromophore and as a hydride supplying co-catalyst, with the formation of a chlorin–phlorin anion intermediate.

In an attempt to prepare more effective systems for H_2 evolution, researchers prepared a photocatalytic system that was able to encapsulate the catalyst in a cage-like structure. More specific, a pyridyl phosphole FeFe hydrogenase mimic was encapsulated in a metal–organic cage structure based on zinc porphyrin.[49] More specifically, the trihedral cage $Fe_4(ZnL)_6$ was composed of six metallated porphyrins that were connected with four Fe(II) corners (Fig. 6). The complex was soluble in organic solvents, therefore upon irradiation in MeCN, using trifluoroacetic acid (TFA) as a proton source in and 4-mercaptobenzoic acid as SED, the system produced low amount of H_2 with no decomposition (Table 2, entry 24). When TEA was used as SED H_2 was produced, but decomposition of the catalyst was observed. It was found that fast photoinduced electron transfer (0.5 ps) occurred from the cage to the catalyst that was present inside the cage, but the charge recombination of this system was also fast (37 ps).

A different approach in homogenous photocatalytic H_2 production was the preparation of complexes where the photosensitizer and the catalyst are covalently linked. According to this approach, a bimetallic porphyrin $MPtX_2$ was synthesized with Zn, Co or Cu and with platinum at the phenanthroline side with either chloride or iodide ligands (Fig. 7).[50] The photoreduction of $MPtX_2$ was performed with a monochromatic LED irradiation at 470 nm and with the use of trimethylamine as SED in the presence of 10% H_2O as a proton source. The zinc complex $ZnPtX_2$ was able to produce H_2, while Cu and Co derivatives showed no activity. The $ZnPtCl_2$ photocatalyst with the chloride ligands proved to be seven times more effective towards H_2 evolution

Table 2 Photocatalytic performance of porphyrin based homogenous H_2 evolving systems

Entry	PS (C)	Catalyst (C)	SED (C)	Solvent	Light source	Irr. time (h)	TON	TOF (h^{-1})	Ref.
1a	ZnTMPyP (4.0×10^{-5} M)	Cat1 (4.9×10^{-4} M)	TEOA 5% (v/v)	MeCN/H_2O (1 : 1 v/v), pH = 7	500 W Xenon lamp $\lambda > 400$ nm	25	280		41
1b	ZnTMPyP (4.0×10^{-5} M)	Cat1 (4.9×10^{-4} M)	TEOA 5% (v/v)	MeCN/H_2O (1 : 1 v/v), pH = 7	500 W Xenon lamp $\lambda > 440$ nm	63	320	8	42
2	ZnTMPyP (4.0×10^{-5} M)	Cat2 (4.9×10^{-4} M)	TEOA 5% (v/v)	MeCN/H_2O (1 : 1 v/v), pH = 7	500 W Xenon lamp $\lambda > 440$ nm	11	77	10	42
3	ZnTMPyP (4.0×10^{-5} M)	Cat3 (4.9×10^{-4} M)	TEOA 5% (v/v)	MeCN/H_2O (1 : 1 v/v), pH = 7	500 W Xenon lamp $\lambda > 440$ nm	26	40	2	42
4	ZnTMPyP (4.0×10^{-5} M)	Cat3-TiO_2 (4.9×10^{-4} M)	TEOA 5% (v/v)	MeCN/H_2O (1 : 1 v/v), pH = 7	500 W Xenon lamp $\lambda > 440$ nm	29	223	9	42
5	ZnTMPyP (4.0×10^{-5} M)	Cat4 (4.9×10^{-4} M)	TEOA 5% (v/v)	MeCN/H_2O (1 : 1 v/v), pH = 7	500 W Xenon lamp $\lambda > 440$ nm	43	425	12	42
6	ZnTMPyP (4.0×10^{-5} M)	Cat5 (4.9×10^{-4} M)	TEOA 5% (v/v)	MeCN/H_2O (1 : 1 v/v), pH = 7	500 W Xenon lamp $\lambda > 440$ nm	40	443	9	42
7	ZnTMPyP (4.0×10^{-5} M)	Cat6 (4.9×10^{-4} M)	TEOA 5% (v/v)	MeCN/H_2O (1 : 1 v/v), pH = 7	500 W Xenon lamp $\lambda > 440$ nm	—	—	—	42
8	ZnTMPyP (4.0×10^{-5} M)	Cat7 (4.9×10^{-4} M)	TEOA 5% (v/v)	MeCN/H_2O (1 : 1 v/v), pH = 7	500 W Xenon lamp $\lambda > 440$ nm	—	—	—	42
9	ZnTMPyP (4.0×10^{-5} M)	Cat8 (4.9×10^{-4} M)	TEOA 5% (v/v)	MeCN/H_2O (1 : 1 v/v), pH = 7	500 W Xenon lamp $\lambda > 440$ nm	50	565	11	42
10a	ZnTMPyP (4.0×10^{-5} M)	Cat9 (4.9×10^{-4} M)	TEOA 5% (v/v)	MeCN/H_2O (1 : 1 v/v), pH = 7	500 W Xenon lamp $\lambda > 440$ nm	50	1135	23	42
10b	ZnTMPyP (4.0×10^{-5} M)	Cat9 (4.9×10^{-4} M)	TEOA 5% (v/v)	MeCN/H_2O (1 : 1 v/v), pH = 7	500 W Xenon lamp $\lambda > 440$ nm	23	290	10	42
11	ZnDC(*p*-NI)PP (1.0×10^{-5} M)	Cat1 (2.0×10^{-3} M)	AA 0.4 M	THF/H_2O (1 : 9 v/v), pH = 7.4	148.5 W LED light	5	5958	—	43
12	SnTMPyP (8.0×10^{-5} M)	Cat1 (9.8×10^{-4} M)	TEOA 10% (v/v)	MeCN/H_2O (1 : 1 v/v), pH = 7	500 W Xenon lamp $\lambda > 440$ nm	100	150		44
13	SnTMPyP (8.0×10^{-5} M)	Cat3 (9.8×10^{-4} M)	TEOA 10% (v/v)	MeCN/H_2O (1 : 1 v/v), pH = 7	500 W Xenon lamp $\lambda > 440$ nm	100	53		44
14	SnTMPyP (8.0×10^{-5} M)	Cat3-TiO_2 (9.8×10^{-4} M)	TEOA 5% (v/v)	MeCN/H_2O (1 : 1 v/v), pH = 7	500 W Xenon lamp $\lambda > 440$ nm	100	131		44
15	SnTMPyP (8.0×10^{-5} M)	Cat7 (9.8×10^{-4} M)	TEOA 10% (v/v)	MeCN/H_2O (1 : 1 v/v), pH = 77	500 W Xenon lamp $\lambda > 440$ nm		—	—	44
16	ZnTMPyP (4.0×10^{-5} M)	$CoCatBF_4$ (4.9×10^{-4} M)	AA/TCEP (100 mM each)	H_2O, pH = 4.5	White LED	25	443		45
17	SnTMPyP (4.9×10^{-4} M)	Cat9 (4.9×10^{-4} M)	TEOA 5% (v/v)	MeCN/H_2O (1 : 1 v/v), pH = 7.0	White LED	96	303		46
18	$SnTPP(COOMe)_4$ (4.0×10^{-5} M)	Cat9 (4.9×10^{-4} M)	TEOA 5% (v/v)	MeCN/H_2O (1 : 1 v/v), pH = 7.0	White LED	48	128		46
19	$SnTPP[PO(OEt)_2]_4$ (4.0×10^{-5} M)	Cat9 (4.9×10^{-4} M)	TEOA 5% (v/v)	MeCN/H_2O (1 : 1 v/v), pH = 7.0	White LED	48	48		46
20	$SnTPP(COOH)_4$ (1.0×10^{-3} M)	Cat1 (1.0×10^{-4} M)	TEOA 60 mM	H_2O, pH = 8.5	White LED	20	1.3		47
21	$ZnTPP(SO_3)^{4-}$ (8.3×10^{-4} M)	—	TEOA 10% (v/v)	H_2O, pH = 7.0	Mercury lamp, 100 W, $\lambda > 400$ nm filter	70	0.03		48
22	$ZnTPP(SO_3)^{4-}$ (6.7×10^{-5} M)	—	Na_2SO_3 800 mM	H_2O, pH = 8.0	Mercury lamp, 100 W, $\lambda > 400$ nm	29	0.11		48
23	$ZnTPP(SO_3)^{4-}$ (2.3×10^{-4} M)	—	TEA 2% (v/v)	H_2O, pH = 10.0	Mercury lamp, 100 W, $\lambda > 400$ nm	21	1.15		48
24	$Fe_4(ZnL)_6$ (8.0×10^{-5} M)	—	4-Mercapto benzoic acid 200 mM	MeCN, TFA 0.03 mM	LED, 40 mW, $\lambda = 470$ nm	2	0.4		49
25	$MPtX_2$	—	TEA 30%	MeCN/TEA/H_2O (6 : 3 : 1 v/v)	LED, 40 mW, $\lambda = 470$ nm	24	15.6	0.66	50
26	Mo_2–$N(CH_3)_3$ (5.0×10^{-5} M)	—	TEOA 188 mM	THF/H_2O (1 : 1 v/v), pH = 9.0	Xenon arc lamp (AM 1.5)	4	640	160	52
27	Mo_2–OCH_3 (5.0×10^{-5} M)	—	TEOA 188 mM	THF/H_2O (1 : 1 v/v), pH = 9.0	Xenon arc lamp (AM 1.5)	4	586	146	52
28	Mo_2–OCF_3 (5.0×10^{-5} M)	—	TEOA 188 mM	THF/H_2O (1 : 1 v/v), pH = 9.0	Xenon arc lamp (AM 1.5)	4	459	115	52
29	MZnP–Ir (1.0×10^{-5} M)	Cat1 (4.0×10^{-5} M)	TEA 800 mM	MeCN/H_2O (2 : 1 v/v)	White OLED, 148.5 mW cm^{-2}	40	82		53
30	TZnP–Ir (1.0×10^{-5} M)	Cat1 (4.0×10^{-5} M)	TEA 800 mM	MeCN/H_2O (2 : 1 v/v)	White OLED, 148.5 mW cm^{-2}	40	246		53
31	ZnP–T–Ir (1.0×10^{-5} M)	—	TEOA 800 mM	MeCN/H_2O (1 : 9 v/v)	White OLED, 148.5 mW cm^{-2}	5		1.42 mmol g^{-1} h^{-1}	54
32	$Ru(bpy)_3^{2+}$ (1.0×10^{-3} M)	CoTMPyP (2.5×10^{-6} M)	AA 100 mM	phosphate buffer 1 M, pH = 7.0	Xenon arc lamp, 175 W, $\lambda > 400$ nm	4	725	8.8	55
33	$[Ru(bpy)_3]^{2+}$ (1.2×10^{-3} M)	$CoTPP(SO_3H_4$ (1.5×10^{-6} M)	AA 300 mM	phosphate buffer 1 M, pH = 6.8	LED, $\lambda = 420$ nm	1.5	6410	120.8 min^{-1}	56

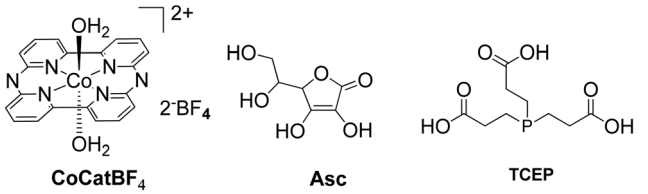

Fig. 5 Chemical structure of the cobalt-based catalyst, and the employed SEDs.

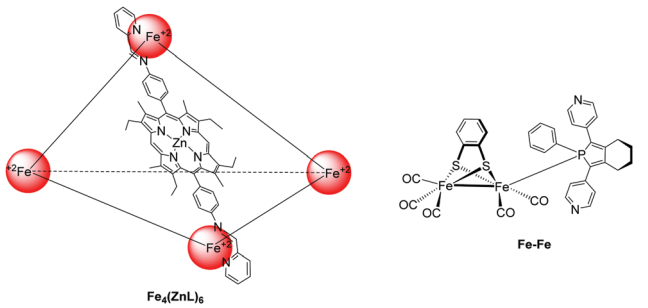

Fig. 6 Chemical structure of the cage $Fe_4(ZnL)_6$ and hydrogenase mimic FeFe.

compared to its iodine analogue $ZnPtI_2$, 15.6 *versus* 2.1 TON, respectively, after 24 h of light irradiation (Table 2, entry 25).

Manton *et al.* synthesized a free base and Zn porphyrin–cobaloxime complex MPyCat where the porphyrin was linked to a cobaloxime *via* a pyridyl cobalt bond (Fig. 8).[51] After 20 h of irradiation with different LED light sources in THF/H_2O with 33% v/v TEA as SED, no H_2 production was detected. In contrary, both complexes MPyCat were able to produce H_2 upon electrochemical conditions.

Moreover, a series of three photocatalysts were able to reduce protons to H_2 and synthesized by combining a zinc porphyrin with a Mo_2 quadruply-bonded unit.[52] The three complexes differ in the X unit of the aryl group in the *para* position of the ligand (Fig. 9). These X units were $N(CH_3)_3$ as electron-donating groups, OCH_3 as intermediate groups or OCF_3 as electron-withdrawing groups. Photocatalytic experiments were

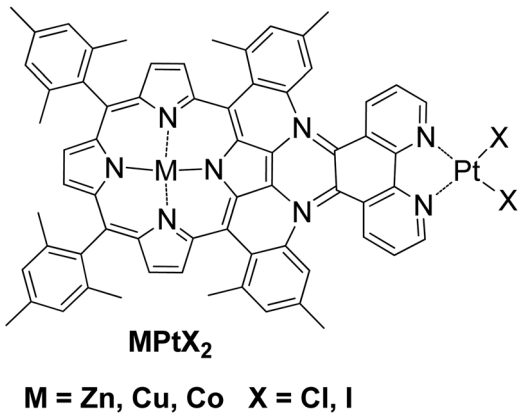

Fig. 7 Chemical structure of dinuclear π-extended porphyrin $MPtX_2$.

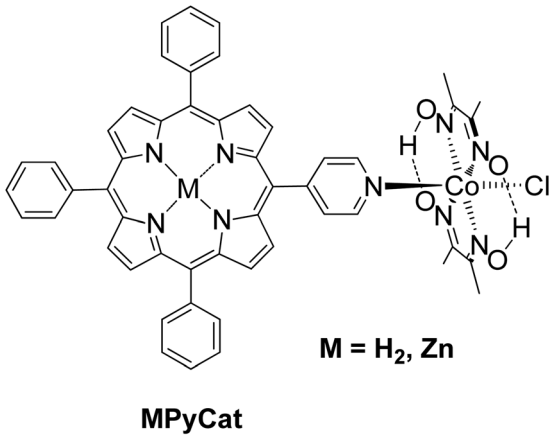

Fig. 8 Chemical structures of porphyrin–cobaloxime complex.

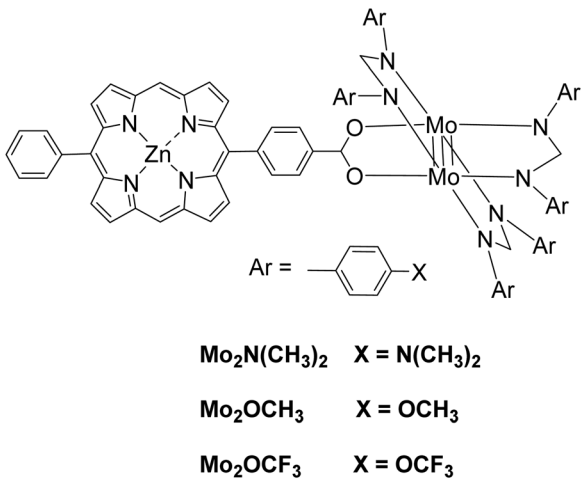

Fig. 9 Chemical structure of photocatalytic complexes Mo_2X.

done with TEOA as SED donor in THF/H_2O (1 : 1 v/v). After irradiation with a Xenon lamp, H_2 was produced and its production ability was increased with the electron-donating ability of the X groups, 640 TON for Mo_2–$N(CH_3)_3$, 586 TON for Mo_2–OCH_3, 459 TON for Mo_2–OCF_3 (Table 2, entries 26–28).

In a different approach, a bimetallic Zn–porphyrin covalently linked to Ir(III) was used as PS and a chloro(pyridine)cobaloxime molecule Cat1 as a catalyst in homogenous H_2 evolution.[53] In this report, two different porphyrins were synthesized, a mono iridium linked MZnP–Ir and a tetra iridium linked TZnP–Ir, where the tetra iridium displayed the highest H_2 production 246 TON, upon 40 h of irradiation (Fig. 10). This could be attributed to the stabilization of the triplet state of the porphyrin by efficient intramolecular energy transfer from the excited state of the porphyrin to the cobaloxime catalyst (Table 2, entries 29 and 30). Moreover, the complexes with the iridium were photostable. In a similar work, Zheng *et al.* synthesized a porphyrin iridium dyad (ZnP–T–Ir, Fig. 10) and applied it in photocatalytic H_2 evolution without any co-catalyst.[54] The researchers observed a H_2 production rate of 1.42 mmol g^{-1} h^{-1}, which is much higher than the control porphyrin lacking the Ir moiety (Table 2, entry 31).

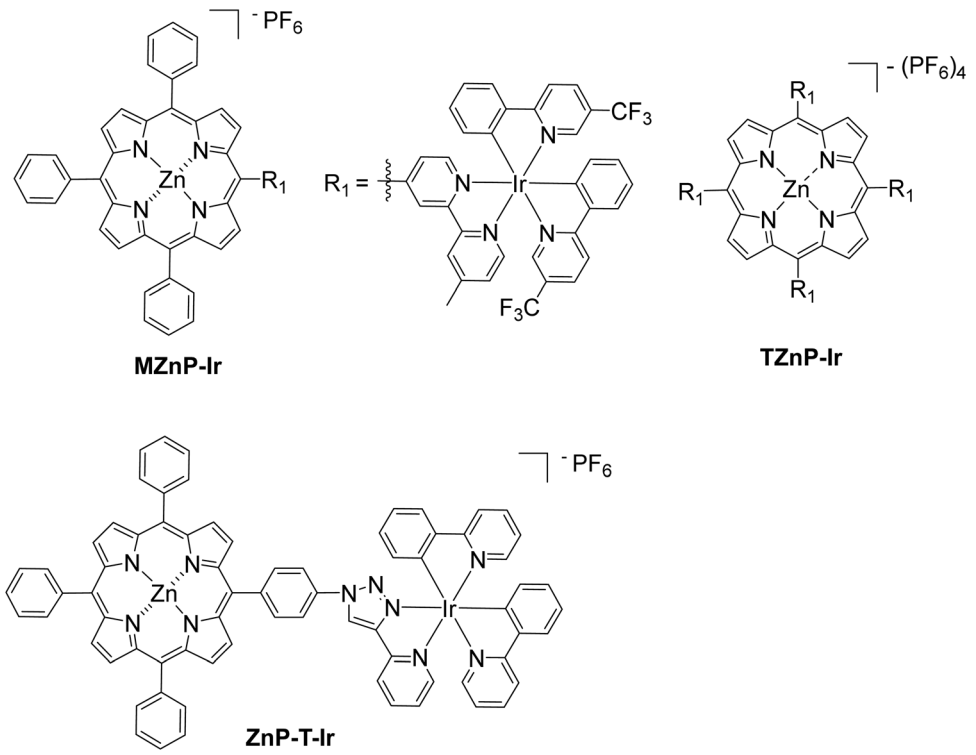

Fig. 10 Chemical structure of bimetallic Ir complexes.

2.1.2 Porphyrins as catalysts in homogeneous H_2 production systems. Porphyrin derivatives with the proper metalation can also be used as catalysts instead of photosensitizers for efficient H_2 evolution. This was achieved by Scandola and co-workers, where a cobalt water-soluble porphyrin CoTMPyP was used as catalyst and $[Ru(bpy)_3]Cl_2$ as PS in aqueous solution (Fig. 3 and 11).[55] This system achieved up to 725 TON with AA as SED, under visible light irradiation (Table 2, entry 32). H_2 production was evolved *via* reductive quenching of the photosensitizer by the SED. Another water-soluble cobalt porphyrin $CoTPP(SO_3H)_4$, was used as catalyst and $[Ru(bpy)_3]Cl_2$ as a photosensitizer, in a H_2 evolution system.[56] The system was able to produce H_2 with 6410 TON in 1 M phosphate buffer at pH 6.8 with AA as SED, after irradiation with a LED light at 420 nm (Table 2, entry 33). Mechanistic studies showed that the photocatalytic system operated *via* a reductive quenching pathway where the excited photosensitizer was reduced by the ascorbic acid, following electron transfer to the catalyst $CoTPP(SO_3H)_4$ for H_2 production.

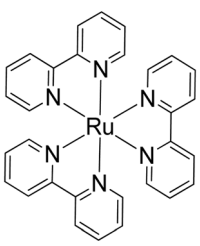

Fig. 11 Chemical structure of a ruthenium based photosensitizer.

2.2 Heterogeneous systems

The following section covers all the recent reports of light-driven H_2 production in heterogeneous systems where one or more of the fundamental components of the photocatalytic system (SED, catalyst, electron donor, electron acceptor) are not in the same phase as the others. Initially, we present the utilization of self-assembled porphyrin nanostructures in photocatalytic H_2 evolution, which was shown as a promising strategy to improve the overall performance of the system. Another form of self-assembly can be considered the metal–organic frameworks (MOFs)[57] since they are formed *via* the self-assembling of organic ligands and metal cations. Porphyrin MOFs will be discussed next followed by the covalent organic frameworks (COFs) towards light-driven H_2 generation. Subsequently, we describe reports which combine porphyrins with 2D materials or metal oxides. All the above systems use, as an unavoidable necessity, a sacrificial electron donor. This issue can be overcome by the construction of a photoelectrochemical device where the necessary electrons are provided by an external circuit and H_2 is generated at the photocathode.

2.2.1 Self-assembled nanostructures of porphyrins for H_2 production. Supramolecular self-assembly has attracted significant scientific attention and the inspiration derive from the process of natural photosynthesis, where the efficient and effective solar energy harvesting is achieved due to the well-organized self-assembled structures of chlorophylls.[58,59] In the laboratory, scientists are synthesizing chemical analogs of chlorophylls, porphyrin and phthalocyanines, and try to produce self-assembled architectures of these chromophores in order to gain enhanced properties in the resulting material.[60] Supramolecular

chromophore self-assemblies aim to improve light-harvesting, energy and electron transfer properties, which are essential for visible-light-driven photocatalytic applications, such as H_2 production and CO_2 reduction.[61]

Porphyrin and phthalocyanine molecules are ideal self-assembly building blocks since they possess symmetric molecular structures, planar geometry, chemical and thermal stability, are easily modified and can utilize plenty of supramolecular interactions such as hydrogen bonding, π–π stacking, axial coordination and noncovalent interactions.[61] There are various protocols to induce self-assembly to chromophores, including reprecipitation or "good" and "bad" solvent method, ionic self-assembly, peptide-assisted self-assembly, acid-base neutralization assisted surfactant self-assembly, microemulsion-assisted self-assembly and other methods.[62] Although the self-assembly of porphyrins is known from the 80's, self-assembled nanostructures of porphyrins had not been employed in photocatalytic H_2 evolution for sever years.[63] In the following reports, several symmetrical and unsymmetrical porphyrins formed distinctive architectures *via* their self-assembly and subsequently applied in light-driven H_2 production.

Bai and Fan and co-workers[64] developed an acid-base surfactant-assisted self-assembly process to fabricate porphyrin nanoparticles of the zinc-tetra(4-pyridyl) porphyrin (ZnTPyP, Fig. 3). For this purpose, they used the cetyltrimethyl ammonium bromide (CTAB) surfactant dissolved in a basic aqueous solution. An acidic solution of the free-base porphyrin derivative (H_2TPyP) was injected into the solution of the surfactant and led to the formation of 3D octahedral architectures. By the addition of Zn^{2+} cations in the self-assembly solution, Zn was inserted into the porphyrin core. Further self-assembly of ZnTPyP was achieved due to the axial interaction between the Zn center and the pyridyl groups, resulting into nanowires (Fig. 12a). These well-defined nanostructures with different morphologies were investigated for their photocatalytic activity using K_2PtCl_4 as co-catalyst. ZnTPyP nanowires exhibited the highest H_2 production activity (47.1 mmol g^{-1} h^{-1}, Table 3, entry 1), while the H_2TPyP nanooctahedra exhibited negligible performance (0.8 mmol g^{-1} h^{-1}). Noteworthy the nanowires showed stable H_2 evolution rate for 75 hours of irradiation and the morphology of the nanostructures was maintained after the photocatalytic reaction.

Further investigation of the same porphyrin was conducted using the same self-assembling protocol towards different architectures.[65] The researchers employed different surfactants (CTAB, MTAB, SDS) and accomplished to obtained various shapes of self-assembled nanostructures namely hexagonal, nanodisc, nanorod and tetragonal assemblies. By altering the pH of the self-assembling solution, they were able to obtain nanorods of different sizes. These nanostructures were utilized for photocatalytic hydrogen evolution and displayed morphology-dependent ($K_{hexagonal} > K_{nanodisc} > K_{nanorod} > K_{tetragonal}$) and size-dependent activity (higher activity for higher aspect ratio length/diameter). An interesting correlation was that the trend of the fluorescence decay time of the different morphologies is consistent with the trend of light driven H_2 production performance, indicating that the electron transfer between the zinc porphyrin molecules in the self-assemblies is more efficient.

The same research group utilized the CTAB surfactant with a different free-base porphyrin, namely 5,10,15,20-tetrakis(4-(hydroxyl)phenyl)porphyrin (THPP).[66] They achieved the self-assembly of the porphyrin into nanorods and nanowires through nucleation and growth process inside the surfactant micelles. When they applied these nanostructures for photocatalytic H_2 evolution using Pt as catalyst, they observed significantly boosted photocatalytic H_2 production performance

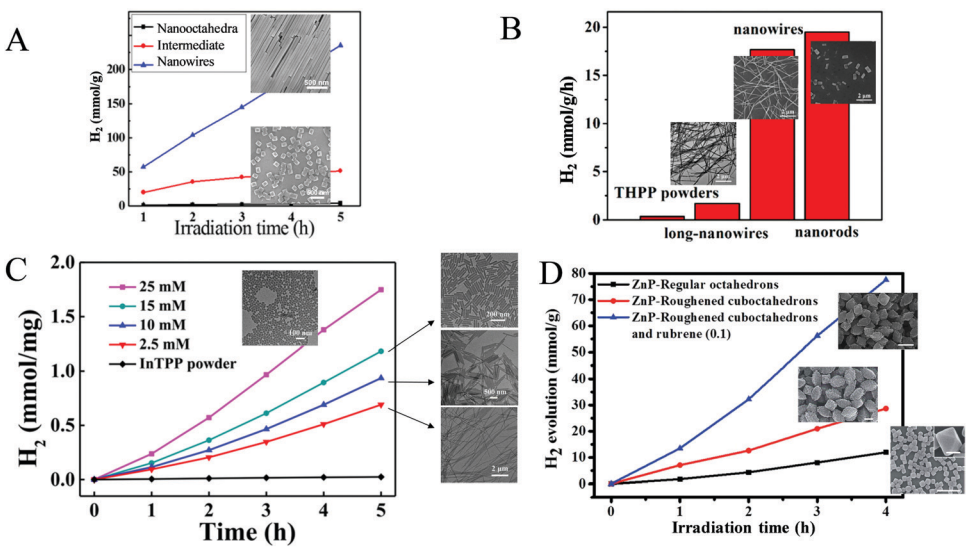

Fig. 12 (A) H_2 evolution plots of ZnTPyP self-assemblies. Reproduced from ref. 64, with permission from American Chemical Society, Copyright 2016. (B) Amount of H_2 evolution of THPP nanowires. Reproduced from ref. 66, with permission from American Chemical Society, Copyright 2018. (C) H_2 production experiments of different InTPP nanocrystals. Reproduced from ref. 67, with permission from American Chemical Society, Copyright 2019. (D) H_2 evolution plots of ZnTPP self-assemblies. Reproduced from ref. 68, with permission from Royal Society of Chemistry, Copyright 2017.

Table 3 Photocatalytic performance of self-assembled nanostructures of porphyrins for H_2 production

Entry	Photocatalysts	Cocatalyst	SED	Solvent and ingredients	Light source	H_2 production rate	Ref.
1	ZnTPyP nanowires	1 wt% Pt	AA (0.2 M)	H_2O, pH = 3.5	300 W Xe lamp, $\lambda > 420$ nm	47.1 mmol g^{-1} h^{-1}	64 and 65
2	H_2THPP nanorods	5 wt% Pt	AA (0.2 M)	H_2O, pH = 4	300 W Xe lamp, $\lambda > 420$ nm	19.5 mmol g^{-1} h^{-1}	66
3	InTPP nanorods	1 wt% Pt	AA (0.2 M)	H_2O, pH = 4	300 W Xe lamp, $\lambda > 400$ nm	845.4 mmol g^{-1} h^{-1}	67
4	ZnTPP cuboctahedrons	—	TEOA 10%	H_2O, pH = 8	300 W Xe lamp, $\lambda > 365$ nm	0.28 mmol g^{-1} h^{-1}	68
5	ZnTPP cuboctahedrons	PVP–Pt (2×10^{-6} M)	TEOA 10%	H_2O, pH = 8 MV (3×10^{-4} M)	300 W Xe lamp, $\lambda > 365$ nm	7.16 mmol g^{-1} h^{-1}	68
6	ZnTPP cuboctahedrons/rubrene	PVP–Pt (2×10^{-6} M)	TEOA 10%	H_2O, pH = 8 MV (3×10^{-4} M)	300 W Xe lamp, $\lambda > 365$ nm	19.39 mmol g^{-1} h^{-1}	68
7	FeTPP–OH H_2O nanoflakes	—	TEOA 10%	H_2O	300 W Xe lamp	0.75 mmol g^{-1} h^{-1}	69
8	TCPP lamellas	—	TEOA 10%	H_2O	300 W Xe lamp	0.0408 mmol g^{-1} h^{-1}	70
9	TCyPP	—	TEOA 10%	H_2O	300 W Xe lamp	0 mmol g^{-1} h^{-1}	70
10	TPyP	—	TEOA 10%	H_2O	300 W Xe lamp	0.0008 mmol g^{-1} h^{-1}	70
11	ZnTCPP nanosheets	3 wt% Pt	AA (0.2 M)	H_2O, pH = 4	300 W Xe lamp	3.4873 mmol g^{-1} h^{-1}	71
12	ZnTCPP powder	3 wt% Pt	AA (0.2 M)	H_2O, pH = 4	300 W Xe lamp	0.6543 mmol g^{-1} h^{-1}	71
13	TCPP powder	3 wt% Pt	AA (0.2 M)	H_2O, pH = 4	300 W Xe lamp	0.0147 mmol g^{-1} h^{-1}	71
14	MnTCPP assemblies	3 wt% Pt	AA (0.2 M)	H_2O, pH = 4	300 W Xe lamp	0.0231 mmol g^{-1} h^{-1}	71
15	FeTCPP assemblies	3 wt% Pt	AA (0.2 M)	H_2O, pH = 4	300 W Xe lamp	0.2033 mmol g^{-1} h^{-1}	71
16	CoTCPP assemblies	3 wt% Pt	AA (0.2 M)	H_2O, pH = 4	300 W Xe lamp	0.0358 mmol g^{-1} h^{-1}	71
17	NiTCPP assemblies	3 wt% Pt	AA (0.2 M)	H_2O, pH = 4	300 W Xe lamp	0.0589 mmol g^{-1} h^{-1}	71
18	TCPP/THPP gels	Pt (0.0386 M)	AA (0.15 M)	H_2O	300 W Xe lamp, λ = [440–780 nm]	1.3 mmol g^{-1} h^{-1}	72
19	TCPP gels	Pt (0.0386 M)	AA (0.15 M)	H_2O	300 W Xe lamp, λ = [440–780 nm]	0.087 mmol g^{-1} h^{-1}	72
20	TSPP fibers	Pt (5×10^{-6} M)	AA (0.1 M)	H_2O	350 W Xe lamp	80 nmol h^{-1}	76
21	TSPP microspheres	Pt (20×10^{-6} M)	AA (0.1 M)	H_2O	450 W Xe lamp, $\lambda > 400$ nm	80 nmol h^{-1}	77
22	PNA–TPP nanospheres	Pt (5×10^{-6} M)	AA (0.1 M)	H_2O	300 W Xe lamp, $\lambda > 400$ nm	16.5 nmol h^{-1}	78
23	FmocFF-ZnTPP fibers	5 wt% Pt	AA (1 M)	H_2O, pH = 4	LED lamp ring of 40 W	1.96 mmol g^{-1} h^{-1}	87
24	$SnPy_3P$-FF	[Co(dmgH)$_2$(Cl)(Py)]	TEOA 5%	H_2O, pH = 7	LED lamp ring of 40 W	7 mmol g^{-1} h^{-1}	88
25	GdH(TPyP)$_2$	5 wt% Pt	AA (1 M)	H_2O, pH = 4	LED lamp ring of 40 W	13.8 mmol g^{-1} h^{-1}	90
26	ZnT(*p*-NI)PP	3 wt% Pt	TEOA 10%	H_2O	500 W Xe lamp	0.973 mmol g^{-1} h^{-1}	91
27	ZnT(*p*-NI)PP nanospheres	3 wt% Pt	TEOA 10%	H_2O	OLED white light	1.50 mmol g^{-1} h^{-1}	92 and 93
28	ZnT(*p*-NI)TP	3 wt% Pt	TEOA 10%	H_2O	OLED white light	4.28 mmol g^{-1} h^{-1}	92
29	ZnD(*p*-NI)PP nanowires	3 wt% Pt	TEOA 10%	H_2O	OLED white light	5.40 mmol g^{-1} h^{-1}	93
30	Zn–Mesoporphyrin IX	Pt (20×10^{-6} M)	TEOA (0.1 M)	H_2O, MV (0.002 M), NaCl (0.5 M), pH = 6	300 W halogen lamp	222.5 nmol h^{-1}	94
31	Zn-Protoporphyrin IX	Pt (30×10^{-6} M)	AA (0.002 M)	H_2O, MOPS (0.050 M), pH = 7.4	300 W halogen lamp	950 nmol h^{-1}	95
32	$H_4DPP^{2+}(Cl^-)_2$	PVP–Pt (0.15 mg mL^{-1})	$AcrH_2$ (0.020 M)	MeOH/MeCN 1 : 1 v/v, TsOH (0.030 M)	300 W Xe lamp, $\lambda > 710$ nm	53[a] mmol g^{-1} h^{-1}	96

[a] Estimated from the graph the authors presented.

compared to the initial porphyrin powders under visible light irradiation. Notably, the photocatalytic H_2 evolution rate of the self-assembled nanostructures was nearly 20 times improved than that of the THPP powder (Fig. 12b). More specifically the nanorods and the nanowires reached 19.5 and 17.6 mmol g^{-1} h^{-1} H_2 evolution rate respectively (Table 3, entry 2), while the powder exhibited only 0.7 mmol g^{-1} h^{-1}.

Bai and Fan and co-workers[67] modified the self-assembling protocol by introducing an organic solvent to dissolve the porphyrin chromophore while keeping the use of CTAB as surfactant. In detail, they dissolved In(III) *meso*-tetraphenylporphine chloride (InTPP) in chloroform and then mixed it with an aqueous solution of CTAB to form microemulsion. After the evaporation of the oil phase, InTPP was self-assembled into uniform nanocrystals through noncovalent π–π stacking and hydrophobic interactions. The morphology of the assemblies depended on the concentration of CTAB and they demonstrated that the self-assembled nanocrystals presented enriched photocatalytic H_2 evolution within 5 h of irradiation (Fig. 12c), compared to the commercial porphyrin powder which showed negligible activity. The photocatalytic performance is influenced by the aspect ratio (length/diameter), with the highest H_2 production rate of 845.4 mmol g^{-1} h^{-1} obtained from the nanorods with the smallest aspect ratio of 1.6 (Table 3, entry 3). The higher H_2 evolution rate was attributed to the larger active surface areas of these nanorods.

In another report, Liu *et al.* reported the self-assembly of ZnTPP into quasi-octahedral nanoparticles starting from zinc porphyrin perchlorate (ZnTPP·ClO_4).[68] After injecting a MeCN solution of ZnTPP·ClO_4 in water and let the reaction proceed for different experimental time (from 30 minutes till 20 days) they observed different morphologies regarding the surface of the nanostructures (from smooth octahedrons to rough cuboctahedrons). The researchers showed that the rough ZnTPP cuboctahedrons exhibited higher photocatalytic activity than the regular octahedrons, with the first ones reaching 0.28 mmol g^{-1} h^{-1} in the presence of TEOA as sacrificial electron donor and in the absence of other cocatalysts (Fig. 12d). After these ZnTPP nanoparticles were utilized in a ternary system containing TEOA, methyl viologen (MV) as the electron mediator and colloidal platinum (PVP–Pt) as catalyst the photocatalytic performance was significantly enhanced since it reached 7.16 mmol g^{-1} h^{-1}. The presence of another chromophore, namely rubrene, further improved the activity to 19.39 mmol g^{-1} h^{-1} (Table 3, entries 4–6).

Another approach from the same research team utilized again a metallated tetra-phenyl porphyrin and the CTAB surfactant.[69] In detail they used iron porphyrin perchlorate (FeTPP·ClO_4) to prepare organic nanocrystals (ONCs) *via* the hydrolysis of FeTPP·ClO_4 in the presence of CTAB. They achieved to prepare uniform and regular 0-dimensional FeTPP–Cl, ultrafine 1 dimensional $[FeTPP]_2O$ and ultrathin 2D FeTPP–OH H_2O ONCs by tuning the pH, and the concentrations of the monomer and of CTAB. After applying these nanostructures in a visible light-driven catalytic system containing TEOA and lacking any other cocatalyst, the scientists revealed the dependence of the photocatalytic performance on the size, the shape and axial ligand of the porphyrin nanocrystals. As it is depicted on Fig. 13a, the FeTPP–OH H_2O nanoflakes displayed the highest production frequency (0.75 mmol g^{-1} h^{-1}, Table 3, entry 7),

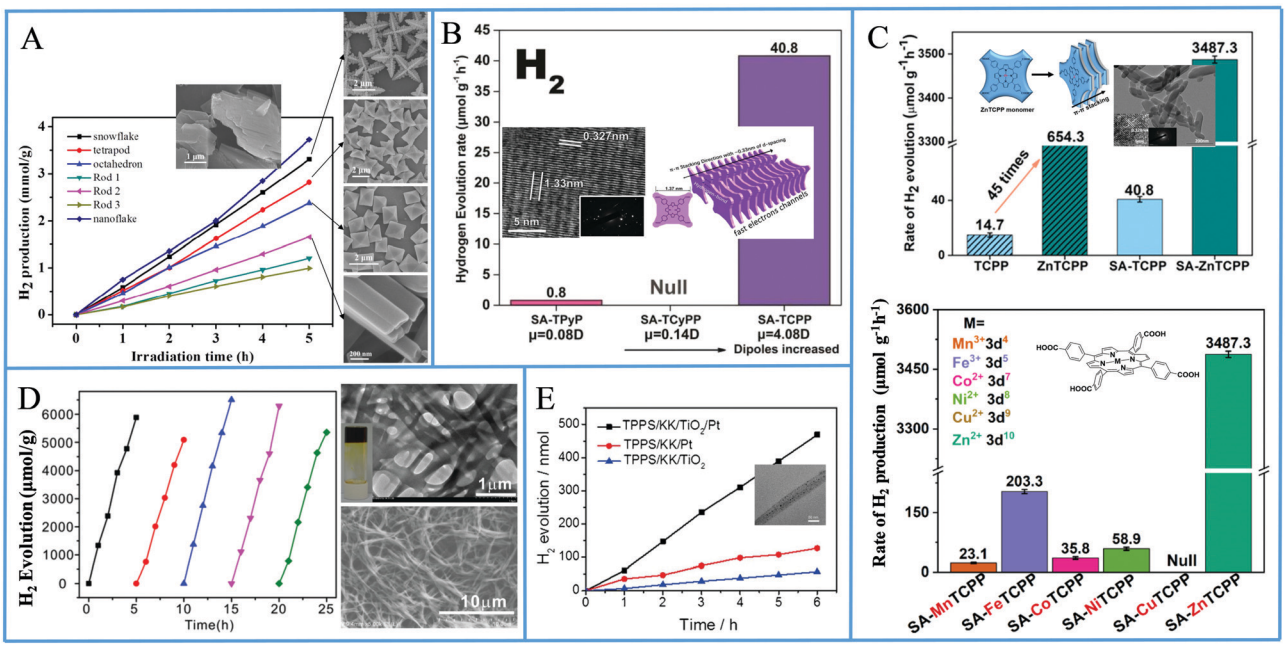

Fig. 13 (A) H_2 production of different FeTPP nanostructures. Reproduced from ref. 69, with permission from American Chemical Society, Copyright 2019. (B) Amount of H_2 evolution of TCPP self-assemblies compared with TPyP and TCyP. Reproduced from ref. 70, with permission from John Wiley and Sons, Copyright 2019. (C) H_2 production using self-assembled nanostructures metallated MTCPP porphyrins. Reproduced from ref. 71, with permission from John Wiley and Sons, Copyright 2019. (D) Recycling H_2 production experiments of LBG/TCPP/THPP/Pt DMF gels, Reproduced from ref. 72, with permission from Royal Society of Chemistry, Copyright 2020. (E) H_2 evolution of TSPP/KK/TiO_2/Pt fibers. Reproduced from ref. 76, with permission from John Wiley and Sons, Copyright 2016.

followed by the FeTPPCl octahedrons (0.48 mmol g^{-1} h^{-1}) and the $[FeTPP]_2O$ nanorods (0.20 mmol g^{-1} h^{-1}).

From the above reports, it is clear that symmetric *meso*-substituted porphyrins with the ability to form self-assembled nanostructures have attracted a lot of scientific interest towards H_2 evolution. In this content, Zhang *et al.* described the ability of self-assembled free-base porphyrins to produce H_2 photocatalytically without the addition of any cocatalysts.[70] In detail, they prepared self-assembled nanostructures of 5,10,15,20-tetrakis (4-carboxylphenyl)porphyrin (TCPP) and 5,10,15,20-tetrakis(4-pyridyl)porphyrin (TPyP) using a simple base-acid solution method, while the self-assembled 5,10,15,20-tetrakis(4-cyanophenyl)-porphyrin (TCyPP) was prepared by the "good–bad" solvent method. TCPP exhibited thin lamellar nanostructures which were able to reduce the aqueous protons to H_2 in the presence of TEOA with a hydrogen production rate of 0.0408 mmol g^{-1} h^{-1}, whereas the TPyP and TCyPP derivatives displayed negligible and null activity respectively (Fig. 13b and Table 3, entries 8–10). Noteworthy the self-assemblies of TCPP were also capable of water oxidation to O_2 in the presence of $AgNO_3$, so they achieved to perform both water splitting half reactions.

In a recent publication by the same research group, the free-base porphyrin TCPP was metallated with various metals (Mn, Fe, Co, Ni, Cu and Zn) and self-assembled nanostructures of these porphyrins were prepared afterwards using CTAB (SA-MTCPP).[71] The authors applied both the self-assembled derivatives as well as the commercial porphyrin powders in photocatalytic H_2 evolution with *in situ* photo-deposited Pt as cocatalyst and AA as SED at pH = 4. ZnTCPP nanosheets presented efficient H_2 evolution reaching 3.4873 mmol g^{-1} h^{-1}, which was 5 times higher than the performance of the unassembled ZnTCPP powder (0.6543 mmol g^{-1} h^{-1}) under full-spectrum irradiation. The other metallated porphyrin assemblies, bearing different 3d orbital electron configuration, exhibited significantly lower activity and this was attributed to the differences in the reduction potential. In detail, the best performing ZnTCPP assemblies had the strongest reduction potential while the self-assembled CuTCPP (SA-CuTCPP), which had the lowest reduction potential, presented no H_2 evolution (Fig. 13c). The photocatalytic activity of the remaining SA-MTCPP followed the reduction potential trend, showing that the position of the CB of porphyrin self-assemblies determines the H_2 production performance (Table 3, entries 11–17).

In a recent publication, Yang *et al.* employed two different free-base porphyrins and an amphiphilic surfactant to create supramolecular gels which were capable of photocatalytic H_2 generation in the presence of Pt co-catalyst.[72] More specifically, 5,10,15,20-tetrakis(4-hydroxyphenyl)porphyrin (THPP) and tetra-(4-carboxylphenyl)porphyrin (TCPP) were dissolved in DMF along with the known gelator *N,N′*-bis(octadecyl)-L-Boc-glutamic diamide (LBG) *via* heating the solution. After cooling to room temperature, gels consisting of fibrous nanostructures were obtained, which were subsequently dried for the photocatalytic experiments. The LBG/TCPP/THPP/Pt system obtained from DMF gels was able to produce H_2 with AA as SED, and the total photocatalytic H_2 generation after 5 h of visible light irradiation was 6.5 mmol g^{-1} (Fig. 13d). This performance is translated to 1.3 mmol g^{-1} h^{-1} H_2 evolution rate and is 15 times higher than the LBG/TCPP/Pt system with only one porphyrin chromophore (Table 3, entries 18 and 19). Emission studies in solution revealed that the TCPP/THPP mixture in DMF solution shows a broadened and red-shifted peak in comparison with that of TCPP or THPP alone, indicating the formation of the TCPP/THPP exciplex in DMF solution. This exciplex was also observed in the gels obtained from DMF and it provides enhanced optical properties for efficient photocatalytic H_2 evolution.

In continuation of the presentation of self-assembled porphyrins towards visible light-driven H_2 production, another approach is the co-assembly with peptides. Yan's group, which has extensively investigated porphyrin–peptide co-assembly,[73–75] moved one step further and applied a co-assembling fiber system composed of a dipeptide and a porphyrin into photocatalytic H_2 production.[76] Aiming to simulate natural hydrogen-producing photobacteria, they designed an acidic, hot, and mineral-containing (Na^+, Ti^{4+}, Pt^{2+}, and so forth) prebiotic soup including L-Lys–L-Lys (KK) and 5,10,15,20-tetrakis(4-sulfonatophenyl)porphyrin, (TSPP). This bioinspired system begins with the spontaneous self-assembly of the porphyrin and the dipeptide into ordered hybrid hierarchical fibers, which are subsequently self-mineralized with TiO_2 and Pt. The authors explained how the positively charged peptide facilitates the TiO_2 and Pt NPs self-mineralization on the surface of the fibers and that the mineralized TiO_2/Pt nanoparticles constitute the reaction center for H_2 production. Under visible-light irradiation, the TSPP/KK/TiO_2/Pt fibers exhibited the highest H_2 production rate of approximately 80 nmol h^{-1}, while noticeable H_2 bubbles appeared in the test tube (Fig. 13e and Table 3, entry 20).[61,76]

One year later the same group employed the same porphyrin (TSPP) with the Fmoc-protected lysine (Fmoc-L-Lys) instead of the unprotected dipeptide, in order to fabricate self-assembled architectures through the one-step co-assembly of the amphiphilic amino acid and the porphyrin chromophore.[77] Fmoc-L-Lys was able to self-assemble into nanofibers *via* π–π stacking and hydrogen bonding. The negatively charged TSPP co-assembled on the surface of the nanofibers through electrostatic interactions, and these nanofibers were further self-assembled into microspheres. The co-assembled microspheres demonstrated enriched light-harvesting ability and were able to produce H_2 photocatalytically using Pt as co-catalyst under visible light illumination (Fig. 14a and Table 3, entry 21). The reaction center was located on the platinum nanoparticles which funneled the energy from the excited porphyrin chromophores and performed the light-induced reduction of protons to molecular hydrogen.

Following the methodology of peptide co-assembly with porphyrin chromophores, Nikoloudakis *et al.* utilized a peptide nucleic acid (PNA) covalently linked to *meso*-tetraphenyl-porphyrin (PNA–TPP) and a boron-dipyrromethene (BODIPY) molecule (PNA–BDP) with the purpose of conveying self-assembling properties to the chromophores.[78] Indeed, the hybrid molecules were able to self-assemble into spherical nanostructures with enhanced light-harvesting properties,

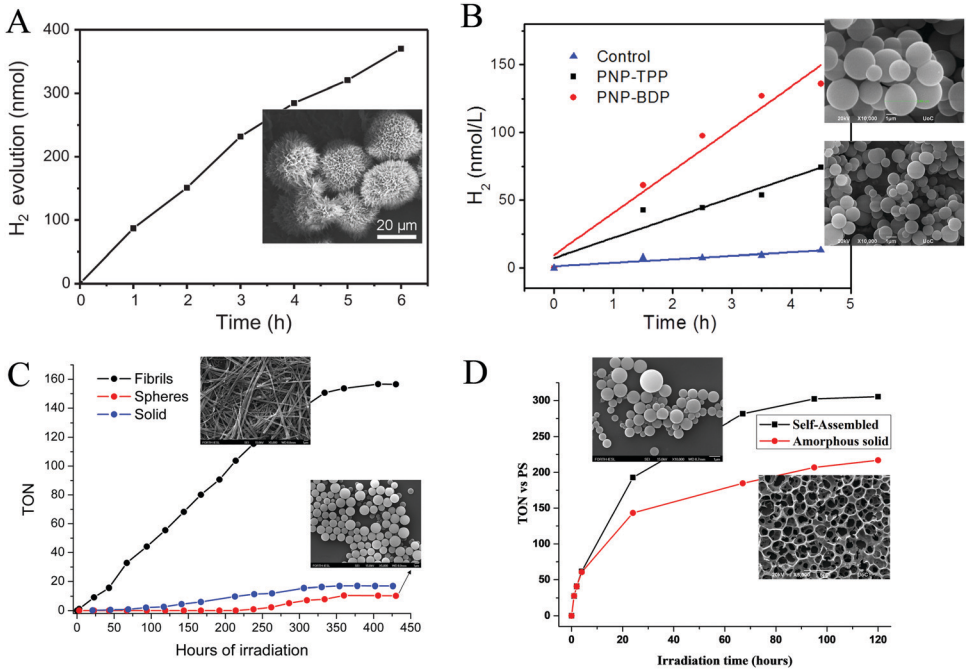

Fig. 14 H_2 production plots of (A) TSPP microspheres, Reproduced from ref. 77, with permission from Elsevier, Copyright 2017. (B) PNA–TPP and PNA–BDP microspheres, Reproduced from ref. 78, with permission from Royal Society of Chemistry, Copyright 2019. (C) FmocFF-ZnTPP fibers and nanospheres Reproduced from ref. 87, with permission from Royal Society of Chemistry, Copyright 2021 and (D) self-assembled $SnPy_3P$-FF. Reproduced from ref. 88, with permission from American Chemical Society, Copyright 2021.

using the "good–bad" solvent self-assembling protocol.[78,79] Subsequently these nanospheres were applied into a photocatalytic system with *in situ* mineralized Pt nanoparticles as photocatalysts and AA as electron donor. Noteworthy the PNA–BDP assemblies exhibited higher activity reaching 30.1 nmol h^{-1} compared to the PNA–TPP nanostructures (16.5 nmol h^{-1}, Table 3, entry 22) as it is presented in Fig. 14b.

The most extensively studied small peptide, famous for its self-assembling properties, is diphenylalanine (Phe–Phe, FF).[80,81] Coutsolelos and co-workers have extensively investigated chromophores such as BODIPYs,[82] porphyrins,[83,84] corroles,[85] and polyoxometalates (POMs)[86] covalently linked with Phe–Phe and the resulting conjugates retained the characteristic of self-assembly. In this concept, we synthesized FmocFF-ZnTPP and examined its well-defined nanostructures as photocatalysts in H_2 production.[87] In detail, following the "good" and "poor" solvent method we obtained spherical and fibrillar self-assembling architectures from the same porphyrin molecule, which presented much different catalytic activity towards H_2 evolution. After photo-deposition of Pt NPs on the fibrillar nanostructures in the presence of AA as SED, H_2 generation was achieved with a rate of 1.96 mmol g^{-1} h^{-1} (Table 3, entry 23). The spherical and the amorphous solid displayed negligible photocatalytic activity and verified that the self-assembly mode controls H_2 production in this system since fibrils were more efficient than spheres or amorphous solid (Fig. 14c).

In another work of Nikoloudakis *et al.*[88] we covalently connected the diphenylalanine dipeptide with tris(pyridyl)porphyrin in order to transfer self-assembling properties to the resulting hybrid. The pyridyl substitution was chosen since it led to superior photocatalytic activity in previous reports from the same group.[44,89] So we prepared the $SnPy_3P$-FF, $ZnPy_3P$-FF and the free-base hybrid and we verified that the metal inside the porphyrin influences the self-assembly mode of the porphyrin–peptide hybrids, since it induces different nanostructures: nanospheres, irregular aggregation and fibrils, respectively. The self-assembled nanostructures and the amorphous solids were employed in photocatalytic hydrogen production using a known cobaloxime complex as molecular catalyst and TEOA as SED. The zinc and free base hybrids did not display any photocatalytic activity, whereas the $SnPy_3P$-FF was able to act as a photosensitizer and produced H_2. Notably, the performance of the self-assembled $SnPy_3P$-FF nanospheres was greater compared to the amorphous chromophore, demonstrating the significance of self-assembly towards improving the light-harvesting ability and the photocatalytic properties of the porphyrin. The best performing system exhibited 305 TON after 120 hours of visible light irradiation, while the H_2 evolution rate at 24 hours was 7 mmol g^{-1} h^{-1} (Fig. 14d and Table 3, entry 24).

Another report from the same team concerned the photocatalytic H_2 production of a series of modified Gd-porphyrins in the presence of Pt NPs.[90] The Gd bisporphyrinate double decker with pyridyl peripheral groups ($GdH(TPyP)_2$) exhibited the highest activity reaching 13.8 mmol g^{-1} h^{-1} (Table 3, entry 25), while the corresponding Gd monoporphyrinate with the same peripheral substitution (Gd(TPyP)acac) was totally inactive. In this study, the authors were able to obtain different supramolecular

architectures by altering the solvent mixture and the peripheral substitution, however, the different nanostructures had no effect on the photocatalytic performance of the complexes.

Porphyrin photosensitizers in combination with Pt nanoparticles have been also reported without the formation of self-assemblies or aggregates. Bodedla *et al.* synthesized *meso*-substituted porphyrins conjugated with four naphthalimide (NI) moieties.[91] The light harvesting properties of the isomeric porphyrins varied with the position of NI onto the phenyl attached to the *meso*-position of porphyrin ring, which affected the H_2 production activity in the presence of Pt co-catalyst. In the photocatalytic system, the porphyrin was suspended in an aqueous TEOA solution and Pt was loaded by the *in situ* photoreduction deposition method. It was found that the *para*-substituted porphyrin isomer ZnT(*p*-NI)PP exhibited the higher H_2 production rate of 0.973 mmol g^{-1} h^{-1} (Fig. 15a and Table 3, entry 26), which was 200 times enhanced compared to ZnTPP, showing the importance of intramolecular energy transfer from the naphthalimide moiety. Moreover the corresponding free base derivative T(*p*-NI)PPH_2 displayed only 0.013 mmol g^{-1} h^{-1} rate, verifying that the zinc metalation was also essential.

The same research group modified the π-linker between the porphyrin and the naphthalimide moieties by inserting an electron-rich thiophene group instead of a phenyl linker.[92] They synthesized the ZnT(*p*-NI)TP which showed superior light-harvesting ability in comparison with ZnT(*p*-NI)PP. After applying these porphyrins in the photocatalytic system following a similar Pt co-catalyst deposition as above, the scientists observed increased photocatalytic activity with a ~2.9 times higher H_2 evolution rate (4.28 mmol g^{-1} h^{-1}) for the ZnT(*p*-NI)TP (Fig. 15b and Table 3, entries 27 and 28). Noteworthy this derivative exhibited also improved stability since it continued to be active for more than 50 hours, while ZnT(*p*-NI)PP reached a plateau after 20 h.

Bodedla *et al.* continued modifying their porphyrin-naphthalimide systems and recently utilized the self-assembly of their complexes in order to further improve the overall photocatalytic performance.[93] More specifically they synthesized the linear shaped di-substituted zinc porphyrin bearing two naphthalimide moieties (ZnD(*p*-NI)PP) which was able to self-assemble into nanowires. The scientists mention that in their previous reports they did not study the solid phase morphology of the porphyrins and that ZnT(*p*-NI)PP self-assembled into nanospheres in the photocatalytic system. The ZnD(*p*-NI)PP nanowires clearly outperformed the tetra- naphthalimide substituted porphyrins because it exhibited a hydrogen evolution rate of 5.4 mmol g^{-1} h^{-1} (Table 3, entry 29) in the presence of Pt co-catalyst, which was 3.6 times higher than the ZnT(*p*-NI)PP nanospheres (Fig. 15c).

Kurtz's group utilized a protein scaffold that incorporates bioinspired porphyrins in order to promote the nucleation of Pt NPs.[94] In detail, they incorporated zinc–protoporphyrin IX and zinc–mesoporphyrin IX in the place of heme in the iron storage protein bacterioferritin (Bfr) by adding the porphyrins to the *E. coli* expression medium, resulting into Bfr–porphyrin dimers with two protein moieties sandwiching a zinc porphyrin. Subsequently, Pt nanoparticles were merged into the Bfrs by reduction using K_2PtCl_4 and $NaBH_4$, with half of the dimers surrounding platinum nanoparticles (Fig. 15d). The best performing system, containing both Pt-free Bfr–porphyrin dimer

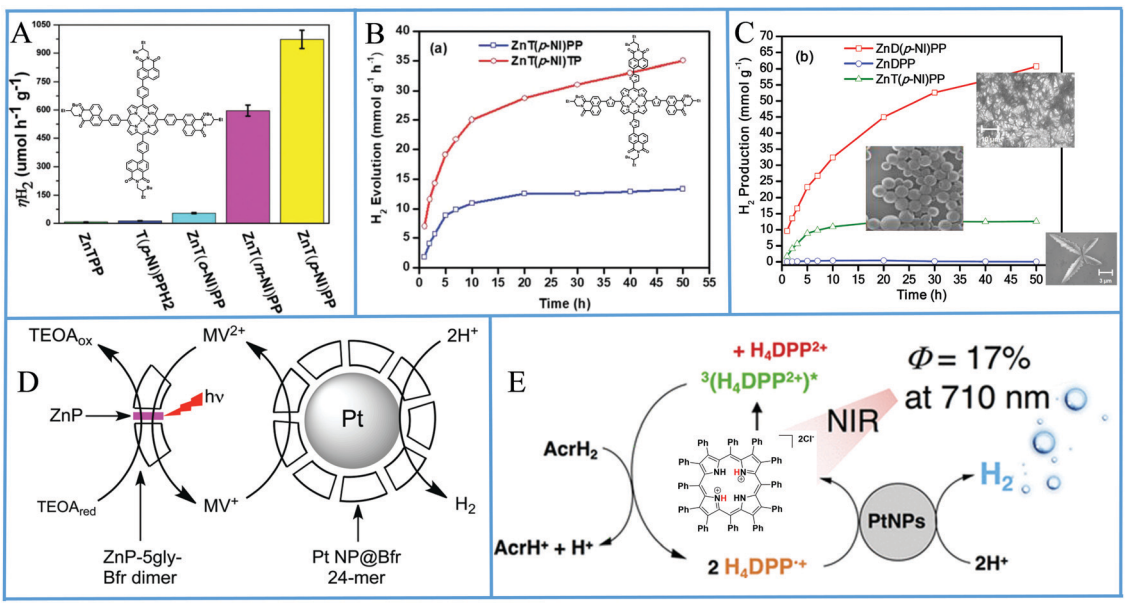

Fig. 15 (A) amount of H_2 evolution of tetra-naphthalimide substituted porphyrins, Reproduced from ref. 91, with permission from Royal Society of Chemistry, Copyright 2018. (B) H_2 evolution plots of tetra-naphthalimide porphyrin with thiophene π-linker, Reproduced from ref. 92, with permission from Royal Society of Chemistry, Copyright 2020. (C) H_2 evolution plots of NI-porphyrin self-assemblies, Reproduced from ref. 93, with permission from American Chemical Society, Copyright 2020. (D) Proposed H_2 production diagram of the Bfr–porphyrin dimer and Pt NPs-Bfr system, Reproduced from ref. 94, with permission from Royal Society of Chemistry, Copyright 2016. (E) Schematic representation of photocatalytic H_2 production by $H_4DPP^{2+}(Cl^-)_2$. Reproduced from ref. 96, with permission from American Chemical Society, Copyright 2020.

and Pt NPs-Bfr along with TEOA as electron donor and MV as electron relay, reached 0.89 μmol H_2 after 4 hours of white light irradiation which is translated into a TON of 60 (Table 3, entry 30). The researchers showed that the activity of the Zn–mesoporphyrin IX was superior to that of zinc–protoporphyrin IX.

The same group improved their photocatalytic system one year later, by using citrate coated Pt nanoparticles which afforded H_2 production without the need of an electron relay.[95] Indeed their modified approach reached 5.7 μmol H_2 after 6 hours of white light irradiation with the Bfr– Zn–protoporphyrin IX dimer, which is 3 fold higher than the Pt NPs-Bfr–porphyrin system (Table 3, entry 31). The scientists also reported that ZnTMPyP was inactive as photosensitizer following their new protocol with citrate coated Pt NPs and ascorbate as SED, while the use of MV in combination with ethylenediaminetetraacetic acid (EDTA) showed noticeable H_2 generation.

From all above examples, one understands that various protocols have been used in order to combine porphyrin PSs along with Pt nanoparticles co-catalysts. Although self-assembly of porphyrins has been extensively studied, there are other ways to construct photocatalytic systems that combine these two constituents. Kotani *et al.* synthesized a diprotonated saddle-distorted dodecaphenylporphyrin $[H_4DPP^{2+}(Cl^-)_2]$, which absorbs in NIR, and poly(vinylpyrrolidone)-protected Pt NPs (PVP–Pt) *via* a known procedure.[96] Afterwards, the chromophore, the Pt NPs co-catalyst, 10-methyl-9,10-dihydroacridine ($AcrH_2$) as SED and *p*-toluenesulfonic acid (TsOH) as proton source were applied towards photocatalytic H_2 production in 1 : 1 MeOH/MeCN using $\lambda >$ 710 nm light irradiation (Fig. 15e). Indeed, the researchers observed NIR light driven H_2 evolution and verified the necessity of each component. The photocatalytic performance was proved to be dependent on the concentration of the SED and the amount of Pt NPs while the concentration of the proton source didn't vary the overall activity. The best performing system reached a TON of 1500 after 3 hours of irradiation and showed an initial H_2 production rate of 53 mmol g^{-1} h^{-1} (Table 3, entry 32) (estimated from the graph the authors presented).

2.2.2 Porphyrin MOFs for H_2 production. MOFs are a class of crystalline micro-/*meso*-porous hybrid materials, also known as coordination polymers, which have attracted tremendous interest in photocatalytic CO_2 reduction.[97] MOFs are formed with inorganic metal ions or clusters connected to organic moieties or ligands. The metal nodes are usually secondary building units that are made of metal complexes and are fixed in place by the organic moieties working as ligands. The MOFs can be used either as a sensitizer or a catalyst and their properties can be modified by altering the metal ion or the organic ligands.

The first example of porphyrin MOFs (PMOFs) applied in photocatalytic H_2 production was reported in 2012 by Rosseinsky and coworkers.[98] The researchers prepared a water-stable, microcrystalline porous MOF by reacting $AlCl_3 \cdot 6H_2O$ with the free-base TCPP and also synthesized the zinc metallated porphyrin MOF with the same procedure. Colloidal platinum nanoparticles were utilized as catalyst for the photocatalytic experiments in a system that contained the porphyrin MOF, EDTA as SED and MV as electron acceptor which mediates electrons to Pt (Table 4, entries 1 and 2). Two years after this report, Sasan *et al.* utilised again the same chromophore, ZnTCPP to create a robust zirconium-porphyrin metal–organic framework (ZrPF).[99] Noteworthy, this is one of the rare examples where no platinum co-catalyst was used. Instead, the scientists incorporated an organometallic $[Fe_2S_2]$ complex inside the MOF, with the zinc center of the porphyrin providing binding sites for this complex and stabilizing the resulting material. Photocatalytic H_2 evolution experiments were conducted in the presence of AA as SED at pH = 5 and reached 3.5 μmol of H_2 production after 120 minutes of visible light irradiation (Fig. 16a and Table 4, entry 3). The di-iron complex acted as a catalyst while the coordination to the porphyrin inside the stable PMOF afforded also high stability to the catalyst.

The following years there was no report on light-driven H_2 production based on porphyrin MOFs until 2018 when Jiang's groups synthesized an aluminum-based porphyrin MOF which included single platinum atoms and applied it in photocatalytic hydrogen evolution. For this purpose, the scientists utilized the TCPP and $AlCl_3 \cdot 6H_2O$ and prepared the Al–TCPP PMOF.[100] Subsequently, the PMOF was heated in water along with K_2PtCl_4 in order to incorporate Pt ions in the porphyrin core to afford Al–TCPP–Pt(II) and then it was reduced at 180 °C in H_2 atmosphere to obtain single Pt atoms inside Al–TCPP. For comparison reasons, PVP-protected Pt nanoparticles were also synthesized and applied in the photocatalytic system. The single Pt atoms confined in the porphyrin MOF were able to produce hydrogen under visible light irradiation in the presence of TEOA as SED with a TOF of 35 h^{-1} which was ~30 times superior to the performance of Pt NPs stabilized by the same PMOF (Fig. 16b). As far as the H_2 production rate is concerned the rate of Al–TCPP–PtNPs was 0.05 mmol g^{-1} h^{-1} while the system with single Pt atoms (Al–TCPP–Pt) exhibited 0.129 mmol g^{-1} h^{-1}, highlighting the potential of such single-atom catalysts in MOFs (Table 4, entry 4).

The same research group created another PMOF based on TCPP and In(III) metal nodes, which was able to act as photosensitizer in the presence of platinum nanoparticles as co-catalysts and produce hydrogen photocatalytically.[101] The authors managed to obtain single crystal of the metal organic framework where In(III) had also completely occupied the porphyrin centers and proved that the metal is out-of-plane (~0.4 Å above the porphyrin plane). Moreover, they synthesized the corresponding In-PMOFs using the metallated CoTCPP, NiTCPP and CuTCPP and they verified from the achieved single crystals that in these MOFs the metal ions stay in-plane of the porphyrin. Interestingly, the InTCPP porphyrin metal organic framework displayed the highest photocatalytic performance (0.341 mmol g^{-1} h^{-1}, Table 4, entry 5) under visible-light irradiation which is much greater than the activities of the other MTCPP (M = Co, Cu, Ni) PMOFs (Fig. 16c). The In-PMOF that had low occupation of the porphyrin centers with In(III) presented ~3.4 times decreased photocatalytic activity. The researchers explained that the out-of-plane In(III) ions are

Table 4 Photocatalytic performance of porphyrin MOFs for H_2 production

Entry	MOF name	Metal node	Linker	Cocatalyst	SED	Solvent and ingredients	Light source	Hydrogen production rate	Ref.
1	Al-PMOF	Al	TCPP	Pt NPs (1×10^{-5} M)	EDTA (0.015 M)	H_2O, MV (8×10^{-3} M), pH = 5.5	300 W Xe lamp $\lambda > 420$ nm	0.200 mmol g^{-1} h^{-1}	98
2	Al-PMOF	Al	ZnTCPP	Pt NPs (1×10^{-5} M)	EDTA (0.015 M)	H_2O, MV, pH = 5.5	300 W Xe lamp, $\lambda > 420$ nm	0.100 mmol g^{-1} h^{-1}	98
3	ZrPF	Zr	ZnTCPP	$[Fe_2S_2]$ (2×10^{-6} M)	AA (0.02 M)	H_2O, Acetate (1.0 M) pH = 5	300 W Xe lamp, $\lambda > 420$ nm	1750 nmol h^{-1}	99
4	Al–TCPP–Pt	Al	PtTCPP	—	TEOA 5%	MeCN, H_2O 5%	300 W Xe lamp, $\lambda > 380$ nm	0.129 mmol g^{-1} h^{-1}	100
5	USTC-8(In)	In	InTCPP	1.5 wt% Pt NPs	TEA 8%	MeCN, H_2O 2%	300 W Xe lamp, $\lambda > 380$ nm	0.341 mmol g^{-1} h^{-1}	101
6	HNTM-Ir	Zr	IrTCPP	—	TEOA 8%	MeCN, H_2O 2%	300 W Xe lamp, $\lambda > 400$ nm	0.0076 mmol g^{-1} h^{-1}	102
7	HNTM-Pt	Zr	PtTCPP	—	TEOA 8%	MeCN, H_2O 2%	300 W Xe lamp, $\lambda > 400$ nm	0.0567 mmol g^{-1} h^{-1}	102
8	HNTM-Ir/Pt	Zr	IrTCPP–PtTCPP	—	TEOA 8%	MeCN, H_2O 2%	300 W Xe lamp, $\lambda > 400$ nm	0.2019 mmol g^{-1} h^{-1}	102
9	Ru-TBP	Ru	TCPP/RuTCPP	—	TEOA 19%	MeCN, H_2O 4%	230 W lamp, $\lambda > 400$ nm	0.13 mmol g^{-1} h^{-1}	103
10	Ru-TBP-Zn	Ru	ZnTCPP	—	TEOA 19%	MeCN, H_2O 4%	230 W lamp, $\lambda > 400$ nm	0.24 mmol g^{-1} h^{-1}	103
11	Pd-PCN-222(Hf)	Hf	PdTCPP	0.92 wt% Pt NPs	TEOA 20%	MeCN, H_2O 2%	300 W Xe lamp $\lambda > 420$ nm	22.674 mmol g^{-1} h^{-1}	104
12	Pd-PCN-222(Hf)	Hf	PdTCPP	—	TEOA 20%	MeCN, H_2O 2%	300 W Xe lamp $\lambda > 420$ nm	2.476 mmol g^{-1} h^{-1}	104
13	PCN-222(Hf)	Hf	TCPP	0.92 wt% Pt NPs	TEOA 20%	MeCN, H_2O 2%	300 W Xe lamp $\lambda > 420$ nm	0.441 mmol g^{-1} h^{-1}	104
14	PCN-22	Ti	TCPP	3 wt% Pt NPs	AA (0.037 M)	H_2O	300 W Xe lamp $\lambda > 420$ nm	8.52 mmol g^{-1} h^{-1}	106
15	PtSA-MNS	Cu	PtTCPP (12 wt% Pt)	—	AA (0.1 M)	H_2O, pH = 4	300 W Xe lamp $\lambda > 420$ nm	11.320 mmol g^{-1} h^{-1}	107
16	PtSA-MNS	Cu	TCPP	—	AA (0.1 M)	H_2O, pH = 4	300 W Xe lamp $\lambda > 420$ nm	0.002 mmol g^{-1} h^{-1}	107
17	ZrTTA-6SH	Zr	H_3TTA-6SH	ZnTFPP with 3 wt% Pt NPs	TEOA 10%	H_2O	300 W Xe lamp	0.110 mmol g^{-1} h^{-1}	108
18	ZrTTA-6SH	Zr	H_3TTA-6SH	NiTFPP with 3 wt% Pt NPs	TEOA 10%	H_2O	300 W Xe lamp	0.071 mmol g^{-1} h^{-1}	108
19	ZrTTA-6SH	Zr	H_3TTA-6SH	FeTFPP with 3 wt% Pt NPs	TEOA 10%	H_2O	300 W Xe lamp	0.017 mmol g^{-1} h^{-1}	108
20	HER-MOF	Hf	ZnTCPP–PtTCPP	—	Phenol ($\sim$0.1 M)	H_2O	LED lamp λ = 400 nm	12 000 h^{-1}	109
21	LP–HER-WOR-MOF	Hf and Zr	ZnTCPP–PtTCPP	—	—	H_2O	LED lamp λ = 400 nm	0.0116 mmol g^{-1} h^{-1}	109
22	PCN-223	Hf	ZnTCPP–PtTCPP	—	CA (0.005 M)	H_2O	LED lamp λ = 420 nm	521 h^{-1}	110
23	$ZnIn_2S_4$@PCN-224	Zr	TCPP	—	Na_2S (0.35 M), Na_2SO_3 (0.25 M)	H_2O	300 W Xe lamp $\lambda > 420$ nm	0.284 mmol h^{-1} 5.675 mmol g^{-1} h^{-1}	111
24	$ZnIn_2S_4$@PCN-224	Zr	TCPP	8 wt% Pt	Na_2S (0.35 M), Na_2SO_3 (0.25 M)	H_2O	300 W Xe lamp $\lambda > 420$ nm	3.41 mmol h^{-1}	111
25	PCN-222	Zr	PtTCPP	—	TEOA 10%	MeCN, H_2O 2%	300 W Xe lamp $\lambda > 400$ nm	0.35108 mmol g^{-1} h^{-1}	112

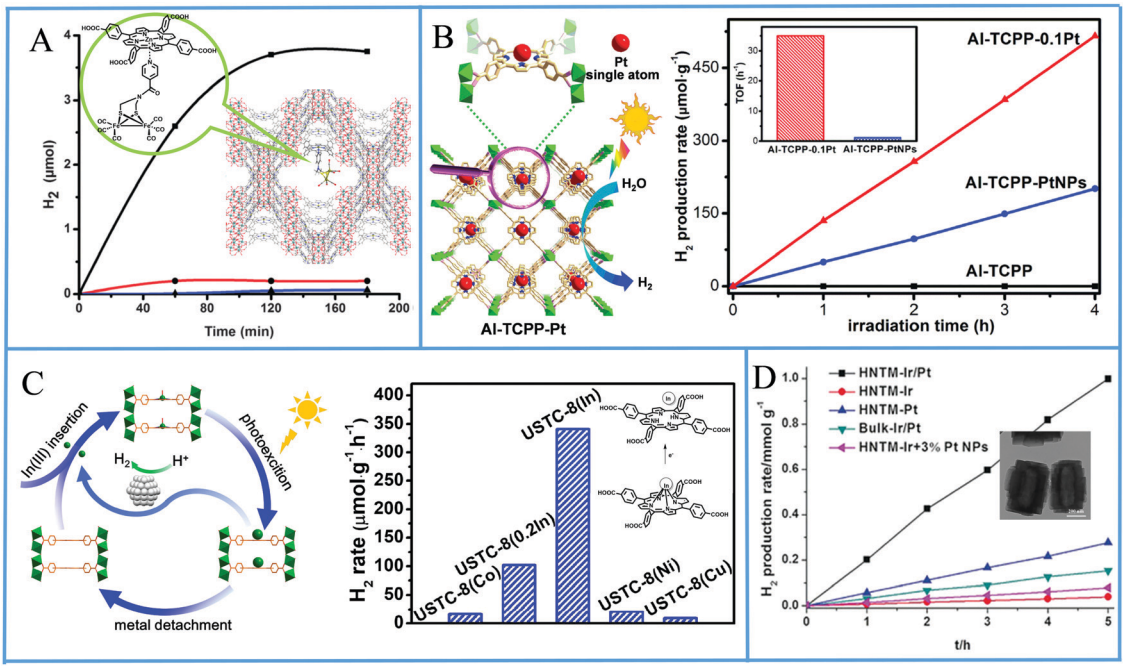

Fig. 16 (A) H_2 evolution plots of ZrPF with $[Fe_2S_2]$ complex, Reproduced from ref. 99, with permission from Royal Society of Chemistry, Copyright 2014. (B) Proposed H_2 evolution diagram of Al–TCPP–Pt along with the production rate, Reproduced from ref. 100, with permission from John Wiley and Sons, Copyright 2018. (C) Amount of H_2 evolution of USTC-8(In) and other USTC-8(M), Reproduced from ref. 101, with permission from American Chemical Society, Copyright 2018. (D) H_2 evolution plots of HNTM-M. Reproduced from ref. 102, with permission from John Wiley and Sons, Copyright 2018.

eagerly detached from the porphyrin after light excitation and therefore avoid the fast back electron transfer. This characteristic leads to greatly enhanced photocatalytic performance in comparison with the equivalent in-plane metallated PMOFs.

He *et al.* further explored the immobilization of single metal atoms on PMOFs towards photocatalytic H_2 evolution.[102] For this purpose, they synthesized the known Zr-porphyrinic MOF hollow nanotubes (HNTM) using TCPP and subsequently incorporated various single noble metal atoms (Ru, Au, Pd, Ir, Pt) in the porphyrin cores. The HNTM-M PMOFs were tested for photocatalytic H_2 production from water splitting under visible light irradiation using TEOA as SED and the reaction solvent was MeCN. The non-metallated HNTM exhibited negligible activity and the HNTM-Ir PMOF showed poor photocatalytic performance (0.0076 mmol g^{-1} h^{-1}). The platinum metallated HNTM presented moderate activity (0.0567 mmol g^{-1} h^{-1}), while the most efficient system was HNTM-Ir/Pt where both noble metals were utilized and reached 0.2019 mmol g^{-1} h^{-1} (Fig. 16d and Table 4, entries 6–8). The last system was stable for three catalytic runs and the morphology of the hollow nanotubes was retained, while no metal NPs were formed.

Lin's group prepared two new PMOFs (Ru-TBP and Ru-TBP-Zn) built from Ru_2 paddlewheel building units and TCPP porphyrin.[103] The Ru_2 units were utilized as catalysts for visible-light-driven H_2 production while the porphyrin moieties played the role of the photosensitizer. The photocatalytic activities of Ru-TBP and Ru-TBP-Zn were studied in MeCN with H_2O as proton source and TEOA as SED and showed linear H_2 productivity with a rate of 0.13 mmol g^{-1} h^{-1} and 0.24 mmol g^{-1} h^{-1} respectively (Fig. 17a and Table 4, entries 9 and 10). The authors also measured the performance of a homogeneous control system with Ru_2 paddlewheels (Ru_2-PD) and ZnTCPP which exhibited negligible activity, highlighting the significance the hierarchical organization of photosensitizing ligands and the catalytic units towards photocatalytic H_2 production.

Li *et al.* utilized a known PMOF, the PCN-222(Hf), based on TCPP porphyrin linker metallated with Pd resulting in Pd-PCN-222 through the self-assembly of $HfCl_4$ and PdTCPP. Pt nanorods with a width of ~3 nm were successfully immobilized into the hexagonal channels (with diameters of 3.7 nm) of Pd-PCN-222(Hf) and the resulting material was employed in photocatalytic hydrogen production.[104] The authors selected PdTCPP porphyrin as photosensitizer due to its long lived phosphorescence and visible-light absorption, and encapsulated the Pt NP co-catalyst in the PMOF for efficient electron–hole separation. Indeed, they achieved a synergetic effect between these components and accomplished a H_2 evolution rate of 22.674 mmol g^{-1} h^{-1} under visible light irradiation (Fig. 17b). The PMOF without the Pt NPs was also examined and exhibited good photocatalytic activity 2.476 mmol g^{-1} h^{-1} indicating that the Pd-porphyrin itself has a critical role in the photocatalytic reaction. Noteworthy the isostructural with PCN-222(Hf) was inactive without Pt NPs and exhibited 0.441 mmol g^{-1} h^{-1} in their presence (Table 4, entry 11–13).

Wang *et al.* utilized analogous PMOF nanosheets, which instead of Hf contained Ti metal nodes,[105] in photocatalysis with Pt NPs as co-catalyst and water as reaction medium.[106] In detail, they synthesized PCN-22 with Ti–oxo clusters and subsequently photodeposited Pt NPs under 300 W Xe lamp irradiation in the presence of AA. The resulting material was able to

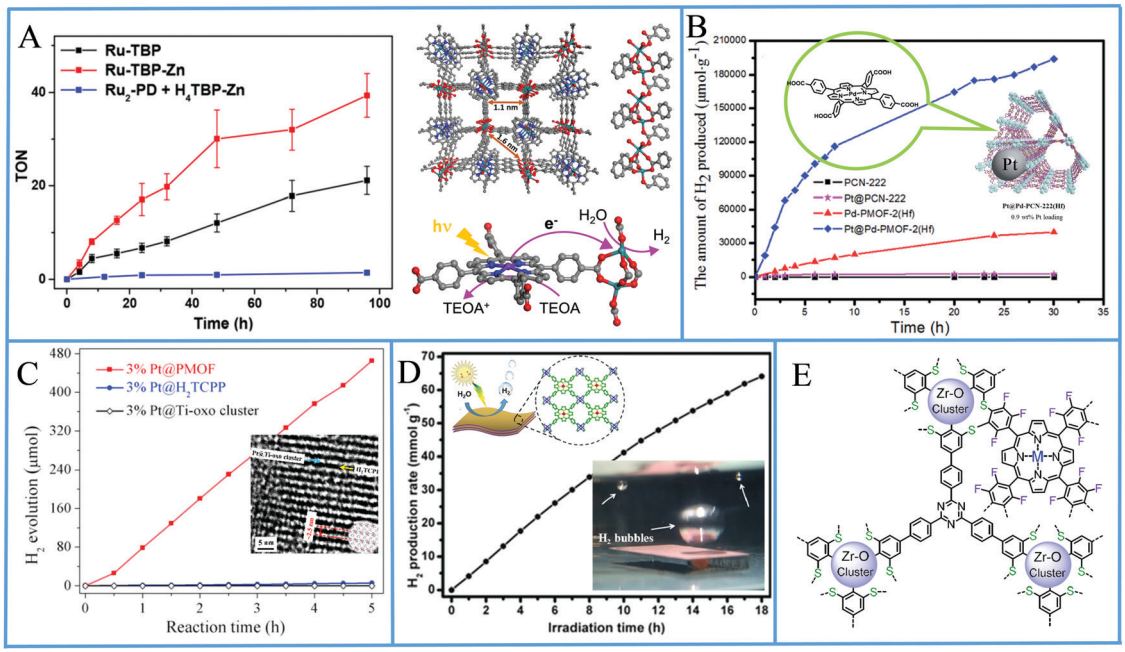

Fig. 17 (A) H_2 evolution plots and proposed H_2 evolution diagram of Ru-TBP PMOFs, Reproduced from ref. 103, with permission from American Chemical Society, Copyright 2018. (B) H_2 evolution plots and schematic illustration of Pd-PCN-222(Hf), Reproduced from ref. 104, with permission from Royal Society of Chemistry, Copyright 2019. (C) Amount of H_2 evolution of PCN-22 PMOFs, Reproduced from ref. 106, with permission from Elsevier, Copyright 2019. (D) H_2 evolution plots of and schematic illustration of PtSA-MNS, Reproduced from ref. 107, with permission from John Wiley and Sons, Copyright 2019. (E) Cross-linking between ZrTTA-6SH MOF and MTFPP porphyrins. Reproduced from ref. 108, with permission from American Chemical Society, Copyright 2020.

act as photocatalyst for visible light driven H_2 evolution and exhibited a rate of 8.52 mmol g^{-1} h^{-1} (Table 4, entry 14). This performance was significantly higher than the system of Pt@TCPP which contained platinum NPs photodeposited on TCPP porphyrin as shown in Fig. 17c. The authors examined the catalytic mechanism and explained that after visible light excitation, the photo-induced electrons are transferred *via* ligand to metal charge transfer from the LUMO orbital of porphyrin linkers to the conduction band of the Ti–oxo clusters and then to Pt NPs, where photocatalytic hydrogen evolution takes place.

Zhou and Mai and co-workers synthesized ultrathin PMOF nanosheets using PtTCPP porphyrin linker and Cu_2–$(COO)_4$ paddle-wheel clusters as metal node in order to prepare a 2-dimensional single-atom-catalyst (SAC) system for photocatalytic H_2 production.[107] Following this approach, which varies from previous post-modification strategies, the authors created the first example of 2D MOF-based SACs and achieved an ultrahigh Pt loading of 12.0 wt%. The resulting nanosheets exhibited great photocatalytic activity for H_2 production (11.320 mmol g^{-1} h^{-1}) in water under visible-light irradiation and AA as SED (Table 4, entries 15 and 16). Furthermore, the 2D PMOF was drop-casted onto a solid surface, forming thin films which kept their photocatalytic activity and exhibited H_2 evolution visible by naked (Fig. 17d).

Diao *et al.* reported one year later the utilization of a 2D, lamellar Zr-MOF (ZrTTA-6SH) as a host for porphyrin guests towards photocatalytic H_2 evolution.[108] Notably in this example the porphyrin is not the linker between the metal nodes. The H_3TTA-6SH linker bear nucleophilic thiol groups and the porphyrin guests (ZnTFPP, NiTFPP, and FeTFPP), on the other hand, contain fluoro groups to enable the sulfide crosslinking as shown in Fig. 17e, resulting in the encapsulation of the porphyrins inside the MOF. Photocatalytic H_2 generation experiments under visible light irradiation in the presence of TEOA as SED and 3 wt% Pt NPs as co-catalyst showed that the material with the ZnTFPP anchored guests exhibit the highest activity (0.110 mmol g^{-1} h^{-1}) followed by the NiTFPP and then the FeTFPP derivatives (Table 4, entries 17–19).

Wang and co-workers[109] constructed an overall photocatalytic water splitting system using MOFs. To achieve this goal, the authors prepared HER-PMOF nanosheets based on ZnTCPP and PtTCPP linkers and WOR-MOF flakes and subsequently integrated these MOFs into liposome (LP) vesicles. The lipid bilayer was selected to separate the oxidative and reductive parts and avoid charge recombination. The HER-MOF consisted of light-harvesting ZnTCPP and catalytic PtTCPP porphyrin linkers and Hf metal nodes, which were initially tested for photocatalytic H_2 evolution in the presence of phenol as SED and exhibited a really high TOF (1.2×10^4 h^{-1}, Table 4, entries 20 and 21). The WOR-MOF comprised of appropriately modified $[Ru(bpy)_3]^{2+}$ photosensitizers and Ir-bpy catalytic centres and was incorporated in the hydrophilic part of the LP, while the HER-PMOF was localized in the hydrophobic lipid bilayer of the LP. Noteworthy, the final liposome–MOF assembly (LP-HER-WOR-MOF) accomplished overall photocatalytic water splitting under visible light

irradiation without any sacrificial reagents, reaching catalytic activity for H_2 836 μmol g^{-1} over 72 h (0.0116 mmol g^{-1} h^{-1}).

The same group presented another work,[110] where they utilized the same PMOF towards visible light-driven H_2 evolution. In their study, the authors compared the molecular catalyst PtTCPP with the corresponding PCN-223 PMOF containing PtTCPP linkers, as well as with the PMOF including both PtTCPP catalytic and ZnTCPP photosensitizing sites (Fig. 18a). Under optimal reaction conditions, the molecular system (in DMF–H_2O 8 : 2) exhibited a TON of 60 after 96 h of visible irradiation using chloranilic acid (CA) as SED, while the PtTCPP PCN-223 showed a TON = 78 in water. Interestingly the PMOF comprising of both PtTCPP and ZnTCPP units displayed much higher photocatalytic activity (TON = 5×10^4), performance which was attributed to the antenna effect between the photosensitizer and the catalyst (Table 4, entry 22).

Jin *et al.*[111] presented another PMOF example with photocatalytic properties, where they achieved both H_2 production as well as degradation of tetracycline hydrochloride pollutant. More specifically the authors prepared $ZnIn_2S_4$@PCN-224 comprising of TCPP porphyrin linkers, Zr metal nodes and $ZnIn_2S_4$ nanocomposites, which exhibited a hydrogen evolution rate of 0.284 mmol h^{-1} in absence of Pt, whereas the presence of platinum increased the performance approximately 12 times (3.41 mmol h^{-1}) (Fig. 18b and Table 4, entries 23 and 24). The researchers advertise that their Pt free system possesses a much higher photocatalytic activity than many $ZnIn_2S_4^-$ based photocatalysts even in presence of Pt cocatalyst, result that could be attributed to the hierarchical heterostructure of $ZnIn_2S_4$@PCN-224, in which the photoexcited carriers are effectively separated and migrated.

The commonly used PtTCPP porphyrin linker has been investigated also in a work by Lin *et al.*, where the authors prepared the zirconium-based PMOF PCN-222 containing different ratios of PtTCPP and free-base TCPP.[112] In detail four different ratios of TCPP/PtTCPP were studied (4 : 1, 3 : 2, 2 : 3, and 0 : 1) with the best performing system being the one with the fully Pt metallated porphyrin linkers (Fig. 18c). Under visible light irradiation, this system reached 0.35108 mmol g^{-1} h^{-1} in the presence of TEOA as SED (Table 4, entry 25). Lowering the ratio of Pt caused a decrease in the overall activity, result that was attributed to the uniformly dispersed catalytic Pt(II) ions.

2.2.3 Porphyrin COFs and COPs for H_2 production. In the previous section, porphyrin MOFs provide among other characteristics, the specific arrangement of porphyrin chromophores in space, utilizing an appropriate metal linker. Another approach to organize porphyrins in a network is through the design of porphyrin-based conjugated organic polymers or covalent organic frameworks, where no metal node is necessary. In this section we analyze the reports where porphyrin COFs are utilized in photocatalytic H_2 evolution systems.

In a recent report, Chen *et al.*[113] designed a series of porphyrin-based conjugated polymers as depicted in Fig. 19a, where metallated porphyrin monomers were connected through a triple bond *via* Sonogashira coupling and contained two metal ions, namely Zn(II) and Co(II). The synthesized materials were utilized in photocatalytic H_2 production with Pt as co-catalyst and TEOA as the best performing SED. The photocatalytic activity was increased by replacing Zn with Co, while the best performing system was the one with both metal centers (ZnZnP < CoCoP < ZnCoP) (Table 5, entries 1–3). The authors attributed the observed differences in the overall performance to the Co–porphyrin units in the ZnCoP system, which acted as an electron acceptor, promoting the charge transfer from the Zn–porphyrin to the Co–porphyrin moieties and resulting in a more effective charge separation.

The same research group improved the aforementioned system in a recent work, by introducing perfluorophenyls groups to the porphyrin moieties metallated with Co (19a).[114] The resulting ZnCoP–F conjugated polymer displayed greater photocatalytic performance than ZnCoP, which contained only phenyl groups. The authors attributed this improvement to the higher electron-withdrawing capacity of perfluorophenyls in the ZnCoP–F system (Table 5, entries 4 and 5). Moreover, the new system was sufficiently active in the absence of Pt cocatalyst, with the Co ions in the Co–porphyrin moieties serving as single atom catalytic sites. To prove this point the authors synthesized a Co-free analogue (ZnH_2P–F conjugated polymer) and found no photocatalytic activity, while both ZnH_2P–F and ZnCoP–F conjugated polymers exhibit much better H_2 production rate after loading with 1.0 wt% Pt.

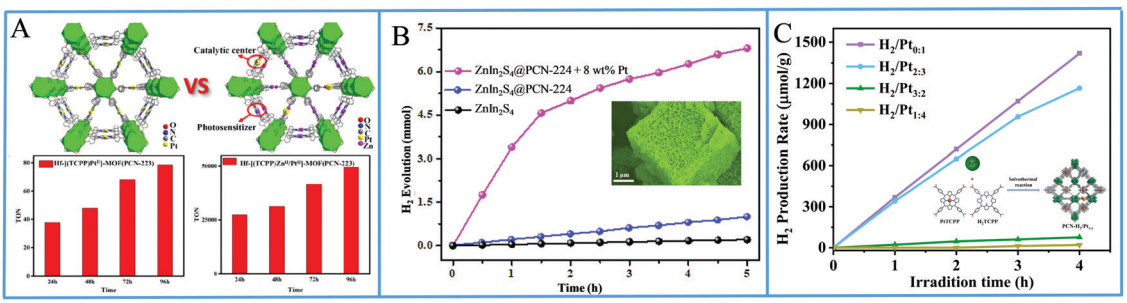

Fig. 18 (A) schematic illustration of PCN-223 PMOFs containing only Pt or both Pt and Zn sites, along with their photocatalytic performance diagrams, Reproduced from ref. 110, with permission from Elsevier, Copyright 2021. (B) H_2 evolution plots of $ZnIn_2S_4$@PCN-224, Reproduced from ref. 111, with permission from Elsevier, Copyright 2021. (C) Amount of H_2 production of PMOF PCN-222 containing different ratios of PtTCPP and free-base TCPP. Reproduced from ref. 112, with permission from American Chemical Society, Copyright 2021.

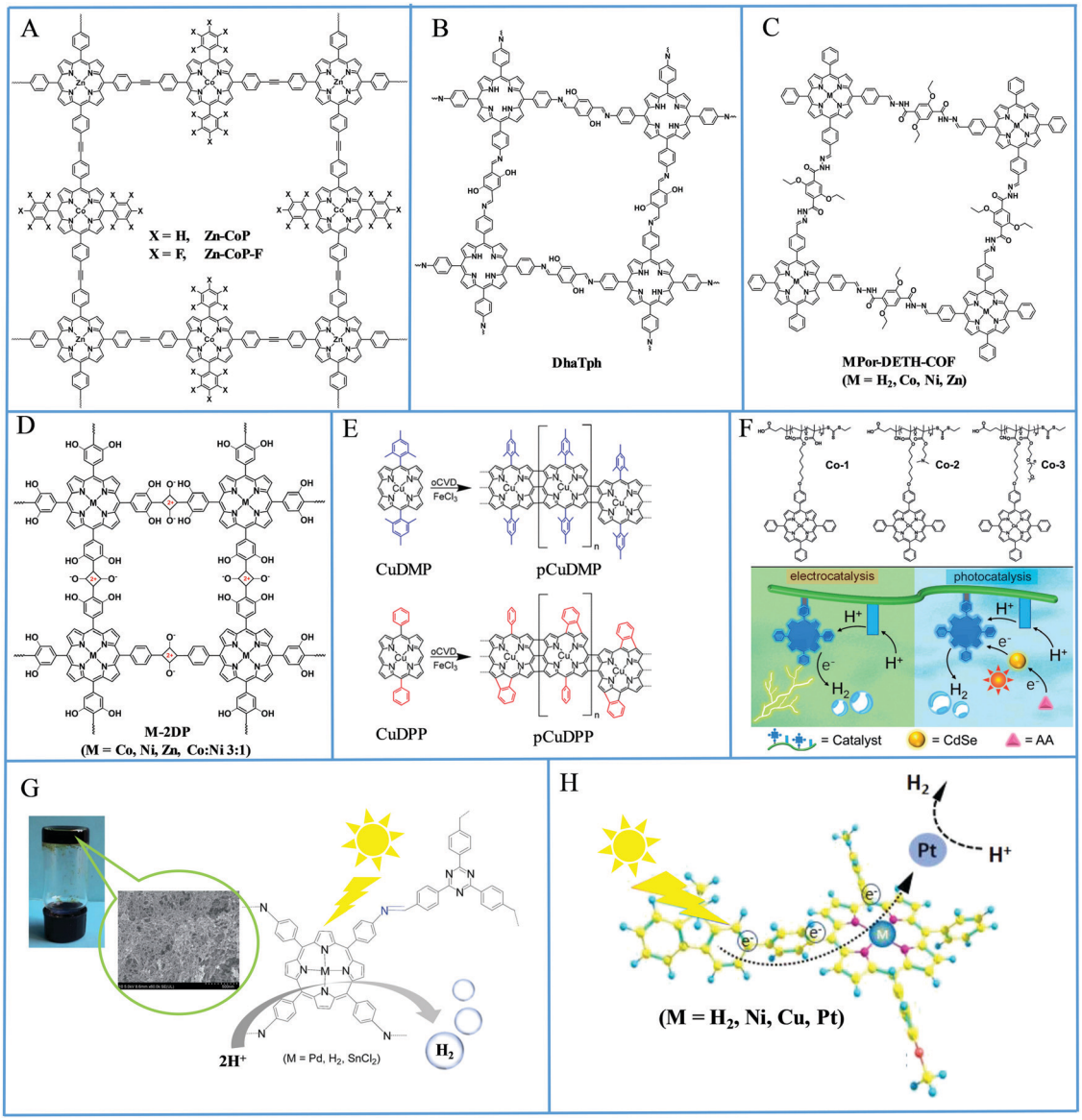

Fig. 19 (A) Molecular structures of ZnZnP, CoCoP, ZnCoP and ZnCoP–F COFs, (B) molecular structure of the DhaTph COF, (C) molecular structures of MPor-DETH-COF where M: H_2, Co, Ni, Zn, (D) molecular structures of M-2DP where M: = Co, Ni, Zn, Co : Ni 3 : 1, (E) molecular structures of fused Cu(II) porphyrins, (F) molecular structures and schematic illustration of the Co–porphyrin polymers with different side-chain groups, Reproduced from ref. 120, with permission from John Wiley and Sons, Copyright 2020. (G) Molecular structures and SEM image of the imine gels based on porphyrin molecular precursors, Reproduced from ref. 121, with permission from Royal Society of Chemistry, Copyright 2018. (H) Schematic illustration of porphyrin conjugated polymers with quaternary ammonium side chains towards H_2 production. Reproduced from ref. 122, with permission from American Chemical Society, Copyright 2021.

In another report, Osakada and coworkers synthesized a covalent organic framework (Fig. 19b) and subsequently prepared 2D-porphyrin polymer nanodisks (of 1 nm thickness) *via* an exfoliation method.[115] In order to achieve this exfoliation the authors utilized the incorporation of metal ions (Mg^{2+} and Cu^{2+}) in combination with pyridine axial ligands to disrupt the π–π stacking of the porphyrin covalent framework through steric interactions. Both materials, the initial COF (DhaTph) and the exfoliated covalent organic nanodisks (e-CONs), were applied in photocatalytic H_2 generation under visible and near-infrared light irradiation using Pt nanoparticles/reduced-graphene oxide (Pt/RGO) as cocatalysts. The later exhibited enhanced photocatalytic activity compared to the initial material, result that might be attributed to the higher surface area between e-CON chromophore and the Pt/RGO cocatalyst (Table 5, entries 6 and 7).

Wang, Wu and co-workers[116] synthesized another covalent organic framework (Fig. 19c), having structural similarities with the COF in the previous report. Metalation with Co, Ni and Zn followed and all four 2D PCOFs (MPor-DETH-COF) were evaluated for their activity in photocatalytic hydrogen production. In detail, the authors employed H_2PtCl_6 as a co-catalyst, TEOA

Table 5 Photocatalytic performance of porphyrin COFs and polymers for H_2 production

Entry	COF/polymer name	Cocatalyst	SED	Solvent and ingredients	Light source	Hydrogen production rate	Ref.
1	ZnCoP	1.0 wt% Pt	TEOA 15%	H_2O	300 W Xe lamp $\lambda > 400$ nm	43 μmol h^{-1}	113
2	CoCoP	1.0 wt% Pt	TEOA 15%	H_2O	300 W Xe lamp $\lambda > 400$ nm	33 μmol h^{-1}	113
3	ZnZnP	1.0 wt% Pt	TEOA 15%	H_2O	300 W Xe lamp $\lambda > 400$ nm	8 μmol h^{-1}	113
4	ZnCoP–F	—	TEOA 15%	H_2O	300 W Xe lamp $\lambda > 400$ nm	58 μmol h^{-1}	114
5	ZnCoP	—	TEOA 15%	H_2O	300 W Xe lamp $\lambda > 400$ nm	27 μmol h^{-1}	114
6	DhaTph	Pt/RGO	EDTA (0.5 M)	H_2O	HAL-320W solar Simulator $\lambda > 420$ nm	0.75[a] μmol h^{-1}	115
7	DhaTph e-CONs	Pt/RGO	EDTA (0.5 M)	H_2O	HAL-320W solar Simulator $\lambda > 420$ nm	1.25[a] μmol h^{-1}	115
8	CoPor-DETH-COF	8 wt% H_2PtCl_6	TEOA 1%	H_2O	300 W Xe lamp $\lambda > 400$ nm	25 μmol g^{-1} h^{-1}	116
9	H_2Por-DETH-COF	8 wt% H_2PtCl_6	TEOA 1%	H_2O	300 W Xe lamp $\lambda > 400$ nm	80 μmol g^{-1} h^{-1}	116
10	NiPor-DETH-COF	8 wt% H_2PtCl_6	TEOA 1%	H_2O	300 W Xe lamp $\lambda > 400$ nm	211 μmol g^{-1} h^{-1}	116
11	ZnPor-DETH-COF	8 wt% H_2PtCl_6	TEOA 1%	H_2O, phosphate buffer 0.1 M, pH = 7.0	300 W Xe lamp $\lambda > 400$ nm	413 μmol g^{-1} h^{-1}	116
12	Co-2DP	1 wt% H_2PtCl_6	TEOA 1%	H_2O	Direct sunlight	1.25[a] μmol h^{-1}	117
13	CoNi-2DP	—	TEOA 30%	H_2O	Direct sunlight	75 μmol g^{-1} h^{-1}	118

[a] Estimated from the graph the authors presented.

as SED and under visible light irradiation they observed H_2 evolution rates of corresponding MPor-DETH-COF, with the following order of M: Co < H_2 < Ni < Zn (Table 5, entries 8–11). An effort to explain this trend was provided *via* DFT calculations based on the tailored charge-carrier dynamics of the synthesized materials.

Babu and coworkers[117] designed and synthesized a different 2D polymer (Co-2DP) based on cobalt porphyrin monomers, as depicted in Fig. 19d. This material was utilized as water splitting photocatalyst, since it was able to perform both H_2 and O_2 evolution reactions under visible light irradiation. Regarding the hydrogen production, the authors used the known Pt co-catalyst and TEOA as SED. Photocatalytic evolution of H_2 and O_2 was observed for 20 catalytic cycles with insignificant decrease in the efficiency, hence proving the stability of this new material. Control experiments with porphyrin monomers demonstrated the importance of the hydroxyl groups for the bifunctional water splitting ability (Table 5, entry 12).

This material was further developed by the same research team in the following years.[118] The authors used different metal ions to metallate the porphyrin 2D-polymer, namely Co(II), Ni(II) and Zn(II), and synthesized the four derivatives described in Fig. 19d. These porphyrin polymers exhibited bifunctional photocatalytic water splitting ability towards both H_2 and O_2 evolution. Like their previous studies, the best light source was proven the direct sunlight and the best performing material was the one, which contained both Co and Ni in 3 : 1 ratio inside the porphyrin cores. This bimetallic (CoNi-2DP) porphyrin polymer displayed long-term stability for 15 cycles of H_2 and O_2 production, it was active for sea and river waters besides pure water and presented significant photocatalytic activity even in the absence of Pt (Table 5, entry 13).

Another type of porphyrin conjugated polymers that were employed in photocatalytic HER were the fused Cu(II) porphyrins reported by Boscher and coworkers.[119] The authors synthesized thin films of fused Cu(II) porphyrin which were proved to be active both in electrocatalytic and photocatalytic H_2 evolution (Fig. 19e). In detail, the synthesized materials showed superior hydrogen production under visible light irradiation in the presence of EDTA as SED, in comparison to the reference non-fused porphyrin thin films. Noteworthy for the photocatalytic experiments the porphyrin-based thin films were deposited on FTO substrates before irradiation by a solar simulator. The most efficient system was the one which contained fused phenyl substituents reaching 9.2 μmol cm^{-2} h^{-1}.

In another report that focused both on electro- and photocatalysis, Xie *et al.* prepared three water-soluble porphyrin polymers with Co metal cores and different side-chain groups (Fig. 19f).[120] The varied side chains were mimicking the enzyme residue groups, which are located close to reaction centers and play significant role in the overall activity. In their photocatalytic studies, the authors used CdSe as photosensitizer, the Co–porphyrin polymers were the catalytic part while ascorbic acid was the SED. Co-2 (Fig. 19f) displayed the highest efficiency reaching a TON = 2.7 × 10^4 at neutral pH and this result was attributed to the strong interactions of its protonated amino side-chain groups with the negatively charged CdSe photosensitizer.

In another work, Liao *et al.* prepared a series of imine gels based on porphyrin molecular precursors and investigated their photocatalytic activity towards hydrogen production.[121] In detail the imine gels were synthesized by reacting the free-base porphyrin 5,10,15,20-tetrakis(*p*-aminophenyl)porphyrin (H_2TAPP) and its Pd- and Sn- metallated derivatives with the 1,3,5-tris-(4-formylphenyl)triazine (TFPT) linker (Fig. 19g). The best performing system was the Pt-doped PdTAPP–TFPT gel, which achieved 1.0744 × 10^5 μmol g^{-1} of hydrogen productivity for 120 h. In this work, ascorbate was utilized as SED while water was the proton source. Interestingly, the Pd based wet gel exhibited considerably higher H_2 evolution efficiency and stability than the dried aerogel, the free base and the Sn-metallated photocatalytic systems. The authors showed that the PdTAPP–TFPT gel was also electrocatalytically activity towards H_2 production after coated on FTO electrodes.

Zhao *et al.* designed porphyrin conjugated polymers with different coordinated metals and applied them in photocatalytic

hydrogen evolution (Fig. 19h).[122] The side chains contained quaternary ammonium salts in order to provide good dispersibility in water and allow the formation of nanoscale aggregates, while the porphyrin core was metallated with Ni, Cu, and Pt. The Pt metallated polymers enabled efficient photocatalytic hydrogen evolution of up to 5.39 mmol g^{-1} h^{-1} without the assistance of co-catalysts and reached 37.9 mmol g^{-1} h^{-1} in the presence of Pt co-catalyst.

2.2.4 2D Materials combined with porphyrins for H_2 production. Graphene oxide (GO) and graphitic carbon nitride (g-C_3N_4) have been widely investigated for their photoelectric and photocatalytic properties. Both have been extensively used as photocatalysts for hydrogen production applications, due to their advanced electronic properties, good stability, and low-cost fabrication. These types of materials can also be functionalized with photosensitizers, such as porphyrins, through covalent or non-covalent interactions. This modification improves the light absorption and diminishes the fast recombination of the electron–hole pairs that are generated through the photocatalysis. Moreover, porphyrin molecules are the ideal candidates for this type of functionalization due to their facile structural modification, different ways of interactions with the materials and their high visible molar coefficient. Therefore, in this section are presented all the latest paradigms of the graphite-based materials with porphyrin derivatives for the photocatalytic hydrogen production. First of all, we will discuss the modified 2D materials with porphyrin molecules *via* covalent bonds and then we will continue our description with the non-covalent examples reported in the literature. Subsequently, Yan and co-workers synthesized a photosensitizer (TPP–GO), comprised of a tetraphenylporphyrin (TPP) covalently linked with an amide bond at a GO and catalysts of the [Fe–Fe]-hydrogenase models ([Fe–Fe]1–[Fe–Fe]3), bearing different phosphine ligands (Fig. 20 and 21).[123] Upon addition of both components in an aqueous ethanol solution, the catalyst was

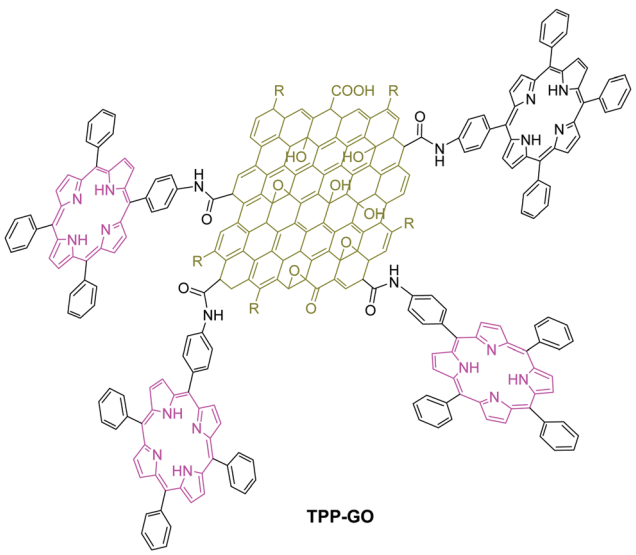

Fig. 20 Photocatalytic hydrogen production of a biomimetic system of a [Fe–Fe]-hydrogenases model as a catalyst and a covalently linked graphene oxide with a porphyrin TPP–GO and cystine.

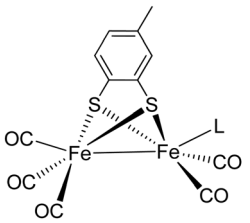

[Fe-Fe] 1 L = CO
[Fe-Fe] 2 L = PPh_3
[Fe-Fe] 3 L = $Ph_2P(2\text{-}C_5H_4N)$

Fig. 21 Chemical structures of [Fe–Fe]-hydrogenase model catalysts.

absorbed non-covalently on the GO surface and photocatalytic H_2 evolution experiments were performed. All the photocatalytic experiments were done in the presence of cysteine as an electron donor, under light irradiation at $\lambda > 380$ nm. Hydrogen production varied with the different catalysts in the following range [Fe–Fe]3 (2.82 TON) > [Fe–Fe]2 (1.80 TON) > [Fe–Fe]1 (1.61 TON), after 5 h of irradiation (Table 6, entries 1–3). When GO was used as photosensitizer in the absence of the porphyrin H_2 production was lower under the same conditions. In the case of a non-covalently linked porphyrin to GO, the system produced less hydrogen compared to the covalently linked porphyrin. Moreover, in the absence of GO H_2 production efficiency was less compared to the presence of GO. Therefore, the best photocatalytic results were obtained when the porphyrin is covalently linked with the GO and in the presence of [Fe–Fe]3 catalyst. Possibly the presence of the pyridine group in catalyst [Fe–Fe]3 assists the proton transfer to diiron due to its protonation, therefore the hydrogen production is accelerated.

The same group performed photocatalytic studies using the same TPP–GO as photosensitizer and a Ni-based catalyst, $NiPPh_2$ in an ethanol aqueous solution (Fig. 22).[124] Upon light irradiation with an Hg lamp and a cutoff filter ($\lambda > 380$ nm) in the presence of ascorbic acid as a sacrificial electron donor almost 1.2 μl H_2 were obtained upon 5 h of irradiation (Table 6, entry 4). The presence of GO and in this case enhances the hydrogen production and the present of all components are necessary to be present for effective hydrogen evolution.

In another report, a MnTPP porphyrin was covalently linked to graphene oxide (MnTPP–GO) and the material was used as photosensitizer in hydrogen evolution experiments (Fig. 23).[125] Upon UV-Vis irradiation in the presence of TEA, for 6 h, 3.8 μmol mg^{-1} of H_2 was produced and this amount increased to 4.6 μmol mg^{-1} in the presence of Pt nanoparticles, under the same conditions (Table 6, entries 5–7). Moreover, the performance of the system was improved further 5.2 μmol mg^{-1} when a surfactant PVP was added, possibly due to prevention of the aggregation of the photocatalyst. Recycling experiments proved the stability of this type of system.

Instead of altering the surface of GO through covalent bonding, another way is to graft GO with metal ions that can act as interfacial linkers. This type of material can then interact with chromophores such as porphyrins with electrostatic interactions or with coordination bonds. Therefore, different metals ($M = K^+$, Ca^{2+}, Zn^{2+}, Cu^{2+}, Co^{2+}, Cr^{3+}) were added onto GO in order to form the M–GO material where the content of ions was about 10%.[126] Then, by adding DPyP porphyrin the DPyP–M–GO

Table 6 Photocatalytic performance of 2D materials combined with porphyrins for H_2 production

Entry	PS (C)	Catalyst (C)	SED (C)	Solvent	Light source	Irr. time (h)	H_2	TOF (h^{-1})	Ref.
1	TPP–GO (4.4×10^{-5} M based on TPP)	[Fe–Fe]1 (4.8×10^{-6} M)	Cystine (1.8×10^{-3} M)	EtOH–water (1 : 24), pH = 1.5	Hg lamp (450 W) ($\lambda > 380$ nm)	5	1.61TON	0.32	123
2	TPP–GO (4.4×10^{-5} M based on TPP)	[Fe–Fe]2 (4.8×10^{-6} M)	Cystine (1.8×10^{-3} M)	EtOH–water (1 : 24), pH = 1.5	Hg lamp (450 W) ($\lambda > 380$ nm)	5	1.80 TON	0.36	123
3	TPP–GO (4.4×10^{-5} M based on TPP)	[Fe–Fe]3 (4.8×10^{-6} M)	Cystine (1.8×10^{-3} M)	EtOH–water (1 : 24), pH = 1.5	Hg lamp (450 W) ($\lambda > 380$ nm)	5	2.82 TON	0.56	123
4	TPP–GO (4.4×10^{-5} M based on TPP)	$NiPPh_2$ (3.0×10^{-5} M)	Ascorbic acid (0.1 M)	EtOH–water (1 : 24), pH = 4.0	Hg lamp (450 W) ($\lambda > 380$ nm)	5	1.2 μl H_2		124
5	TPP–GO (4.4×10^{-5} M based on TPP)	—	TEA (10% vol)	Water	UV-Vis	6	3.8 μmol mg^{-1}		125
6	TPP–GO (4.4×10^{-5} M based on TPP)	Pt	TEA (10% vol)	Water	UV-Vis	6	4.6 μmol mg^{-1}		125
7	TPP–GO/PVP (4.4×10^{-5} M based on TPP)	Pt	TEA (10% vol)	Water	UV-Vis	6	5.2 μmol mg^{-1}		125
8	GO (10 mg in 60 ml)	—	TEOA (10% vol)	Water	300 W Xe lamp	8	137 μmol g^{-1}		126
9	TPPy–GO (10 mg in 60 ml)	—	TEOA (10% vol)	Water	300 W Xe lamp	8	686 μmol g^{-1}		126
10	DPyP–Cr^{3+}–GO (10 mg in 60 ml)	—	TEOA (10% vol)	Water	300 W Xe lamp	8	928 μmol g^{-1}		126
11	DPyP–Co^{2+}–GO (10 mg in 60 ml)	—	TEOA (10% vol)	Water	300 W Xe lamp	6	1677 μmol g^{-1}		127
12	DPyP–Co–GO (10 mg in 60 ml)	—	TEOA (10% vol)	Water	300 W Xe lamp	2	1093 μmol g^{-1}		128
13	GO–Sm–DPyP	—	TEOA (16.7% vol)	Water	300 W Xe lamp	8	4.39 mmol g^{-1}		129
14	$[ZnTMPyP]^{4+}/MoS_2$/RGO	—	TEOA	Water, pH = 7.0	300 W Xe lamp		2560 μmol g^{-1} h^{-1}		130
15	GO/THPP/PSA	—	TEA	Water	light at λ = 450 nm	8	44.3 μmol g^{-1} h^{-1}		131
16	*p*TCPP/Pt/g-C_3N_4	Pt	TEOA (10% vol)	Water	Hg lamp (450 W) with a cut off filter ($\lambda > 380$ nm)		1208 μmol g^{-1} h^{-1}		132
17	*m*TCPP/Pt/g-C_3N_4	Pt	EDTA	Water	Light irradiation ($\lambda > 400$ nm)	6	48.4 μmol		133
18	ZnMT3PyP/Pt/g-C_3N_4	Pt	AA (50 mM)	Water	Light irradiation ($\lambda > 420$ nm)	8	437 μmol g^{-1}		134
19	ZnMT4PyP/Pt/g-C_3N_4	Pt	AA (50 mM)	Water	Light irradiation ($\lambda > 420$ nm)	8	524 μmol h^{-1}		135
20	2%NP/g-C_3N_4	Pt	H_2O:TEOA (9 : 1 vol%)	Water	LED monochromatic lamp (3 W, 420 nm)	3	2297 μmol g^{-1} h^{-1}		137
21	g-C_3N_4–Cu-TCPP	—	TEOA (10 vol%)	Water	300 W Xe lamp	2	10 mmol g^{-1}		138
22	g-C_3N_4–Cu-THPP	—	TEOA (16.7 vol%)	Water	300 W Xe lamp	6	7.50 μmol h^{-1}		139
23	g-C_3N_4–ZnPy-5	Pt	AA (50 mM)	Water	300 W Xe lamp ($\lambda >$420 nm)		418 mmol h^{-1}		140
24	g-C_3N_4–ZnPy-6	Pt	AA (50 mM)	Water	300 W Xe lamp ($\lambda >$420 nm)		585 mmol h^{-1}		140
25	g-CNU-TDPP	Pt	TEOA (10%)	Water	300 W Xe lamp		7.6 mmol g^{-1} h^{-1}		141

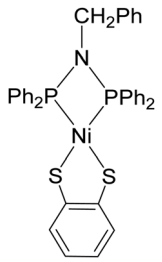

NiPPh$_2$

Fig. 22 Chemical structure of a mononuclear nickel catalyst (NiPPh$_2$).

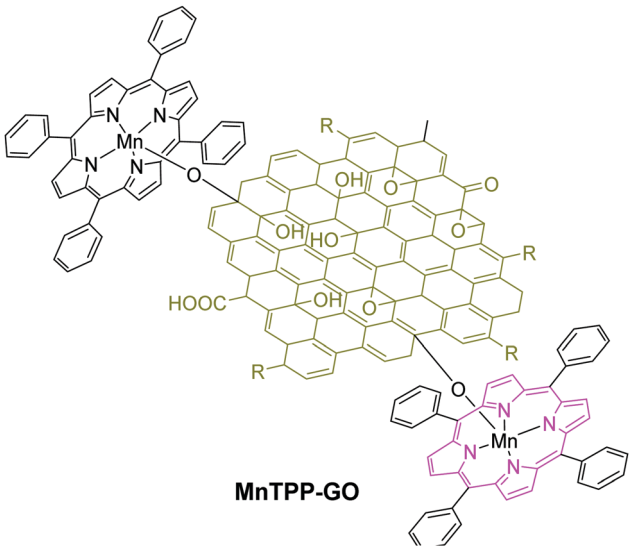

Fig. 23 Chemical structure of MnTPP–GO photocatalyst.

material was prepared and by mixing just GO with DPyP the DPyP–GO nanocomposite was synthesized (Fig. 24 and 25). The photocatalytic studies were performed upon irradiation with 300 W Xe lamp as the light source, in the presence of TEA as a sacrificial electron donor. GO, DPyP–GO and DPyP–Cr^{3+}–GO after 8 h of visible irradiation produced 137, 686 and 928 μmol g^{-1}, respectively (Table 6, entries 8–10). The highest photocatalytic activity was performed from DPyP–Cr^{3+}–GO photocatalyst possibly due to the stronger coordination interaction between metal ions and the porphyrin. The porphyrin on the material was used as an antenna system, able to absorb light quite efficiently, while the GO acted as the electron transfer support. The metal ions promote the transfer of the photogenerated electrons and finally improve the photocatalytic performance of the system. Moreover, the same group prepared another metal implanted bispyridyl porphyrin with graphene oxide DPyP–Co^{2+}–GO photocatalyst.[127] This material with the absence of a cocatalyst under visible irradiation produced 1677 μmol g^{-1}, compared to DPyP–GO that evolved 1131 μmol g^{-1} (Table 6, entry 11). The presence of Co^{2+} ions between the porphyrin and the graphene oxide promotes efficient electron transfer and therefore improves the photocatalytic activity of the material. Next, since metal nanoparticles have a better activity as co-catalysts compared to the metal ions, a photocatalyst DPyP–Co–GO was prepared.[128] The photocatalytic activity towards hydrogen production of DPyP–Co–GO was 2 times higher 1093 μmol g^{-1} compared to DPyP–Co^{2+}–GO after 2 h of irradiation (Table 6, entry 12). This improved activity is attributed to the higher light absorption and the strong interaction between the components. The same group in a later report combined the photoactive porphyrin DPyP with a rare earth ion (Ln) and graphene oxide in order to improve the performance of the photocatalyst (Fig. 26).[129] Therefore, GO–Sm–DPyP nanohybrid was prepared and its hydrogen evolution performance was studied. In this structure, Sm^{3+} is combined with the oxygen groups of GO, when porphyrin was introduced Sm^{3+} was coordinated with the N atoms of the pyridyl group. Upon, photocatalytic studies the hybrid material GO–Sm–DPyP performed the maximum hydrogen production 4.39 mmol g^{-1} compared to GO-DPyP 3.09 mmol g^{-1} and GO 2.58 mmol g^{-1} after 8 h of irradiation under a Xenon lamp (Table 6, entry 13). This enhanced evolution and stability of the system is attributed to the improved communication and efficient electron transfer between the GO and the porphyrin due to the presence of Sm^{3+}. In another report, a water-soluble porphyrin $[ZnTMPyP]^{4+}$ was used as a photosensitizer in combination with a MoS_2-reduced graphene oxide (MoS_2/RGO) as catalyst in order to form a hybrid system for effective hydrogen evolution (Fig. 24).[130] The system was irradiated with a Xe lamp in the presence of triethanolamine as a sacrificial electron donor and showed a high H_2 evolution rate of 2560 μmol g^{-1} h^{-1} at pH 7 in the case of 5 : 1 ratio of MoS_2 to RGO (Table 6, entry 14). According to the mechanistic studies the exited sate of the porphyrin is quenched by the catalyst (MoS_2/RGO) through an oxidative quenching.

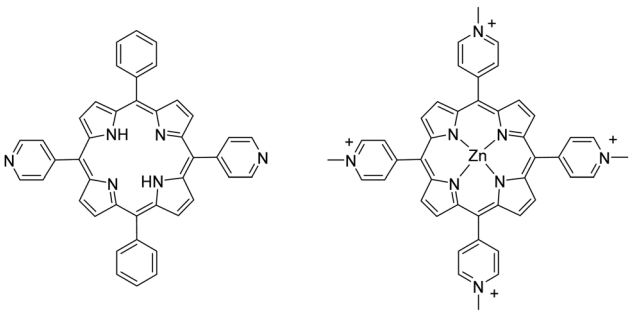

DPyP **[ZnTMPyP]$^{4+}$**

Fig. 24 Chemical structures of DPyP and $[ZnTMPyP]^{4+}$ porphyrins.

Another research group in order to enhance the light absorption combined two different dyes onto GO, a porphyrin molecule (THPP) and pyrene sulfonic acid (PSA) (Fig. 27).[131] Therefore, the dyes were non covalently attached onto GO and a nanohybrid material (GO/THPP/PSA) was constructed. This nanohybrid material showed better photocatalytic activity for H_2 evolution compared to all other combinations. More specifically, H_2 production was 7 times, 2.8 and 1.4 times greater than GO, GO/THPP and GO/PSA, respectively. After monochromatic irradiation at λ = 450 nm for 8 h, GO/THPP/PSA evolved hydrogen with a

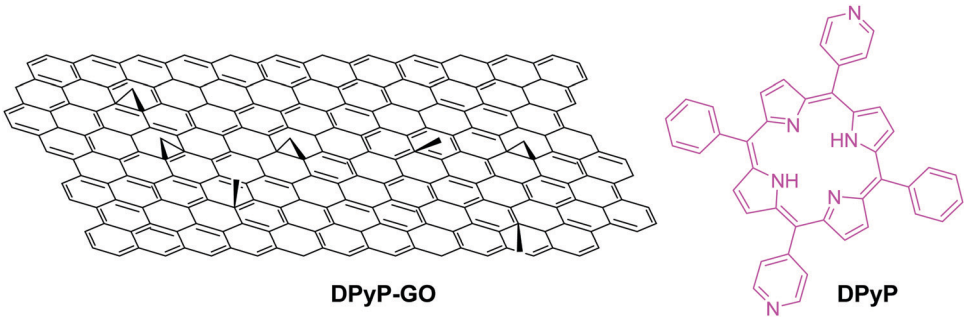

Fig. 25 Chemical structure of DPyP and DPyP–GO.

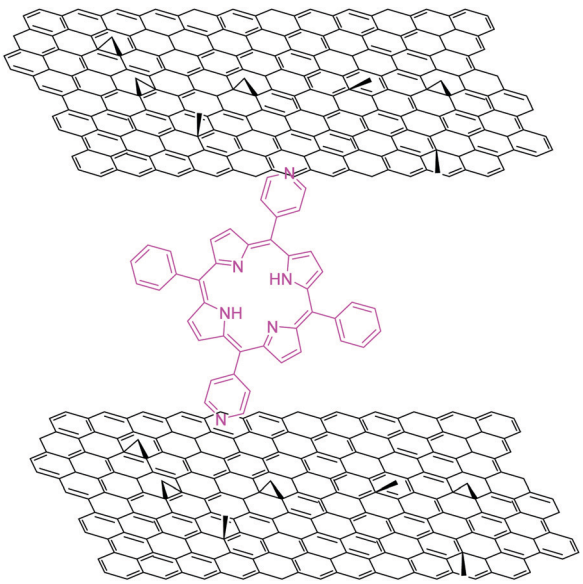

Fig. 26 Chemical structure of GO–Sm–DPyP.

rate of 44.3 μmol g^{-1} h^{-1}, in the presence of TEA, as sacrificial electron donor (Table 6, entry 15). This improved hydrogen production of the hybrid material is attributed mainly to the complementary absorption efficiency of THPP and PSA and to the strong interaction of GO with the two dyes.

As discussed in the introduction part, another efficient photocatalyst for hydrogen evolution is graphitic carbon nitride (g-C_3N_4). Sensitization of this catalyst with porphyrin dyes can enhance the hydrogen production and improve the stability of the system. In this report, 4-tetracarboxyphenyl porphyrin (*p*TCPP) was combined with g-C_3N_4 *via* π–π stacking interactions and studied towards hydrogen evolution in 10% vol TEOA aqueous solution under visible light irradiation (Fig. 28).[132] The hydrogen evolution rate of *p*TCPP/Pt/g-C_3N_4 was 1208 μmol g^{-1} h^{-1} that is higher compared to *p*TCPP/g-C_3N_4 and Pt/g-C_3N_4 that reached 30 and 564 μmol g^{-1} h^{-1} respectively (Table 6, entry 16). Hence, the combination of Pt nanoparticles as co-catalyst and *p*TCPP as a chromophore are important factors for improving the photocatalytic activity of g-C_3N_4, due to the electron transfer acceleration and the prevention of the recombination of electrons and holes in g-C_3N_4. Another research group investigated the influence of the position of the carboxylic acid on the porphyrin phenyl ring (*p*TCPP and *m*TCPP, Fig. 28).[133] The hybrid material *m*TCPP/Pt/g-C_3N_4 showed the highest H_2 evolution of 48.4 μmol under 6 h of UV-vis and visible light ($\lambda > 400$ nm) irradiation in the presence of EDTA (Table 6, entry 17). The system was quite stable, since after four consecutive recycles, the amount of hydrogen

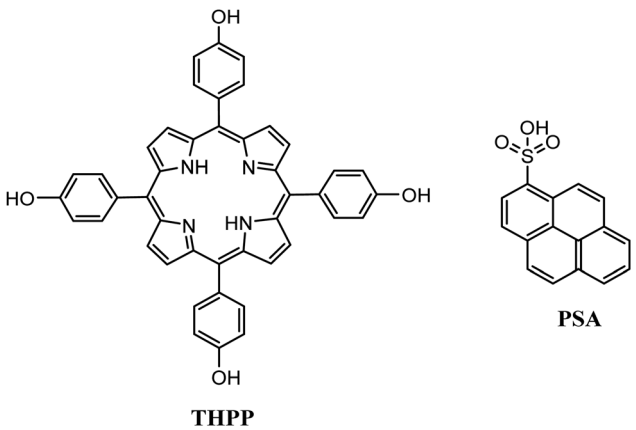

Fig. 27 Chemical structure of THP and PSA.

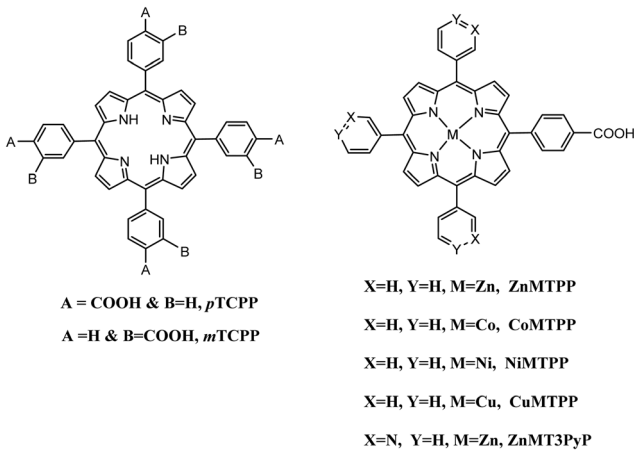

Fig. 28 Chemical structure of TCPP, ZnMTPP, CoMTPP, NiMTPP, CuMTPP and ZnMT3PyP.

evolution hardly changed. In another example, an asymmetric zinc porphyrin ZnMT3PyP, bearing three pyridines at the phenyl rings and a benzoic acid was sensitized onto Pt/g-C_3N_4 in order to produce hydrogen upon visible light irradiation.[134] For comparison another asymmetric porphyrin was used with three phenyl rings. The dye bearing the three pyridine groups showed greater photocatalytic hydrogen production with a rate of 437 μmol g^{-1} compared to ZnMTPP/Pt/g-C_3N_4 (293 μmol g^{-1}) under visible light irradiation in the presence of ascorbic acid (Table 6, entry 18). This difference is due to efficient electron transfer from ZnMT3PyP to Pt/g-C_3N_4. Moreover, ZnMT3PyP/Pt/g-C_3N_4 had a greater stability during the photoreaction compared to ZnMTPP/Pt/g-C_3N_4 due to the presence of N atoms, that are combined with ascorbic acid and it is easier to regenerate the electrons. The same research group prepared a series of asymmetric zinc porphyrins and studied the influence of the N atom position on the photoactivity.[135] Under the same condition, in the presence of ascorbic acid as SED and upon visible light irradiation they concluded that the N atom position affects the photocatalytic hydrogen production. The best hydrogen production activity was obtained of 524 μmol h^{-1} was exhibited with ZnPy-4-Pt/g-C_3N_4, where the N atom is at the *para* position of the phenyl ring (Table 6, entry 19). This nanohybrid material has the lowest steric hindrance therefore, it is easier to combine with g-C_3N_4 and AA.

Subsequently, the effect on hydrogen evolution of different metals on the photosensitizer that is loaded onto carbon nitride (C_3N_4) was examined.[136] The sensitizers were a Co, Ni, or a Cu metallated porphyrin with three 4-pyridines and a benzoic acid at the *meso* position of the phenyl ring (CoMTPP, NiMTPP, CuMTPP, Fig. 28). The best hydrogen evolution remained the ZnMTPP/C_3N_4 material under $\lambda > 420$ nm light irradiation. The other metallated dyes produced hydrogen following the sequence of CoMTPP < NiMTPP< CuMTPP. The different hydrogen production ability of the porphyrins may be attributed to the different light absorption of the dyes and the diverse electron transfer between the porphyrin and C_3N_4. A novel hybrid material comprised of a naphthalimide porphyrin (NP) absorbed through π–π stacking onto a two-dimensional graphitic carbon nitride (g-C_3N_4) (Fig. 29).[137] The hybrid material with 2% weight ratio of NP (2%NP/g-C_3N_4), exhibited a photocatalytic hydrogen production of 2297 μmol g^{-1} h^{-1}, with a good stability and reproducibility (Table 6, entry 20). In comparison with pristine g-C_3N_4 and 2%ZnTCPP/g-C_3N_4, they both exhibited less hydrogen evolution of 698 μmol g^{-1} h^{-1} and 900 μmol g^{-1} h^{-1}, respectively.

In another report, a new nanocomposite g-C_3N_4–Cu-TCPP was prepared comprised of a tetra carboxyphenyl porphyrin *p*-TCPP and Cu as an interfacial linker.[138] A pillar-like structure was formed and the material enhanced the photocatalytic hydrogen production. The nanocomposite upon the photocatalytic reaction was fairly stable and its H_2 release rate was 10.3 times higher than that of pure g-C_3N_4 and 9.6 times higher than TCPP-g-C_3N_4 (Table 6, entry 21). Following the previous research of small metal linkage of porphyrins with graphitic carbon nitride, a C_3N_4–Cu-THPP nanohybrid was synthesized, bearing a tetrakis-(4-hydroxyphenyl)porphyrin (THPP) (Fig. 30).[139] This composite showed a great photocatalytic activity that was 17.3 times higher compared to g-C_3N_4 and 11.6 times greater than g-C_3N_4/THPP. Therefore, the presence of Cu was the key factor of the enhanced hydrogen production (Table 6, entry 22).

In addition, the presence of pyrimidine groups and N atoms at the peripheral of a zinc porphyrin (ZnPy) was studied.[140] Asymmetric porphyrins bearing one benzoic acid and three pseudo pyrimidines (ZnPy-5 and ZnPy-6) were used as sensitizers at Pt-loaded g-C_3N_4 for visible-light-driven H_2 evolution. The pseudo pyrimidine groups act as electron-donating groups whereas benzoic acid acts as electron-withdrawing/anchoring group. It was found that the presence of pyrimidine groups improves the photosensitization on g-C_3N_4 and exhibit H_2 evolution production activity of 585 mmol h^{-1} for g-C_3N_4–ZnPy-6

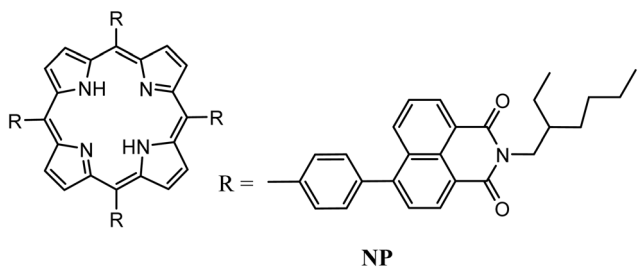

Fig. 29 Chemical structure of NP.

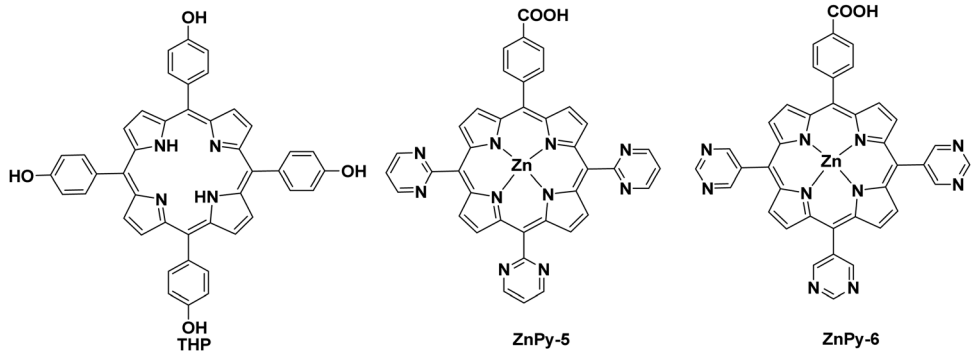

Fig. 30 Chemical structure of THP, ZnPy-5, ZnPy-6.

and 418 mmol h^{-1} for g-C_3N_4–ZnPy-5 (Table 6, entries 23 and 24). It is evident that the presence and the position of N atoms in the pseudo-pyrimidines influence the activity. Therefore, both porphyrins increased the electron transfer towards g-C_3N_4 and ZnPy-6 with the lowest steric hindrance of N atoms showed better performance for H_2 evolution compared to ZnPy-5. In all the above examples graphitic carbon nitride is coupled *via* noncovalent interactions with a porphyrin molecule. Another approach, that is not commonly used is the covalent linkage between the porphyrin and the g-C_3N_4. A tetrakis driazinyl phenyl porphyrin (TDPP) was copolymerized with urea in order to synthesize a g-CNU-TDPP material (Fig. 31).[141] This material doped with porphyrin *via* covalent bond performed 4 times greater photocatalytic activity 7.6 mmol g^{-1} h^{-1} compared to the undoped g-CNU (Table 6, entry 25). The H_2 evolution photocatalytic reaction was carried out in aqueous solution using TEOA (10%) as sacrificial agent and 2 wt% Pt as cocatalyst.

2.2.5 Metal oxides combined with porphyrins for H_2 production. Metal oxides are a large class of inorganic materials that are widely studied. This type of materials is composed of low-cost and earth-abundant elements. Also, they can be structurally modified quite easily, alerting their physical and chemical properties. Therefore, metal oxide-based materials have been received a large interest for various applications.[142–146]

The most common metal oxide that has been developed is TiO_2 and upon its structural modification with a co-catalyst like Pt can become appropriate for H_2 evolution.[147] In order to extend the light absorption of metal oxide photocatalysts from the UV light to visible light it is essential to modify the metal oxide. One way to achieve it is the insertion of a dye-sensitized material that is able to absorb visible light. In this part of the review, we will focus on porphyrin-based molecules, that have been used as sensitizers since 2014.

Inoue and coworkers constructed a system able to produce hydrogen and useful oxygenated products from water under visible light irradiation.[148] A tin(IV) tetracarboxyphenyl porphyrin Sn(IV)TCPP was used as a sensitizer and absorbed on a Pt-doped TiO_2, in aqueous acetonitrile with cyclohexane. Upon irradiation with light the system 0.49 μmol of H_2 and oxygenated cyclohexane products, cyclohexeneoxide, 2-cyclohexenol, 2-cyclohexenone, and cyclohexanone from the substrate, cyclohexene (Table 7, entry 1). The system did not produce any products after the photocatalytic reaction at the absence of the photosensitizer and upon addition of sulphuric acid with $C > 10^{-4}$ M the porphyrin was desorbed from the TiO_2 due to its protonation. The same porphyrin Sn(IV)TCPP was used as a photosensitizer in a photocatalytic hydrogen evolution reaction.[149] Platinum dioxide (PtO_2) was used as a heterogeneous proton-reduction catalyst and triethanolamine (TEOA) as sacrificial electron. After optimization of the system 4.8 μmol h^{-1} of H_2 was produced upon visible light irradiation (Table 7, entry 2). When EDTA was used as SED lower amount of hydrogen was produced 0.42 μmol h^{-1} compared to TEOA possibly due to its lower reduction rate ($E_{ox(TEOA)}$ = 1.07 V and $E_{ox(EDTA)}$ = 1.17 V) or due to fewer amine units. It was found that hydrogen production occurred *via* a reductive mechanism and chlorin species were formed upon the photocatalytic reaction as the main intermediate. A series of *meso* substituted tin-based porphyrins ($SnTPP(SO_3H)_4$, $SnTPP(COOH)_4$, SnTPyP, $SnTMPyP(OH)_2$, $SnTMPyP(Cl)_2$) were synthesized and used as photosensitizers for photocatalytic hydrogen evolution reaction under visible light irradiation.[150] The photosensitizers with different functional groups were absorbed onto a Pt/TiO_2 surface and various parameters were evaluated during the photochemical reaction such as the pH, Pt/TiO_2 concentrations, light intensities and Pt nanoparticles with diverse surface stabilizers. After evaluation of the above parameters, the maximum hydrogen evolution was obtained for $SnTPyP/TiO_2/Pt$ in the presence of EDTA at pH = 9.0 obtaining 232 μmol of H_2 (Table 7, entry 3). It was resolved that the reduced species formed after the

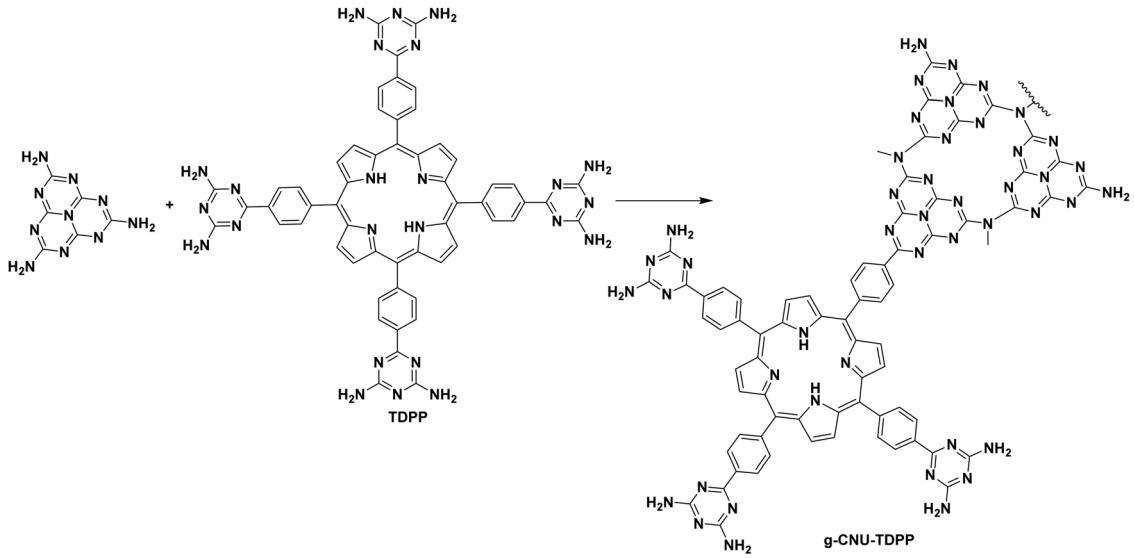

Fig. 31 Chemical structure of g-CNU-TDPP.

Table 7 Photocatalytic performance of metal oxides combined with porphyrins for H_2 production

Entry	PS (C)	Catalyst (C)	SED (C)	Solvent	Light source	Irr. time (h)	TON/H_2	H_2	Ref.
1	Sn(IV)TCPP	TiO_2/Pt (4.8×10^{-6} M)	10% aq. acetonitrile	Water	($\lambda > 480$ nm)	5		0.49 μmol	148
2	Sn(IV)TCPP	PtO_2 (22 mg L^{-1})	TEOA, 60 mM	Aqueous phosphate buffer (0.1 M)	Visible light ($\lambda > 400$ nm)			4.8 μmol h^{-1}	149
3	SnTPyP	TiO_2/Pt	EDTA	Water	$\lambda > 390$–650 nm	4		232 μmol	150
4	ZnTCPP	SnO_2/TiO_2	TEOA, 0.2 M	Water	Visible light ($\lambda > 420$ nm)	12	261	10.2 μmol h^{-1}	151
5	ZnTCPP	SnO_2/ZnO	TEOA, 0.2 M	Water	Visible light ($\lambda > 420$ nm)	9	516	75 μmol h^{-1} g^{-1}	152
6	TCPP	Cu_2O	TEOA	Water	Visible light ($\lambda > 420$ nm)	8		2 mmol mg^{-1}	153
7	TCPP	Cu_2O/NiO	TEOA	Water	Visible light ($\lambda > 400$ nm)	6		3 mmol g^{-1}	154
8	TCPP	TiO_2–Cu	TEOA	Water	300 W Xenon lamp	6		8 mmol g^{-1}	155
9	Al(III)TCPP	TiO_2/Pt	H_2O/CH_3CN (1/9 v/v)	Water, pH = 4.01	420 nm LED light	2		0.3 μmol	156
10	PdTCP	TiO_2	TEOA 15 vol%	CH_3CN/H_2O (1 : 1 v/v), pH = 8.0	White LED lamp, 40 W	120		52 μmol	157
11	Pt TCP	TiO_2	TEOA 15 vol%	CH_3CN/H_2O (1 : 1 v/v), pH = 8.0	White LED lamp, 40 W	200		146 μmol	157
12	PdTCP/PtTCP	TiO_2	TEOA 15 vol%	CH_3CN/H_2O (1 : 1 v/v), pH = 8.0	White LED lamp, 40 W	200	22 733	30.2 mmol g^{-1}	157
13	ZnP-dyad	TiO_2/Pt	Ascorbic acid 0.5 M	Water, pH = 5.0	White light, 80 mW	120	12 800	173 000 μmol g^{-1} h^{-1}	158
14	YD2-o-C8	TiO_2/Pt	Ascorbic acid 0.5 M	Water, pH = 5.0	White light, 80 mW	120	11 900	272 000 μmol g^{-1} h^{-1}	158
15	LG-5	TiO_2/Pt	TEOA 20 vol%	Water	Xe lamp, 450 W	5	6582	3291 μmol g^{-1} h^{-1}	159
16	LG-DtT	TiO_2/Pt	TEOA 20 vol%	Water	Xe lamp, 450 W	5	13 282	6641 μmol g^{-1} h^{-1}	159
17	LGtT	TiO_2/Pt	TEOA 20 vol%	Water	Xe lamp, 450 W	5	14 792	7396 μmol g^{-1} h^{-1}	159
18	TSPP	Cu_2O	TEOA	Water	Xe lamp, 300 W	6		0.83 mmol g^{-1} h^{-1}	160
19	TSPP	ZnO NR-Cu	TEOA	Water	Xe lamp, 300 W	6		0.69 mmol g^{-1} h^{-1}	161
20	ZnTmMpHPP	TiO_2	CH3OH	Water	Xe lamp, 300 W	7		326.3 μmol h^{-1}	162
21	THP	TiO_2/Cu	TEOA	Water	Xe lamp, 300 W	6		13 mmol g^{-1}	163
22	THPP	TiO_2/Pt	TEOA 10 vol%	Water	Visible light ($\lambda > 420$ nm)	5		576.8 μmol g^{-1} h^{-1}	164
23	PdTHPP	TiO_2/Pt	TEOA 10 vol%	Water	Visible light ($\lambda > 420$ nm)	5		2025.4 μmol g^{-1} h^{-1}	164
24	ZnTHPP	TiO_2/Pt	TEOA 10 vol%	Water	Visible light ($\lambda > 420$ nm)	5		1239.8 μmol g^{-1} h^{-1}	164
25	THPP	NiO	TEOA 20 vol%	Water	Xe lamp, 300 W	8		8 mmol g^{-1}	165
26	TpTph	TiO_2	Ascorbic acid 0.25 M	Water	Xe lamp, 300 W ($\lambda > 420$ nm)	4		5602 μmol h^{-1} g^{-1}	166
27	BDP-Por-BDP(Im)	$PtTiO_2$	Ascorbic acid 1 M	Water	white LED lamp, 40 W	72	18 600	225 mmol h^{-1} g^{-1}	167

photocatalytic reaction were long-lived in order to complete the electron transfer and that the chromophore was not essential to be bound onto TiO_2 surface for H_2 evolution. In an effort to exclude the use of noble metal cocatalysts onto TiO_2, a graphene-like MoS_2 has been added onto TiO_2 as an alternative cocatalyst promoting higher H_2 evolution rates upon photocatalytic reaction. In a report, Zn tetracarboxyphenyl porphyrin (Fig. 3) sensitized MoS_2/TiO_2 nanocomposite as a photocatalyst. The system was able to absorb visible light and produce H_2 with a rate of 10.2 μmol h^{-1} and a TON of 261 after 12 h of irradiation (Table 7, entry 4).[151] Upon comparison with ZnTCPP-Pt/TiO_2 under the same photocatalytic conditions the photocatalyst with MoS_2 produce H_2 with 1.45 times higher rate displaying the high activity of MoS_2. The same research group replaced TiO_2 with ZnO and prepared ZnTPP-MoS_2/ZnO nanocomposite that was able to produce H_2 with a hydrogen evolution rate of 75 μmol h^{-1} g^{-1} under visible light irradiation (Table 7, entry 5).[152] Cuprous oxide Cu_2O can be used as a cocatalyst sensitized with free base tetracarboxyphenyl porphyrin TCPP/Cu_2O.[153] The composite upon visible light irradiation produced higher hydrogen compared to pure TCPP or pure Cu_2O. Also, the system proved to be quite stable, since after five recycles the hydrogen production barely changed 2 mmol mg^{-1} (Table 7, entry 6). In addition, the same porphyrin TCPP was introduced onto an antennae-like Cu_2O/NiO heterostructure in order to enhance the photocatalytic hydrogen production.[154] Therefore, upon light irradiation in aqueous TEOA solution the rate of H_2 evolution followed the order Cu_2O/NiO/TCPP > Cu_2O/NiO > pure Cu_2O (Table 7, entry 7). This result indicates that NiO and Cu_2O can improve the photocatalytic hydrogen activity in the presence of the porphyrin photosensitizer, due to the strong interaction between the three components and due to electric field, that ids produced at the interface of Cu_2O kai NiO. In an attempt to prepare stable and highly efficient photocatalysts, TiO_2 microsphere (TiO_2MS) was linked *via* metallic Cu with a tetracarboxyphenyl porphyrin TCPP.[155] The linkage between copper and the porphyrin was done with coordination and electrostatic interactions. This hybrid material was active towards H_2 evolution and produced about 6 times more hydrogen compared to TiO_2MS and 3.8 times higher in the absence of Cu (TiO_2MS-TCPP) (Table 7, entry 8). These results indicate the importance of Cu in the hybrid material facilitating the electron transfer from TCPP to TiO_2 MS. Another research group produced a photocatalyst composed of aluminum porphyrin adsorbed onto TiO_2 nanoparticles with Pt clusters (Al(III)TCPP/TiO_2/Pt).[156] The system upon irradiation and with the absence of a sacrificial electron donor was able to produce at the same time H_2 and H_2O_2 from water upon only one-photon (Table 7, entry 9). In addition, Coutsolelos and coworkers established an alternative methodology of H_2 evolution by self-organizing porphyrin based photocatalysts onto a TiO_2 scaffold.[157] Among the synthesized porphyrins ZnTCP, PdTCP, PtTCP (Fig. 32) only PdTCP and PtTCP showed photocatalytic activity. When PdTCP porphyrin was adsorbed onto TiO_2, *H*-aggregates were formed, whereas in the case of PtTCP *J*-aggregates were shaped. Upon photocatalytic experiments, the hydrogen evolution of PtTCP/TiO_2 material was greater (146 μmol H_2) compared to PdTCP/TiO_2 (52 μmol H_2) (Table 7, entries 10 and 11). This difference at their catalytic performance might be due to the variation of self-organization of the two porphyrins onto TiO_2. In the case of adsorption of both porphyrins onto TiO_2 (PdTCP/PtTCP/TiO_2) the system became more efficient towards H_2 evolution producing 30.2 mmol g^{-1} (Table 7, entry 12). This result is considered to be one of the most efficient efforts on H_2 evolution of this type of systems.

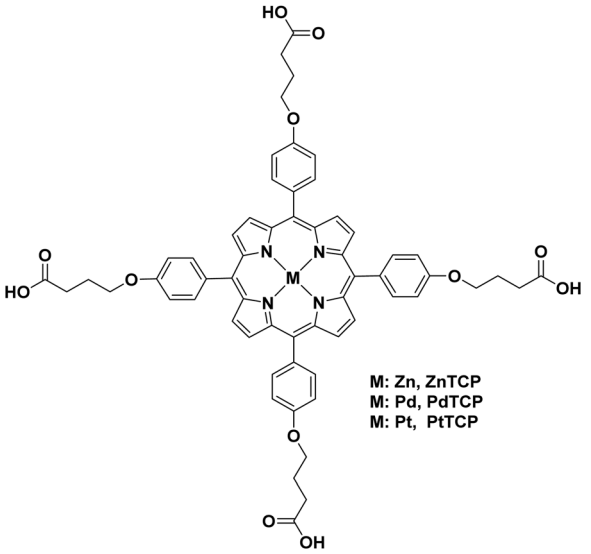

Fig. 32 Chemical structure of ZnTCP, PdTCP, PtTCP.

Push–pull porphyrins were found to have a large impact on the power conversion efficiency when used as sensitizers in dye-sensitized solar cells (DSCCs). Inspired by DSCC this type of porphyrins were investigated as photosensitizers for H_2 production. The presence of a carboxylic group on the dye act as an anchoring group and is attached onto TiO_2. Therefore, ZnP-dyad and YD2-o-C8 dyads were synthesized and attached onto platinized TiO_2 particles and photodriven H_2 evolution experiments were conducted (Fig. 33).[158] All measurements were done in an aqueous solution in the presence of ascorbic acid as sacrificial electron donor. The YD2-o-C8/TiO_2/Pt material produced 19.11 ml of H_2, while ZnP-dyad/TiO_2/Pt 15.95 ml of H_2 (Table 7, entries 13 and 14).

Three different porphyrin-based dyes were synthesized and their photocatalytic H_2 production was evaluated.[159] The dyes LG-5, and LG-DtT possessed three different 4-ethynyl thiophene and a cyanoacrylic acid as an anchoring group (Fig. 34). Photocatalytic hydrogen production measurements were conducted in the presence of TEOA as sacrificial electron donor under visible light irradiation. All the photocatalytic systems composed of the dyes attached onto TiO_2/Pt *via* the anchoring group. The LG-tT/TiO_2/Pt material proved to be the most efficient system with a H_2 evolution rate of 7396 μmol g^{-1} h^{-1} after 5 h of light irradiation. The activity towards H_2 evolution followed the order LG-tT/TiO_2/Pt > LGDtT/TiO_2/Pt > LG5/TiO_2/Pt (Table 7, entries 15–17).

In another attempt to prepare an efficient nanocatalyst for H_2 generation, tetrakis sulfophenyl porphyrin (TSPP) was synthesized and assembled with cubic Cu_2O (Fig. 35).[160] Since

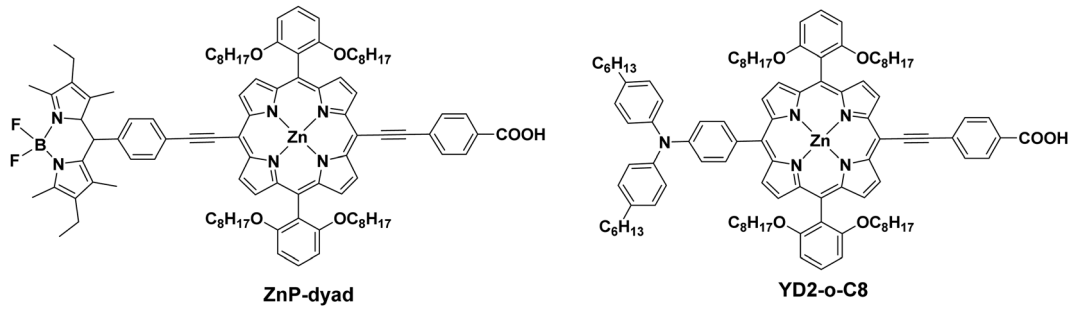

Fig. 33 Chemical structure of ZnP-dyad and YD2-o-C8.

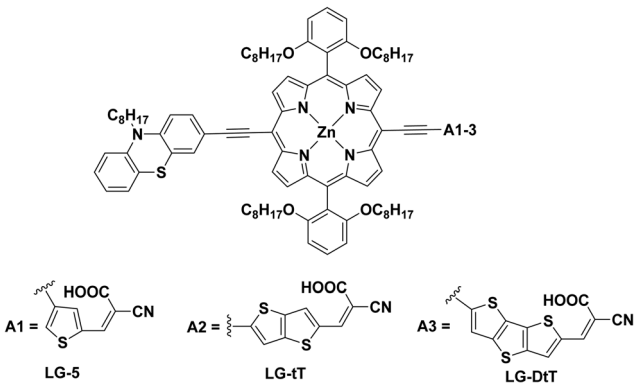

Fig. 34 Chemical structure of LG-5, LG-tT and LG-DtT.

porphyrins with sulfonyl groups possess stronger electron-withdrawing abilities they were used as an alternative dye. Therefore, the combination of light-harvesting TSPP porphyrin (electron donor) and Cu_2O cubic phase (electron acceptor) improved the photocatalytic performance towards hydrogen production. The TSPP/Cu_2O composite upon light irradiation produces 0.83 mmol h^{-1} g^{-1} of hydrogen, in the presence of TEOA as a SED (Table 7, entry 18). This hydrogen evolution was 5 times higher compared to Cu_2O. The same porphyrin TSPP was used as a light harvester and was attached on a copper-implanted ZnO nanorod.[161] This nanocomposite showed high photocatalytic performance upon H_2 production of 0.69 mmol g^{-1} h^{-1} (Table 7, entry 19).

It is well known that modification of TiO_2 with porphyrin dyes can enhance the photocatalytic H_2 production. A plethora of porphyrins have been used varying their anchoring groups. In this report a *m*-methoxy-*p*-hydroxylphenyl porphyrin (ZnTmMpHPP) was linked to TIO_2 (Fig. 35).[162] The hydrogen evolution rate of this photocatalyst was 2 times higher than pure TiO_2, reaching 326.3 μmol h^{-1} (Table 7, entry 20). In a different example, tetrahydroxyphenyl porphyrin THP was bound to TiO_2 microsphere with the presence of copper nanoparticles (CuNPs) (Fig. 35).[163] The prepared nanocomposite TiO_2 microsphere/CuNPs/THPP upon light irradiation showed enhanced photocatalytic activity towards H_2 production by a factor of 14 compared to the pure TiO_2 microsphere (Table 7, entry 21). This high activity and stability of the system might be due to the special interaction between TiO_2 microsphere/CuNPs and THPP.

A series of free-base and metalated *meso*-carboxyphenyl porphyrins were synthesized and linked with TiO_2.[164] Upon addition of Pt nanoparticles, the hybrids THPP-TiO_2/Pt, PdTHPP-TiO_2/Pt and ZnTHPP-TiO_2/Pt were formed (Fig. 35). Upon photocatalytic hydrogen evolution experiments, all materials produced hydrogen, with PdTHPP-TiO_2/Pt achieving the best result 2025.4 μmol g^{-1} h^{-1}. The ZnTHPP-TiO_2/Pt photocatalyst with the zinc metallated porphyrin achieved a hydrogen rate of 1239.8 μmol g^{-1} h^{-1}, greater than THPP-TiO_2/Pt

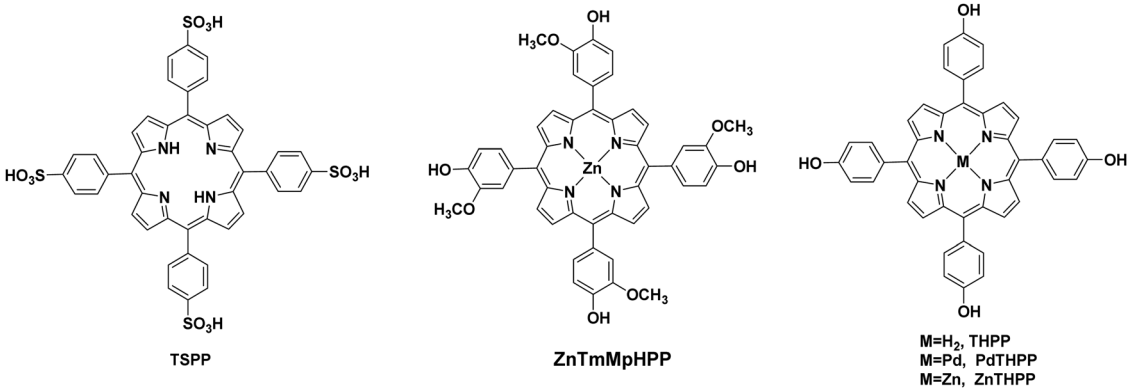

Fig. 35 Chemical structures of TSPP, ZnTmMpHPP and MTHPP (M = H_2, Pd, Zn).

576.8 μmol g^{-1} h^{-1}, due to the effective light harvesting and electron transfer of ZnTHPP to TiO_2 (Table 7, entries 22–24). The best activity of PdTHPP-TiO_2/Pt might be attributed to the presence of the two metal catalysts Pd and Pt. Two-dimension nanomaterials of NiO were sensitized with tetrahydroxyphenyl porphyrins (THPP) in order to form effective photocatalysts.[165] The system showed a high and stable photocatalytic activity towards hydrogen production (Table 7, entry 25).

A porphyrin-based organic polymer was synthesized (TpTph) and TiO_2 was loaded onto the polymer in order to form photocatalyst TpTph-TiO_2 (Fig. 36).[166] The hydrogen evolution ability of the system TpTph-TiO_2 was investigated and it was found that the H_2 production was much greater (5602 μmol h^{-1} g^{-1}) compared to TpTph (21 μmol h^{-1} g^{-1}) and bulk TiO_2 (39 μmol h^{-1} g^{-1}) (Table 7, entry 26).

Our research group recently reported the synthesis of BODIPY-(Zn)Porphyrin hybrids (Fig. 37) and their application in photocatalytic H_2 production from water utilizing platinum-doped titanium dioxide nanoparticles ($PtTiO_2$).[167] More specifically the hybrid photosensitizers were employed in a dye-sensitized photocatalytic system (DSP) after their chemisorption onto the surface of the $PtTiO_2$. The authors showed that the covalent attachment of the BDP moiety (BDP-Por) illustrated greater efficiency (17 500 TONs) compared to the axial coordination (BDP(Im)-Por, 13 700 TONs) while the triad system BDP-Por-BDP(Im) overwhelmed the other hybrids in terms of activity (18 600 TONs). Noteworthy, photoelectrochemical studies of the synthesized hybrids on TiO_2 films displayed the same trend in terms of photocurrent density values.

2.2.6 Porphyrin DSPECs for H_2 production. In this paragraph, the Dye-sensitized photoelectrochemical cells (DSPECs) towards hydrogen production are described. The target of such systems is to create water-splitting devices with the advantage of separately hydrogen and oxygen production.[34] The important advantage of these systems is the absence of sacrificial agents while a common negative aspect is the need of external electrical bias to accomplish the conversion of H_2O to O_2 and H_2. However, there are examples where this issue was overwhelmed and only the energy input from sunlight was necessary.

One example of DSPEC towards H_2 production was provided by Moore and coworkers.[168] The authors grafted Co(II) and Fe(II) metalloporphyrins to a gallium phosphide semiconductor and

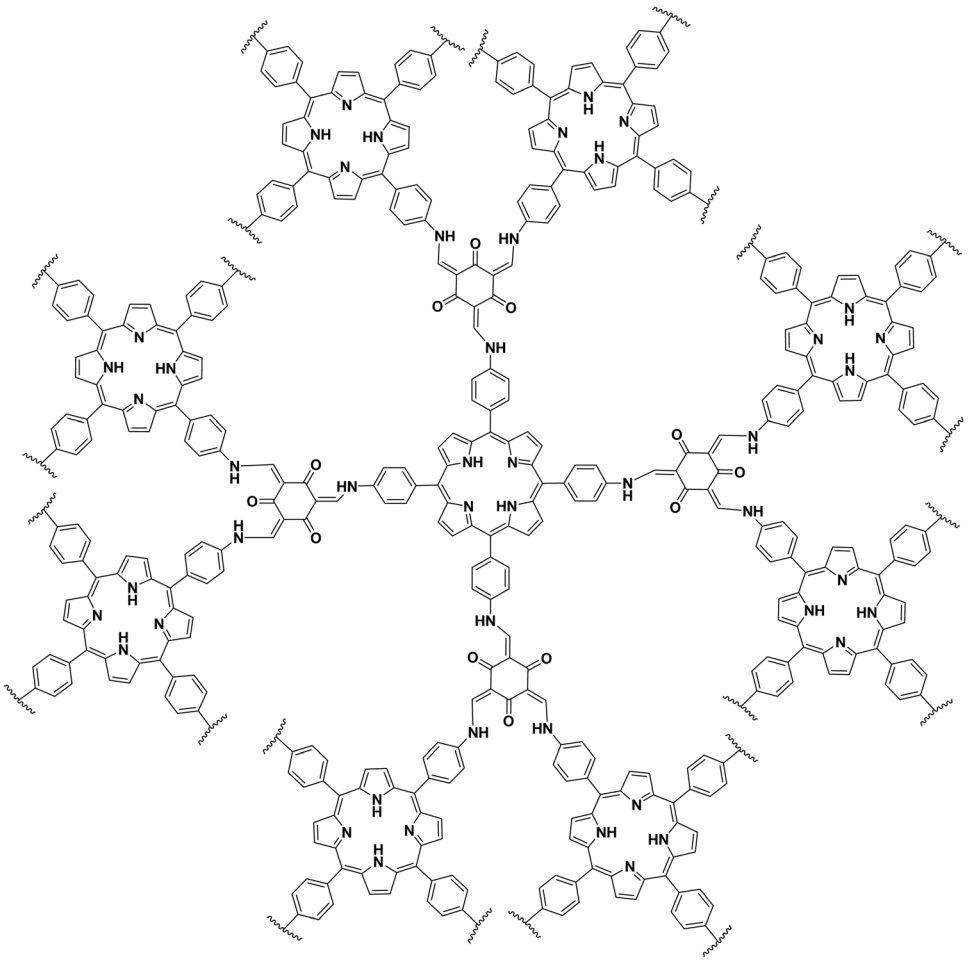

TpTph

Fig. 36 Chemical structure of TpTph.

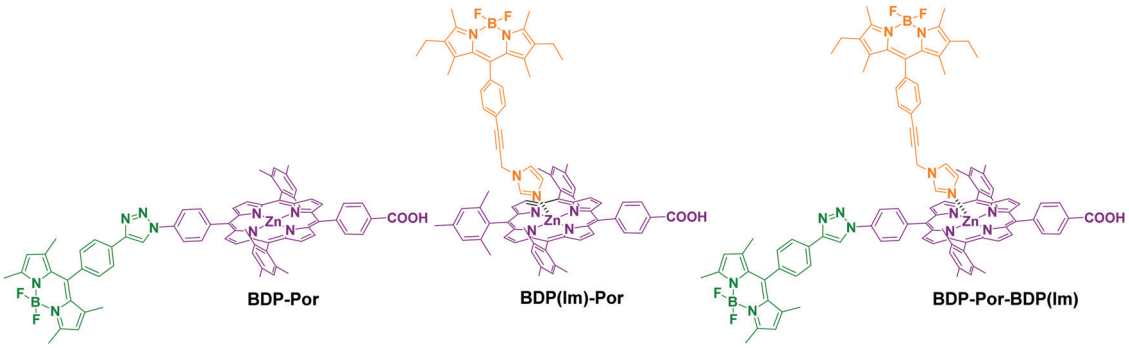

Fig. 37 Chemical structures of BDP-Por, BDP(Im)-Por and BDP-Por-BDP(Im).

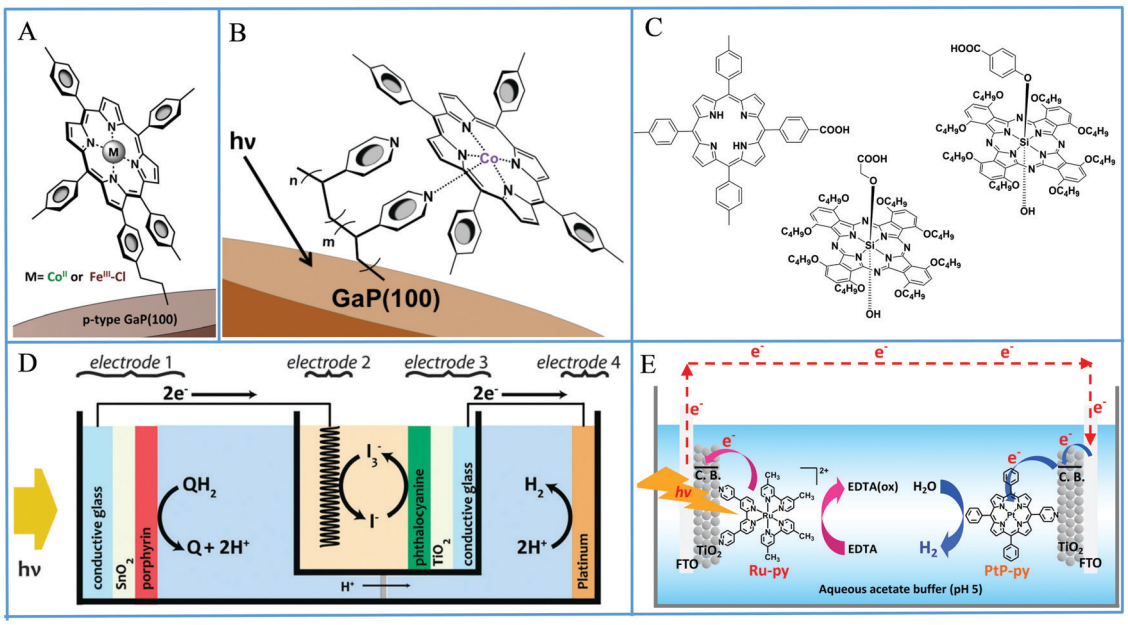

Fig. 38 (A) Schematic illustration of the GaP semiconductor grafted with metalloporphyrins, Reproduced from ref. 168, with permission from Royal Society of Chemistry, Copyright 2016. (B) Schematic illustration of the polypyridine modified GaP semiconductor binding Co–porphyrin catalyst, Reproduced from ref. 169, with permission from American Chemical Society, Copyright 2017. (C) Molecular structures of the free base porphyrin and the Si phthalocyanines used in the tandem cell, (D) schematic illustration of the tandem system with a TiO_2–phthalocyanine DSSC, Reproduced from ref. 170, with permission from Royal Society of Chemistry, Copyright 2016. (E) Graphic representation of the DSPEC with a TiO_2/ruthenium-dye photoanode and the Pt-porphyrin/TiO_2 cathode. Reproduced from ref. 172, with permission from American Chemical Society, Copyright 2019.

created a photocathode for visible light-driven H_2 evolution which displayed enhanced photoelectrochemical efficiency over unmodified electrodes. The porphyrins contained a 4-vinylphenyl group (Fig. 38a) in order to be attached to the semiconductor, while the resulting hybrid material with cobalt inside the porphyrin core exhibited greater hydrogen production rate and stability in comparison to the analogous assemblies with Fe(II). The same research group further improved their system by utilizing a polypyridine coating on the surface of GaP semiconductor to provide binding sites for the coordination of the cobalt porphyrin catalysts (Fig. 38b).[169] Indeed their approach enhanced the overall performance of the photocathode.

Sherman *et al.* prepared a tandem cell composed of two dye-sensitized photoanodes, which was able to generate H_2 under visible light irradiation and in the absence of any applied electrical bias.[170] The authors utilized a free-base porphyrin and a Si phthalocyanine as chromophores to harvest distinct portions of the visible spectrum (Fig. 38c). Although a DSPEC based on SnO_2-porphyrin photoanode was not able to oxidize hydroquinone and use the resulting electrons to produce hydrogen at the cathode, when it was incorporated in a tandem system with a TiO_2–phthalocyanine DSSC (Fig. 38d), the additional electrons provided by the DSSC enabled efficient H_2 generation.

In another study Sakai,[171] Ozawa and coworkers applied a platinum(II) porphyrin bearing single pyridyl anchoring group on a TiO_2 cathode and showed that it catalyze H_2 production electrocatalytically. As a side investigation of this work, the

authors constructed DSPECs with a FTO/TiO_2/ruthenium-dye photoanode and the Pt-porphyrin anchored on the FTO/TiO_2 cathode (Fig. 38e) where they observed a small photo-induced electric current between the electrodes. The same research group further explored this system and altered the methyl groups on the Ru complex (Fig. 38e) with phenyl ones.[172] The new DSPEC comprised of the Pt-porphyrin cathode and the TiO_2/Ru-py photoanode gave substantial H_2 evolution upon visible light irradiation, without applying any external bias. The electron donor in both above studies was EDTA.

Light assisted hydrogen production can be also achieved from porphyrin-modified glassy carbon electrodes.[173] Ramírez and co-workers applied Co(II) and Cu(II) octaethyl-porphyrins supramolecular systems on glassy carbon electrodes as photo-electrocatalysts and showed that no photosensitizer was required for hydrogen evolution (Fig. 39a). The irradiation wavelength, the anchoring group and the supramolecular aggregation were proven significant factors related to the photoelectrochemical performance. Another work published by the same research group explored graphite paste electrodes with Co(II) and Fe(III) octaethyl-porphyrins.[174] Both modified systems presented photoelectrocatalytic hydrogen production, which was enhanced when a mixture of the two metallated porphyrins was deposited on the graphite paste electrode. The authors quantified the overall performance of the later system to 70.9 μmol h^{-1} cm^{-2} of hydrogen which corresponds to a TON of 8100. Subsequently, the researchers further improved this system by incorporating *N*-octylpyridinium hexafluoro-phosphate ionic liquid as binder and using the Co-octaethyl-porphyrin.[175]

Tetrasubstituted metalloporphyrins have been used also by other research groups towards the construction of DSPECs for hydrogen production. In a similar study, Li *et al.* used tetraphenyl-manganese(III) porphyrin (MnTPP) as photosensitizer deposited on a $CuFe_2O_4$ electrode and applied the resulting photocathode in photoelectrochemical water splitting where it was proven productive (Fig. 39b).[176] Tuncel and co-workers synthesized a supramolecular assembly based on cucurbit[7]uril hosts covalently connected to a free-base porphyrin core (TTP-4CB7) (Fig. 39c) and applied this assembly in visible light driven hydrogen production.[177] The authors showed that TPP-4CB7 by its own can act as a photocatalyst towards H_2 evolution but photo-catalytic activity was significantly improved in the presence of TiO_2. The CB7 moieties were utilized as anchoring groups to coordinate with TiO_2 and form a homogenous system. The final nanocomposite which contained both TiO_2 and Pt co-catalyst, exhibited efficient hydrogen production 24.5 mmol h^{-1} g^{-1} at an onset potential of −10 mV and in the absence of any SED. In another report, Li *et al.* prepared long chain coordination complexes based on Zr(IV) *meso*-tetraphenyl porphyrin (ZrTPP)

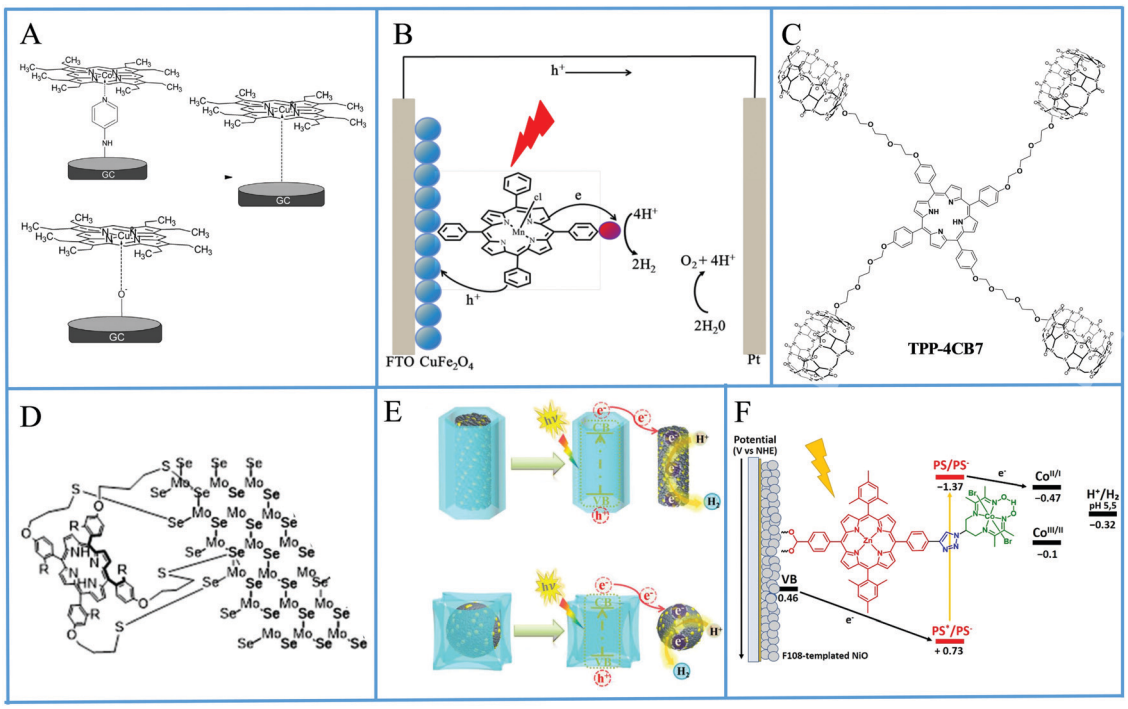

Fig. 39 (A) Schematic illustration of Co(II) and Cu(II) octaethyl-porphyrin supramolecular systems on glassy carbon electrodes, Reproduced from ref. 173, with permission from Elsevier, Copyright 2017. (B) Schematic illustration of tetraphenyl-manganese(III) porphyrin as photosensitizer deposited on a $CuFe_2O_4$ electrode, Reproduced with permission from ref. 176, which is an open access article distributed under the Creative Commons Attribution License (CC BY), MDPI. (C) Molecular structures of the free base porphyrin covalently connected to the cucurbit[7]uril hosts, (D) schematic illustration of the tetra-substituted porphyrins bearing thiol groups covalently attached on exfoliated $MoSe_2$ nanosheets, Reproduced from ref. 179, with permission from Royal Society of Chemistry, Copyright 2020. (E) Graphic representation of the electron transfer root from the PMOFs to the Pt/C nanowires and Pt/C nanodots, Reproduced from ref. 181, with permission from John Wiley and Sons, Copyright 2020. (F) Energy diagram of the porphyrin-cobalt dyad on the NiO towards photoelectrochemical hydrogen production. Reproduced from ref. 182, with permission from John Wiley and Sons, Copyright 2021.

linked *via* the bridging group of a dicarboxylic acid.[178] These 1-dimensional complexes displayed efficient electrocatalytic hydrogen evolution as well as photoelectrochemical performance.

Blanco *et al.* explored the covalent attachment of tetra-substituted porphyrins bearing thiol groups on exfoliated $MoSe_2$ nanosheets (Fig. 39d) towards hydrogen production both electrocatalytically and photoelectrochemically.[179] The resulting hybrid materials exhibited an enhancement of the hydrogen evolution onset potential under white light irradiation in comparison to the initial material. The same research group further improved their system through the conjugation of these porphyrins with $MoS_2/Ag_2S/Ag$ nanocomposites deposited on a Digital Versatile Disc.[180]

Zhang and co-workers utilized the known porphyrin MOFS in order to confine Pt/C quantum dots (QDs) inside their pores and apply them in photoelectrocatalysis.[181] More specifically the authors used PCN-222 with nanochannels and PCN-221 with nanocages to host ultrafine Pt/C nanowires and uniform Pt/C nanodots, respectively (Fig. 39e). Under visible light irradiation, these host-guest materials exhibited highly efficient electrocatalytic performance towards hydrogen evolution reaction. Moreover, it was shown that both materials had fast and shape-dependent charge transfer behavior since the charge transfer from PCN-222 to the Pt/C nanowires was faster than from PCN-221 to Pt/C nanodots. Charisiadis *et al.* have recently contributed in the field of photoelectrochemical hydrogen evolution utilizing a Zn–porphyrin covalently connected to a cobaloxime molecule.[182] The porphyrin moiety was equipped with a carboxylic acid anchoring group to be attached on NiO semiconductor (Fig. 39f). The resulting photocathode was employed in photoelectrochemical H_2 production and this was the first report of a noble metal free porphyrin-cobalt dyad aiming to this application.

3. Porphyrins for CO_2 reduction

The direct conversion of solar irradiation into chemical energy through the CO_2 reduction represents a very interesting and promising scientific area. The photocatalytic CO_2 reduction typically involves a PS which absorbs light and generates charge separate states (electrons and holes). The excited electrons are then used to activate a catalyst where the CO_2 reduction takes place. Porphyrin based materials have been extensively employed in photocatalytic CO_2 reduction, mainly as catalysts. It has been demonstrated that several metallo-porphyrins with transition metals (Fe, Co, Ni, *etc.*) present high activity towards the electro- and the photo-catalytic CO_2 reduction.[183,184] Moreover, due to their exceptional optical properties and their fast charge transfer ability, porphyrin derivatives have been also used as photosensitizers in photocatalytic CO_2 reduction systems.[185] The porphyrin based catalytic systems that will be described is this section will be divided in homogeneous molecular materials and various heterogeneous approaches such as MOFs, COFs, porphyrin-supported systems on metal oxides, porphyrins in combination with nanomaterials and DSPECs.

3.1 Homogeneous systems

Homogenous catalytic systems contain a catalyst, a PS and a SED that are all soluble in a solution. In these systems, the molecular structure of the components is usually well-defined, and this enables the determination of the corresponding catalytic mechanism. Moreover, the homogenous systems present higher selectivity and it is easier to identify the structural parameters that influence the catalytic performance.

3.1.1 Porphyrins as catalysts in homogeneous CO_2 reduction systems. The first porphyrin-based photocatalytic CO_2 reduction was reported from Neta and co-workers.[186] They reported that light irradiation of iron tetraphenylporphyrin (FeTPP, Fig. 40), in DMF containing 5% TEA as SED, was able to catalyze the reduction of CO_2 to CO (Table 8, entry 1). The catalysis performed in the absence of any additional PS and the Fe(0) state was identified as the catalytic active state. Bonin *et al.* also studied in more detail the photocatalytic activity of FeTPP and compared its efficiency with two other iron porphyrins, namely CAT and FCAT (Fig. 40).[187] During these studies they showed that the UV irradiation ($\lambda < 300$ nm) is mandatory in order to observe CO_2 to CO reduction. The photocatalytic experiments were performed in CH_3CN, since they observed that photodegradation of DMF leads to non-negligible CO formation. Catalysts CAT and FCAT demonstrated higher activity compared to the FeTPP (Table 8, entries 2–4), due to the presence of the –OH groups that stabilize the coordination of CO_2 to the Fe(0) metal center *via* intramolecular hydrogen bonds and then protonate it, acting also as an extra proton source. The selectivity towards CO formation is high (93%), since the competitive H_2 production process is

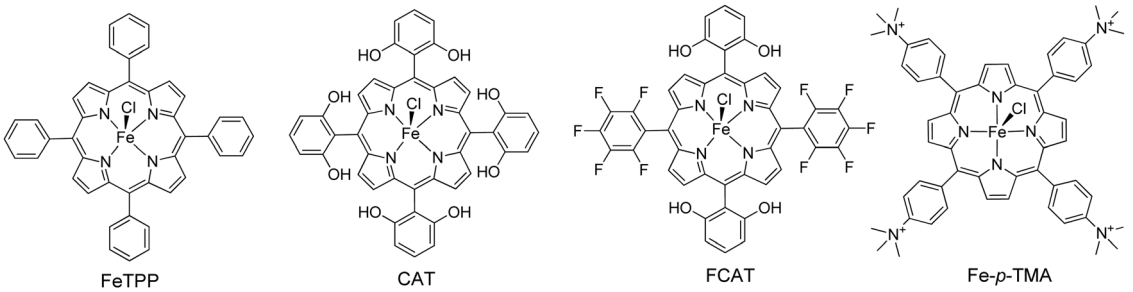

Fig. 40 Structure of iron porphyrin molecular catalysts for CO_2 reduction.

Table 8 Photocatalytic performance of homogeneous porphyrin based CO_2 reduction systems

Entry	Catalyst (C)	PS (C)	SED	Solvent	Light source	Irrad. time	TON	TOF (h^{-1})	Selectivity (%)	Ref.
1	FeTPP, 0.01 mM	—	TEA, 5%	DMF	Xenon lamp, 300 W	170 h	70	—		186
2	FeTPP, 0.01 mM	—	TEA, 0.36 M	CH_3CN	Xenon lamp, BG40 optical filter	10 h	17	—	8	187
3	CAT, 0.01 mM	—	TEA, 0.36 M	CH_3CN	Xenon lamp, BG40 optical filter	10 h	28	7.7	93	187
4	FCAT, 0.01 mM	—	TEA, 0.36 M	CH_3CN	Xenon lamp, BG40 optical filter	10 h	23	6.7	76	187
5	CAT, 0.002 mM	$Ir(ppy)_3$, 0.2 mM	TEA, 0.36 M	CH_3CN	Xenon lamp, 150 W, $\lambda > 420$ nm	55 h	140		93	188
6	CAT, 0.002 mM	9CNA, 0.2 mM	TEA, 0.05 M	CH_3CN	Xenon lamp, 150 W, $\lambda > 400$ nm	45 h	60		100	188
7	Fe-p-TMA, 0.002 mM	—	TEA, 0.05 M	CH_3CN	Solar simulator, $\lambda > 420$ nm	47 h	33		100	189
8	Fe-p-TMA, 0.002 mM	—	BIH, 0.02 M	CH_3CN	Solar simulator, $\lambda > 420$ nm	47 h	63		100	189
9	Fe-p-TMA, 0.002 mM	Purpurin	TEA, 0.05 M	CH_3CN/H_2O (1/9), pH = 6.7	Solar simulator, $\lambda > 420$ nm	47 h	60		95%	190
10	Fe-p-TMA, 0.002 mM	$Ir(ppy)_3$, 0.2 mM	TEA, 0.05 M	CH_3CN	Solar simulator, $\lambda > 420$ nm	102 h	367 (CO) 79 (CH_4)		78 (CO) 17 (CH_4)	191
11	Fe-p-TMA, 0.002 mM	$Ir(ppy)_2(bpy)$, 0.2 mM	TEA, 0.05 M	CH_3CN	Solar simulator, $\lambda > 420$ nm	47 h	178 (CO) 32 (CH_4)		57 (CO) 10 (CH_4)	192
12	Fe-p-TMA, 0.002 mM	$Ir(ppy)_3$, 0.2 mM	TEA, 0.05 M	CH_3CN	Solar simulator, $\lambda > 420$ nm	47 h	198 (CO) 31 (CH_4)		78 (CO) 12 (CH_4)	191 and 192
13	Fe-p-TMA, 0.002 mM	$Ir(ppy)_2(bpy)$, 0.2 mM	TEA, 0.05 M	CH_3CN/H_2O (3/7)	Solar simulator, $\lambda > 420$ nm	47 h	24 (CO) 3 (CH_4)		75 (CO) 9 (CH_4)	192
14	Fe-p-TMA, 0.01 mM	Phen2, 1 mM	TEA, 0.1 M	DMF	Solar simulator, $\lambda > 435$ nm	102 h	140 (CO) 29 (CH_4)		75 (CO) 15 (CH_4)	193
15	Fe-p-TMA, 0.006 mM	PMI-OH, 0.87 mM	SA, 0.5 M	H_2O	150 W EKE bulb	48 h	30 (CO)			195
16	CAT, 0.0002 mM	CuPP, 0.1 mM	BIH, 0.1 M	DMF	White LED, $\lambda > 400$ nm	23 h	16 109	7650	95	196
17	CoTPPS, 0.01 mM	$[Ru(bpy)_3]Cl_2$, 0.5 mM	AA, 0.1 M	H_2O, pH = 6.7	Xenon lamp, $\lambda > 400$ nm	4 h	926	456	82	198
18	CoTPPS, 0.0005 mM	$[Ru(bpy)_3]Cl_2$, 0.5 mM	AA, 0.1 M	H_2O, pH = 6.7	Xenon lamp, $\lambda > 400$ nm	4 h	4000	2400	41	198
19	CoTPPS, 0.005 mM	CuPS, 0.5 mM	AA, 0.1 M	H_2O, pH = 6.7	Xenon lamp, $\lambda > 400$ nm	4 h	1085	380	90	199
20	CoTMPyP, 0.005 mM	CuPS, 0.5 mM	AA, 0.1 M	H_2O, pH = 6.7	Xenon lamp, $\lambda > 400$ nm	4 h	2680	1600	77	199
21	Co(oTMPyP), 0.005 mM	CuPS, 0.5 mM	SA, 0.1 M	H_2O, pH = 6.7	Xenon lamp, $\lambda > 400$ nm	12 h	4000 (CO)	1170	90	200
22	Co(TMAP), 0.005 mM	CuPS, 0.5 mM	SA, 0.1 M	H_2O, pH = 6.7	Xenon lamp, $\lambda > 400$ nm	8 h	460 (CO)	210	77	200
23	FeCl-1-Ru, 0.05 mM		TEA, 5%	DMF	Mercury lamp, $\lambda > 305$ nm	24 h	11.4			201
24	Co-1-Ru, 0.05 mM		TEA, 5%	DMF	Mercury lamp, $\lambda > 305$ nm	24 h	4.7			201
25		[Dyad 1 pic]PF_6, 0.05 mM	TEOA, 20%	DMF	Xenon lamp, $\lambda > 520$ nm	6 h	27	6		202
26		[Dyad 2 pic]OTf, 0.05 mM	TEOA, 20%	DMF	Xenon lamp, $\lambda > 520$ nm	8 h	32	4		202
27		[Dyad 3 pic]OTf, 0.05 mM	TEOA, 20%	DMF	Xenon lamp, $\lambda > 520$ nm	7 h	332	60		202
28		Zn-1-Re, 0.05 mM	TEA, 5%	DMF	Mercury lamp, 200 W, $\lambda > 375$ nm	24 h	13			206
29		Re-TXP-Zn, 0.05 mM	TEOA, 20% and BIH, 0.1 M	DMF	Xenon lamp, 200 W, $\lambda > 450$ nm	24 h	195			207
30		ZnP-phen = Re, 0.05 mM	BIH, 0.05 M and PhOH 0.1 M	DMA	LED lamp, $\lambda = 420$ nm	24 h	900		99.9	208
31	$Mn(phen)(CO)_3Br$, 2 mM	ZnTPP, 0.5 mM	TEA, 0.1 M	CH_3CN/H_2O (20/1)	Xenon lamp, 500 W	3 h	119 (CO) 19 (HCOOH)			210
32	$Mn(HPEAB)(CO)_3Cl$, 0.0015 mM	ZnTPP, 0.0019 mM	TEA, 16.7%	CH_3CN/H_2O (95/5)	LED diode, $\lambda = 625$ nm	100 min	0.3	0.75		211

also limited by the –OH groups. The highest catalytic activity was observed with CAT reaching 28 TON after 10 h of irradiation. The relative low catalytic performance was attributed to the degradation of the catalysts, due to the progressive hydrogenation of the porphyrin macrocycle under the continuous UV light irradiation.

The same group, in an effort to increase the stability of the catalytic system, examined the performance of iron catalyst CAT in presence of a PS.[188] When they used an iridium complex ($Ir(ppy)_3$, Fig. 41) as PS, CO formation was observed with high efficiency (140 TON) and selectivity (93%) (Table 8, entry 5). However, $Ir(ppy)_3$ in an expensive compound and for that reason, a cheaper organic chromophore such as 9-cyanoanthracene (9CNA, Fig. 41) was also studied. In this case the catalytic performance was reduced (60 TON), but the selectivity was even better (100%) (Table 8, entry 6). In both cases, visible light ($\lambda > 400$ nm) was employed for the excitation of the PS. Under these conditions the catalytic activity remained stable for more than 50 h of irradiation, indicating that no significant degradation of the iron catalyst CAT occurs. Rao *et al.* reported another approach to enhance the stability of the catalytic system.[189] More specifically, they prepared a modified tetraphenyl iron porphyrin (Fe-p-TMA, Fig. 40) by introducing positively charged trimethylammonio groups at the *para* position of each phenyl ring. This catalyst reduces CO_2 to CO with high selectivity (100%), under visible light irradiation ($\lambda > 420$ nm) in CH_3CN without the assistance of a PS and remains stable for several days. In the presence of TEA as SED the CO formation reached 33 TON, while when they used 1,3-dimethyl-2-phenyl-2,3-dihydro-1*H*-benzo[d]imidazole (BIH) as SED the TON increased to 63 (Table 8, entries 7 and 8). Catalyst Fe-p-TMA demonstrated increased activity compared to CAT, since the formed Fe(0)–CO_2 adduct is stabilized more efficiently by through-space coulombic interactions between the positive charge of the trimethylamino substituents ($^{+}N(Me)_3$) and the partially negative charged oxygen atoms of the CO_2. The positively charged trimethylammonio groups make catalyst Fe-p-TMA water soluble and based on this property, its catalytic performance was further examined in aqueous solution.[190] Under visible light irradiation ($\lambda > 420$ nm) and with the assistance of a low-cost organic PS, such as purpurin (Fig. 41), Fe-p-TMA selectively reduce CO_2 into CO with catalytic selectivity of 95% and turnover number up to 60 (Table 8, entry 9). The catalytic CO reduction was maintained for more than 48 h of irradiation and is limited mainly by the progressive degradation

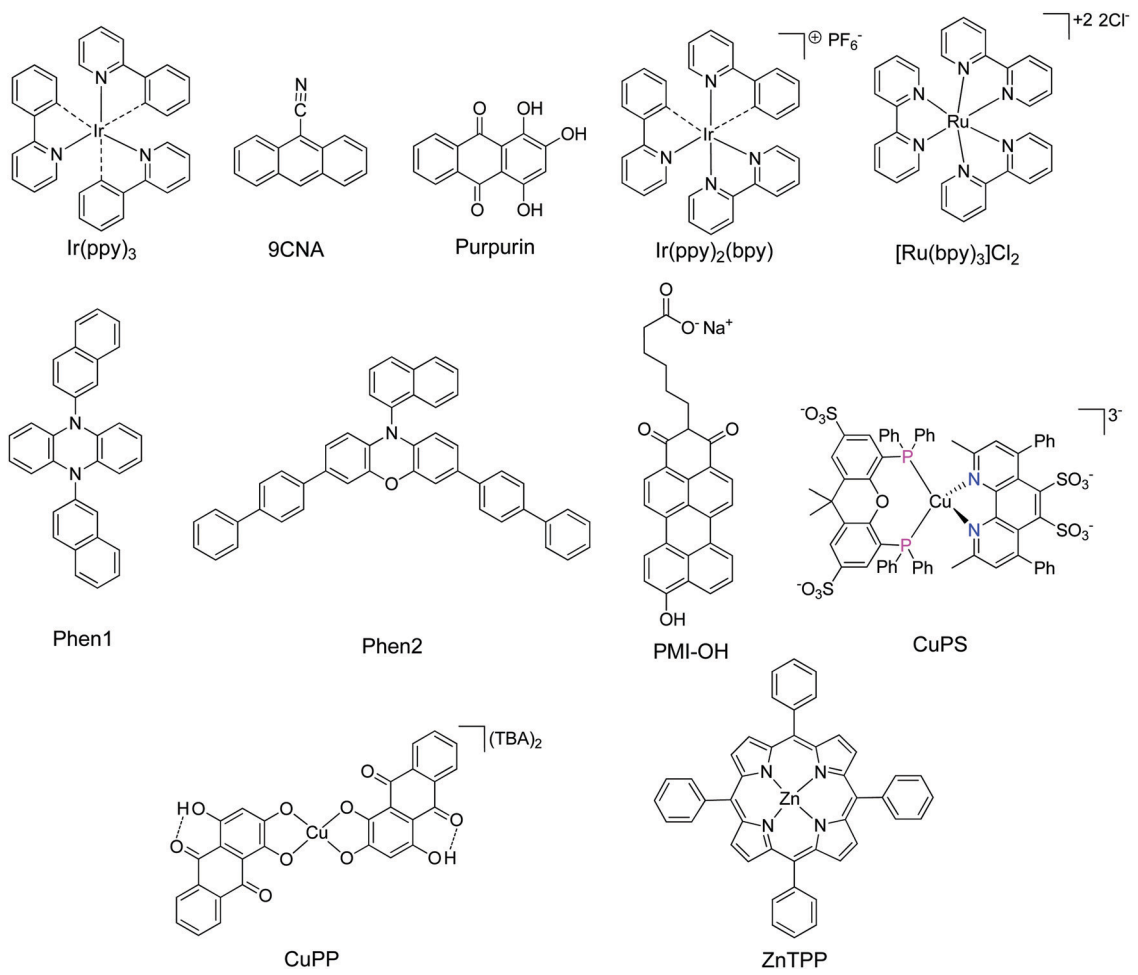

Fig. 41 Structure of molecular derivatives employed as PS for CO_2 conversion.

of the purpurin PS. Interestingly, the same group reported that Fe-p-TMA catalyst can also catalyze the eight-electron reduction of CO_2 to CH_4 upon visible light irradiation at ambient pressure and temperature.[191] The catalytic system operates in CH_3CN solution, using $Ir(ppy)_3$ (Fig. 41) as PS and TEA as SED. After 102 h of irradiation, the gaseous products that formed were CO, CH_4 and H_2 with TONs of 367, 79 and 26 respectively (Table 8, entry 10). CO was the major product of the photocatalysis and CH_4 production begins only after a large amount of CO has built up, indicating that CO is an intermediate in the CH_4 formation process. The catalytic activity is retained for more than 4 days with no evidence for degradation of the sensitizer or catalyst, highlighting the exceptional stability of the system. Robert and Bonin and co-workers were further examined the efficiency of catalyst Fe-p-TMA in the presence of a modified iridium-based PS ($Ir(ppy)_2(bpy)$, Fig. 41).[192] In CH_3CN solution the main reduction product was CO (178 TON) and a considerable amount of CH_4 (32 TON) was also produced (Table 8, entry 11). Under the same experimental conditions $Ir(ppy)_3$ PS presented similar catalytic performance (Table 8, entry 12), indicating that $Ir(ppy)_2(bpy)$ is a suitable alternative PS. Three different amines (TEA, TEOA and DIPEA) were examined as SEDs and TEA demonstrated the best efficiency. Remarkably, the CO_2 reduction to CO and CH_4 was also observed in 70% aqueous solution (Table 8, entry 13). The TONs of both CO and CH_4 were lower compared to the CH_3CN solution due to the limited CO_2 solubility in the catalytic solvent mixture and the instability of the PS upon prolonged irradiation. The same group reported that Fe-p-TMA catalyst retains its ability to perform the $8e^-/8H^+$ reduction of CO_2 to CH_4, even after the replacement of the iridium based PSs with cheaper organic PSs.[193] The phenoxazine-based organic PS (Phen2, Fig. 41) demonstrated efficient reduction of CO_2 to CO and CH_4 with TONs of 149 and 29, respectively (Table 8, entry 14). The catalysis was performed in DMF solution with TEA as SED and the catalytic system is stable for more than 4 days of continuous visible-light ($\lambda > 435$ nm) irradiation. Moreover, they noticed that the addition of an external acid such as 2,2,2-trifluoroethanol (TFE), increased the efficiency of the system since the production of both CO and CH_4 was noticeably improved. Notably, when Phen2 was replaced by a phenazine-based PS (Phen1, Fig. 41), only CO formation was observed. This result was attributed to the lower reducing ability of Phen1, which hampers the reduction of CO_2 beyond CO. The same group in a recent report evaluated six phenoxazine derivatives as visible light photosensitizers for the photo-initiated CO_2 to CO reduction, using Fe-p-TMA as catalyst in CH_3CN solution.[194] The photcatalytic studies demonstrated that the production of CO is strongly related to the oxidation potential of the Phen sensitizer. This unexpected result indicates that photosensitizer regeneration by the SED is the rate-limiting step of this catalytic system. Stupp and co-corkers also examined the catalytic activity of Fe-p-TMA catalyst in combination with an amphiphilic hydroxyl-substituted perylene monoimide (PMI-OH, Fig. 41) chromophore.[195] The water-soluble PMI-OH exhibits reversible structural, optical, and electrochemical properties in response to pH. The catalysis was performed in basic conditions using sodium ascorbate (SA) as SED and CO formation was observed with a TON of 30 (Table 8, entry 15). In a recent work, Han and co-workers reported the preparation of a highly active copper purpurin complex (CuPP, Fig. 41), which was employed as PS with an iron porphyrin (CAT, Fig. 40) as catalyst for visible-light-driven CO_2 reduction.[196] The coordination of the redox-active Cu center directly to the purpurin dye red-shifted the absorption maxima of purpurin to the visible region. Moreover, electrochemical studies revealed that the incorporation of Cu produces a much more reducing PS, facilitating challenging multielectron reductions. Under visible-light irradiation and in the presence of BIH as SED, this system achieves 16 109 TON of CO from CO_2 with 95% selectivity (Table 8, entry 16), which is among the highest reported for a homogeneous noble metal-free system.

Apart from iron porphyrins, cobalt metallated porphyrins have been used extensively as catalysts for the electo- or photo-catalytic reduction of CO_2.[197] Sakai and co-workers reported that the water soluble cobalt porphyrin CoTPPS (Fig. 42) achieves with high selectivity the CO_2 to CO reduction in fully aqueous media.[198] A ruthenium complex ($[Ru(bpy)_3]Cl_2$, Fig. 41) was utilized as PS and AA as SED. Under visible light irradiation ($\lambda > 400$ nm) CO formation was observed with high efficiency (926 TON) and selectivity (82%) (Table 8, entry 17). Interestingly, when they reduced the concentration of the catalyst from 10 μM to 0.5 μμ the TON increased to 4000, but the selectivity of the system was significantly reduced to 41% (Table 8, entry 18). The catalysis is active for 4 h and the degradation of the ruthenium PS is proposed as the major cause for the cease of photocatalysis. The same group successfully replaced the precious metal-based $[Ru(bpy)_3]Cl_2$ PS with an earth-abundant copper(I)-based water

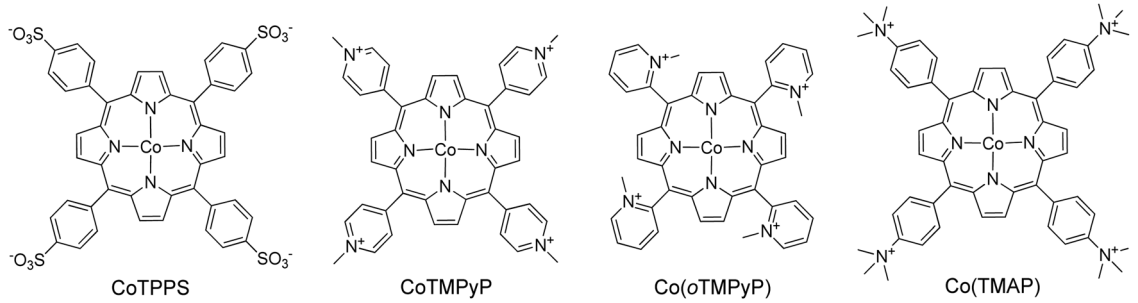

Fig. 42 Structure of cobalt porphyrin molecular catalysts for CO_2 reduction.

soluble PS (CuPS, Fig. 41).[199] CoTPPS in the presence of CuPS in aqueous solution catalyzed the CO_2 to CO reduction with high selectivity (90%), achieving 1085 TON (Table 8, entry 19). In an effort to explore the effect of the peripheral groups of the cobalt metalloporphyrin catalyst onto the CO_2 photodriven reduction, they replaced the four sulfonatophenyl groups with *N*-methylpyridinium. Under the same experimental conditions, the new catalyst CoTMPyP (Fig. 42) demonstrated improved catalytic performance (2680 TON, Table 8, entry 20) compared to CoTPPS, but the CO selectivity over H_2 formation was decreased from 90 to 77%. Electrochemical studies revealed that the multielectron chargeable character of CoTMPyP is responsible for the outstanding catalytic enhancement. Catalyst CoTMPyP can store up to 6-electrons and the final CO releasing step is assisted *via* intramolecular electron transfer from the reducing equivalents stored within the four methylpyridinium acceptor moieties. The same group in a later report examined two more positively charged cobalt catalysts, Co(TMAP) and Co(oTMPyP) (Fig. 42) in combination with the molecular CuPS PS.[200] Catalyst Co(oTMPyP) presented significantly superior activity achieving efficient CO_2 to CO reduction with a TON of 4000 after 12 h of irradiation (Table 8, entries 21 and 22).

In all the above examples the catalyst and the PS were not covalently connected and the electronic communication between the two components was usually controlled by the diffusion in the solution. Schwalbe and co-workers integrated the catalyst and the PS into a single molecular structure, in order to accelerate the electron transfer between them.[201] They prepared two different dinuclear complexes (FeCl-1-Ru and Co-1-Ru, Fig. 43), where a Ru complex was covalently connected with a phenanthroline-extended porphyrin. The porphyrin ring was metallated with Fe or Co and served as catalyst, while the Ru moiety was the PS. Photocatalytic studies demonstrated that dyads FeCl-1-Ru and Co-1-Ru can reduce CO_2 to CO in the presence of TEA as SED with relatively low activity (11.4 and 4.7 TON, respectively) (Table 8, entries 23 and 24). In both dyads, the covalently connected Ru complex increased the catalytic activity relative to the reference compounds where the Ru PS was absent. The Ru fragment shifted the reduction potentials of the catalysts to less negative values and thus the photochemical quenching reaction with the SED became more efficient, improving the CO_2 reduction activity. Furthermore, they revealed that near UV-light ($\lambda > 305$ nm) was necessary for CO_2 reduction, suggesting that in this system the Ru complex is not a "real" PS and probably through an antenna effect in the near UV region assists the photochemical reaction.

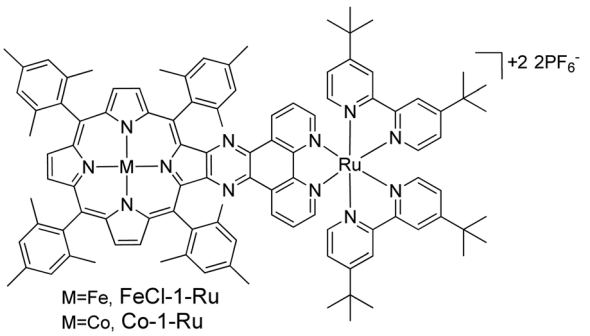

Fig. 43 Structure of the PS-catalyst dyads FeCl-1-Ru and Co-1-Ru.

3.1.2 Porphyrins as chromophores in homogeneous CO_2 reduction systems. Porphyrin derivatives have been employed in photocatalytic CO_2 reduction systems mainly as catalysts, due to their interesting electrochemical properties. However, zinc porphyrins are also good candidates and possess several advantages for the sensitization of a catalyst. More specific, they present intense absorption in the visible region, their excited state redox potentials can be easily tuned, they present good photoinduced electron-transfer ability and their structure strongly relates to chlorophylls that are utilized in natural photosynthesis for light harvesting and charge separation. For all these reasons zinc porphyrins have been also used as PS for the photocatalytic CO_2 reduction. Perutz and co-workers reported the synthesis and the photocatalytic activity of three dyads where a zinc porphyrin was covalently connected with a rhenium bipyridine tricarbonyl complex (Fig. 44).[202] In these assemblies the porphyrin part acts as PS and the Re compound as catalyst, since this family of Re complexes have been used extensively for photocatalytic and electrocatalytic CO_2 reduction.[203–205] In the first dyad [Dyad 1 pic]PF_6 the two components were connected through an amide linkage, in [Dyad 2 pic]OTf an additional methoxybenzamide ring was introduced between the PS and the catalyst, while [Dyad 3 pic]OTf has an extra saturated bridge between the two parts. They examined three different linkages in an effort to increase the catalytic activity by reducing the rate of charge recombination between the PS and the catalyst. The photocatalytic studies were performed in DMF and TEOA was used as SED. Under visible light irradiation ($\lambda > 520$ nm) the three dyads were able to perform the CO_2 to CO reduction. The dyad with the methylene spacer ([Dyad 3 pic]OTf) presented higher catalytic activity (by a factor of ten) compared to the other two, achieving more than 330 TON (Table 8, entries 25–27). The reason for the enhanced activity in [Dyad 3 pic]OTf is the flexibility of the Re unit to adopt the best orientation and the closest approach to the porphyrin unit. This favorable conformation slowed down charge separation and charge recombination processes. Moreover, they studied the influence of the sixth ligand on the Re metal center by replacing the 3-picoline with a bromide anion. However, the catalytic performance of the bromide complexes was very similar to that of the corresponding cationic dyads. Finally, in all cases the catalytic activity stops after some hours of irradiation due to the complete bleaching of the porphyrin ring.

Tschierlei, Schwalbe and co-workers developed a series of heterodinuclear complexes, where a porphyrin unit was connected with a rhenium phenanthroline tricarbonyl chloride catalytic center (Fig. 44), for application in photocatalytic CO_2 to CO reduction.[206] The linker between the two components was an extended delocalized π-system with partial electron storage ability and this was expected to enhance the catalytic performance. The porphyrin ring was metallated with various metals (H_2, Zn, Cu, Pd, Co, and Fe), in an effort to examine the influence of the metal on the photochemical activity.

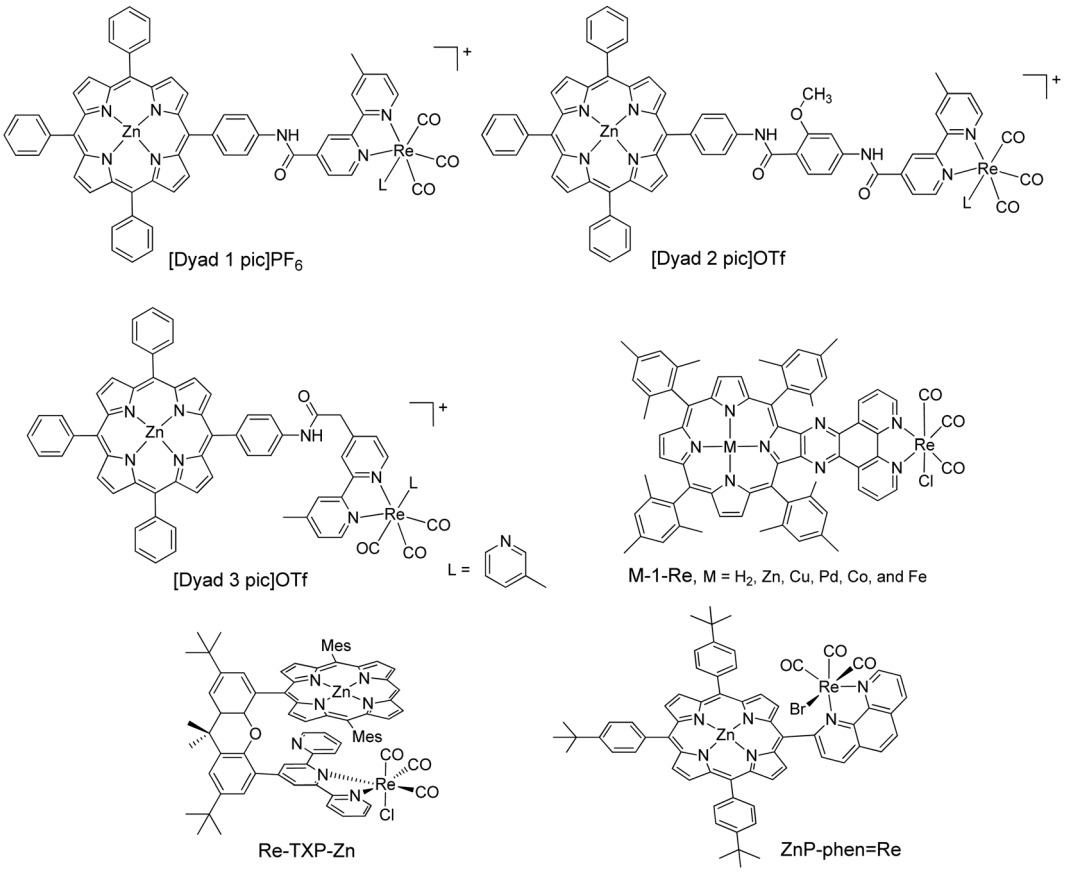

Fig. 44 Structure of the porphyrin-Re dyads studies for CO_2 reduction.

Interestingly, the zinc derivative (Zn-1-Re, Fig. 44) was the most active compound in this series showing a TON of 13 after 24 h of illumination using a >375 nm cutoff filter (Table 8, entry 28), while all other complexes were inactive under these conditions. The superior activity of Zn-1-Re was attributed to the strong impact of the Zn metal on the nature of the excited states of the porphyrin unit, favoring the electron transfer process from the porphyrin chromophore to the Re catalyst.

The same group reported an analogue dyad (Re-TXP-Zn), consisting of a porphyrin unit as photosensitizer and a rhenium terpyridine unit as catalytically active site (Fig. 44).[207] In this hetero-Pacman architecture the two moieties were connected together through a rigid xanthene backbone, which breaks the conjugation between the two components, but still can facilitate energy or electron transfer between the photosensitizer and the catalyst due to their close proximity. Photocatalytic experiments using BIH as SED revealed that the Re-TXP-Zn heterodimer catalyzes the CO_2 to CO reduction, achieving a TON of 195 after 24 h of irradiation (Table 8, entry 29). The catalytic performance was reduced by changing the SED from BIH to TEA and by using the non-metallated porphyrin ring. Moreover, the intramolecular dyad presented higher catalytic performance compared to the intermolecular systems that consisted of a 1 : 1 mixture of the corresponding mononuclear analogues, indicating that the close proximity of the photosensitizer and catalytic active species appears to be highly advantageous.

Kuramochi *et al.* reported another chromophore-catalyst dyad (ZnP-phen=Re), in which a rhenium phenanthroline tricarbonyl catalyst was directly connected with the *meso*-position of a zinc porphyrin (Fig. 44).[208] The photocatalytic CO_2 reduction studies were carried out in *N,N*-dimethylacetamide (DMA) solutions containing BIH as electron donor and phenol as proton source. The formation of CO was observed with high selectivity and activity, achieving more than 900 TONs (Table 8, entry 30). Interestingly, the catalytic activity stops after 24 h of irradiation, due to the consumption of BIH, while further addition of BIH to the reaction mixture regenerated the photocatalytic system, with the same catalytic rate. Emission spectroscopy studies revealed that porphyrin phosphorescence was efficiently quenched by BIH, suggesting that the electron transfer process proceeds *via* the T_1 long-lived excited state of the porphyrin. The high durability of ZnP-phen=Re dyad was attributed to the rapid electron transfer from the reduced zinc porphyrin to the Re complex, suppressing the undesired electron accumulation on the zinc porphyrin.

The same group continued their studies on the ZnP-phen = Re dyad and examined in more detail various basic parameters that influence the catalytic performance.[209] Initially, the role of the Zn metal of the porphyrin ring was investigated. The dyad with the free base porphyrin presented significantly lower catalytic activity compared to the Zn analogue. This was assigned to the very fast decomposition of the non-metallated

porphyrin, due to hydrogenation of the pyrrole double bonds. Moreover, the BIH was replaced by TEA, which is a weaker reductant and is more often used as SED in similar catalytic systems. The CO was produced with high selectivity, but the performance (TONs) was lower for more than one order of magnitude compared to the BIH. Finally, the effects of several proton sources (water, methanol, 2,2,2-trifluoroethanol (TFE), phenol, acetic acid), having different acidities, were examined. The presence of TFE and phenol enhanced significantly the catalytic activity with the trend TFE > PhOH > $H_2O \approx$ MeOH, while acetic acid deactivated completely the catalytic system.

Replacement of Re-based catalysts with their Mn-analogues would be a huge step towards the development of more affordable and abundant catalysts. However, the Mn derivatives are photosensitive, undergoing decarbonylation after photoexcitation, and therefore the use of an additional PS is mandatory. Toward this goal, Zhang *et al.* reported a homogeneous catalytic system where a manganese phenanthroline tricarbonyl complex ($Mn(phen)(CO)_3Br$, Fig. 45) was employed as catalyst and zinc tetraphenyl porphyrin (ZnTPP, Fig. 41) as photosensitizer.[210] In this case the catalyst and the PS were not covalently connected and the electronic communication between the two components was controlled by the diffusion. Under visible light irradiation, CO_2 could be reduced to CO (119 TON) as gas product and formic acid (19 TON) as liquid product (Table 8, entry 31).

Shipp *et al.* synthesized two molecular Re and Mn tricarbonyl complexes bearing a bipyridyl ligand functionalized with sterically hindering substituents (Fig. 45), and their propensity to act as catalysts for the photochemical reduction of CO_2 has been examined.[211] The electron-withdrawing amide groups were selected to reduce the reduction potential of the catalysts, allowing the use of less strongly-reducing PS. No photochemical CO_2 reduction was observed for the rhenium complex ($Re(HPEAB)(CO)_3Br$) in the presence of ZnTPP (Fig. 41) as PS and TEA as SED. This was attributed to the short (3.6 ns) triplet excited state lifetime of the Re catalyst, which prevents the bimolecular diffusion-controlled electron transfer. Notably, the manganese complex ($Mn(HPEAB)(CO)_3Br$, Fig. 45) can act as a CO_2 to CO reduction catalyst after photosensitization by ZnTPP under red light irradiation ($\lambda > 600$ nm), achieving 0.3 TONs (Table 8, entry 32). The relatively low catalytic activity is likely due to inefficient reduction of the catalyst by the reduced porphyrin, since this process was only weakly thermodynamically favorable.

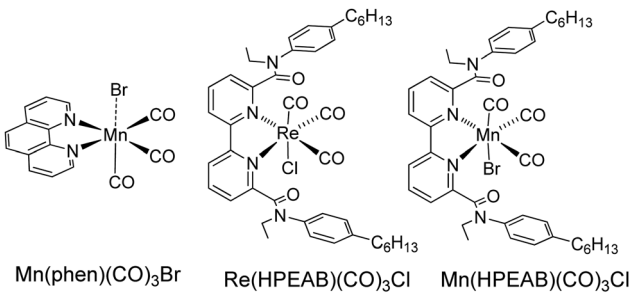

Fig. 45 Structure of molecular Mn and Re catalysts for CO_2 reduction.

The problems associated with the application of molecular catalysts in the visible-light driven reduction of CO_2 include, among others, low product selectivity and simultaneous hydrogen production. Biocatalysts are promising candidates to overcome these issues, due to their excellent reaction and substrate selectivity, especially for the reduction and utilization of CO_2. Thus, several photocatalytic CO_2 reduction systems were developed based on enzymes that served as biocatalysts.[212] Amao *et al.* reported the efficient reduction of CO_2 to formic acid with a catalytic system where formate dehydrogenase (FDH) was employed as catalyst, a water-soluble zinc porphyrin (ZnTPPS) as PS and TEOA as SED (Fig. 46a).[213] In this system the presence of an extra electron carrier molecule facilitates the electronic communication between the PS and the catalyst and enhances the catalytic activity. Thus, a series of 2,2′-bipyridinium (2,2′-BPs) salt derivatives (Fig. 46b) were used as electron carriers to investigate their effect in the light-induced conversion of CO_2.[214] The photocatalytic studies demonstrated that redox potential and dihedral angle of 2,2′-BPs influence the activity. The highest formic acid production rate (70 μM h^{-1}) was obtained with 1,10-ethylene-2,20-bipyridinium dibromide (DB, Fig. 46b), since it possess the lowest redox potential and the smallest dihedral angle.

Interestingly, when the electron carrier DB was replaced by 1,1′-diaminoethyl-4,4′-bipyridinium salt (DAV, Fig. 46c), the production rate of formic acid increased to 120 μM h^{-1}.[215] The improvement of CO_2 photoreduction was ascribed to the higher affinity of DAV for FDH enzyme and its stronger interaction with the ZnTPPS porphyrin, due to the presence of the positively charged amino groups. The same group in an effort to improve the catalytic performance of this system examined a series of viologen-based 4,4′-bipyridinium (4,4′-BPs) salts (Fig. 46c) as electron carriers.[216] The derivatives with the cationic aminoethyl-groups (DAV and AMV) presented higher formic acid production rates (120 and 100 μM h^{-1}, respectively) compared to the 4,4′-BPs with the anionic carboxymethyl-groups (CMV and DCV, 50 and 39 μM h^{-1}, respectively). Interestingly, this catalytic system retains its activity even in ionic liquid media.[217] Two viologen derivatives with carbamoyl groups (CV and CMV, Fig. 46c) were also synthesized and applied as electron carriers to the FDA-based photoinduced CO_2-formic acid conversion system.[218] Both of them presented higher catalytic activity compared to the non-substituted MV (Fig. 46c). However, the compound with only one carbamoyl group (CMV) was more efficient compared to di-substituted CV, achieving formic acid production rates similar to DAV. The above results indicate that the presence of aminoethyl or carbamoyl group in 4,4′-BPs improves the catalytic performance. Thus, Miyaji and Amao prepared the ACBP (Fig. 46c) electron carrier, which possess in its structure both the amino and the carbamoyl group.[219] Nevertheless, the photocatalytic formation of formic acid, in presence of ACBP was very low, even lower than that observed for MV. This was attributed to the low energy level of the singly occupied molecular orbital (SOMO) of ACBP, which influences negatively the reduction rate of CO_2. The same group prepared a nicotinamide-modified viologen derivative (NEMBP, Fig. 46c) and was applied as

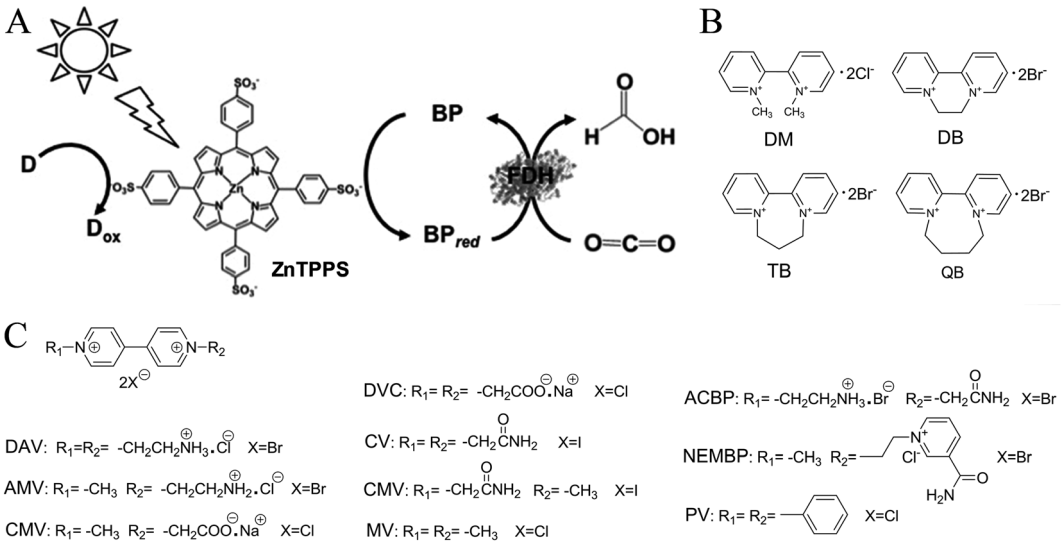

Fig. 46 (A) Schematic representation of the visible-light driven redox system for the reduction of CO_2 to formate using FDH enzyme, (B) chemical structures of various 2,2′-bipyridinium salts. (C) Various 4,4′-bipyridinium salts.

electron carrier.[220,221] The nicotinamide group was introduced in an effort to enhance the affinity of NEMBP with FDH, since the nicotinamide group is present in the structure of the natural occurring NAD^+ co-enzyme. However, the NEMBP derivative presented disappointing results in all kinetic parameters for CO_2 to formic acid reduction, most likely due to the unfavorable SOMO energy level. Similarly, the visible-light induced formation of malic acid from pyruvic acid and CO_2 with the application of malic enzyme (ME) as biocatalyst was also reported from the same group.[222,223] ME is an attractive biocatalyst for the carbon–carbon bond formation, using CO_2 as a feedstock, since it catalyzes the insertion of CO_2 as a "carboxy group" into pyruvic acid. In this system, ZnTPPS was employed as PS, TEOA as SED and PV (Fig. 46c) as electron mediator. In the presence of magnesium ions (co-factor for ME) the formation of malic acid was observed, while in the catalytic system without Mg^{2+} only the intermediate oxaloacetic acid was obtained.

The conversion of CO_2 into methanol is of great importance since methanol is a fuel with high energy density and is an important precursor for the industrial synthesis of chemicals such as plastics and silicone. Amao and Kataoka reported the photocatalytic conversion of CO_2 to methanol with a system consisting of three different dehydrogenases (formate dehydrogenase (FDH), aldehyde dehydrogenase (AldDH) and alcohol dehydrogenase (ADH), Fig. 47a).[224] In this system a water-soluble porphyrin (H_2TPPS) was used as PS, TEOA was the SED, MV was employed as electron mediator and the production of methanol proceeds *via* formate and formaldehyde as intermediates. Under visible-light irradiation, the formation of methanol was observed with very low selectivity since the major product of the photoreduction was formic acid. Ji *et al.* followed the same biocatalytic approach for the photo-activated reduction of CO_2 to methanol.[225] However, instead of a simple porphyrin derivative, they utilized a macromolecular structure (TCPP/EY_4/Rh_4, Fig. 47b) as PS. The preparation of TCPP/EY_4/Rh_4 hybrid involves the amidation of the tetra carboxy-porphyrin (H_2TCPP) by melamine, followed by sensitization with eosin Y (EY), and finally the covalent linkage of a rhodium-based organometallic

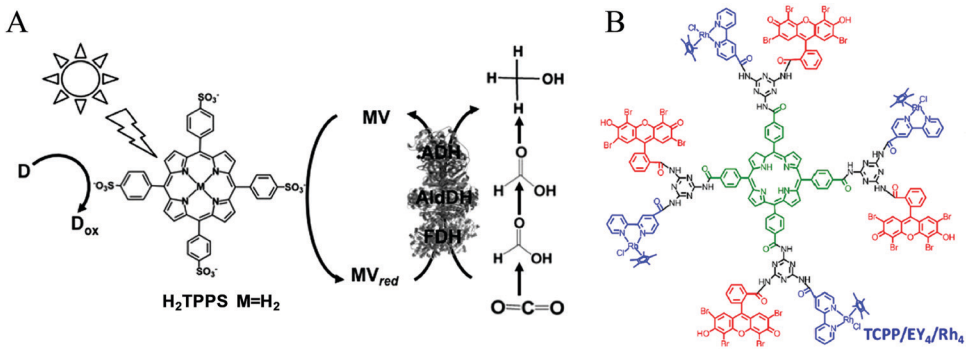

Fig. 47 (A) Schematic representation of the visible-light driven redox system for the reduction of CO_2 to methanol using three different dehydrogenases FDH, AldDH and ADH. Reproduced from ref. 224, with permission from Elsevier, Copyright 2018. (B) Chemical structure of the macromolecular hybrid TCPP/EY_4/Rh_4.

complex $[Cp^*RhCl_2]_2$. The fabricated TCPP/EY_4/Rh_4 macromolecule was found to self-assemble into supramolecular assemblies in water through π–π stacking and hydrogen bonding, mimicking the structure and function of chlorosomes in green photosynthetic bacteria. Photocatalytic studies in the presence of TEOA, demonstrated an efficient photogeneration of NADH. The sensitization of the porphyrin core by EY improved the absorbance in the visible region, while the Rh complex served as mediator, accelerating the electron transfer efficacy, and eliminating the charge recombination. When this NADH photoregeneration process was coupled with a mixture of three dehydrogenases (FDH, AldDH and ADH), 38 μM methanol was synthesized from CO_2 after 2 h of visible light irradiation.

3.2 Heterogeneous systems

Although homogeneous catalytic systems display high activity and selectivity in the photocatalytic CO_2 reduction, their practical application is limited due to the difficulties in catalyst separation from the reaction mixture and recycling.[226,227] One promising approach to address this issue is to anchor homogeneous molecular photocatalysts onto a solid support or to combine homogeneous catalysts with metal–organic frameworks (MOFs). The resulting catalytic systems may be considered as "heterogenized" homogeneous systems since they possess the advantages of both homogeneous and heterogeneous catalysts.

3.2.1 Metal–organic frameworks (MOFs) for CO_2 reduction. Jiang and co-workers prepared a stable porphyrin-based MOF (PMOF), denoted as PCN-222, through the assembly of the free base tetra-carboxy-porphyrin (H_2TCPP) with Zr_6-node clusters (Fig. 48a).[228] PCN-222 shows high CO_2 uptake ability and under visible-light irradiation, it can efficiently convert CO_2 to formate exhibiting a rate of 60 μmol g^{-1} h^{-1} (Table 9, entry 1). Upon irradiation, the H_2TCPP linkers behave as an antenna absorbing visible light and then inject electrons to the Zr oxo-clusters. The Zr^{4+} is reduced to Zr^{3+} which is able to reduce CO_2 to $HCOO^-$ in the presence of TEOA as SED (Fig. 48b). No other products were detected, suggesting that the catalyst is highly selective toward this conversion. For comparison, H_2TCPP was also employed as a photocatalyst under similar conditions. However, only traces of formate were produced (Fig. 48c), confirming that the photocatalytic activity can be greatly enhanced by assembling H_2TCPP onto MOFs. Jin also synthesized PCN-222 and after the addition of Zn^{2+} ions in the PMOF he states the improvement of the catalytic activity, reaching a rate of 120 μmol g^{-1} h^{-1} for the CO_2 to formate reduction (Table 9, entry 2).[229] Moreover, Hariri *et al.* utilized metallated tetra carboy-porphyrins (MTCPP, M = Fe, Co, Ni, and Cu) for the construction of the isostructural PMOFs, PCN-222(M) (M = Fe, Co, Ni, and Cu).[230] All the metalloporphyrin-based MOFs presented higher catalytic activity compared to the non-metallated PCN-222. The presence of the metal centers on the porphyrin linkers promotes CO_2 adsorption and activation and improves the conversion efficiency. Production of formate was observed in all cases with similar conversion rates in the range of 313–373 μmol g^{-1} h^{-1} (Table 9, entries 3–6). The Ni metallated MOF (PCN-222(Ni)) achieved slightly increased performance (373 μmol g^{-1} h^{-1}) in comparison with the other mesoporous materials PCN-222(M) (M = Fe, Co and Cu).

Ye and co-workers followed a similar approach and prepared MOF-525 using H_2TCPP as linker and Zr_6 oxo-clusters as metal nodes.[231] Additionally, they post-metallated the porphyrin units with Co and Zn, generating the isostructural MOF-525-

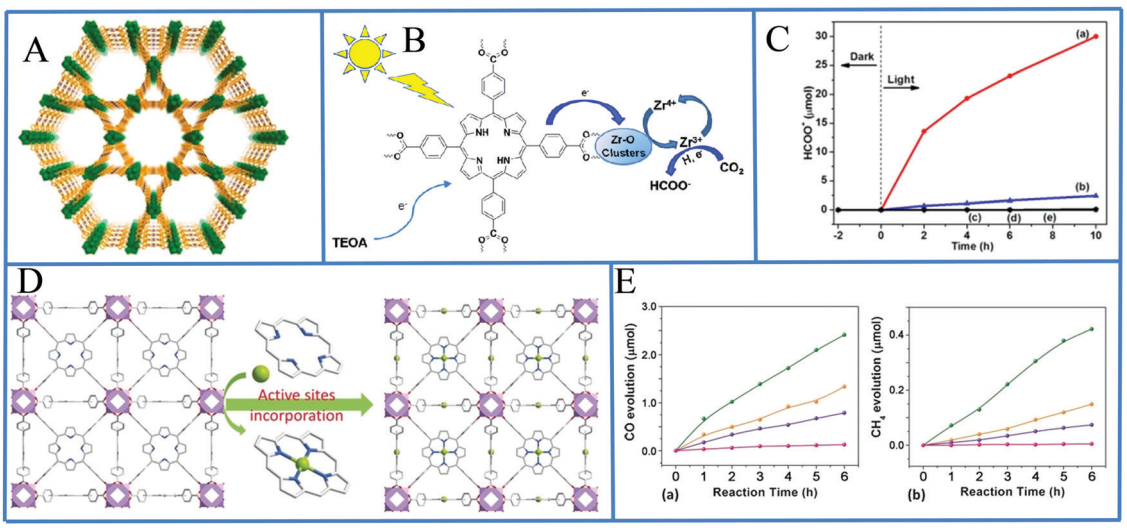

Fig. 48 (A) View of the 3D network of PCN-222. Reproduced from ref. 228, with permission from American Chemical Society, Copyright 2015. (B) Proposed mechanism for photocatalytic CO_2 reduction over PCN-222 under visible-light irradiation. Reproduced from ref. 228, with permission from American Chemical Society, Copyright 2015. (C) Amount of $HCOO^-$ produced as a function of the time of light irradiation over (a) PCN-222 and (b) H_2TCPP. Reproduced from ref. 229, with permission from Royal Society of Chemistry, Copyright 2020. (D) View of the 3D network of MOF-525-Co featuring a highly porous framework and incorporated active sites. Reproduced from ref. 231, with permission from John Wiley and Sons, Copyright 2016. (E) Time time-dependent (a) CO and (b) CH_4 evolution over MOF-525-Co (green), MOF-525-Zn (orange) and MOF-525 (purple) photocatalysts. Reproduced from ref. 231, with permission from John Wiley and Sons, Copyright 2016.

Table 9 Photocatalytic performance of porphyrin MOFs for CO_2 reduction

Entry	MOF name	Metal node	Linker	Cocatalyst or additives	SED	Solvent	Light source	Major products Rate	Ref.
1	PCN-222	Zr	H_2TCPP	—	TEOA, 9%	CH_3CN	Xenon lamp, 300 W, $\lambda > 420$ nm	$HCOO^-$, 60 μmol g^{-1} h^{-1}	228
2	PCN-222-Zn	Zr	H_2TCPP	—	Ethylene glycol, 20 mM	H_2O	Xenon lamp, 300 W, $\lambda > 420$ nm	$HCOO^-$, 120 μmol g^{-1} h^{-1}	229
3	PCN-222(Fe)	Zr	FeTCPP	—	TEOA, 9%	CH_3CN	Xenon lamp, 500 W, $\lambda > 420$ nm	$HCOO^-$, 347 μmol g^{-1} h^{-1}	230
4	PCN-222(Co)	Zr	CoTCPP	—	TEOA, 9%	CH_3CN	Xenon lamp, 500 W, $\lambda > 420$ nm	$HCOO^-$, 313 μmol g^{-1} h^{-1}	230
5	PCN-222(Ni)	Zr	NiTCPP	—	TEOA, 9%	CH_3CN	Xenon lamp, 500 W, $\lambda > 420$ nm	$HCOO^-$, 373 μmol g^{-1} h^{-1}	230
6	PCN-222(Cu)	Zr	CuTCPP	—	TEOA, 9%	CH_3CN	Xenon lamp, 500 W, $\lambda > 420$ nm	$HCOO^-$, 333 μmol g^{-1} h^{-1}	230
7	MOF-525-Co	Zr	CoTCPP	—	TEOA, 20%	CH_3CN	Xenon lamp, 300 W, $\lambda > 400$ nm	CO, 201 μmol g^{-1} h^{-1} CH_4, 36.8 μmol g^{-1} h^{-1}	231
8	MOF-525-Zn	Zr	ZnTCPP	—	TEOA, 20%	CH_3CN	Xenon lamp, 300 W, $\lambda > 400$ nm	CO, 112 μmol g^{-1} h^{-1} CH_4, 11.6 μmol g^{-1} h^{-1}	231
9	MOF-525	Zr	H_2TCPP	—	TEOA, 20%	CH_3CN	Xenon lamp, 300 W, $\lambda > 400$ nm	CO, 64 μmol g^{-1} h^{-1} CH_4, 6.2 μmol g^{-1} h^{-1}	231
10	Rh-PMOF-1	Zr	Rh(TCPP)Cl	—	TEOA, 20%	CH_3CN	Xenon lamp, 300 W, $\lambda > 400$ nm	$HCOO^-$, 78 μmol g^{-1} h^{-1}	121
11	ZrPP-1-Co	Zr	CoTHPP	—	TEOA, 20%	CH_3CN	Xenon lamp, 300 W, $\lambda > 420$ nm	CO, 14 μmol g^{-1} h^{-1} CH_4, 0.5 μmol g^{-1} h^{-1}	233
12	PCN-138	Zr	H_2TCPP and TBTB	—	TIPA, 20%	H_2O	Xenon lamp, 300 W, $\lambda > 420$ nm	$HCOO^-$, 125 μmol g^{-1} h^{-1}	234
13	PCN-224(Cu)	Zr	CuTCPP	—	—	H_2O	Xenon lamp, 300 W, $\lambda > 300$ nm	CO, 3.72 μmol g^{-1} h^{-1} CH_4, 1.36 μmol g^{-1} h^{-1}	235
14	PCN-224(Cu)/TiO_2	Zr	CuTCPP	TiO_2 NPs	—	H_2O	Xenon lamp, 300 W, $\lambda > 300$ nm	CO, 37.21 μmol g^{-1} h^{-1} CH_4, 0.21 μmol g^{-1} h^{-1}	235
15	CTU/TiO_2	Zr	CuTCPP	TiO_2 NPs	—	H_2O	Xenon lamp, 300 W, $\lambda > 300$ nm	CO, 31.32 μmol g^{-1} h^{-1} CH_4, 0.15 μmol g^{-1} h^{-1}	236
16	PCN-221(Fe)	Zr	FeTCPP	—	H_2O, 1,2%	EtOAc	Xenon lamp, 300 W, $\lambda > 400$ nm	CO, 0.52 μmol g^{-1} h^{-1} CH_4, 1.52 μmol g^{-1} h^{-1}	237
17	$MAPbI_3$@PCN-221(Fe)	Zr	FeTCPP	Perovskite QDs	H_2O, 1.2%	EtOAc	Xenon lamp, 300 W, $\lambda > 400$ nm	CO, 14.16 μmol g^{-1} h^{-1} CH_4, 6.24 μmol g^{-1} h^{-1}	237
18	PMOF/Re	Zr	ZnTCPP	Re(bpy) catalyst and 3% TFE	BIH	DMF	LED lamp, 60 W, $\lambda > 500$ nm	CO, 2204 TON or 535 μmol g^{-1} h^{-1}	238
19	Al-PMOF	Al	AlTCPP	—	TEOA, 16.7%	CH_3CN	Mercury lamp, 3 × 125 W	$HCOO^-$, 165 μmol g^{-1} h^{-1}	240
20	NH_2-rGO/Al-PMOF	Al	AlTCPP	NH_2-rGO	TEOA, 16.7%	CH_3CN	Mercury lamp, 3 × 125 W	$HCOO^-$, 685 μmol g^{-1} h^{-1}	240
21	Co/PMOF	Co	CoTCPP	—	TEOA, 16.7%	CH_3CN	Mercury lamp, 3 × 125 W	$HCOO^-$, 77 μmol g^{-1} h^{-1}	241
22	PMOF 1	Cd	H_2TCPP	—	TEA, 20%	CH_3CN	Xenon lamp, 300 W, $\lambda > 420$ nm	CO, 10 μmol g^{-1} h^{-1}	239
23	PMOF 1	Cd	H_2TCPP	$Ru(bpy)_3Cl_2$	TEA, 20%	CH_3CN	Xenon lamp, 300 W, $\lambda > 420$ nm	CO, 56 μmol g^{-1} h^{-1}	239
24		In	H_2TCPP	—	L-AP	EtOAc	Xenon lamp, 300 W, $\lambda > 400$ nm	CO, 144 μmol g^{-1} h^{-1}	242
25	D-TiMOF	Ti	ZnTCPP and NH_2BDC	—	TEOA, 20%	CH_3CN	Xenon lamp, $\lambda > 350$ nm	CO, 59.55 μmol g^{-1} h^{-1}	244
26	Zn/PMOF	Zn	H_2TCPP	—	H_2O	Gas phase	Mercury lamp, 300 W	CH_4, 8.7 μmol g^{-1} h^{-1}	245
27	PCN-601	Ni	NiTCPP	—	H_2O	Gas phase	Xenon lamp, $\lambda > 410$ nm	CO, 6 μmol g^{-1} h^{-1} CH_4, 10.1 μmol g^{-1} h^{-1}	246
28	2D/Zn-MOF	Zn	ZnTCPP	ZIF-67	TEOA, 16.7%	CH_3CN/MeOH (4/1)	Xenon lamp, $\lambda > 420$ nm	CO, 117.8 TON	248
29	3D/Zn-MOF	Zn	ZnTCPP	ZIF-67	TEOA, 16.7%	CH_3CN/MeOH (4/1)	Xenon lamp, $\lambda > 420$ nm	CO, 63.6 TON	248
30	PPF-3	Co	H_2TCPP	Au NPs	EtOH, 20%	CH_3CN	Xenon lamp, 300 W, $\lambda > 400$ nm	$HCOO^-$, 42.7 μmol g^{-1} h^{-1}	250
31	g-CNQDs/PMOF	Co	CoTCPP	g-CNQDs	TEOA, 20%	CH_3CN/H_2O (3/1)	Mercury lamp, 300 W, $\lambda > 420$ nm	CO, 16.1 μmol g^{-1} h^{-1} CH_4, 6.86 μmol g^{-1} h^{-1}	252

Co and MOF-525-Zn, respectively (Fig. 48d). The incorporation of metal centers into porphyrin rings of PMOFs is a promising approach to fabricate stable single-atom catalysts for CO_2 photoreduction. In both cases the presence of the metal centers increased significantly the CO_2 adsorption ability of the PMOFs. Photocatalytic CO_2 reduction studies were conducted using TEOA as SED and resulted in the efficient conversion of CO_2 to CO and CH_4. MOF-525-Co showed the highest catalytic activity (Fig. 48e), achieving a CO evolution rate of 201 μmol g^{-1} h^{-1}, and a CH_4 evolution rate of 36.8 μmol g^{-1} h^{-1} (Table 9, entry 7). These values are much higher compared to MOF-525-Zn and MOF-525 (Table 9, entries 8 and 9). The MOF-525-Co composite presents enhanced catalytic performance since the CO_2 reduction takes place not only in the Zr clusters but also in the Co metal centers. Additionally, MOF-525-Co exhibits excellent stability and retained its photocatalytic activity for three recycling cycles.

Liu *et al.* reported the preparation of Rh-PMOF-1 using Zr_6 clusters as metal nodes and a tetra carboxy-porphyrin metallated with Rh (RhTCPP) as linker (Fig. 49a).[232] In this case the porphyrin was already metallated before the construction of the PMOF. Under light irradiation Rh-PMOF-1 showed excellent catalytic activity towards CO_2 reduction, leading to the formation of formate ion with up to 99% selectivity and a rate of 78 μmol g^{-1} h^{-1} (Table 9, entry 10). The crystalline catalyst can be isolated from the reaction mixture by centrifugation and can be reused for 3 times without loss of activity. In this system, the Rh-porphyrin has a dual role, since it acts as antenna absorbing visible light and injecting electrons to the Zr_6 oxo-clusters, and also as a catalytic center carrying out the CO_2 reduction.

Chen *et al.* reported the preparation of ZrPP-1 PMOF where Zr_6 clusters were also used as metal nodes.[233] However, instead of the common tetra carboxy-porphyrins, polyphenolate-decorated porphyrin (THPP) was employed as linkers (Fig. 49b). These unusual PMOFs based on phenolic porphyrins were very robust in acidic media, and more impressively remain intact even upon immersion in saturated NaOH solution. Since photocatalysis is strongly associated with the metal inside the porphyrin core, for the construction of the PMOFs apart from the free base porphyrin a series of metallated analogues (with Zn, Cu, Fe and Co) were also employed as linkers, to study their effects on the catalytic properties. Upon light illumination, no noticeable CO evolution was observed for the non metallated ($ZrPP\text{-}1\text{-}H_2$) and the Zn metallated (ZrPP-1-Zn) PMOF. The corresponding PMOFs metallated with Cu and Fe displayed efficient photocatalytic activity for the CO_2 to CO reduction (Fig. 49b). The Co-substituted analogue (ZrPP-1-Co) exhibited the highest efficiency with a CO generation rate of 14 μmol g^{-1} h^{-1} and also a small amount of CH_4 (0.5 μmol g^{-1} h^{-1}), was detected in the gaseous and liquid phases (Table 9, entry 11). These catalysts exceptionally stable and can be recycled without appreciable loss of activity. Based on theoretical calculations they proposed the following catalytic mechanism: the uniformly distributed porphyrins absorb incident photons and transfer generated electrons to the Co^{2+} cations. Then successive reductive quenching steps, from Co^{2+} to Co^{+} and finally to Co^{0}, occur with the aid of TEOA as SED. The Co^{0} species can activate CO_2 (with structural transition from the linear to the bent) to form an excited adduct Co^{2+}–CO, which dissociates upon irradiation and liberates CO.

Qiu *et al.* were also used Zr_6 oxo-clusters as metal nodes for the preparation of the mixed-ligand MOF PCN-138 (Fig. 49c).[234] In this MOF two different carboxy-derivatives were employed as linkers, more specifically the free base tetra carboxy porphyrin (H_2TCPP) and the 4,4′,4″-(2,4,6-trimethylbenzene-1,3,5-

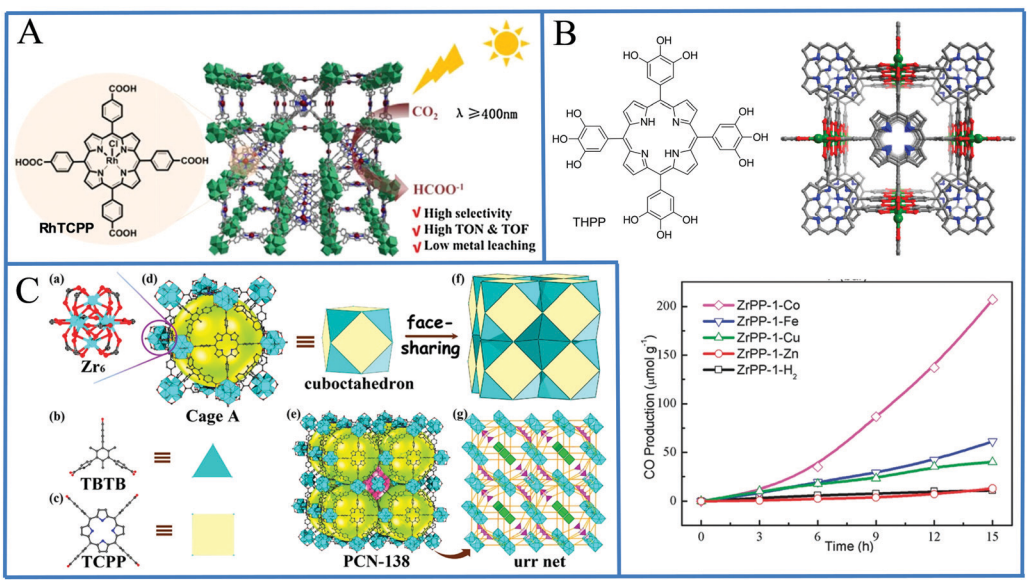

Fig. 49 (A) Chemical structure of RhTCPP and representation of catalytic behavior of Rh-PMOF-1. Reproduced from ref. 232, with permission from Elsevier, Copyright 2018. (B) Chemical structure of THPP, 3D view ZrPP-1 PMOF and time courses of CO evolution from CO_2 photoreduction with catalysts ZrPP-1-M under visible-light irradiation. Reproduced from ref. 233, with permission from John Wiley and Sons, Copyright 2018. (C) Structure of PCN-138. Reproduced from ref. 234, with permission from American Chemical Society, Copyright 2019.

triyl)tribenzoate (TBTB). The combination of these two ligands resulted in the formation of an unusual cuboctahedron Archimedean solid, which possess large cages facilitating the CO_2 adsorption. PCN-138 presented efficient photocatalytic activity toward CO_2 reduction in the presence of triisopropanolamine (TIPA) as SED, producing formate as the only product with a rate of 125 μmol g^{-1} h^{-1} (Table 9, entry 12). Recycling studies suggested that PCN-138 is stable and can be reused without an obvious decrease in the activity during four continuous runs. In this system, the porphyrins act as PS absorbing the irradiation and transferring photoelectrons to the Zr–oxo clusters, while the Zr metal centers act as catalysts enabling the reduction of CO_2 to $HCOO^-$.

Wang and co-workers reported the preparation of PCN-224(Cu) with the employment of copper metallated tetra carboxyporphyrins (CuTCPP) as linkers and Zr_6 clusters as metal nodes (Fig. 50a).[235] Under irradiation PCN-224(Cu) catalyzed the CO_2 reduction, producing CO and CH_4 with a rate of 3.72 and 1.36 μmol g^{-1} h^{-1}, respectively (Table 9, entry 13). Interestingly, the *in situ* integration of TiO_2 NPs resulted in the formation of a new material PCN-224(Cu)/TiO_2 that presented significantly improved catalytic efficiency and selectivity, producing CO with a rate of 37.21 μmol g^{-1} h^{-1} (Table 9, entry 14). The enhanced photocatalytic performance in the presence of TiO_2 NPs was attributed to the operation of a Z-scheme mechanism, which suppressed the unfavorable recombination of charge carriers. The same group synthesized a similar composite material CTU/TiO_2.[236] The only difference compared to PCN-224(Cu)/TiO_2 is the use of two different carboxy-linkers (CuTCPP and terephthalic acid (BDC)) instead of only one (CuTCPP). However, this modification did not improve the catalytic performance, since the CO production rate for CTU/TiO_2 was 31.32 μmol g^{-1} h^{-1} (Table 9, entry 15). Wu *et al.* reported the construction of PCN-221(Fe), using also Zr_6 metal nodes and iron metallated carboxy-porphyins as linkers.[237] PCN-221(Fe) exhibited low CO_2 reduction activity producing CO and CH_4 with a rate of 0.52 and 1.52 μmol g^{-1} h^{-1}, respectively (Table 9, entry 16). Noteworthy, the encapsulation of low-cost $CH_3NH_3PbI_3$ ($MAPbI_3$) perovskite QDs into the pores of PCN-221(Fe) by a sequential deposition route (Fig. 50b) significantly enhanced the photocatalytic performance. The novel composite material $MAPbI_3$@PCN-221(Fe) catalyzed the CO_2 reduction to CO and CH_4 with conversion rates of 14.16 and 6.24 μmol g^{-1} h^{-1}, respectively (Table 9, entry 17), using water as electron source. The close contact of QDs to the Fe catalytic sites, enables the photogenerated electrons to transfer rapidly form the QDs to the Fe catalytic sites and enhance the overall photocatalytic activity. Moreover, the composite photcatalyst $MAPbI_3$@PCN-221(Fe) displayed increased stability compared to the parent PCN-221(Fe). This was attributed to the competitive light absorption between perovskite QDs and PCN-221(Fe), which can decrease the photodegradation of PCN-221(Fe).

Choi *et al.* followed an alternative approach and combined the light harvesting properties of PMOFs with the catalytic performance of molecular reduction catalysts.[238] More specific, a PMOF was initially prepared with Zr_6 metal nodes and ZnTCPP porphyrin as linkers. Then the postmodification with a well know Re bipyridine catalyst resulted in the formation of

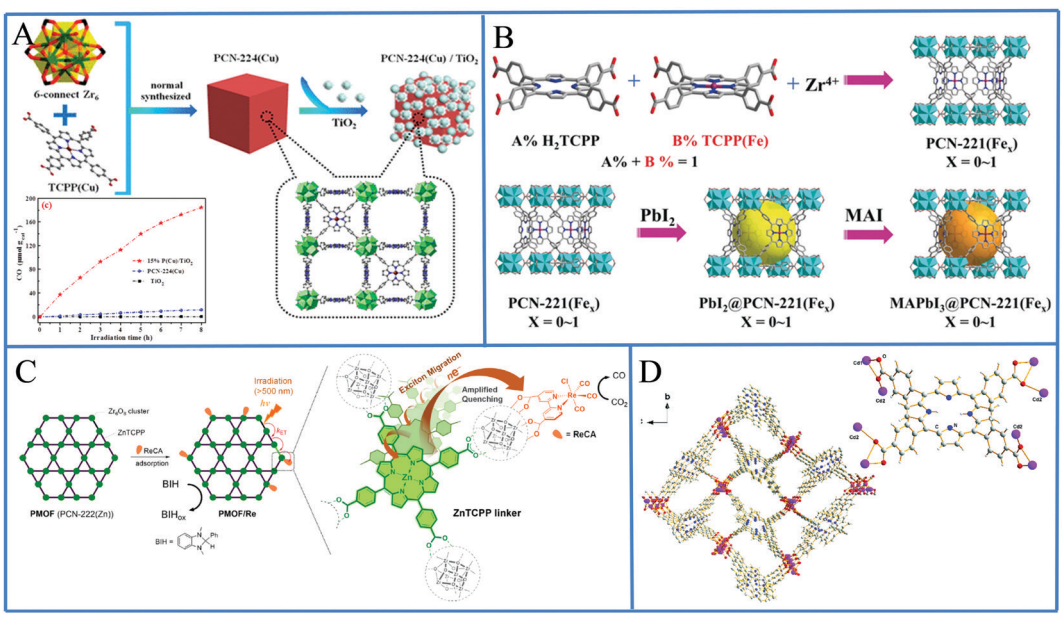

Fig. 50 (A) View of PCN-224(Cu), schematic representation of PCN-224(Cu)/TiO_2 composite material and CO evolution from these materials. Reproduced from ref. 235, with permission from American Chemical Society, Copyright 2019. (B) Preparation of composite material $MAPbI_3$@PCN-221(Fe) after encapsulation perovskite QDs into the pores of PCN-221(Fe). Reproduced from ref. 237, with permission from John Wiley and Sons, Copyright 2019. (C) Schematic representation of the PMOF/Re hybrid system for photocatalytic CO_2 reduction. Reproduced from ref. 238, with permission from American Chemical Society, Copyright 2021. (D) The coordination mode of the free base H_2TCPP linker and view of the PMOF 1 mesoporous material. Reproduced from ref. 239, with permission from Royal Society of Chemistry, Copyright 2019.

the hybrid photocatalyst PMOF/Re (Fig. 50c). The Re complex bears carboxylate anchoring groups and it was chemically anchored to the Zr oxo-clusters. PMOF/Re demonstrated high CO_2 to CO conversion activity achieving more than 2200 TONs, in the presence of BIH as SED and 3% trifluoroethanol (TFE) as additive (Table 9, entry 18). The obtained high CO selectivity (>99%) indicate that the catalysis occurs mainly at the anchored Re catalyst, rather than on the Zr_6 clusters, which produce mainly formate.[228] The high catalytic performance arises mainly from the efficient and rapid photoelectron transfer from the porphyrin linkers to the Re catalytic centers, mimicking the natural photosynthetic systems.

Apart from Zr other metals were also employed as metal nodes for the preparation of PMOFs. Sadeghi *et al.* reported the preparation of Al-PMOF with the application of Al^{3+} metal ions as metal nodes and the tetra carboxy-porphyrin (H_2TCPP) as linker.[240] During the formation process of this PMOF the porphyrin ring was also metallated with Aluminum. Al-PMOF employed as photocatalyst and CO_2 to formate reduction was observed with a rate of 165 μmol g^{-1} h^{-1}, in MeCN as solvent and TEOA as SED (Table 9, entry 19). Remarkably, the incorporation of amine-functionalized graphene (NH_2-rGO) into the Al-PMOF resulted in the formation of a new photocatalyst NH_2-rGO/Al-PMOF. The catalytic activity of this composite material was significantly improved, producing formate with a rate of 685 μmol g^{-1} h^{-1} (Table 9, entry 20). The same group reported the preparation of Co/PMOF using Co metal ions as metal nodes and tetra carboxy-porphyrin as organic linker.[241] Under visible-light irradiation and in the presence of TEOA as SED, Co/PMOF presented efficient CO_2 photoconversion to formate with a rate of 77 μmol g^{-1} h^{-1} (Table 9, entry 21). Co/PMOF reusability and stability were examined through recycling tests and there were no remarkable losses of photoactivity even after three cycles of photoreaction.

Li *et al.* used Cd^{2+} metal ions as metal nodes and in combination with the free base carboxy-porphyrin (H_2TCPP) they contracted PMOF 1 (Fig. 50d).[239] PMOF 1 in the presence of TEA as SED demonstrated a relative low CO_2 to CO catalytic activity with a conversion rate of 10 μmol g^{-1} h^{-1} (Table 9, entry 22). However, after the addition of $Ru(bpy)_3Cl_2$ as co-catalyst the efficiency of CO production was increased about 5-fold, reaching 56 μmol g^{-1} h^{-1} (Table 9, entry 23). The Ru complex was found to act not only as light absorber but also as a photocatalyst, increasing the photogenerated charge separation by eliminating the holes. The catalytic system presented moderate stability, since during the second cycle a reduction on the CO production rate was observed.

Wang and *et al.* used In^{3+} ions as metal nodes, H_2TCPP as linker and after the encapsulation of Fe^{3+} ions In–FeTCPP-MOF was obtained (Fig. 51a).[242] Under light irradiation In–FeTCPP-MOF presented efficient CO_2 to CO activity (144 μmol g^{-1} h^{-1}), in the presence of L-ascorbgyl palmitate (L-AP) as SED (Table 9, entry 24). In this system the MOF matrix provides the electrons to the iron catalytic centers, where the CO_2 reduction takes place. Moreover, In–FeTCPP-MOF can be recycled for three cycles of 24 h photocatalytic reactions without deactivation (Fig. 51a). The cobalt analogue (In–CoTCPP-MOF) was also prepared, though its catalytic performance was lower compared to the iron one.

One of the first reported MOFs used for CO_2 reduction is NH_2-MIL-125(Ti), which is composed of titanium oxo-clusters and 2-aminoterephthalic acid (NH_2BDC) as organic linker.[243] However, the CO_2 conversion efficiency of NH_2-MIL-125(Ti) is limited due to its weak electron transfer ability. To overcome this problem Chen *et al.* reported the preparation of a dual ligand Ti-based MOF (D-TiMOF), where Zn carboxy-porphyrin (ZnTCPP) and NH_2BDC share the coordination nodes of the Ti oxo-clusters.[244] The incorporation of the porphyrin unit enhanced

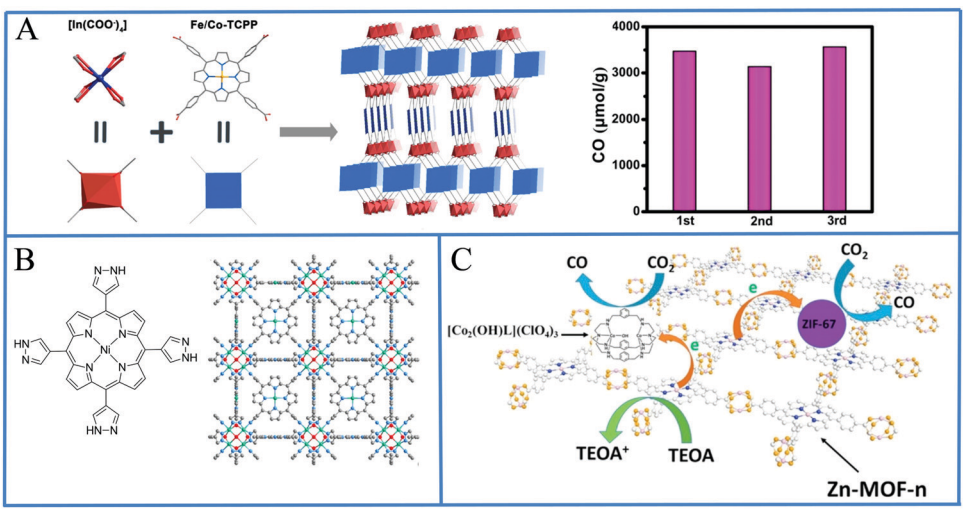

Fig. 51 (A) Synthesis and structure of the In–Fe/CoTCPP-MOFs and recycle experiments for CO production with In–Fe–TCPP–MOF. Reproduced from ref. 242, with permission from American Chemical Society, Copyright 2020. (B) Chemical structure of pyrazolyl-substituted porphyrin and crystal structure of PCN-601. Reproduced from ref. 246, with permission from American Chemical Society, Copyright 2020. (C) Schematic representation of 2D/Zn-MOF. Reproduced from ref. 248, with permission from Elsevier, Copyright 2018.

the optical absorption properties and significantly facilitated the electron transfer from the porphyrin to Ti clusters. D-TiMOF presented high CO_2 reduction activity, producing selectively CO with a rate of 59.55 μmol g^{-1} h^{-1} (Table 9, entry 25). In addition, photocatalytic recycling studies were performed and the obtained D-TiMOF showed stable catalytic performance for three cycles.

All the above photocatalytic CO_2 reductions studies with the PMOFs photocatalysts were performed in the liquid phase and require the addition of an organic compound as SED. The organic solvents are usually toxic and environmentally not friendly, and also the use of SEDs makes this approach economically unfavorable. An alternative method includes the realization of the CO_2 reduction studies in the gas phase, using water vapor as SED. Moreover, since the catalysis proceeds in the gaseous phase can take full advantage of the high gas uptake of MOFs. Sharifnia and co-workers prepared Zn/PMOF by using Zn as metal nodes and H_2TCPP as linkers.[245] The catalytic experiments were performed in the gas phase and Zn/PMOF catalyzed the CO_2 to CH_4 conversion with a rate of 8.7 μmol g^{-1} h^{-1} (Table 9, entry 26).

Cao co-workers reported the construction of PCN-601 which is composed of Ni_8 oxo-clusters and Ni metalloporphyrin ligands connected *via* pyrazolyl groups (Fig. 51b).[246] In contrast to the carboxylate groups, the pyrazolyl substituents of the porphyrin possess a larger π-conjugation system and cause higher π–d orbital overlaps with the Ni oxo-nodes. These features offer stronger coordination bonds and faster ligand-to-metal electron transfer for the reduction process at the reactive Ni clusters. The photocatalytic studies were also conducted in the gas phase with H_2O vapor as SED and PCN-601 demonstrated efficient and durable photocatalytic activity, converting CO_2 to CO and CH_4 with rates of 6 and 10.1 μmol g^{-1} h^{-1}, respectively (Table 9, entry 27). Additionally, PCN-601 exhibited fairly reproducible activity for 5 cycles in 50 h. Liu and co-workers also performed photocatalytic CO_2 reduction studies in gas phase using H_2O vapor as SED.[247] However, instead of PMOF material they examined two porphyrin precursors (CoTCPP and NiTCPP) that can be used of the preparation of PMOFs. CoTCPP showed better CO_2 to CO conversion activity (0.4 μmol g^{-1} h^{-1}) compared to NiTCPP (0.24 μmol g^{-1} h^{-1}), due to the higher activity and adsorption ability of cobalt metal sites. This work can provide guidance for the synthesis of porphyrin-based MOF.

In general, the efficiency of bulk PMOFs is limited, mainly as a result of the low optical absorption efficiency of the photoactive units embedded in MOF matrices and the fast charge recombination of the photogenerated electron–hole pairs. In addition, adsorption of substrates and desorption of products in micropores show lower mass transport rates than on surfaces. An attractive approach to address these challenges is the development of ultrathin two dimensional (2D) MOF nanosheets. Sun and co-workers reported the preparation of ultrathin 2D PMOF nanosheets (2D/Zn-MOF) using Zn ions as metal nodes and ZnTCPP as linker (Fig. 51c).[248] As control the corresponding 3D bulk MOF (3D/Zn-MOF) was also prepared. Both PMOFs were applied as PS with a zeolitic imidazolate framework (ZIF-67) as catalyst for the CO_2 photoreduction. 2D/Zn-MOF presented higher photocatalytic activity and selectivity for CO_2 to CO reduction (TON_{CO} = 117.8, TON_{H_2} = 11.6, and $selectivity_{CO}$ = 91.0%) compared to 3D/Zn-MOF (TON_{CO} = 63.6, TON_{H_2} = 7.5, and $selectivity_{CO}$ = 89.5%) (Table 9, entries 28 and 29). The enhanced performance of 2D/Zn-MOF arises from the improved CO_2 adsorption capacity and charge transport capability, as well as the longer lifetime of the electron–hole pairs. In an effort to replace ZIF-67 with a molecular catalyst, a highly efficient dinuclear cobalt complex $[Co_2(OH)L](ClO_4)_3$ (L = $N[(CH_2)_2NHCH_2(m\text{-}C_6H_4)CH_2NH(CH_2)]_3N$)[249] ($Co_2$) was used as catalyst with 2D/Zn-MOF as PS (Fig. 51c).[248] However, under the same experimental conditions this combination presented lower catalytic activity (TON_{CO} = 68.7, TON_{H_2} = 15.6, and $selectivity_{CO}$ = 81.5%).

Chen *et al.* prepared thin porphyrin paddle-wheel framework nanosheets (PPF-3) by the coordination of Co metal nodes with the free base carboxy-porphyrin (H_2TCPP), following a PVP-assisted solvothermal synthetic route.[250] PVP molecules were used as structural direction agents to restrain growth along the c-axis, leading to the formation of sheet-like structures. To further improve the light absorption ability of PPF-3, Au nanoparticles (Au NPs) were successfully loaded on the surface of PPF-3 nanosheets by electrostatic interactions. Photocatalytic studies showed than CO_2 was reduced to formate as the sole product, with a production rate of 42.7 μmol g^{-1} h^{-1} (Table 9, entry 30). During the catalysis, Au NPs serve mainly as light-harvesting antennas, injecting photoelectrons to the Co catalytic centers (Fig. 52a). Moreover, when they used thicker nanosheets or PPF-3 without Au NPs the catalytic performance was significantly reduced. Computational studies were also performed to study the catalytic properties of 2D PMOs, using density functional theory (DFT) calculations.[251] Cobalt porphyrin (CoTCPP) was selected as linker, while Co, Zn and Zr oxo-clusters were tested as metal nodes. The computational results demonstrated

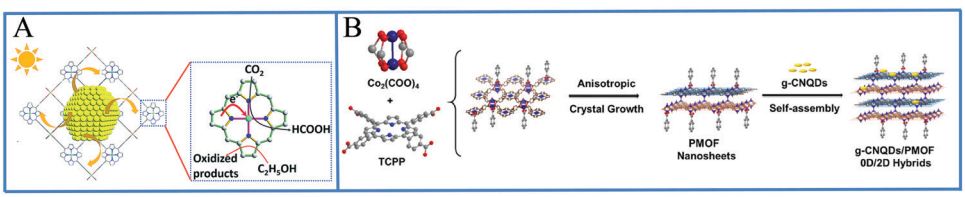

Fig. 52 (A) Proposed mechanism for plasmon-enhanced photocatalytic activity of PPF-3 towards CO_2 reduction. Reproduced from ref. 250, with permission from Royal Society of Chemistry, Copyright 2019. (B) Schematic illustration of the preparation of g-CNQDs/PMOF hybrids. Reproduced from ref. 252, with permission from American Chemical Society, Copyright 2019.

that the PMOF with the Co oxo-cluster (Co-PMOF) is the most promising material for the CO_2 to CH_4 reduction, due to the collaborative contribution of the Co oxo-cluster and the cobalt porphyrin during the catalysis.

Zheng *et al.* reported a novel hybrid material (g-CNQDs/PMOF) by coordinating zero-dimensional carbon nitride quantum dots (g-CNQDs) with 2D ultrathin porphyrin MOF.[252] The thickness of the 2D-PMOF is in the range of 1.7–4.6 nm (equal to 4–10 coordination layers) and contains Co oxo-clusters connected together by CoTCPP linkers. g-CNQDs were then tightly adsorbed on the PMOF through hydrophobic and π–π stacking interactions (Fig. 52b). The hybrid g-CNQDs/PMOF presented improved catalytic activity compared to the unmodified PMOF, producing CO and CH_4 with evolution rates of 16.1 and 6.86 μmol g^{-1} h^{-1}, respectively (Table 9, entry 31). In this system g-CNQDs provide photo-generated electrons to the Co catalytic sites, enhancing not only the catalytic activity for CO_2 reduction but also the selectivity for CH_4 production.

3.2.2 Covalent–organic frameworks (COFs) for CO_2 reduction. Another promising class of porous crystalline materials for the CO_2 photoreduction is the covalent organic frameworks (COFs). These organic polymer networks are receiving enormous attention in photocatalysis because of their unique properties such as: high stability, easy preparation and modification, adjustable periodical structures with atomic precision, large surface area, permanent porosity, and extremely low density. Liu *et al.* prepared an ultrathin 2D imine based COF (COF-367-Co) through the covalent connection of cobalt tetra amino-porphyrin (CoTAPP) with 4,4′-biphenyldialdehyde (BPDA) (Fig. 53a).[253] Into the reaction system excess amount of 2,4,6-trimethylbenzaldehyde (TBA) was added to hinder the axial π–π stacking into bulk COF material, ensuring the formation of ultrathin 2D COF nanosheets with few-layer number. The catalytic activity of COF-367-Co was examined in aqueous solution with $[Ru(bpy)_3]Cl_2$ as PS and AA as SED. CO was detected as the main product with a production rate of 10 162 μmol g^{-1} h^{-1} (accounting for a TON of 20.2), while the selectivity was 78% (Table 10, entry 1).

Lan and co-workers synthesized a series of crystalline 2D rigid porphyrin-tetrathiafulvalene COFs (TTCOF-M, M = 2H, Zn, Ni, Cu) by Schiff-base condensation between the corresponding tetra amino-porphyrin (TAPP-M, M = 2H, Zn, Ni, Cu) and 2,3,6,7-tetra (4-formylphenyl)-tetrathiafulvalene (TTF) by solvothermal method (Fig. 53b).[254] The covalent coupling between porphyrins and TTF within COF enables the efficient electron transfer from the TTF to the porphyrin moiety. The photocatalytic studies of all TTCOF-M were conducted in aqueous solution without additional PS and SED. Among them, TTCOF-Zn exhibited the highest CO production rate of 2.1 μmol g^{-1} h^{-1} and selectivity (*ca.* 100%) (Table 10, entry 2). At the same time, the formation of O_2 was also detected, since the photo-generated holes in TTF are capable of oxidizing H_2O, which serves as SED.

Wang *et al.* following an already published procedure prepared COF-366[255] and examined its activity towards CO_2 reduction.[256] The synthesis COF-366 involves the imine-bond formation between tetra amino-porphyrin (H_2TAPP) and terephthaldehyde (TPA) (Fig. 54a). COF-366 has good carrier mobility and visible light absorption capacity, but its photocatalytic performance was low with a CO_2 to CO conversion rate of 3.9 μmol g^{-1} h^{-1} (Table 10, entry 3). In an effort to increase the catalytic efficiency they replaced TPA with 2,5-dibromoterephthalaldehyde (BDB), resulting in the formation of TAPBB-COF (Fig. 54b).[256] The presence of bromine functional groups adjusted the valence band of TAPBB-COF to a more suitable position, resulting in an improved catalytic performance by a factor of 3. TAPBB-COF selectively reduced CO_2 with H_2O as

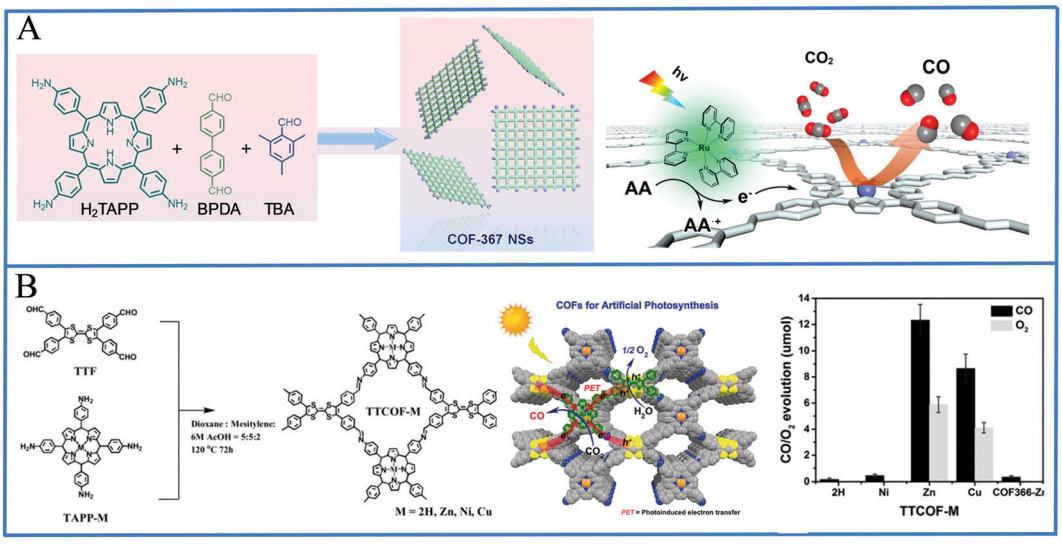

Fig. 53 (A) Schematic illustration of synthesis of the COF-367 NSs and proposed mechanism for the photocatalytic conversion of CO_2 into CO over COF-367-Co NSs under visible-light irradiation with $[Ru(bpy)_3]Cl_2$ as the PS and AA as the electron donor. Reproduced from ref. 253, with permission from American Chemical Society, Copyright 2019. (B) Schematic representation of the synthesis of TTCOF-M through the condensation of TTF and TAPP-M, structure of TTCOF-M and catalytic performance of TTCOF-M. Reproduced from ref. 254, with permission from John Wiley and Sons, Copyright 2019.

Table 10 Photocatalytic performance of porphyrin COFs for CO_2 reduction

Entry	COF name	Porphyrin	Organic linker	Cocatalyst or additives	SED	Solvent	Light source	Major products rate	Ref.
1	COF-367-Co	CoTAPP	BPDA	$Ru(bpy)_3Cl_2$	AA, 0.1 M	H_2O	Xenon lamp, 300 W, $\lambda > 420$ nm	CO, 10 162 μmol g^{-1} h^{-1} or 20.2 TON	253
2	TTCOF-Zn	ZnTAPP	TTF	—	—	H_2O	Xenon lamp, 300 W, $\lambda > 420$ nm	CO, 2.1 μmol g^{-1} h^{-1}	254
3	COF-366	H_2TAPP	TPA	—	—	H_2O	Xenon lamp, $\lambda >$ 430 nm	CO, 3.9 μmol g^{-1} h^{-1}	256
4	TAPBB-COF	H_2TAPP	BDB	—	—	H_2O	Xenon lamp, $\lambda >$ 430 nm	CO, 12.4 μmol g^{-1} h^{-1}	256
5	NiP-TPE-COF	NiTAPP	TPE	$Ru(bpy)_3Cl_2$	TEOA, 16.7%	CH_3CN/H_2O (3/1)	Xenon lamp, 300 W, $\lambda > 400$ nm	CO, 525 μmol g^{-1} h^{-1}	257
6	CoP-TPE-COF	CoTAPP	TPE	$Ru(bpy)_3Cl_2$	TEOA, 16.7%	CH_3CN/H_2O (3/1)	Xenon lamp, 300 W, $\lambda > 400$ nm	CO, 2414 μmol g^{-1} h^{-1}	257
7	PD-COF-23-Ni	NiTAPP	DPP-CHO	—	TEOA, 9.1%	CH_3CN/H_2O (3/2)	Xenon lamp, 300 W	CO, 40 μmol g^{-1} h^{-1}	258
8	PD-COF-23	H_2TAPP	DPP-CHO	—	TEOA, 9.1%	CH_3CN/H_2O (3/2)	Xenon lamp, 300 W	CO, 20.9 μmol g^{-1} h^{-1}	258
9	COF-367-Co^{III}	Co^{III}TAPP	BPDA	—	TEA, 18%	CH_3CN	Xenon lamp, 300 W, $\lambda > 380$ nm	$HCOO^-$, 93 μmol g^{-1} h^{-1} CO, 5.5 μmol g^{-1} h^{-1} CH_4, 10.1 μmol g^{-1} h^{-1}	259
10	COF-367-Co^{II}	Co^{II}TAPP	BPDA	—	TEA, 18%	CH_3CN	Xenon lamp, 300 W, $\lambda > 380$ nm	$HCOO^-$, 48.6 μmol g^{-1} h^{-1} CO, 16.5 μmol g^{-1} h^{-1} CH_4, 12.8 μmol g^{-1} h^{-1}	259
11	Ni-PCD@TD-COF	NiTAPP	TP and DBT	$Ru(bpy)_3Cl_2$	TEOA, 20%	CH_3CN/H_2O (3/1)	Xenon lamp, $\lambda >$ 420 nm	CO, 478 μmol g^{-1} h^{-1}	260
12	α-Fe_2O_3@Por-CTF	H_2TBPP-CHO	TPh	$Ru(bpy)_3Cl_2$ and α-Fe_2O_3	TEOA, 20%	DMF	Visible light	CO, 320 μmol g^{-1} h^{-1}	261
13	COP-P	H_2TBPP	—	—	H_2O	—	Xenon lamp, 300 W	CO, 4.58 μmol g^{-1} h^{-1}	262
14	COP-P/TiO_2	H_2TBPP	—	TiO_2 NPs	H_2O		Xenon lamp, 300 W	CO, 5.7 μmol g^{-1} h^{-1} CH_4, 0.26 μmol g^{-1} h^{-1}	263

a SED, and CO was evolved with a rate of 12.4 μmol g^{-1} h^{-1} (Table 10, entry 4).

Lv *et al.* reported the synthesis of two metalloporphyrin based COFs (NiP-TPE-COF and CoP-TPE-COF) using 4,4′,4″,4‴-(ethane-1,1,2,2-tetrayl) tetrabenzaldehyde (TPE) and the corresponding tetra amino-porphyrin (MTAPP, M = Ni, Co) (Fig. 54c).[257] The catalytic studies were conducted in the presence of $[Ru(bpy)_3]Cl_2$ as PS and TEOA as SED. NiP-TPE-COF

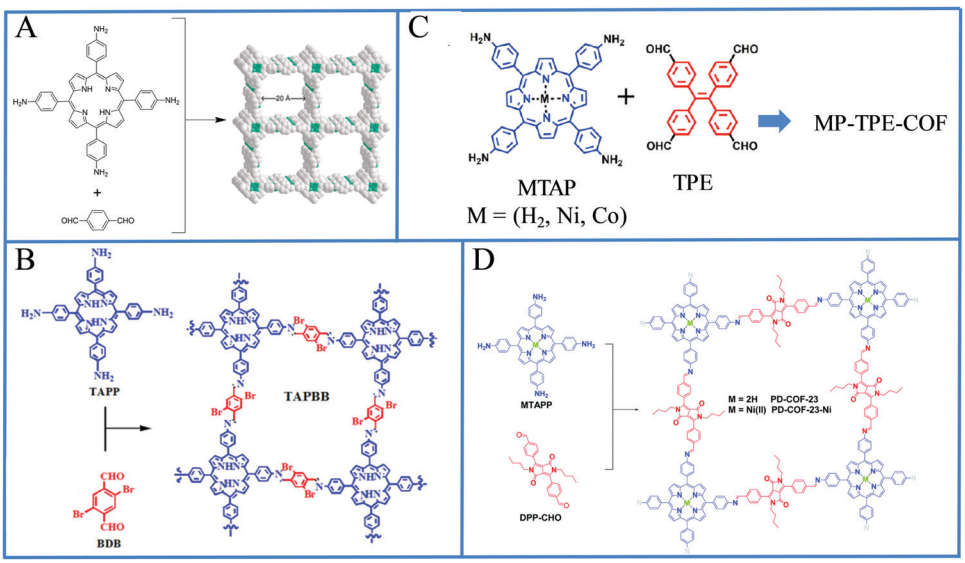

Fig. 54 (A) Preparation of COF-366 through condensation reaction between H_2TAPP and terephthaldehyde. Reproduced from ref. 256, with permission from John Wiley and Sons, Copyright 2020. (B) Synthetic procedure of TAPBB-COF. Reproduced from ref. 256, with permission from John Wiley and Sons, Copyright 2020. (C) Schematic depiction for the synthesis of MP-TPE-COF, (D) synthetic route for PD-COF-23 and PD-COF-23-Ni. Reproduced from ref. 258, with permission from Royal Society of Chemistry, Copyright 2020.

exhibited efficient CO evolution rate of 525 μmol g^{-1} h^{-1} (Table 10, entry 5) and 93% selectivity. On the other hand, CoP-TPE-COF provided higher catalytic activity (2414 μmol g^{-1} h^{-1}, Table 10, entry 6) but with significantly lower selectivity (61%). The high catalytic activity can be attributed to the rapid transfer of photogenerated electrons, while the selectivity is directly related to the competitive reaction of the protons.

Xu *et al.* prepared two donor–acceptor 2D COFs, PD-COF-23 and PD-COF-23-Ni from acid-catalyzed Schiff-base reaction between the free base (H_2TAPP) or the Ni metallated (NiTAPP) porphyrin and a di-formyl substituted diketopyrrolopyrrole derivative (DPP-CHO) (Fig. 54d).[258] PD-COF-23-Ni showed higher CO production efficiency of 40 μmol g^{-1} h^{-1} (Table 10, entry 7) than PD-COF-23 (20.9 μmol g^{-1} h^{-1}, Table 10, entry 8), in the absence of any additional PS. The selectivity of both COFs is high (99%) and only a trace amount of CH_4 was detected. During the catalysis electron transfer from the porphyrin moiety to DPP unit takes place and subsequently, CO_2 is reduced to CO by the two electrons accumulated near DPP. Meanwhile, when the porphyrin is metallated the Ni center also catalyzes the CO_2 reduction.

Gong *et al.* constructed COF-367-Co from the condensation of cobalt metallated porphyrin CoTAPP with 4,4′-biphenyldicarboxaldehyde (BPDA) (Fig. 55a).[259] In this COF the spin state of cobalt can be manipulated by simply changing the oxidation state of Co centered in the porphyrin ring. The photocatalytic CO_2 reduction studies demonstrated that COF-367-Co^{III}(Co^{III}, S = 0) exhibits enhanced activity and remarkably higher selectivity to formate than COF-367-Co^{II} (Co^{II}, S = 1/2) (Table 10, entries 9 and 10). COF-367-Co^{III} possesses higher charge separation efficiency and lower energy barrier for the $HCOO^-$ formation than COF-367-Co^{II} and these accounts for the improved activity of the former. This work provides a significant guideline to regulate the catalytic performance by rationally manipulating the spin state of metal centers.

Wang and co-workers developed a novel material (Ni-PCD@TD-COF), where inside the pores of a COF nanostructure (TD-COF) they incorporated metalloporphyrin-based carbon dots (Ni-PCD) (Fig. 55b).[260] The COF scaffold prepared with the imine-bond formation between 2,4,6-triformylphloroglucinol (TP) and 2,6-diaminobenzo[1,2-*d*:4,5-*d*′]bisthiazole (DBT). Then NiTAPP porphyrin was introduced and after selective pyrolysis of glucose Ni-PCD@TD-COF was obtained. The photocatalytic activity of Ni-PCD@TD-COF was evaluated in the presence of $[Ru(bpy)_3]Cl_2$ as PS and TEOA as SED. Efficient CO evolution was observed with a rate of 478 μmol g^{-1} h^{-1} (Table 10, entry 11) and high selectivity (98%). When Ni metal was replaced with Co the catalytic activity increased, while the selectivity decreased to only 49%. Notably, the photocatalytic system is also effective for low concentration of CO_2, simulating flue gas from the power plant.

Jin and co-workers fabricated a porphyrin-based covalent triazine framework (Por-CTF) decorated with α-Fe_2O_3 nanoparticles, denoted as α-Fe_2O_3@Por-CTF.[261] The covalent triazine framework Por-CTF was prepared *via* polycondensation of terephthalamidine (TPh) with tetra formyl-substituted porphyrin derivative (H_2TBP-CHO) and then the *in situ* growth of a-Fe_2O_3 NPs resulted in the formation of α-Fe_2O_3@Por-CTF

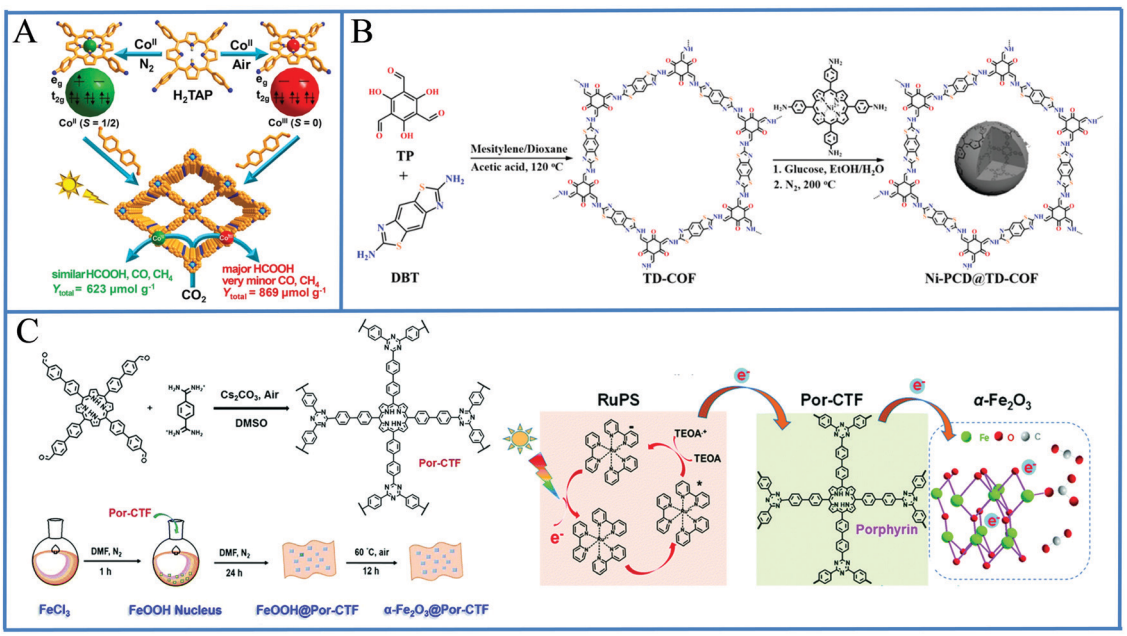

Fig. 55 (A) Rational fabrication of COF-367-Co featuring different spin states of Co ions toward photocatalytic CO_2 reduction. Reproduced from ref. 259, with permission from American Chemical Society, Copyright 2020. (B) Schematic illustration for the synthesis of TD-COF and Ni-PCD@TD-COF. Reproduced from ref. 260, with permission from John Wiley and Sons, Copyright 2020. (C) Synthetic route for the Por-CTF, fabrication of the α-Fe_2O_3@Por-CTF hybrid photocatalyst and proposed electron transfer mechanism for the photochemical CO_2 reduction. Reproduced from ref. 261, with permission from Royal Society of Chemistry, Copyright 2019.

(Fig. 55c). Under irradiation and in the presence of $[Ru(bpy)_3]Cl_2$ as PS and TEOA as SED, CO evolution was observed with a ratio of 320 μmol g^{-1} h^{-1} (Table 10, entry 12). In this ternary system, the porous framework serves as electron relay facilitator, enabling the electron transfer from the Ru PS to the Fe catalytic sites, and reducing the photocurrent carrier recombination.

Another promising method for the development of photocatalytic CO_2 reduction systems is the use of microporous covalent organic polymers (COPs) as photocatalysts. Zhang *et al.* prepared a porphyrin based COP (COP-P) based on tetrabiphenylporphyrin (H_2TBPP) through the Scholl reaction.[262] The catalytic performance of COP-P was evaluated in the presence of H_2O as SED, and CO was produced with a rate of 1.23 μmol g^{-1} h^{-1}. Interestingly, hollowrization and post-sulfonation modulated the photocatalytic performance of COP-P, giving 4.8 times enhanced production of CO (7.54 μmol g^{-1} h^{-1}, Table 10, entry 13). Post-sulfonation improved the separation and transfer ability of photogenerated carriers, while hollowrization increased the surface area of COP-P polymer and thereby enhanced CO_2 uptake. The same group in an effort to increase the catalytic performance reported the preparation of a hybrid material COP-P/TiO_2, where TiO_2 NPs were composited with the COP-P polymer.[263] The formation of COP-P/TiO_2 involved the hydrothermal *in situ* synthesis of TiO_2 in the presence of COP-P polymer template. The COP-P/TiO_2 composite material presented improved photocatalytic activity (5.7 μmol g^{-1} h^{-1}) relative to the initial COP-P or with the material fabricated through simple physical mixing of COP-P with TiO_2 NPs. In this system CH_4 was also detected but with much smaller rate (0.26 μmol g^{-1} h^{-1}, Table 10, entry 14).

3.2.3 Metal oxides combined with porphyrins for CO_2 reduction. Metal oxides, as traditional photocatalysts, have been widely used in many photochemical and photophysical fields. Among them, TiO_2 is one of the most widely used photocatalyst due to its low toxicity, high stability, and low cost. However, the poor absorbance of visible light and the low separation efficiency of photogenerated carriers limit its overall photocatalytic efficiency. A promising approach to overcome these problems is the sensitization of TiO_2 with organic dyes. Peng and co-workers reported a catalytic system where an asymmetric zinc porphyrin (ZnPy, Fig. 56) was used to sensitize nanosized TiO_2.[264] ZnPy contains three pyridyl substituents and one carboxy-group which serve as an anchoring group. After visible light irradiation, the ZnPy-TiO_2 composite material catalyzed the CO_2 to CO and CH_4 conversion, in a gaseous system using H_2O vapor as SED. The maximum efficiency was observed with 1% ZnPy loading on TiO_2, producing CO and CH_4 with rate of 8.07 and 1.01 μmol g^{-1} h^{-1}, respectively (Table 11, entry 1).

Mele *et al.* also prepared two novel composite materials by loading polycrystalline TiO_2 powder with lipophilic copper phthalocyanine or porphyrin (CuPc and CuPp, Fig. 56).[265] The photocatalytic studies demonstrated that the presence of the sensitizers is beneficial, and enables the reduction of CO_2 in aqueous suspension, affording formic acid. CuPc presented higher catalytic activity compared to CuPp, producing formate with a rate of 26 μmol g^{-1} h^{-1}.

Wang and co-workers utilized a Zn porphyrin–Ru polypyridyl complex (ZnPyP–RuBiPy, Fig. 56) to sensitize TiO_2 nanotubes.[266] The ZnPyP–RuBiPy derivative consists of one porphyrin unit in the center, which is surrounded by four peripheral ruthenium

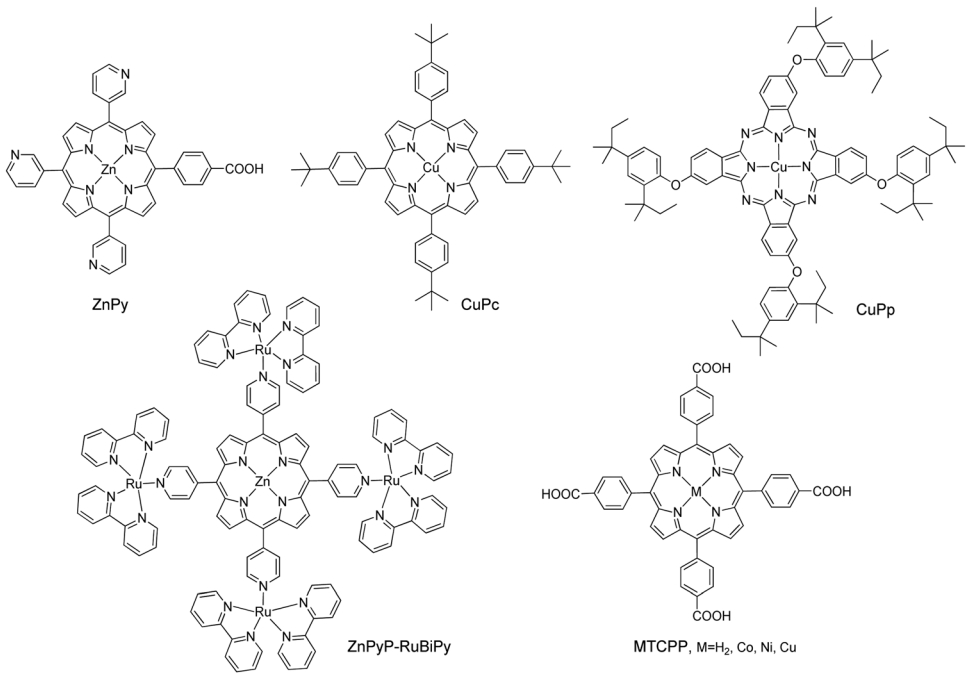

Fig. 56 Chemical structure of the porphyrin derivatives that were employed with TiO_2 for CO_2 photoreduction.

polypyridyl molecules. The ZnPyP–RuBiPy/TiO_2 composite material demonstrated efficient catalytic activity, producing methanol as the only product with a rate of 68 μmol g^{-1} h^{-1} (Table 11, entry 2).

Wang *et al.* prepared a series of tetra carboxy-porphyrins (MTCPP, M = H_2, Co, Ni, Cu) (Fig. 56) for the sensitization of commercial P25 TiO_2.[267] In all the cases the photocatalytic CO_2 reduction activity of the assembled MTCPP/TiO_2 nanocomposites was significantly improved compared to the bare P25. The enhanced catalytic activity of the composite material was attributed to a strengthened capability in light absorption and enhanced separation efficiency of photo-induced electrons and holes. In addition, the incorporated metal atoms inside the porphyrin ring also play an important role in the adsorption and activation of CO_2 molecules. Among the various porphyrin derivatives, CuTCPP presented the highest performance producing CO and CH_4 with rates of 13.6 and 1.0 μmol g^{-1} h^{-1}, respectively (Table 11, entry 3). The other porphyrin complexes showed lower activity with the order NiTCPP > CoTCPP > H_2TCPP.

Following the same approach, Wang and co-workers anchored CuTCPP to $P25_m$ TiO_2 NPs.[268] Initially, the commercial P25 TiO_2 were hydrothermally treated, resulting in the formation of $P25_m$, which possess an enlarged specific surface area and increased number of hydroxyl groups on the surface. The influence of CuTCPP content on the photocatalytic activity was investigated and the highest catalytic performance was observed when the hydrothermally treated $P25_m$ were sensitized by 0.5% CuTCPP, producing CH_4 and CO with rates of 19.39 and 2.68 μmol g^{-1} h^{-1}, respectively (Table 11, entry 4). On the other hand, the non-sensitized $P25_m$ TiO_2 presented significantly lower performance (0.42 μmol g^{-1} h^{-1} CH_4 and 1.7 μmol g^{-1} h^{-1} CO), under the same conditions. Noteworthy in the composite material the major product of the CO_2 reduction was CH_4.

Gao *et al.* utilized the free base tetra carboxy porphyrin (H_2TCPP) for the sensitization of TiO_2 nanosheets, following a simple self-assemble approach (Fig. 57a).[269] Ultrathin TiO_2 nanosheets were selected in this work, since they present higher catalytic activity compared to the corresponding TiO_2 nanotubes or nanoparticles. The composite H_2TCPP/TiO_2 material demonstrated high catalytic activity and after visible irradiation the formation of both CO and CH_4 was observed. The amount of H_2TCPP in H_2TCPP/TiO_2 composites had significant influence on the photoreduction activity (Fig. 57a). The TiO_2 nanosheets with 11.5% H_2TCPP showed the best catalytic performance with a CO production rate of 141.74 μmol g^{-1} h^{-1} (Table 11, entry 5), which is more than 37 times higher compared to the pristine TiO_2 nanosheets. In this system, H_2TCPP works as the light-harvesting unit to generate light-induced photoelectrons, while the connection between the H_2TCPP and TiO_2 facilitates the electron injection to the CB of TiO_2 as well as inhibiting the recombination of electron–hole pairs. Then the highly active facets of TiO_2 nanosheets serve as catalytic centers and efficiently convert the CO_2 into CO and CH_4.

Apart from TiO_2 other materials were also sensitized with porphyrin chromophores for the development of efficient CO_2 photoreduction systems. Viswanathan and co-workers explored the photo catalytic activity of Lanthanum modified sodium tantalate ($Na_{(1-x)}La_xTaO_{(3+x)}$), in conjunction with Co tetra phenylporphyrin (CoTPP) as sensitizer (Fig. 57b).[270] The composite material after UV-visible irradiation catalyzed the efficient CO_2 reduction, producing methanol and ethanol as the main products with rates of 36.2 and 21.4 μmol g^{-1} h^{-1}, respectively (Table 11, entry 6). Sensitized tantalate absorbs both visible and UV irradiation, resulting in the direct injection of photo electrons to the conduction band of active $Na_{(1-x)}La_xTaO_{(3+x)}$ surface, where the catalytic CO_2 conversion takes place. The presence of CoTPP besides sensitization also hinders charge carrier recombination.

Dye-sensitized photocatalysis (DSP) is another emerging approach for the development of efficient CO_2 reduction systems. In DSP the PS and the catalyst are anchored onto the surface of a semiconductor such as TiO_2, which serves as scaffold and electron mediator. This approach has received much attention due to the easy fabrication, facile tunability, the improvement of stability, and no limitation of solvent selection based on the immobilization of components on TiO_2 particles. Won *et al.* prepared a series of Zn–porphyrin dyes and anchored onto a TiO_2 along with the well-studied Ru bipyridine catalyst to construct a dye-sensitized photocatalytic system (DSP) (Fig. 57c).[271] For the porphyrin

Table 11 Photocatalytic performance of metal oxides combined with porphyrins for CO_2 reduction

Entry	Metal oxide	Porphyrin	Cocatalyst or additives	SED	Solvent	Light source	Major products rate	Ref.
1	TiO_2 (powder)	ZnPy	—	H_2O	Gas phase	Xenon lamp, 300 W	CO, 8.07 μmol g^{-1} h^{-1} CH_4, 1.01 μmol g^{-1} h^{-1}	264
2	TiO_2 (powder)	ZnPyP–RuBiPy	—	Na_2SO_3	H_2O	Xenon lamp, 500 W, $\lambda > 400$ nm	CH_3OH, 68 μmol g^{-1} h^{-1}	266
3	TiO_2 (P25)	CuTCPP	—	H_2O	Gas phase	Xenon lamp, 300 W	CO, 13.6 μmol g^{-1} h^{-1} CH_4, 1.0 μmol g^{-1} h^{-1}	267
4	TiO_2 ($P25_m$)	CuTCPP	—	H_2O	Gas phase	Xenon lamp, 300 W	CO, 2.68 μmol g^{-1} h^{-1} CH_4, 19.39 μmol g^{-1} h^{-1}	268
5	TiO_2 (NSs)	H_2TCPP	—	TEOA, 20%	CH_3CN	Xenon lamp, 300 W, $\lambda > 420$ nm	CO, 141.74 μmol g^{-1} h^{-1} CH_4, 2.97 μmol g^{-1} h^{-1}	269
6	$Na_{(1-x)}La_xTaO_{(3+x)}$	CoTPP	—	H_2O	H_2O	Mercury lamp, 77 W	MeOH, 36.2 μmol g^{-1} h^{-1} EtOH, 21.4 μmol g^{-1} h^{-1}	270
7	TiO_2	ZnP_{CA}	Re catalyst	BIH, 0.1 M	DMF	Xenon lamp, 450 W, $\lambda > 550$ nm	CO, 1028 TON	271
8	TiO_2	ZnP_{CNPA}	Re catalyst	BIH, 0.1 M	DMF	Xenon lamp, 450 W, $\lambda > 550$ nm	CO, 820 TON	271
9	TiO_2	ZnP	Re catalyst	BIH, 0.1 M and TEOA	DMF	LED lamp, 450 W, $\lambda > 500$ nm	CO, 2488 TON	272

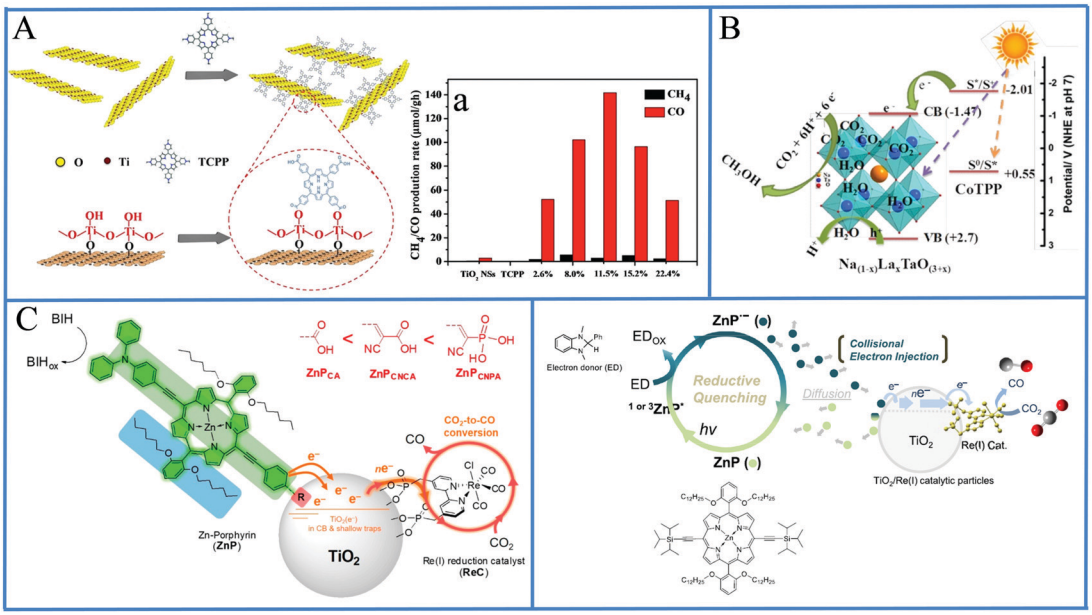

Fig. 57 (A) Schematic illustration of the synthesis of H_2TCPP/TiO_2 nanosheets and photocatalytic CO_2 reduction performance over different porphyrin loadings. Reproduced from ref. 269, with permission from Elsevier, Copyright 2019. (B) Photocatalytic reduction of CO_2 on CoTPP sensitized $Na_{(1-x)}La_xTaO_{(3+x)}$. Reproduced from ref. 270, with permission from Elsevier, Copyright 2016. (C) Sequential electron transfer process in a DSP hybrid system from zinc porphyrin PS to TiO_2 (molecular immobilizer and electron mediator) and finally to Re reduction catalyst. Reproduced from ref. 271, with permission from American Chemical Society, Copyright 2018. (D) Schematic description of the overall reduction processes with ZnP porphyin. Reproduced from ref. 272, with permission from American Chemical Society, Copyright 2020.

chromophores three different anchoring groups (–COOH, –CNCOOH, $-CNPO_3H_2$) were utilized to examine their influence on the CO_2 catalytic activity, while the Re complex was immobilized onto the TiO_2 surface through two methyl phosphonic acid groups. The porphyrin with the –COOH anchoring group (ZnP_{CA}) showed the best activity producing CO with a TON of 1028 after 42 h of irradiation (Table 11, entry 7). However, the porphyrin with the $-CNPO_3H_2$ group (ZnP_{CNPA}) revealed the highest stability, showing no leveling-off tendency for >90 h giving a TON of 820 (Table 11, entry 8). The high performance of ZnP_{CA} can be attributed to the more efficient electron injection due to the favorable electronic delocalization of the carboxylic acid. On the other hand, in the ZnP_{CNPA} derivative the phosphonic acid group presents the stronger binding affinity and suppresses desorption from TiO_2. The same group in a subsequent report utilized a Zn porphyrin (ZnP, Fig. 57d) without any anchoring groups in the analogous TiO_2/Ru-catalyst system.[272] ZnP possess bulky alkyl groups, which significantly lowers the possibility of an electron injection pathway through chemical or physical adsorption of the porphyrin onto the TiO_2 surface. In this system, without any dye immobilization on the TiO_2 surface, the dissolved porphyrin can effectively transport its excited-state electrons to the heterogeneous catalytic TiO_2/Re particles *via* a collisional electron transfer pathway. Interestingly, this binary hybrid system exhibited more efficient photochemical CO_2-to-CO conversion activity (2488 TON after 46 h, Table 11, entry 9) compared to the corresponding ternary system. The enhanced CO_2-to-CO conversion efficiency was attributed to the better light-absorbing ability of the porphyrin is solution compared to the immobilized form onto the TiO_2.

3.2.4 Nanomaterials and porphyrins for CO_2 reduction. Another promising approach for the construction of heterogeneous systems is the attachment of homogeneous molecular photocatalysts onto solid well-defined nanostructures. To this end various inorganic semiconductor nanomaterials were combined with porphyrin based photocatalysts to develop efficient photoinduced CO_2 reduction systems. Graphite carbon nitride ($g\text{-}C_3N_4$) is a promising semiconductor material since it presents visible-light absorption, rich marginal amino groups, high stability, and earth-abundant nature. Ye and co-workers reported the covalent attachment of a hematoporphyrin based derivative with low molecular weight oligomers of (melems) (OM) through Schiff base chemistry.[273] Subsequent metallization of porphyrin units with Co generated the Co-POM hybrid material (Fig. 58a). Co-POM presented higher activity than Co–porphyrin (Co-P) and OM in the presence of TEOA as SED, producing CO with a rate of 17 μmol g^{-1} h^{-1} (Table 12, entry 1). The carbon nitride moiety is the light-harvesting antenna and the photogenerated electrons are transferred to Co-P units for the reduction of Co^{II} to Co^{I}, which serve as the catalytic centers for the CO_2-to-CO conversion.

Lin *et al.* fabricated a highly efficient $g\text{-}C_3N_4$/FeTCPP heterogeneous catalyst by integrating tetra carboxy-porphyrin (FeTCPP) with $g\text{-}C_3N_4$ nanosheets *via* a simple self-assembly approach (Fig. 58b).[274] The strong interaction between the two components originates from both the π–π stacking of tri-*s*-triazine units with the porphyrin aromatic ring and *via* the

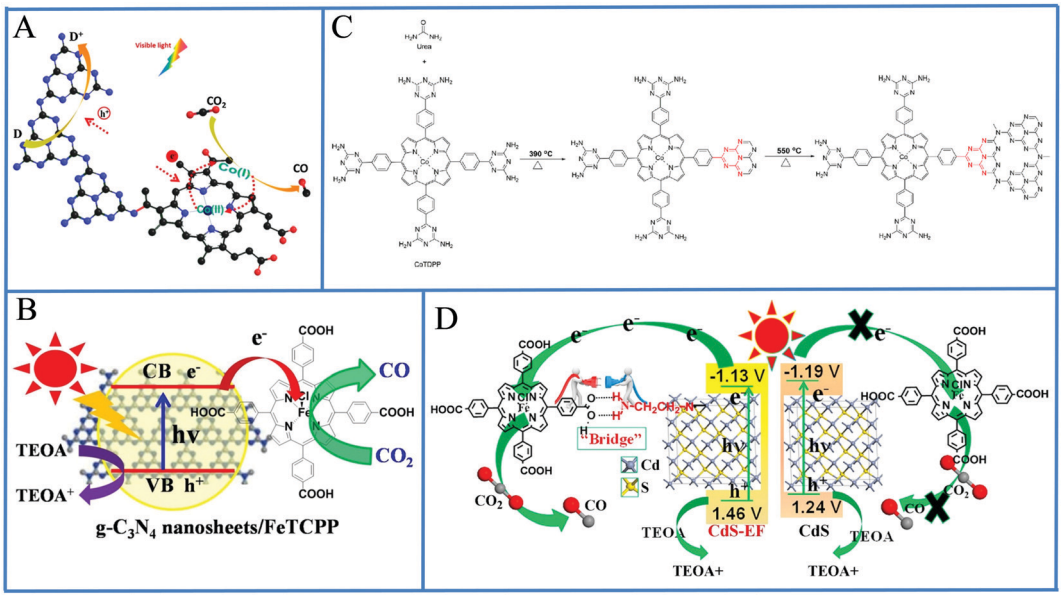

Fig. 58 (A) CO_2 reduction with a Co–porphyrin loaded C_3N_4 heterojunction system. Reproduced from ref. 273, with permission from Elsevier, Copyright 2017. (B) Structure of g-C_3N_4/FeTCPP heterogeneous catalyst system. Reproduced from ref. 274, with permission from Elsevier, Copyright 2018. (C) Schematic illustration of the formation of g-CNU-CoTDPP nanoparticle photocatalysts. (D) Schematic diagram of CO_2 photoreduction over CdS-EF/FeTCPP and CdS/FeTCPP hybrid catalysts. Reproduced from ref. 276, with permission from Elsevier, Copyright 2018.

hydrogen bonding of the carboxyl groups on FeTCPP with the amino groups of g-C_3N_4 nanosheets. The obtained g-C_3N_4/FeTCPP hybrid exhibits high activity for CO_2 reduction under visible-light irradiation, producing CO with a rate of 1087 μmol g^{-1} h^{-1} (Table 12, entry 2) and selectivity up to 98%. The catalytic reduction of CO_2 includes photoexcitation of g-C_3N_4 nanosheets, charge transfer from g-C_3N_4 to FeTCPP, formation of Fe^0TCPP and finally evolution of CO. Thus, the cost-effective g-C_3N_4 nanosheets act as the light-harvesting unit and iron based FeTCPP serves as the catalytic site. The presence of the carboxyl substituents in the phenyl rings improves the photocatalytic activity since it enhances the interaction between g-C_3N_4 nanosheets and FeTCPP, and stabilizes the CO_2 adduct *via* intramolecular hydrogen bonding formation.

Tian *et al.* reported the preparation of semiconductor nanoparticles through covalent coupling and assembly of metalloporphyrin with condensed carbon nitride derived from urea (g-CNU).[275] In detail, 5,10,15,20-tetrakis(4-(2,4-diaminotriazinyl)phenyl)-metalloporphyrin (MTDPP, M = Fe, Co, Ni) was employed as an organic monomer and after copolymerization in the presence of urea the g-CNU-MTDPP (M = Fe, Co, Ni) nanoparticle photocatalysts were fabricated (Fig. 58c). Among the three hybrids, the cobalt-metallated material (g-CNU-CoTDPP) presented the higher performance catalyzing the CO_2 to CO reduction with a rate of 57 μmol g^{-1} h^{-1} (Table 12, entry 3) and selectivity of 79%. This nanoparticle photocatalyst showed exceptional photo stability against photo-corrosion under light irradiation, due to effective charge separation and transfer, enabling for long-term utilization.

CdS is another semiconductor material that was employed for the sensitization of iron porphyrin molecular catalysts. CdS is a traditional semiconductor with a narrow band gap (2.4 eV),

Table 12 Photocatalytic performance of nanomaterials combined with porphyrins for CO_2 reduction

Entry	Nanomaterial	Porphyrin	Cocatalyst or additives	SED	Solvent	Light source	Major products rate	Ref.
1	g-C_3N_4 (melon)	Co–P	—	TEOA	Gas phase	Xenon lamp, 300 W, $\lambda > 400$ nm	CO, 17 μmol g^{-1} h^{-1}	273
2	g-C_3N_4 (nanosheets)	FeTCPP	—	TEOA, 20%	CH_3CN/H_2O (3/1)	Xenon lamp, 300 W, $\lambda > 420$ nm	CO, 1087 μmol g^{-1} h^{-1}	274
3	g-C_3N_4 (condensed nanosheets)	CoTDPP	—	TEOA, 20%	CH_3CN	White LED lamp, 5 W, $\lambda > 400$ nm	CO, 57 μmol g^{-1} h^{-1}	275
4	CdS	FeTCPP	—	TEOA, 20%	CH_3CN/H_2O (3/1)	Xenon lamp, 300 W, $\lambda > 420$ nm	CO, 7.5 μmol g^{-1} h^{-1}; CH_4, 0.18 μmol g^{-1} h^{-1}	276
5	CdS/Bi_2S_3	FeTCPP	—	TEOA, 20%	CH_3CN/H_2O (3/1)	Xenon lamp, 300 W, $\lambda > 420$ nm	CO, 37.9 μmol g^{-1} h^{-1}; CH_4, 0.2 μmol g^{-1} h^{-1}	277
6	$CuInS_2$/ZnS QDs	FeTPP	—	TMPD, 0.1 M	DMSO	Laser pointer, 4.5 mW, 450 nm	CO, 55 TON	278
7	$CuInS_2$/ZnS QDs	FeTMA	—	TEOA, 0.015 M	H_2O	Laser pointer, 4.5 mW, 450 nm	CO, 450 TON	279
8	$CuInS_2$/ZnS QDs	CoTPPS	—	SA, 5 mM and TCEP, 5 mM	H_2O	LED, 450 nm	CO, 84 101 TON	280

excellent light harvesting capability, and sufficiently negative CB potential, which make it a promising visible-light absorber. Li *et al.* prepared ethylenediamine-functionalized CdS (CdS-EF) and pure CdS without functionalization (CdS) and both of them were employed as light absorbers in combination with FeTCPP catalyst for CO_2 photoreduction (Fig. 58d).[276] The CdS-EF/FeTCPP hybrid photocatalyst presents enhanced catalytic activity compared to CdS/FeTCPP, producing CO and CH_4 with rates of 7.5 and 0.18 μmol g^{-1} h^{-1}, respectively (Table 12, entry 4). The photocatalytic process mainly consists of three steps, the generation of photoelectrons in CdS-EF upon illumination, followed by the electron injection to FeTCPP, and finally CO_2 reduction on FeTCPP. The superior activity of CdS-EF/FeTCPP hybrid system was attributed to the formation of hydrogen bonds between the amino groups of CdS-EF and the carboxyl groups of FeTCPP. These H-bonds provide efficient channels for interfacial electron transfer and facilitate the electronic interaction between CdS and FeTCPP.

The same group reported the preparation of CdS/Bi_2S_3 heterostructures which were also employed as photosensitizer with the FeTCPP molecular catalyst.[277] The narrow band gap semiconductor Bi_2S_3 was coupled with CdS *via* an ion exchange reaction to improve the charge separation efficiency and enhance the visible-light harvesting ability of CdS. Interestingly, the obtained CdS/Bi_2S_3/FeTCPP hybrid presented enhanced activity, catalyzing the CO to CO and CH_4 reduction with rate of 37.9 and 0.2 μmol g^{-1} h^{-1}, respectively (Table 12, entry 5). Two major reasons may account for the enhanced performance: (i) the Bi_2S_3 improves charge separation efficiency and (ii) the amount of surface defects on CdS nanorods are reduced during the ion-exchange reaction.

Colloidal quantum dots (QDs) were also employed as photosensitizers for CO_2 reduction. Quantum confinement of their electrons makes their absorption and electrochemical properties tunable by simply changing their diameter. Moreover, QDs have large surface area-to-volume ratios, and their surface enable the adsorption of molecular catalysts to form quasi-static complexes that mediate fast and efficient charge transfer between sensitizer and catalyst. Weiss and co-workers reported the photosensitization of an iron porphyrin catalyst (FeTPP) with colloidal, heavy metal-free $CuInS_2/ZnS$ quantum dots (QDs) (Fig. 59a).[278] Upon irradiation at 450 nm, the QD donates three electrons to form the catalytically active species Fe^0TPP, which binds CO_2 and reduces it to CO with 84% selectivity. The catalytic system achieved a TON of 55, using *N,N,N′,N′*-tetramethyl-*p*-phenylenediamine (TMPD) as SED (Table 12, entry 6). The catalyst sensitization in this system is highly efficient, due to the ultrafast electron transfer between the QD and FeTPP. This ultrafast photoreduction is attributed to the formation of a quasistatic QD/FeTPP complex, probably driven by the interaction between Fe and sulfur on the surface of the QD.

The same group one year later extended this work by combining negatively charged colloidal $CuInS_2/ZnS$ QDs with positively charged trimethylamino-functionalized iron porphyrin catalyst (FeTMA).[279] The catalytic studies were performed in H_2O using TEOA as SED and a TON of 450 was obtained after 30 h of irradiation with selectivity of ~99% (Table 12, entry 7). The catalytic performance increased significantly compared to the previous system, in which both the $CuInS_2$ QDs and the FeTPP porphyrin were uncharged and dissolved in DMSO. This enhancement was attributed to the formation of electrostatically assembled superstructures, where one FeTMA is funneled photoelectrons from several QDs. The creation of these catalytically active superstructures is driven by the binding of negatively charged carboxylate tail groups on the QDs with the positively charged trimethylamino groups on the FeTMA (Fig. 59b). Three years later, the same team utilized positively charged $CuInS_2/ZnS$ colloidal QDs as PS and a negatively charged Co–porphyrin (CoTPPS) as catalyst (Fig. 59c).[280] The synthesized QDs were coated in ligands terminated with amines/ammoniums groups (A-QDs), or with trimethylammoniums groups (TMA-QDs). The catalytic studies with the A-QDs were performed in pure water and CO formation was observed with an exceptional high TON of 84 101 and selectivity 99.1% (Table 12, entry 8). The enhanced catalytic activity was attributed to the strong electrostatic attraction of the QDs with the catalyst, which promotes fast multielectron delivery and colocalization of protons, CO_2, and catalyst at the source of photoelectrons. Moreover, the TMA-QDs presented lower performance (38 473 TON) compared to A-QDs, under the same conditions. This was ascribed to the presence of free amines in A-QDs, which capture CO_2 as carbamic acid that serves as a reservoir for CO_2, effectively increasing its solubility in water, and lowers the onset potential for catalytic CO_2 reduction by the Co–porphyrin. The breakthrough efficiency of this system represents a significant step in the development of reaction networks for direct solar-to-fuel conversion.

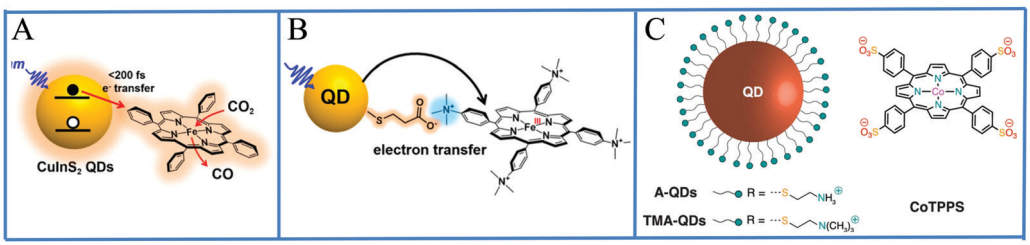

Fig. 59 Photocatalytic CO_2 reduction with $CuInS_2/ZnS$ QDs as PS and as catalyst: (A) the neutral FeTPP, Reproduced from ref. 278, with permission from American Chemical Society, Copyright 2017. (B) The positively charged FeTMA Reproduced from ref. 279, with permission from American Chemical Society, Copyright 2018 and (C) the negatively charged CoTPPS. Reproduced from ref. 280, with permission from American Chemical Society, Copyright 2021.

3.2.5 Porphyrin DSPECs for CO_2 reduction. Porphyrins have been applied in dye-sensitized photoelectrochemical cells (DSPECs) towards CO_2 reduction and have scientific attracted increasing interest. Isaacs and co-workers[281] studied both the electrocatalytic and the photoelectrochemical reduction of CO_2 using an ITO electrode modified by porphyrin–ruthenium complex cations and polyoxometalate anions. More specifically they utilized the Mn(III), Zn(II) and Ni(II) metallated TPyP porphyrin coordinated to four Ru-bis(pyridine)chloride moieties *via* the pyridyl groups as the cation (Fig. 60a) and the polyoxotungstate $[SiW_{12}O_{40}]^{4-}$ as the anion to form the multilayer modified ITO. The researchers showed that the prepared ITO electrode was able to perform electrocatalytic reduction of carbon dioxide in the dark towards HCOOH, CO and MeOH, while photoelectrochemical experiments revealed the formation of formaldehyde as an extra reduction product (Table 13, entry 1). The change in the product distribution indicated that there is a change in the reduction mechanism under light irradiation. Zhao and co-workers utilized another metallated porphyrin, namely CoTPP (cobalt *meso*-tetraphenylporphyrin) towards CO_2 photoelectrochemical reduction.[282] More specifically the researchers immobilized CoTPP onto g-C_3N_4 *via* π–π supramolecular interactions and observed efficient CO_2 reduction under visible light irradiation towards the generation of formic acid with very high selectivity (Table 13, entry 2).

In another report, Kou *et al.* synthesized a dyad (ZnDMP-Re) comprising of a zinc-porphyrin sensitizer moiety bearing a carboxylic anchoring group and a rhenium-complex catalytic moiety for CO_2 reduction (Fig. 60b).[283] The authors initially showed that ZnDMP-Re dyad was able to perform photoreduction of CO_2 in solution with TEA as SED and then applied this system is a photoelectrochemical scheme without any sacrificial reagents. In detail, the adsorbed dyad on p-type NiO nanoparticles was deposited on FTO as working electrode and exhibited light induced reduction of CO_2 to CO in DMF solution using platinum as counter electrode (Table 13, entry 3). Noteworthy the performance was improved *via* the co-adsorption of ZnTCPP as additional photosensitizer to the dyad. The same research group further examined this system in a recent report by doping NiO with Li ions in order to promote the hole carrier mobility within the semiconductor.[284] In this system the authors co-adsorbed the ZnTMP photosensitizer and the Re complex catalyst (Fig. 60c) on the NiO semiconductor and indeed observed enhanced CO_2 photoreduction under 6% of Li ions doping (Table 13, entry 4).

Zeng *et al.* prepared porphyrin–graphene nanocomposites in aqueous media utilizing the intramolecular electrostatic interactions as well as the π–π stacking between TPPyP and reduced graphene oxide (rGO) (Fig. 60d).[285] Zn metallation was followed to afford the nanohybrid photoelectrocatalyst rGO/TPPyP-Zn which was applied in CO_2 reduction under visible light irradiation. The best performing system was rGO/TPPyP-Zn nanocomposite which

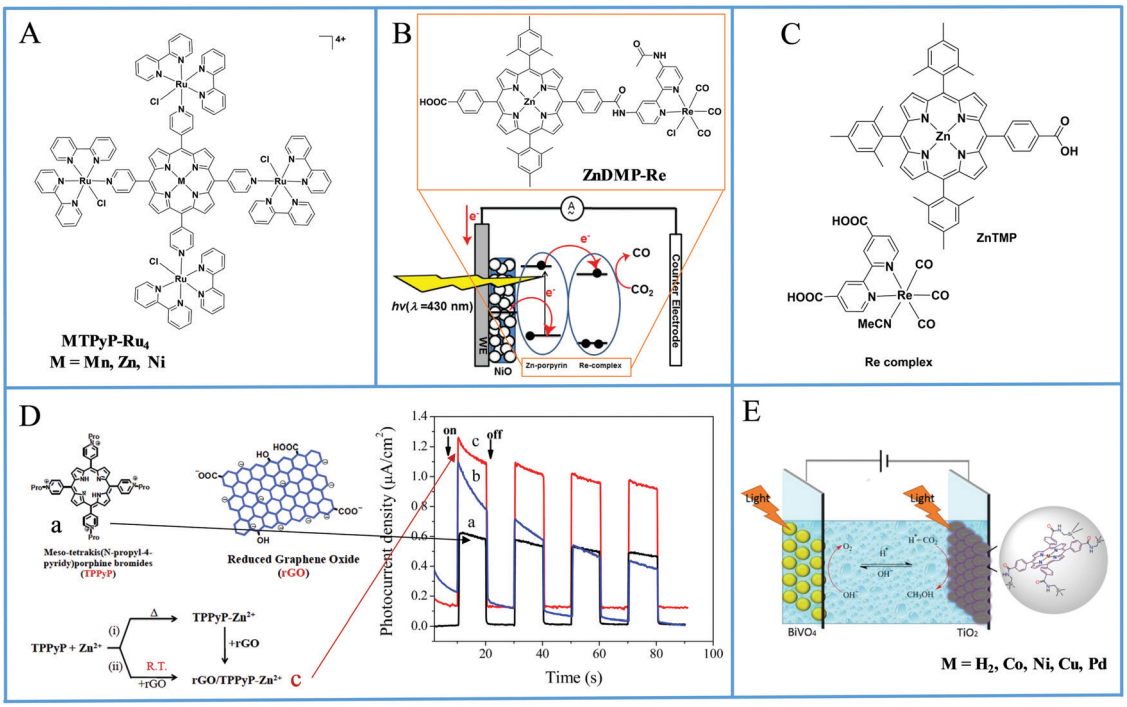

Fig. 60 (A) Molecular structures of metallated TPyP porphyrin coordinated to four Ru-bis(pyridine)chloride moieties *via* the pyridyl groups, (B) schematic illustration of the photoelectrochemical scheme using ZnDMP-Re dyad, Reproduced from ref. 283, with permission from Elsevier, Copyright 2014. (C) Molecular structures of the ZnTMP photosensitizer and Re complex catalyst, (D) chemical structures and photocurrent density of TPPyP, reduced graphene oxide (rGO) and the nanohybrid photoelectrocatalyst rGO/TPPyP-Zn, Reproduced from ref. 285, with permission from Elsevier, Copyright 2018. (E) Schematic illustration of the artificial photosynthesis cell consisted of metalloporphyrin-modified TiO_2/FTO electrodes photocathode and $BiVO_4$ photoanode. Reproduced from ref. 286, with permission from Elsevier, Copyright 2019.

exhibited higher photocurrent than TPPyP and rGO/TPPyP composites (Table 13, entry 5).

Symmetrical porphyrins, as in the previous report, have attracted significant attention for photoelectrochemical CO_2 reduction. In the same direction, Jing and co-workers[286] prepared porphyrin-modified TiO_2/FTO electrodes based on the TCPP (*meso*-tetra-*p*-carboxyphenyl-porphyrin), and the corresponding metallated with Co, Ni, Cu and Pd derivatives. In detail, the TiO_2/FTO electrodes were initially functionalized with amino groups *via* aminopropyltriethoxysilane and subsequently covalently linked with MTCPP porphyrins yielding TiO_2 modified photocathodes. The authors showed that these photocathodes can efficiently convert CO_2 to MeOH photoelectrocatalytically and afterwards combined them with a $BiVO_4$ photoanode, which was performing water oxidation, to form an artificial photosynthesis cell (Fig. 60e and Table 13, entry 6).

In another report, Wang and co-workers[287] synthesized zirconium PMOF hollow nanotubes using the widespread TCPP and afterwards anchored Au, Cu, and Co as single porphyrin-metal atom catalysts to facilitate CO_2 conversion (named as HNTM-Au-SA, HNTM-Cu-SA, and HNTM-Co-SA, Fig. 61a). The authors investigated the electrochemical CO_2 reduction in dark as well as under visible light irradiation, where they observed high TOF performance (Table 13, entry 7). The photo-coupled electrochemical experiments showed that similar activity could be obtained at a lower overpotential with a positive shift of 20, 100, and 130 mV for the Co, Cu and Au modified PMOF, respectively. This trend was consistent with the calculated energy gaps while gas chromatography and NMR experiments verified that the reduction products were CO and HCOOH. The same research group further explored this system and prepared 2D PMOF nanosheets (MOF-NS) using again TCPP and zirconium salt (Fig. 61a).[288] In this report, the authors employed Cu, Co and Fe as anchored elements to improve the catalytic activity of the material. Under visible-light irradiation, CO_2 was efficiently converted to CO with a 100 mV positive shift compared to the electrocatalytic measurement under dark, for the MOF-NS-Co system (Table 13, entry 8).

Reisner and co-workers designed a tandem photoelectrochemical device able to convert carbon dioxide to carbon monoxide coupled with water oxidation in the absence of external bias.[289] The authors utilized the noble metal free Co(II)-*meso*-tetrakis(4-methoxyphenyl) porphyrin (CoTMPP), as a molecular catalytic moiety immobilized *via* π–π intramolecular interactions onto carbon nanotubes sheets. Perovskite photocathodes were prepared using the above porphyrin–carbon nanotubes assemblies and subsequently incorporated in a tandem device with a $BiVO_4$ photoanode bearing a known Co WOC (Fig. 61b). The above tandem call was able to convert CO_2 to CO and H_2 at the photocathode while water oxidation was performed at the photoanode (Table 13, entry 9). The authors revealed that light intensity is an important factor determining the selectivity of the system and showed that the highest selectivity towards CO formation was achieved at 0.1 sun light intensity.

In the following reports copper metallated porphyrins were utilized for the conversion of carbon dioxide into alcohols. Brito *et al.* modified the surface of Ti/TiO_2 nanotube electrodes by immobilizing the Cu(T4H3MPP) metallated porphyrin (Fig. 61c) and investigated the photoelectrocatalytic performance of the resulting photoanodes for CO_2 reduction.[290] The authors showed that their system has selectivity towards the formation of MeOH and EtOH, while displayed enhanced activity compared to photocatalysis and electrocatalysis in the same conditions (Table 13, entry 10). Another report by Cheng and co-workers used the Cu(II)-*meso*-tetra-*p*-carboxyphenyl-porphyrin to prepare PMOFs nanosheets (NSs) on top of which CuS NPs were attached providing the catalytic moieties for CO_2 reduction.[291] This catalytic system was employed as electrocathode for CO_2 conversion in the two-compartments

Table 13 Photocatalytic performance of porphyrin DSPECs for CO_2 reduction

Entry	Porphyrin	Semiconductor	Solvent and ingredients	Products	Light source	Ref.
1	MTPyP-Ru_4	ITO	0.1 M $NaClO_4$(aq)	HCOOH, CO, MeOH and CH_2O	500 W Xe–Hg lamp	281
2	CoTPP	g-C_3N_4/FTO	0.1 M KCl(aq)	HCOOH	300 W Xe lamp	282
3	ZnDMP-Re	NiO/FTO	NBu_4PF_6 (0.1 M) in DMF	CO	500 W Xe lamp	283
4	ZnTMP	Li-NiO/FTO	NBu_4PF_6 (0.1 M) in DMF	CO	500 W Xe lamp	284
5	TPPyP-Zn	Glassy carbon	0.1 M Na_2SO_3(aq)	not studied	500 W Xe lamp $\lambda >$ 420 nm	285
6	MTCPP	TiO_2/FTO	0.1 M $NaHCO_3$(aq)	MeOH	300 W Xe lamp	286
7	HNTM-Au-SA	Gas diffusion electrode	0.1 M $KHCO_3$(aq)	CO and HCOOH	300 W Xe lamp $\lambda >$ 420 nm	287
8	MOF-NS-Co	Gas diffusion electrode	0.1 M $KHCO_3$(aq)	CO and HCOOH	300 W Xe lamp $\lambda >$ 420 nm	288
9	CoTMPP	Perovskite/NiO_x/FTO	[6,6]-Phenyl C_{61} butyric acid methyl ester (PCBM)/polyethylenimine/Ag	CO and H_2	Solar light simulator	289
10	Cu(T4H3MPP)	Ti/TiO_2 nanotubes	0.1 M Na_2SO_4(aq)	MeOH and EtOH	300 W Xe lamp	290
11	CuTCPP	Copper foam	0.5 M $NaHCO_3$(aq)	EtOH	300 W Xe lamp	291
12	Cu@porphyrin-COFs	Electrodeposited Copper	0.5 M $KHCO_3$(aq)	MeOH, EtOH, ($CH_3CH(OH)_2$) and (CH_3COCH_3)	300 W Xe lamp	292
13	HOOC-(Zn)DMP-tpy-Ru	NiO	0.1 M Bu_4NPF_6 in MeCN : H_2O 9 : 1	—	White LED PAR38 lamp (17 W)	293

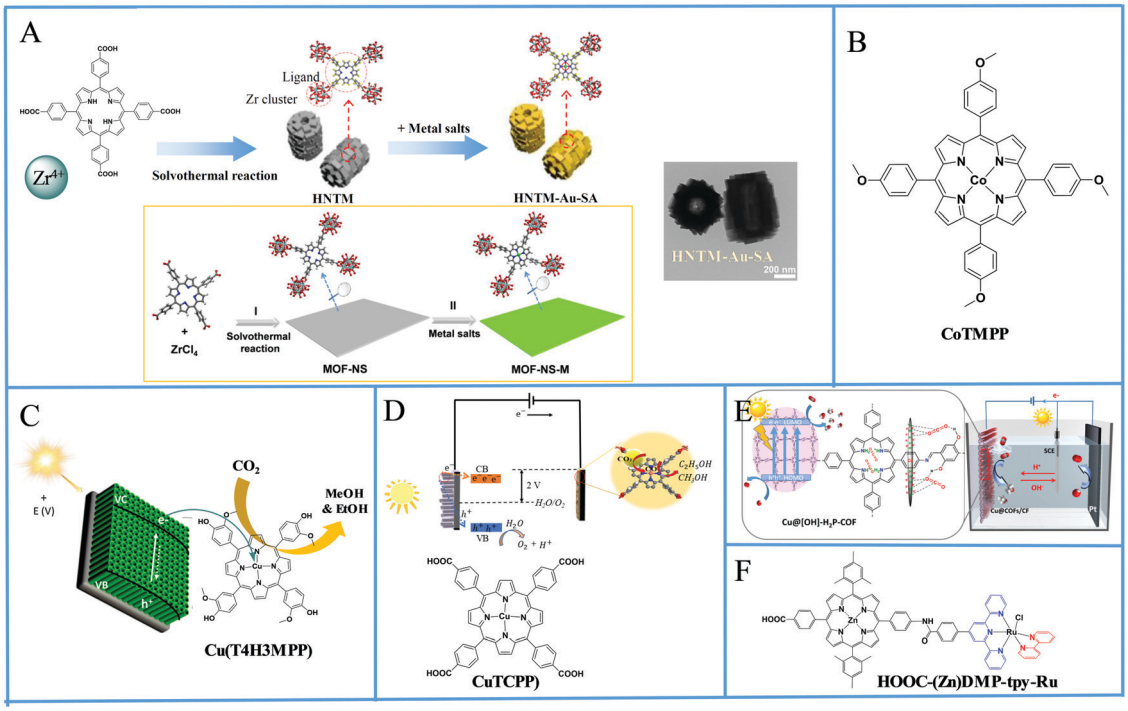

Fig. 61 (A) Schematic illustration PMOF hollow nanotubes HNTM-Au-SA, HNTM-Cu-SA, and HNTM-Co-SA as well as the 2D PMOF nanosheets (MOF-NS) using the same TCPP porphyrin and $ZrCl_4$ salt, Reproduced with permission from ref. 287, which is an open-access article distributed under the Creative Commons Attribution 4.0 International License, 2019 Springer Nature. (B) Molecular structure of CoTMPP porphyrin, (C) chemical structure of Cu(T4H3MPP) and schematic illustration of the resulting photoanodes, Reproduced from ref. 290, with permission from Elsevier, Copyright 2020. (D) Two-compartment photoelectrochemical cell with CuTCPP as a catalyst for CO_2 reduction, Reproduced from ref. 291, with permission from Elsevier, Copyright 2020. (E) Schematic illustration of the photoelectrochemical cell consisted of Cu@porphyrin-COFs nanorods photocathode, Reproduced from ref. 292, with permission from Elsevier, Copyright 2020. (F) Chemical structure of Zn porphyrin–ruthenium complex dyad.

photoelectrochemical cell with TiO_2 nanotube photoanodes performing water oxidation (Fig. 61d) and exhibited efficient and selective light induced CO_2 conversion to ethanol (Table 13, entry 11).

Wang *et al.*[292] prepared the same porphyrin COFs we previously reported in the heterogeneous photocatalytic H_2 production paragraph (Fig. 19b). In detail, the authors synthesized porphyrin COF nanorods and subsequently electrodeposited Cu on them (Fig. 61e). The resulting material Cu@porphyrin-COFs nanorods presented high photoelectrocatalytic performance for CO_2 reduction, producing methanol, ethanol, ethane-1,1-diol and acetone (Table 13, entry 12). The authors showed *via* ^{13}C labeling experiments that the liquid products derived from CO_2 and *via* DFT calculations that hydroxyl groups of free-base porphyrin COFs have an important role in the catalytic process. Charisiadis *et al.* contributed in the field of DSPECs towards CO_2 reduction by applying a Zn porphyrin–ruthenium complex dyad (Fig. 61f) anchored on a NiO photocathode to fabricate a p-type DSPEC (Table 13, entry 13).[293]

4. Phthalocyanines for photocatalytic H_2 evolution

Because of their high light-harvesting ability and outstanding physicochemical and optical features, Pc derivatives have been widely exploited as photosensitizers or catalysts in the field of photocatalytic H_2 production from water. Their chemical diversity results in photophysical properties that can be modulated. Many Pc derivatives have been, therefore, prepared to date in order to investigate the relationship between molecular structure and photocatalytic performance in more depth. Recent examples of both Pc-based photosensitizers and catalysts in photocatalytic hydrogen production will be described in the following section.

4.1 Metal oxides combined with phthalocyanines

The success of phthalocyanine in the field of artificial solar energy conversion devices, particularly in molecular photovoltaics,[36] has inspired chemists to investigate the activity of Pc derivatives covalently and/or non-covalently linked to semiconductors as a sensitizer for photocatalytic hydrogen production. Previous reports on Pc-based DSSCs have emphasized the lack of directionality of the excited state of the Pcs and poor coupling of the LUMO with the TiO_2 conduction band as bottle-neck that mainly limits the power conversion efficiencies.[36,294] Later research demonstrated that the rational design of push–pull Pc derivatives with an anchoring group that provides charge transfer directionality from the Pc to the semiconductor is an effective technique for overcoming this challenge.[294] The engineering of Pc derivatives for the DSSCs

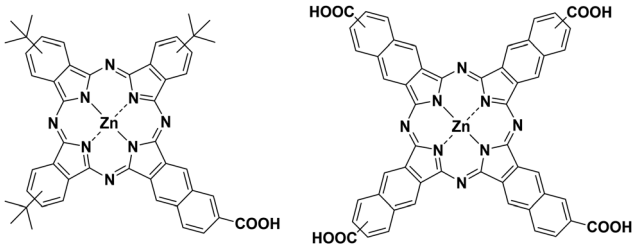

Fig. 62 Molecular structures of Zn-tri-PcNc and Zn-tetra-Nc and schematic representation of a H_2 production of Zn-tri-PcNc-TiO_2-AA photocatalyst.

system have been focused on molecular structures based on unsymmetrical functionalized A_3B type derivatives with an anchoring group.[295] As a result, asymmetric phthalocyanine derivatives have been favoured for panchromatic sensitization of semiconductors in photocatalytic hydrogen production as well.

Zhang *et al.* reported unsymmetrically substituted ZnPc bearing three *tert*-butyl groups and the carboxylic acid anchoring group (Zn-tri-PcNc) and symmetrical tetra-carboxy-zinc naphthalocyanine (Zn-tetra-Nc) derivatives (Fig. 62) as dyes to sensitized TiO_2 for photocatalytic H_2 production.[296] Zn-tri-PcNc and Zn-tetra-Nc show strong visible/near-IR light absorption at 694 and 766 nm, respectively, and Pc sensitized/TiO_2 exhibit broader absorption spectra from 550 to 900 nm compared to that of pristine TiO_2. The photocatalytic performance of Zn-tri-Pc-Nc and Zn-tetra-Nc sensitized TiO_2 was investigated in the presence of Pt as a co-catalyst and EDTA as a sacrificial reagent. After irradiation of 5 h, Zn-tri-PcNc/TiO_2 achieved a H_2 yield of 567.4 μmol with a TON of 7565, which is much higher than that of Zn-tetra-Nc/TiO_2 (236.5 μmol H_2 with a TON of 3153). The higher photocatalytic activity of Zn-triPcNc was attributed to a good balance between diminishing dye aggregation by introducing bulky *tert*-butyl groups and improving the charge transfer directionality in the excited state, which was achieved by the push–pull structure.

Even though the efficiency of solar energy conversion devices is governed by several factors based on photo-induced charge generation and separation, one of the most important parameters is the light-harvesting ability of the photoactive component. Thus, light-harvesting systems with broad absorption to cover large portions of the solar spectrum are very desirable. However, the preparation of a single dye to fulfil this requirement with dye sensitization systems remains a major challenge. In this respect, the combination of two or more dyes with a complementary optical property appears to be an attractive strategy to cover the entire visible region and even the near-infrared part (NIR). This tactic has been widely used in DSSCs to achieve panchromatic sensitization of TiO_2 films.[36,295] The related approach is also used in semiconductor-based photocatalysts, particularly TiO_2, by complexing TiO_2 with either small molecules such as acids or alcohols, (TEA, EDTA, ascorbic acid (AA) *etc.*) or D–π–A organic dyes to increase the light-harvesting ability. Many kinds of electron donor molecules have been used both as a sacrificial reagent for the formation of charge-transfer complexes on the surface of TiO_2 to increase the photocatalytic activity of photocatalyst.[297] In this case, it is worthy to mention that the absorption expansion of the semiconductor is based on the ligand-to-metal charge transfer (LMCT) between the absorber and the semiconductor rather than the common dye sensitization mechanism. However, LMCT complexes (TiO_2-small molecule) are not sufficient for the development of the stable visible light photocatalyst.

In 2015, further developments were reported by Zhang *et al.* in terms of panchromatic and stable photocatalytic systems involving the addition of ascorbic acid on TiO_2 and co-sensitization with ZnPc (Fig. 63).[298] As mentioned, Pcs possess attractive light absorption features in the visible and near-infrared regions of the solar spectrum, exhibiting a very intense absorption at 300–400 nm (Soret band) and at 700 nm (Q band), but are transparent over a large area of the visible spectrum which makes them interesting dyes to be employed in this cocktail approach. The Zn-tri-PcNc-TiO_2-AA photocatalytic system exhibited a much higher photoactivity (162.2 μmol h^{-1}) for H_2 production than that of the LMCT AA-TiO_2 complex (126.2 μmol h^{-1}), mainly due to its improved light-harvesting efficiency in the visible and near IR spectral region. Indeed, it was confirmed by DRS spectra that Zn-tri-PcNc-TiO_2 absorbs in the range of 600–900 nm, but the co-sensitized Zn-tri-PcNc-TiO_2-AA system exhibits a much broader absorption in the range of 400–900 nm, including the characteristic absorption bands of

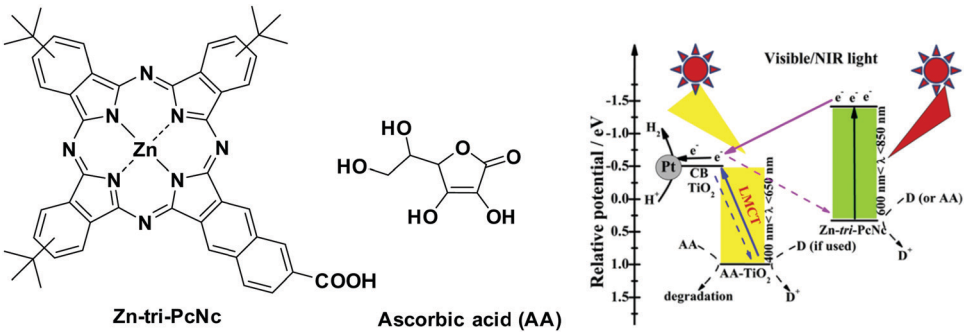

Fig. 63 Schematic representation of H_2 production of Zn-tri-PcNc-TiO_2-AA photocatalyst. Reproduced from ref. 298, with permission from Elsevier, Copyright 2015.

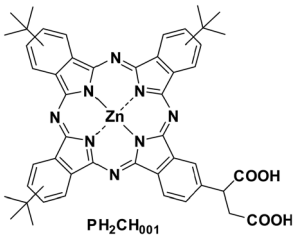

Fig. 64 Molecular structure of PH_2CH_{001}.

the surface AA-TiO_2 complex and Zn-tri-PcNc molecules. This two-channel system, which collects photoelectrons in both the 400–600 nm and 600–800 nm range, resulted in higher hydrogen production than single components.

TiO_2 has several considerable advantages in terms of non-toxicity and stability. The additional improvement of photocatalytic activity could be achieved by tuning of surface area, crystal structure, shape, size *etc.* In particular, the introduction of porosity into TiO_2 in a hierarchical architecture plays an important role not only to increase the surface area and pore volume but also to improve the light-scattering and light-harvesting abilities of photocatalysts.[299] Amritanjali Tiwari *et al.* introduced unsymmetrical ZnPc (PCH001) (Fig. 64) decorated with three *tert*-butyl and two carboxylic acid groups, to sensitize hierarchical porous TiO_2 (HPT) particles.[300] The ZnPc sensitized Pt/HPT photocatalyst showed attractive H_2 producing activity (2260 μmol mmol g^{-1} in 5 h) with the highest TON of 18 080 when compared with the reference N716 Ru(II)-bipyridyl dye. The high hydrogen production is attributed to the hierarchically porous structures of TiO_2, which allow excellent transport of the reactant mass and higher light absorption capacity, as well as the efficient electron transfer arising from the push–pull structure of asymmetric ZnPc.

As mentioned previously, many photocatalytic systems require noble metal-based co-catalysts to increase hydrogen production efficiency by trapping photoexcited electrons and reducing charge recombination on the TiO_2 surface. Despite the benefits of co-catalyst, both the supply and cost of these noble metals such as platinum (Pt) limit their practical applications. Recently, Moon *et al.* reported the use of CuPc sensitized TiO_2 as the photocatalyst in photocatalytic hydrogen evolution without the aid of noble metal as a cocatalyst.[301] The photocatalytic performance of CuPc/TiO_2 catalysts was tested in the aqueous methanol solution in which methanol also acts as a sacrificial reagent. The photocatalyst CuPc/TiO_2 produced an H_2 production rate of 0.95 μmol h^{-1} with a high apparent quantum yield (AQY) of 6.68% at 420 nm monochromatic light irradiation. In this system, TiO_2 acts as an electron mediator and CuPc serve as both a sensitizer and a charge transfer mediator. Upon photoexcitation of the photocatalyst with $\lambda > 420$ nm visible light, the excited electron–hole pair occurs only at the CuPc rather than TiO_2, while the excited electron is transferred to the CB of TiO_2 and used in the hydrogen evolution reaction, while the holes at HOMO of CuPc were scavenged by methanol (Fig. 65). Due to the absence of photo-induced electron and hole pair in TiO_2, the internal charge recombination is avoided in the CuPc/TiO_2 nanocomposite.

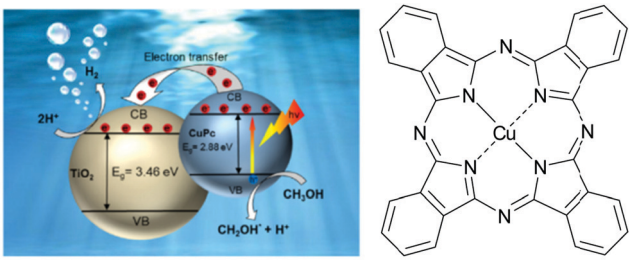

Fig. 65 Proposed mechanism of photocatalytic H_2 evolution with CuPc/TiO_2 nanocomposites. Reproduced from ref. 301, with permission from Elsevier, Copyright 2020.

The nature of central metal atoms at the inner cavity of the Pc macrocycles also impacts on the physical, electronic, and optical properties of the Pcs and indeed the catalytic activity of Pcs is strongly related to central metal atoms. This aspect is particularly important in the case of electrocatalytic activity of the Pc derivatives since in most cases metal atoms act as the catalytic active center of the multi-electron reaction process. In order to investigate the influence of the central metal on the performance of photocatalytic hydrogen evolution, tetracarboxylic acid Pc derivatives with Zn and Co atoms as central metals (Fig. 66) have been reported by Ince and coworkers.[302] The hydrogen production rate of ZnPc/TiO_2 and CoPc/TiO_2 photocatalyst in the presence of Pt co-catalyst was determined as the 3448 and 3328 μmol g^{-1} h^{-1}, respectively. The improved photocatalytic activity of ZnPc sensitized TiO_2 was attributed to superior the spectral response of Pc sensitizers, in fact, ZnPc/TiO_2 revealed a significant red-shift of the Pcs Q-band absorption with a high molar extinction coefficient.

Despite the outstanding optical and photophysical properties of Pcs, the solar energy conversion efficiency of this family of sensitizers has been mainly limited by the strong tendency of Pcs to form aggregates both in solution and in the solid-state; this is more pronounced than in porphyrins, due to their more π-extended system. In the case of solar cells, significant progress in Pc-sensitized DSSCs came with the ZnPc 1 (known as TT40) bearing bulky 2,6-diphenylphenoxy peripheral substituents which completely suppresses macrocycle aggregation and impressive power conversion efficiencies over 6% were achieved (Fig. 67).[303,304]

A new Pc derivative in which the oxygen atoms in the bulky phenoxy substituents were replaced with stronger electron-donating sulfur atoms (ZnPc 2) was also used as photosensitizer into the DSSC device, exhibited a relatively low photovoltaic conversion efficiency of 2.5% as compared with that of ZnPc 1.[305]

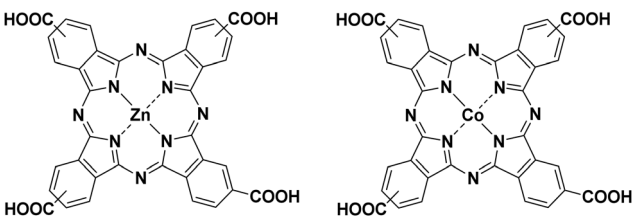

Fig. 66 Molecular structures of tetracarboxylic acid ZnPc and CoPc.

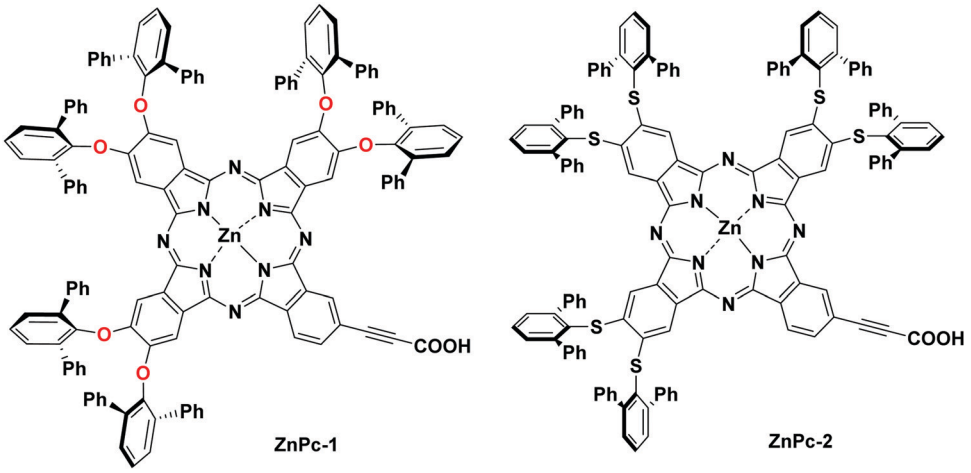

Fig. 67 Molecular structures of phthalocyanine sensitizers ZnPc-1 and ZnPc-2.

Ince *et al.* recently compared the photocatalytic activity of ZnPc-1 and ZnPc-2 sensitized TiO_2 photocatalysts in the photocatalytic hydrogen evolution process in the absence and presence of co-catalyst.[306] The produced hydrogen amount of ZnPcs derivatives (ZnPc-1/TiO_2 and ZnPc-2/TiO_2) were found as 1.221 mmol g^{-1} h^{-1} and 0.864 mmol g^{-1} h^{-1} with a corresponding solar-to-hydrogen (STH) efficiencies of 3.15% and 2.22% respectively, for the first hour. In the presence of Pt, hydrogen generation increased after 8 hours of illumination, reaching 32 808 mmol g^{-1} and 16 067 mmol g^{-1} for ZnPc 1 and 2, respectively. The introduction of the thioether units ZnPc-2 at the peripheral positions of the Pc results in a dramatic red shift in the absorption spectra, by decreasing the LUMO level and increasing the HOMO level of ZnPc-2 in comparison with the levels of ZnPc-1 derivative. However, the expansion of the light-harvesting range of ZnPc-2 could not positively affect on the H_2 evolution performance of ZnPc-2 even in the presence of the co-catalyst. The authors suggested that lower LUMO and higher HOMO energy levels of ZnPc-2 which might be hindering both the efficient electron transfer and dye regeneration could constitute a possible explanation for low hydrogen production.

Only very recently, new Pc sensitizers ZnPc-3 and ZnPc-4 peripherally anchored through an imidazole group have been synthesized in order to investigate the effect of the anchoring group on the performance of photocatalytic hydrogen evolution, by the same authors (Fig. 68).[307] The photocatalytic performance of ZnPc-3 was compared with ZnPc-5 (known as TT1) in which the carboxy group is directly attached to the macrocycle in the same conditions. The photocatalytic performance of ZnPcs sensitized TiO_2 was tested in the presence of TEOA without using any co-catalyst. ZnPc-3 was capable of efficient photocatalytic H_2 generation, exhibiting the highest H_2 evolution rates of 0.4006 mmol g^{-1} h^{-1}, whereas the composite of ZnPc-4/TiO_2 and ZnPc-5/TiO_2 show the relatively low photocatalytic activity of 0.3319 mmol g^{-1} h^{-1} and 0.3555 mmol g^{-1} h^{-1}, respectively. After 20 h irradiation, ZnPc-3 produces a hydrogen production rate of 3.4187 mmol g^{-1} with a TON of 14 863, higher than ZnPc-5 in the absence of co-catalyst. All ZnPcs exhibited a similar light-harvesting ability and proper HOMO–LUMO energy levels. The origin of the photocatalytic activity differences was, thus, attributed to the efficient electron injection into the semiconductor's conduction band for the ZnPc3/TiO_2 photocatalyst. The reason for the high performance of ZnPc-3 is claimed to be due to the fact that the stronger electron-withdrawing character of imidazole facilitates the electron injection from excited Pc into the semiconductor's conduction band. The low performance of symmetrically substituted derivative, ZnPc-4, was explained by the extension of electron

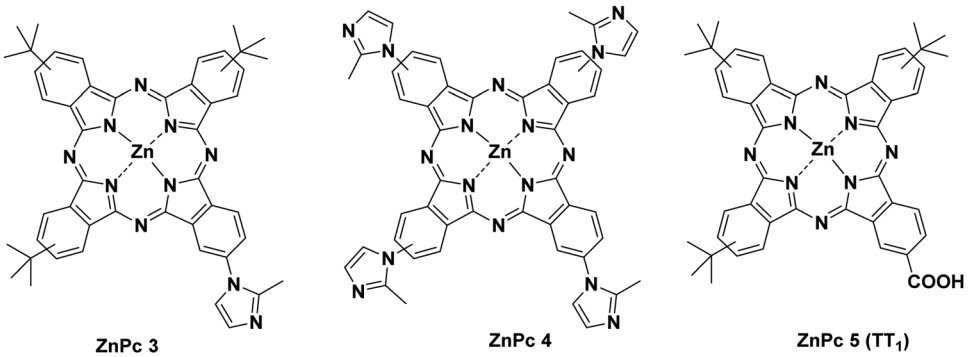

Fig. 68 Chemical structures of ZnPc-3, ZnPc-4, and ZnPc-5.

delocalization over the whole molecule limiting the directional charge transfer.

As a member of the synthetic porphrinoid family, subphthalocyanines (SubPcs) have been widely utilized as attractive building blocks in the construction of efficient artificial photosynthetic devices that mimic the natural photosynthetic systems for the conversion and storage of solar energy. SubPcs are aromatic compounds with a 14–π electron system consisting of a central boron atom, a lower homolog of Pcs, which possess a cone-shaped structure, in contrast to the wide range of planar aromatic compounds.[308] Their high solubility in common organic solvents arising from a low tendency to aggregate and particularly their intense absorption in the visible region (500–700 nm), render them ideal light-harvesting material in the concept of artificial photosynthetic systems. SubPcs are synthetically versatile compounds, and their physicochemical properties can be optimized by introducing appropriate groups in the peripheral or axial positions. SubPcs have been extensively used in organic photovoltaic solar cells as both electron donor and acceptor components owing to their tunable HOMO–LUMO energy levels together with excellent charge transport properties.[309] SubPc sensitizers decorated with various peripheral substituents have been incorporated into dye-sensitized solar cells, yet moderate power conversion efficiencies were obtained due to their low-lying LUMO levels.[310,311]

Inspired by the potential for use of SubPc in DSSCs, Ince and co-workers introduced SubPc derivatives as sensitizers for the sensitized photocatalyst. This is the very first example of SubPc as a sensitizer in the field of photocatalytic H_2 production.[312] To compare the influence of the anchoring group position on the photocatalytic activity of SubPcs, a series of SubPcs having a carboxylic acid anchoring group at either a peripheral (SubPc 1–2) or axial (SubPc 3) position were synthesized (Fig. 69). SubPc3/TiO_2 exhibited the best photocatalytic activity with a hydrogen evolution rate of 1396 μmol h^{-1} which is much higher than that of SubPc 1 and 2 (771 and 658 μmol g^{-1}, respectively). The activity of all SubPcs increases significantly after 8 h irradiation, the evolved hydrogen amounts of SubPc1–3/TiO_2 reaches to 5038, 5135 and 8062 μmol g^{-1}, respectively. Further improvement of hydrogen generation up to 22 345 μmol g^{-1} (for SubPc 3) was achieved by using Pt as a co-catalyst. SubPc 3/TiO_2 photocatalyst gave the highest hydrogen production rate, which is attributed to its higher LUMO energy level, which provides sufficient driving force for an efficient charge transfer from the LUMO orbital of the dye to the conduction band of TiO_2.

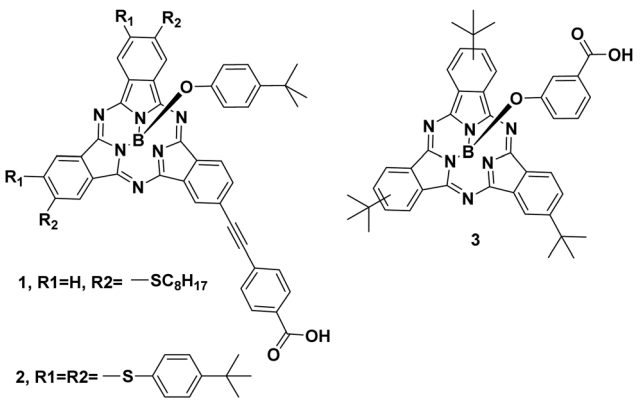

Fig. 69 Molecular structures of SubPc 1, 2 and 3.

4.2 Phthalocyanine DSPSCs for H_2 production

Over the last ten years, there have been a significant advance in the design and development of dye-sensitized photoelectrochemical cells (DSPECs) for water splitting.[32] Similar to DSSCs, nevertheless both devices share a common architecture, the semiconductor photoelectrodes are sensitized by molecular dyes. Porphyrins and phthalocyanines have shown great potential as sensitizers in DSSCS, so the interest in incorporating these chromophores into photoelectrodes for applications in DSPECs is not surprising. Porphyrins have received more attention than Phthalocyanines as sensitizers in DSPECs and in a previous section of this review, the most relevant articles have been summarized. As aforementioned, Sherman *et al.* reported a tandem DSPEC system for the light driven generation of H_2 from hydroquinone using only light energy and no applied electrical bias.[170] The tandem cell configuration is based on the combination of a dye-sensitized photoelectrochemical cell based on a SnO_2 photoanode, which is sensitized by a free-base porphyrin, in series with dye-sensitized solar cells in which a TiO_2 photoanode is sensitized by a Si phthalocyanine. There is a niche for the development of phthalocyanine-based DSPECs and we expect this research topic to accelerate in the future.

A promising approach for the engineering of a photoelectrochemical water-splitting system is based on an organo-photocathode of a p–n bilayer and a semiconductor photoanode. In 2016, Abe *et al.* reported a water-splitting system comprising of a TiO_2 photoanode and a ZnPc/C60 bilayer modified by Pt as a photocathode.[313] This system demonstrated stoichiometric decomposition of water into H_2 and O_2 successfully occurred at bias voltages lower than the theoretical value (*i.e.*, 1.23 V), with efficiencies *ca.* 0.1% at a small bias voltage of 0.25 V. Remarkably, distinct from the reference system TiO_2/Pt, the system is capable of water splitting without any externally applied bias was observed. Abe and co-workers extended this work but exploring other metal oxides as photoanode. In 2017, a photoelectrochemical water-splitting system employing WO_3 as a photoanode and Pt loaded ZnPc/C60 bilayer as photocathode was reported.[314] Although the system led to the stoichiometric formation of H_2 and O_2 due to water decomposition under a low bias voltage of 0.1 V, the most efficient water-splitting occurred at 0.6 V with *ca.* 0.07%. In the case of the reference system WO_3/Pt bias voltages more than 0.4 V were needed to be applied for water splitting. The same research group reported in 2020 a photoelectrochemical water-splitting system based on the same Pt loaded ZnPc/C60 bilayer photocathode but using a photoanode comprised with a mixed-valence cobalt(II,III) oxide (Co_3O_4) disperse in a Nafion membrane on a nanoporous $BiVO_4$.[315] The stoichiometric generation of H_2 and O_2 occurred by applying a bias voltage as low as 0.1 V, which was superior to the reference system comprising $BiVO_4$ and Pt, ant the light-to-

hydrogen conversion efficiency was *ca.* 0.08% at 0.6 V. The presence of a cobalt cocatalyst not only improved the water oxidation process but also the stability of the device even in an acidic medium.

4.3 Graphitic carbon nitrides combined with phthalocyanines

In addition to TiO_2, another interesting photocatalyst material is graphitic carbon nitrides (g-C_3N_4) which has been successfully used in photocatalytic H_2 evolution reactions. The effectiveness of g-C_3N_4 is related to its 2D planar structure, relatively narrow energy bandgap (2.7 eV), adequate energy levels, chemical and thermal stability. Graphite carbon nitride attracts particular attention as a low-cost alternative to its inorganic relatives as it contains earth-abundant elements (C, H, N). However, in order to overcome the low absorption and charge mobility of g-C_3N_4 (<460 nm), bandgap engineering through metal doping and dye sensitization must be employed.[316]

Zhang *et al.* explored the influence of panchromatic co-sensitization on the photocatalytic activity of graphitic carbon nitride-based photocatalysts.[317] They reported complementary absorption spectra over g-C_3N_4 for an indole-based D–π–A organic dye (LI-4) and an asymmetric ZnPc derivative (Zn-tri-PcNc) (Fig. 70). Zn-tri-PcNc exhibits absorption in the region of 650–700 nm, and LI-4 shows strong absorption in the visible region between 400–600 nm. Upon irradiation of the LI-4/g-C_3N_4/Zn-tri-PcNc photocatalyst, the photogenerated electrons from both sensitizers and internal excitation of g-C_3N_4 are transferred to the co-catalyst Pt loaded on g-C_3N_4 and used for H_2 production. Improved light-harvesting was achieved by sensitization of g-C_3N_4 with both dyes, thus leading to H_2 production activity of 371.4 μmol h^{-1} with a TON of 7428 h^{-1}, which is higher than the one achieved with each dye separately (LI-4/g-C_3N_4; 233.8 μmol h^{-1} and Zn-tri-PcNc/g-C_3N_4; 132.3 μmol h^{-1}) under visible/near-infrared (NIR) light irradiation.

To determine the effect of the number of carboxylic acids and nature of the substituents on the performance of Pc sensitized g-C_3N_4, Li and Peng reported on a series of symmetrically and unsymmetrically substituted ZnPcs with different peripheral groups (Fig. 71).[318] Although all ZnPc derivatives have identical optical and electrochemical characteristics, the electron transport and charge recombination kinetics between these compounds and the semiconductor were shown to be the most important factors influencing photocatalytic activity. When placed onto g-C3N4, symmetrical PCs exhibit more efficient electron transport and reduced charge recombination kinetics than asymmetric Pcs, as evidenced by PL quenching and time-resolved fluorescence studies. Zn-tri-PcNc-1, which possesses a "push–pull" structure with three bulky *tert*-butyl groups and carboxylic acid anchoring group, was sensitized with g-C_3N_4 photocatalyst and resulted in an H_2 production efficiency of 203 μmol h^{-1} with a maximal AQY of 0.71%. On the other hand, the symmetric ZnPcs gave a slightly lower H_2 production efficiency than those of the asymmetric ZnPcs. Once again, this result confirmed that the lack of charge transfer directionality of the symmetrical ZnPc and weak coupling of LUMO with the conduction band of g-C_3N_4 was detrimental to the conversion efficiency of the photocatalytic system. The incorporation of two carboxylic acid functions in Zn-tri-PcNc-2 has led to the best photoactivity with the highest H_2 production rate of 263 μmol h^{-1} and a TON of 12 826 under $\lambda \geq 500$ nm light irradiation for 10 h, which corresponds to an AQY of 0.92%. This result is mainly due to an enhancement in the electron transfer rate from the excited sensitizer to the g-C_3N_4 surface and the increased electron lifetime for H_2 production which directly affects the photoactivity. Additionally, when Zn-tri-PcNc-2 and Zn-tri-PcNc-3, consisting of *tert*-butyl and *n*-butoxy groups respectively, were compared and Zn-tri-PcNc-2 showed a higher photoactivity due to the higher steric hindrance of the *tert*-butyl group and its stronger electron-donating ability. The H_2 production of ZnPcs over g-C_3N_4 decreased in the order Zn-tri-PcNc-2 > Zn-tri-PcNc-1 > Zn-tri-PcNc-3 > Zn-tetrad-Nc-3 > Zn-tetrad-Pc-1 > Zn-tetrad-Pc-2. This result shed light on the importance of charge transfer directionality, aggregation degree of Pcs and number of anchoring groups toward photocatalytic efficiency.

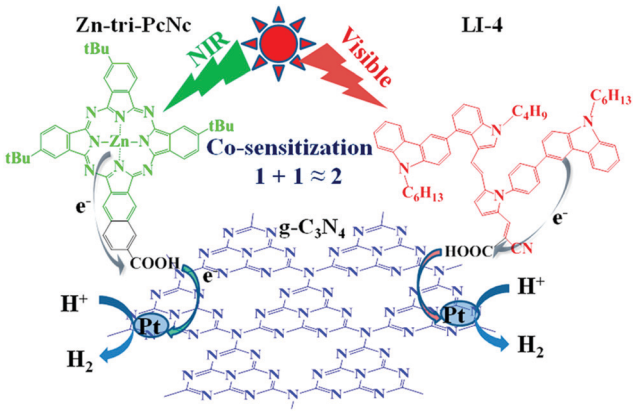

Fig. 70 H_2 production over LI-4/g-C_3N_4/Zn-tri-PcNc. Reproduced from ref. 317, with permission from American Chemical Society, Copyright 2015.

Following a similar approach, Li and co-workers reported on a highly asymmetric A2BC type ZnPc (Zn-di-PcNcTh) bearing four bulky 2,6-diphenylphenoxy substituents (Fig. 72), a thiophene unit and a carboxyl-naphthalene unit with the goal of studying the influence of molecular structure, symmetry and carboxyl anchoring group of ZnPc derivatives on the photosensitized H_2 production performance over g-C_3N_4.[319] The symmetrical analogue containing eight bulky 2,6-diphenylphenoxy substituents (Zn-tetrad-Pc-1) was also prepared and tested for the comparison purposes.[320]

The Zn-di-PcNcTh derivatives show an important redshift of about 39 nm in the absorption maximum at 739 nm relative to the symmetrical Pc analogue (Zn-tetrad-Pc-1). Zn-di-PcNcTh-1 was used to sensitize Pt-loaded g-C_3N_4 for H_2 production, which showed an H_2 production efficiency of 249 μmol h^{-1} with TON of 9960.8, much higher than the pristine Pt/g-C_3N_4. A higher AQY (3.05%) was obtained under 730 nm monochromatic light irradiation, higher than that of Zn-tetrad-Pc-1 (1.14%) without the carboxyl group. The origin of this lower H_2 production

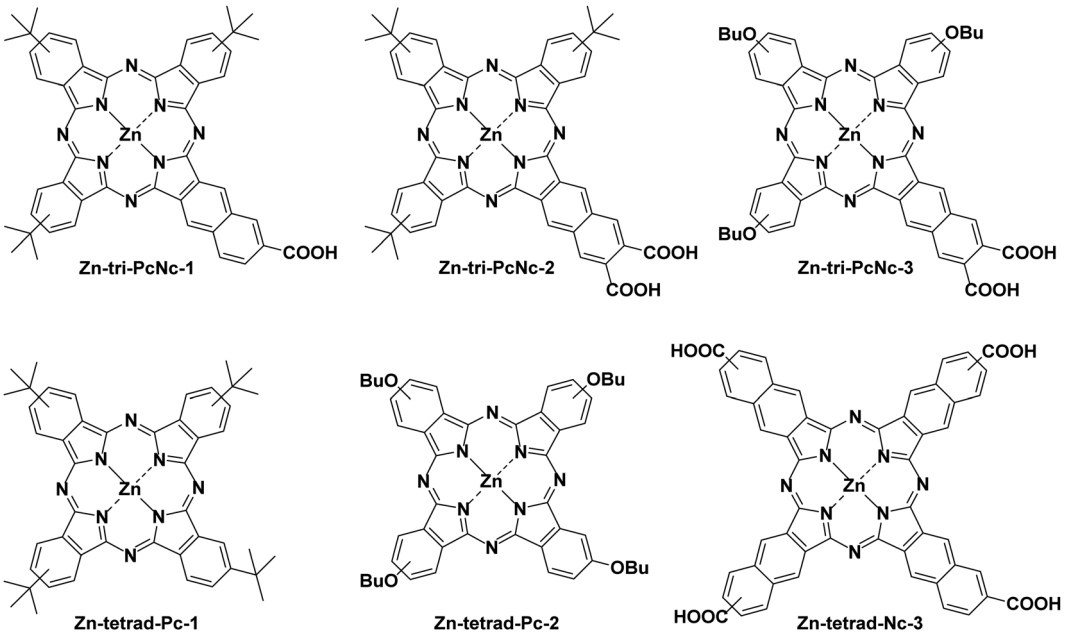

Fig. 71 Molecular structures of ZnPc derivatives.

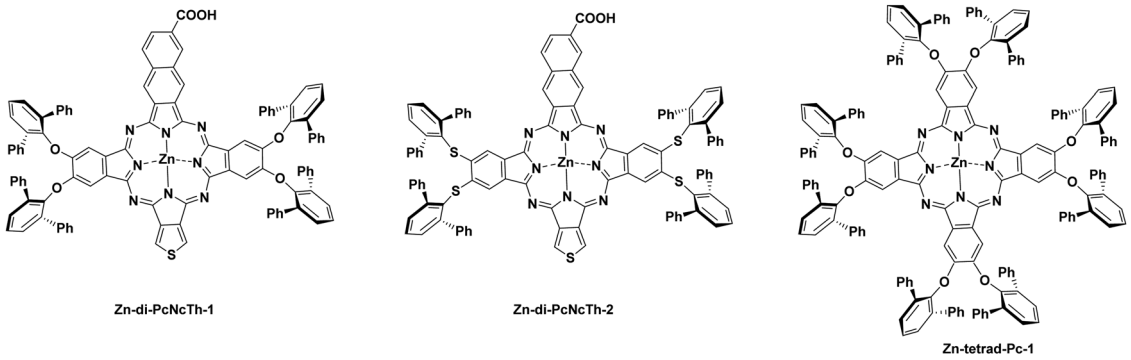

Fig. 72 Molecular structures of A_2BC type ZnPcs.

activity of the symmetrical Zn-tetrad-Pc-1 was ascribed to both the lack of directionality and lower dye loading on the Pt/g-C_3N_4 owing to the absence of the anchoring group. Co-adsorbent was not required since the peripherally substituted bulky groups suppressed the aggregation of both Pc. In the following report, the same authors used electron-rich diphenylthiophenol derivative instead of diphenylphenoxy in order to produce a redshift in the absorption into the near–IR region.[321] The novel Zn-di-PcNcTh-2 shows maximum absorbance at 744 nm, thus representing redshifts of *ca.* 16 nm, compared to Zn-di-PcNcTh-1. After optimizing the photocatalytic condition, the Zn-di-PcNcTh-2 sensitized Pt/g-C_3N_4 showed H_2 evolution activity ($\sim$232 μmol h^{-1}) with TON of $\sim$23 187 h^{-1} during the first run of 10 h visible light irradiation and much higher AQY values (4.57%, 5.53%, 4.09% and 2.35% at 730, 760, 780 and 800 nm, respectively) compared to the Zn-di-PcNcTh-1.

In 2018, Liu *et al.* reported a ZnPc derivative, with a carboxyl-naphthalene unit and three 15-crown-5 ether moieties at the peripheral positions (Fig. 73), as a photosensitizer of Pt/g-C_3N_4.[322] The resulting photocatalyst exhibits an H_2 evolution activity of 163 μmol h^{-1} with a TON of 3105 h^{-1}. Since the crown ethers can encapsulate alkali metals, Li^+, Na^+, or K^+ were added to the ZnPc solution before the dye sensitization process to assess the effect of alkali cation on the H_2 production activity. It was determined that when alkali metals are inserted in the Pc, photocatalytic activity is enhanced. The best activity of 476 μmol h^{-1} with a TON of 9067 h^{-1} was obtained when K^+ ions combine with ZnPc's 15- crown-5 ethers. This result is arising from the positive effect of increased electron injection from the excited Pc to the g-C_3N_4 and decreased charge recombination which was confirmed by fluorescence quenching experiments. In addition, the photocatalytic activity order of the alkali ions is Li < Na < K, which is compatible with the radii of these ions and the strength of the ion-ether interaction.

A nanohybrid catalyst constituted by a SiPc covalently bonded to an N-doped ultrasmall reduced graphene oxide

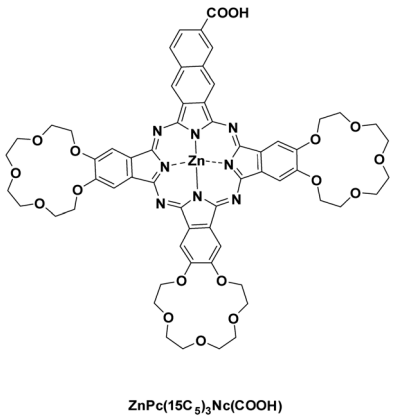

Fig. 73 Molecular structure of unsymmetrically substituted three 15-crown-5 ethers combining with alkali metal ions (such as Li^+, Na^+, or K^+).

(N-usRGO) nanosheet was reported by Yang and co-workers.[323] The SiPc was grafted to N-usRGO through 1,3-dipolar cycloaddition of azomethine ylides and the resulting material exhibits a much improved photocatalytic activity compared to N-usRGO, due to the better electron transfer from photoexcited Pcs to the Pt co-catalyst in the SiPc-N-usRGO ensembles (Fig. 74). Upon photoexcitation of N-usRGO/SiPc/Pt catalyst at >400 nm, the photoexcited electrons are transferred from the SiPcs to the N-usRGO nanosheet and then to the Pt co-catalyst onto the N-usRGO nanosheets. This cascade of electron transfer processes finally realized a hydrogen production amount of 4.5 μmol g^{-1} in 6 h with AQY of 1.3% at 365 nm.

Similarly, covalent functionalization of graphene with a manganese phthalocyanine (MnPc) by a 1,3-dipolar cycloaddition reaction was demonstrated to improve the light-absorption of the nanohybrid photocatalyst into the visible-light range.[324] Photophysical measurements confirmed that, in a hybrid catalyst in which graphene not only acts as an electron acceptor but also could act as an electron mediator, an efficient photo-induced electron transfer process occurs from the MnPc to the graphene. MnPcG/Pt photocatalyst exhibits much improved photocatalytic activity with an H_2 production activity of 8.59 and 1.45 μmol mg^{-1} under 10 h of UV-vis and visible light (>400 nm) irradiation, respectively, compared to non-covalently functionalized graphene MnPcCl/G. This result was attributed to the slow rate of the recombination process and the fast electron transfer dynamics.

4.4 Phthalocyanines as catalysts in H_2 production systems

Apart from the use of Pc derivatives as dye sensitizers, attention has also been drawn to the use of Pc derivatives as a water reduction catalysis. For example, Yaun *et al.* demonstrated that NiPc, with an iridium complex as a photosensitizer, is an efficient and stable catalyst for visible-light-driven hydrogen production in a homogeneous system.[325] This system exhibited a hydrogen production amount of 112.2 mmol with TON up to 680 after irradiation for 8 h irradiation. The H_2 evolution rate in NiPc–IrPS–TEOA system dramatically decreased when irradiation time was prolonged to 24 h due to the decomposition of the iridium complex rather than the NiPc catalyst. Furthermore, the stability of NiPc–IrPS–TEOA system was compared with a similar system in which NiPc is replaced by a $[Ni(bpy)_3]^{2+}$, in this organometallic complex the bonds between the metal and the ligand are dative. The 24 h visible light irradiation of $[Ni(bpy)_3]^{2+}$-IrPS-TEOA revealed that the deactivation of the H_2 evolution system is due to the decomposition of $[Ni(bpy)_3]^{2+}$. This result was attributed to the presence of strong Ni–N Sigma bonds in the center of the Pc macrocycle which prevents the removal of Ni cation from the central cavity of the Pc and therefore leads to higher chemical stability. A possible reaction mechanism of the light-driven H_2 production from NiPc–IrPS–TEOA system is illustrated in Fig. 75. Upon photoexcitation, the electron travels from IrPS to the NiPc which leads to the formation of the H-NiPc intermediate by breaking of Ni–N coordination bonds in NiPc. It is inferred that the site of initial protonation in NiPc is the pyridyl N with dechelation and that proton transfer from this ligand leads to the formation of [H–NiPc–H] complex followed by transformation into [Ni–H–H–Pc] species which is responsible for H_2 generation.

Song and co-workers reported on a catalyst for photoinduced H_2 generation based on a biomimetic model inspired on [FeFe]-hydrogenases, a family of metalloenzymes that can catalyze proton reduction to hydrogen in different microorganisms, as

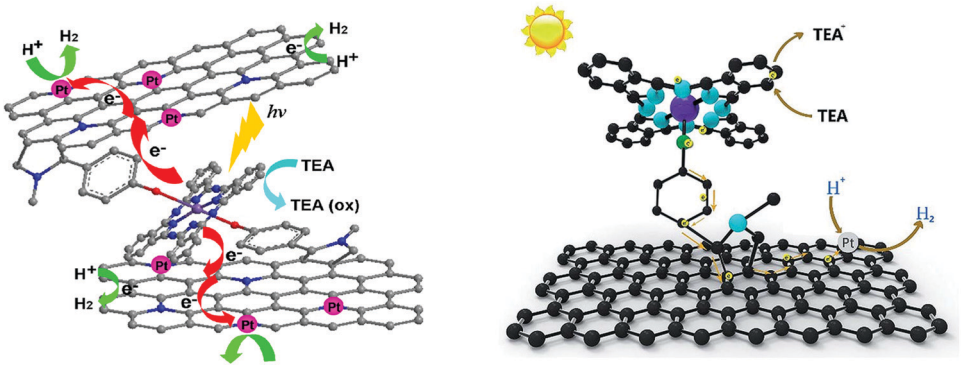

Fig. 74 (a) Mechanism of H_2 evolution in N-usRGO/SiPc/Pt photocatalyst. (b) The electron transfer in MnPcG/Pt photocatalyst. Reproduced from ref. 323, with permission from American Chemical Society, Copyright 2015.

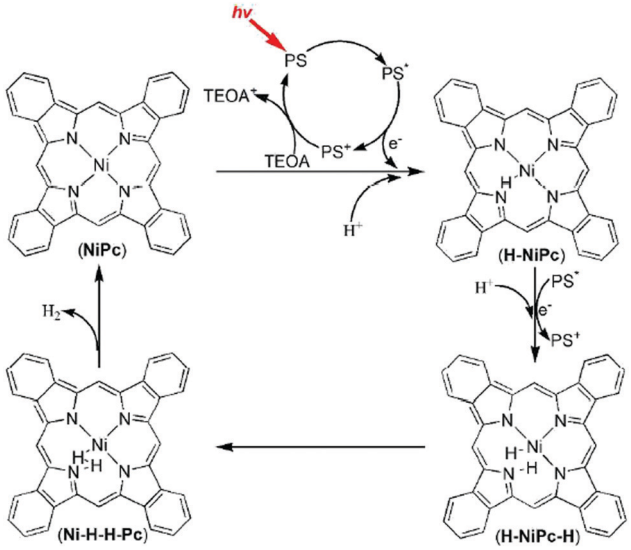

Fig. 75 Proposed mechanism of hydrogen formation by NiPc–IrPS–TEOA system. Reproduced from ref. 325, with permission from Royal Society of Chemistry, Copyright 2016.

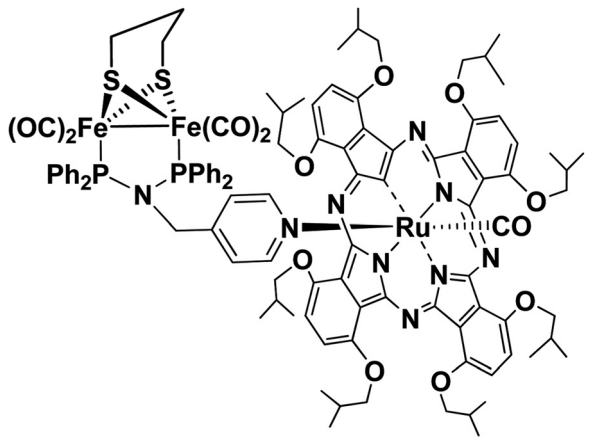

Fig. 76 Model complex for the active site of [FeFe]-hydrogenases.

an active site and RuPc as a photosensitizer (Fig. 76).[326] This photoactive complex catalyst was tested in a catalytic system composed of Et_3N as an electron donor and H_2O as a proton source under visible-light ($\lambda > 400$ nm) irradiation. However, the system exhibited low catalytic efficiency with 0.13×10^{-3} mmol of H_2 after 180 min irradiation. The weak intramolecular ET from the excited RuPc macrocycle to the catalytic diiron complex as well as the low stability of the catalyst under the experimental conditions accounted for the low catalytic performance.

5. Phthalocyanines for photocatalytic CO_2 reduction

Pc derivatives have been widely used in photocatalytic CO_2 conversion to boost light absorption and charge separation efficiency by heterogenizing semiconductors through a variety of immobilization approaches, as previously indicated. This section will focus on heterostructured composite systems in which Pcs are used as either sensitizers or catalysts for photocatalytic CO_2 reduction (Table 14).

5.1 Phthalocyanines as catalysts in heterogeneous CO_2 reduction systems

Although most catalysts for solar activated CO_2 reduction are mainly based on semiconductor-based materials, as already mentioned, the absorption of sunlight and the charge separation in single photocatalyst systems are limited. To address such challenges, the construction of a Z-scheme heterojunction that can strike a good compromise between charge separation, charge transfer directionality and improved light-harvesting ability appears to be a much more feasible way of improving solar energy conversion systems. Many Pc derivatives have been used in the construction of Z-scheme photocatalysts for photocatalytic CO_2 conversion. The coupling of Pcs derivatives with suitable semiconductors to form Z-scheme photocatalysts provides both extended absorptions in the range of the solar emission spectrum as well as superior charge transfer and separation due to their appropriate band alignment, rich redox chemistry, and high photochemical stability.

Among the metal oxide semiconductors, $BiVO_4$ is a promising photocatalyst since it offers several advantages such as chemical stability and narrow bandgap. However, its photocatalytic performance is mainly limited by slow charge separation, poor absorption in the visible range and low reduction potential. Nevertheless, attempts to enhance the charge separation process have been made by controlling the morphology, doping of metal atoms and forming heterostructures.[327]

As an example, Bian *et al.* fabricated dimension-matched ZnPc/$BiVO_4$ nanocomposites as an efficient photocatalyst for photocatalytic reduction of CO_2 based on a novel Z-scheme charge transfer mechanism.[328] ZnPc/BVNS nanocomposite was prepared by hydrogen bond interaction between the hydroxyl groups on BVNS and N atoms in the ligand of ZnPc, resulting in a stable and efficient Z scheme system (Fig. 77). As a major product, ZnPc/$BiVO_4$ photocatalyst converts CO_2 into CO, while the formation of CH_4 is also detected. Notably, the photocatalytic performance of ZnPc/$BiVO_4$ composite on CO_2 reduction achieved 16-fold higher quantum efficiency than that of $BiVO_4$ NPs. This dramatically enhanced photocatalytic activity was attributed to the established direct Z-scheme system, which promoted efficient charge separation, good match of band positions of ZnPc with BVTS and superior catalytic activity of central Zn^{2+} cation. In this particular case, upon photoexcitation, excited electrons in the CB of BVNS recombine with the holes in the HOMO of the ZnPc due to the compatible band positions of ZnPc and BVNS. Thus, electrons and holes with stronger reduction and oxidation abilities remain in ZnPc and BVTS, leading to increased photocatalytic activity. It should be noted that in this system, the electron transfer from the ligand to the central metal cation increases the catalytic activity of Zn for CO_2 reduction.

Table 14 Photocatalytic H_2 production performance of phthalocyanine derivatives

PS	Catalyst	SED	Solvent	Light source	Irr. time	H2 production	TON	AQY	Ref.
Zn-Tri-PcNc	TiO_2/Pt(0.1 wt%)	EDTA	Water	Visible light ($\lambda > 420$ nm)	5	567.4 μmol	7565	0.2%@700 nm	304
Zn-Tetra-Nc	TiO_2/Pt(0.1 wt%)	EDTA	Water	Visible light ($\lambda > 420$ nm)	5	236.5 μmol	3153		304
Zn-Tri-PcNc	TiO_2-AA/Pt	AA	Water	$\lambda > 420$ nm)	5	162.2 μmol h^{-1}		0.97%@700 nm	306
ZnPc (PCH-001)	Pt/TiO_2 (HPT)	TEOA	Water	$\lambda > 420$ nm	5	2260 μmol	18 080	11.57% @690	308
CuPc	TiO_2	CH3OH	Water	Visible light ($\lambda > 420$ nm)	7	0.95 μmol h^{-1}		6.68%@420 nm	309
ZnPc	TiO_2/Pt	TEOA	Water	Visible light ($\lambda > 420$ nm)	8	3448 μmol g^{-1} h^{-1}	—	—	310
CoPc	TiO_2/Pt	TEOA	Water	Visible light ($\lambda > 420$ nm)	8	3328 μmol g^{-1} h^{-1}	—	—	310
ZnPc1 (TT40)	TiO_2/Pt	TEOA	Water	Visible light ($\lambda > 420$ nm)	8	5.387 mmol g^{-1} h^{-1}			314
ZnPc2	TiO_2/Pt	TEOA	Water	Visible light ($\lambda > 420$ nm)	8	2.259 mmol g^{-1} h^{-1}			314
ZnPc 3	TiO_2	TEOA	Water	Visible light ($\lambda > 420$ nm)	20	3.4187 mmol gmmol g^{-1}	14 863		315
ZnPc4	TiO_2	TEOA	Water	Visible light ($\lambda > 420$ nm)	20	1.3078 mmol g^{-1}	3441		315
ZnPc 5 (TT1)	TiO_2	TEOA	Water	Visible light ($\lambda > 420$ nm)	20	1.3042 mmol g^{-1}	3142		315
SubPc 1	TiO_2/Pt	TEOA	Water	Visible light ($\lambda > 420$ nm)	8	20 332 μmol g^{-1}	—	—	320
SubPc 2	TiO_2/Pt	TEOA	Water	Visible light ($\lambda > 420$ nm)	8	16 179 μmol g^{-1}	—	—	320
SubPc 3	TiO_2/Pt	TEOA	Water	Visible light ($\lambda > 420$ nm)	8	22 345 μmol g^{-1}	—	—	320
LI-4/Zn-tri-PcNc	g-C_3N_4/Pt	AA	Water	Visible light ($\lambda > 420$ nm)	30	371.4 μmol h^{-1}	7428	1.75%@700 nm	325
Zn-Tri-PcNc-1	g-C_3N_4/Pt	AA	Water	$\lambda > 5000$ nm	10	203 μmol h^{-1}		0.71%@700 nm	326
Zn-Tri-PcNc-2	g-C_3N_4/Pt	AA	Water	$\lambda > 5000$ nm	10	263 μmol h^{-1}		0.92%@700 nm	326
Zn-Tri-PcNc-3	g-C_3N_4/Pt	AA	Water	$\lambda > 5000$ nm	10	101 μmol h^{-1}		0.35%@700 nm	326
Zn-Tetrad-Pc-1	g-C_3N_4/Pt	AA	Water	$\lambda > 5000$ nm	10	47.7 μmol h^{-1}		0.17%@700 nm	326
Zn-Tetrad-Pc-2	g-C_3N_4/Pt	AA	Water	$\lambda > 5000$ nm	10	40.9 μmol h^{-1}		0.15%@700 nm	326
Zn-Tetrad-Pc-3	g-C_3N_4/Pt	AA	Water	$\lambda > 5000$ nm	10	54.5 μmol h^{-1}		0.19%@700 nm	326
Zn-Di-PcNcTh-1	g-C_3N_4/Pt	AA	Water	$\lambda > 420$ nm	10	249 μmol h^{-1}	9960.8 h^{-1}	3.05%@730 nm	327
Zn-Tetrad-Pc-1	g-C_3N_4/Pt	AA	Water	$\lambda > 420$ nm	10	126.3 μmol h^{-1}	—	1.14%@730 nm	328
Zn-Di-PcNcTh-2/g-C3N4	g-C_3N_4/Pt	AA	Water	Visible light ($\lambda > 420$ nm)	10	232 μmol h^{-1}	23 187 h^{-1}	5.53%@760	329
ZnPc–Pt	g-C_3N_4/Pt	TEOA	Water	Visible light ($\lambda > 420$ nm)	10	163 μmol h^{-1}	3105 h^{-1}	1.88%@700	330
ZnPc–Pt/K^+	g-C_3N_4/Pt	TEOA	Water	Visible light ($\lambda > 420$ nm)	10	476 μmol h^{-1}	9067 h^{-1}	2.74%@700	330
ZnPc–Pt/Na^+	g-C_3N_4/Pt	TEOA	Water	Visible light ($\lambda > 420$ nm)	10	280 μmol h^{-1}		2.41%@700	330
ZnPc–Pt/Li^+	g-C_3N_4/Pt	TEOA	Water	Visible light ($\lambda > 420$ nm)	10	159.2 μmol h^{-1}		2.06%@700	330
SiPc	N-usRGO/Pt	TEA	Water	Xe lamp,	6	4.5 μmol g^{-1}		1.3%@365	331
MnPc	Graphene Pt	TEA	Water	$\lambda > 400$ nm	10	1.45 μmol mg_1		0.06%@670	332
IrPS	NiPc	TEOA	Water	Visible light ($\lambda > 420$ nm)	8	112.2 μmol	680		333
RuPc	[FeFe]-Hydrogenases	TEA	Water		3	0.13 × 10^{-3} mmol	—		334

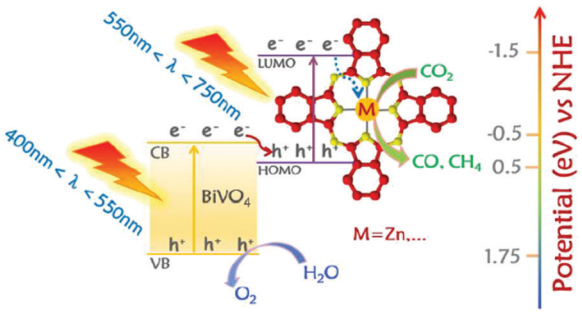

Fig. 77 Z-Scheme mechanism of ZnPc/BVNS nanocomposite. Reproduced from ref. 328, with permission from John Wiley and Sons, Copyright 2019.

Although the conversion efficiency of this Pc-based photocatalyst seems promising, the same authors stated that the limited photocatalytic activity was due to the aggregation tendency of ZnPc, which prevents the usage of the optimum amount of ZnPc required for catalytic activity.

The degree of aggregation of organic planar macrocyclic compounds like phthalocyanine has been shown to have a significant impact on light absorption, emission, active center area, and charge separation, all of which are important for photoinduced electron transfer processes.[40] Therefore, macrocycle aggregation should be suppressed in such applications, specifically on a solid support surface. Considering this, in a later work, the same collaborators further improved the efficiency and stability of ZnPc/$BiVO_4$ based Z-scheme heterojunction by using a graphene layer to minimize self-aggregation of ZnPc onto BVNS.[329] Acid treatment of graphene increases the number of hydroxyl groups on the surface and enabled ZnPc to bind to both BVNS and graphene surface *via* hydrogen bonding. Indeed, the optimized ultrathin ZnPc/graphene/$BiVO_4$ heterojunctions exhibited superior photocatalytic conversion of CO_2 to CO, (14-fold higher) than that of bare $BiVO_4$ nanosheet. This improvement can be attributed to two main factors: (i) graphene's two-dimensional structure and further functionalization of graphene with OH groups allows for a larger amount of highly dispersed ZnPc assembly on BVNS with the proper thickness; (ii) graphene acts as an electron bridge for optimum electronic coupling between ZnPc and $BiVO_4$, resulting in increased charge separation in the Z scheme (Fig. 78).

Very recently, the further improved conversion efficiency of CO_2 to CO has been achieved by CuPc/Au-BVNS heterojunctions, which exhibit a 9-time and 35-time increase in photoactivity compared to pristine BVNS and the $BiVO_4$ nanoflake, respectively.[330] The authors attributed this success to the use of Au nanoparticles as an interfacial modulator, which improved electron transfer directionality in BVNS to CuPc, as well as increased CuPc loading amounts due to a superior interaction between AuNP and the N-atom of the Pc macrocycle. Indeed, as compared to the previously reported H-bond interfacial interaction, the Au nanoparticle had a better connection with the N-atom of the MPc ligand, resulting in a faster Z-scheme charge-transfer mechanism. The CuPc/Au-BVNS heterojunction system produced CO and CH_4 as main reduction products by a direct Z-scheme charge carrier transfer mechanism, wherein the photogenerated electrons of the CuPc and holes of the BVNS are protected, while the photogenerated electrons of the BVNS and holes of the CuPc are recombined. The protected electrons of CuPc are efficiently utilized for the reduction of CO_2 to CO (Fig. 79).

Another semiconductor photocatalyst that has been used for photocatalytic CO_2 reduction is tungsten trioxide (WO_3), as its narrow bandgap (2.4–2.8 V) and stable physicochemical properties make it a promising candidate for photocatalytic applications.[331] On the other hand, the use of WO_3 in the photocatalytic process encounters many limits such as small surface area, limited charge separation and absorption in the visible region. Since the HOMO energy band level of Pcs is close to the CB level of WO_3, combining Pc and WO_3 under the Z scheme system has been found to be a feasible way to increase the photocatalytic activity of WO_3-based photocatalysts. Recently, Li *et al.* reported Z-scheme FePc/WO_3 composite for the reduction of CO_2 to CH_4.[332] Compared to the WO_3 nanoplate, FePc/P-WO_3 nanocomposites exhibited 8-fold high photocatalytic activity for converting CO_2 to CO and CH_4. This success was explained by the high surface area of nanocomposites, the better charge separation between FePc and WO_3 and the catalytic activity of central metal cation in the Pc macrocycle (Fig. 80).

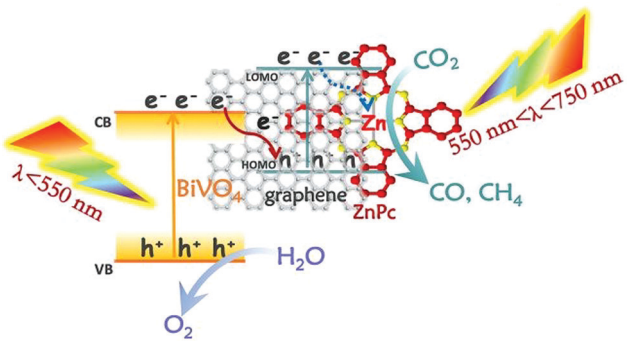

Fig. 78 Graphene-modulated ZnPc/$BiVO_4$ Z-scheme heterojunction. Reproduced from ref. 329, with permission from Royal Society of Chemistry, Copyright 2020.

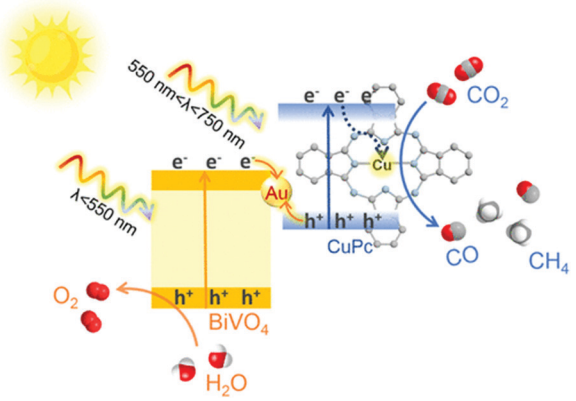

Fig. 79 CuPc/Au-BVNS Z-scheme heterojunction. Reproduced from ref. 330, with permission from American Chemical Society, Copyright 2021.

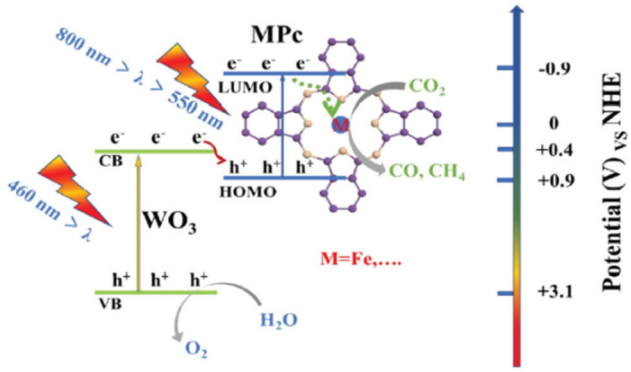

Fig. 80 FePc/P-WO_3 Z-scheme heterojunction. Reproduced from ref. 332, with permission from Elsevier, Copyright 2020.

Metal-free organocatalyst such as graphitic carbon nitride (g-C_3N_4) has drawn a lot of attention due to its suitable band position, high photochemical stability, two-dimensional structure and low cost which make it favourable alternatives to the metal oxide-based semiconductors.[333] Recent studies have shown that coupling g-C_3N_4 with metal oxide in heterostructure form or coupling with a similar 2D structure of organic semiconductors like Pcs has a positive effect on charge separation as well as efficient solar photon harvesting and photocatalytic activity. For example, Li *et al.* reported a heterostructure g-C_3N_4/CuPc composite for photocatalytic conversion of CO_2. In this study, the ultrathin dimension-matched metal phthalocyanine/treated g-C_3N_4 (MPc/T-CN) was constructed through the H-bonding formation between N atom of Pc and hydroxyl groups on CN. The treatment of g-C_3N_4 nanolayers with HNO_3 solution increases the number of hydroxyl groups on the CN surfaces, resulting in a uniform distribution of MPc on the CN and preventing Pc aggregation on the surface, improving the photocatalytic activity and stability of the MPc/CN heterojunction. When comparing the photoactivity, this hybrid photocatalyst exhibited a 10-fold higher CO production rate than pristine g-C_3N_4.[334] The advanced photocatalytic activity was ascribed to the unexpected transfer of excited high-level-energy electrons (HLEEs) from g-C_3N_4 to the ligand of CuPc and then to the central metal ions (Cu^{2+}) with potential catalytic function for CO_2 reduction reactions (Fig. 81).

Due to the excellent CO_2 adsorption capacity and the suitable band edge position, which has a good match with CN for effective HLEEs transfer, the CuPc-based system exhibit better photocatalytic activity than FePc and CoPc. This study emphasized in particular that the formation of dimensional match interface by coupling with two-dimensional g-C_3N_4 and planar Pc ensures increased charge transfer.

Of the transition metal-containing Pc derivatives, cobalt phthalocyanine (CoPc) has been identified as one of the most promising electrocatalysts for CO_2 reduction owing to its ultrahigh selectivity and reasonable efficiencies for CO production.[335] Immobilization of molecular catalysts onto conductive supports has proven to be a promising tactic to promote the selectivity and stability of the resulting hybrid photocatalyst.

For this purpose, a hybrid heterogeneous photocatalyst was prepared in which polymeric CoPc as a catalytic center was immobilized onto mesoporous carbon nitrite as a light harvester in order to be used in CO_2 reduction under visible light irradiation.[336] The deposition of CoPPc on mpg-CNx by an *in situ* polymerization method gives the formation of the polymer–CNx interface which allows efficient photoexcited electron transfer from CNx to the attached CoPPc catalyst. The photocatalytic activities of pristine mpg-CNx and the mpg-CNx/CoPPc hybrid catalyst were tested in CO_2-saturated MeCN with TEOA as a sacrificial electron donor. While mpg-CNx/CoPPc exhibits a high conversion efficiency for the CO_2 to CO, the former one generates only trace amounts of CO. Indeed, this hybrid catalyst generated 1076 μmol g^{-1} CO after 60 h with 85% selectivity and 90 turnovers. In the CO_2 reduction process, upon photoexcitation, the electron travels from the CNx to CoPc, forming Co(I) centre on which CO_2 binds followed by a second electron transfer from mpg-CNx led to the conversion of CO_2 to CO (Fig. 82). The success of this hybrid catalyst has been attributed to both controlling the amount of catalyst and creating a better interface between Pc and CNx that facilitates electron transfer thanks to the *in situ* polymerization technique.

Liu *et al.* demonstrated the improved photocatalytic reduction of CO_2 using the hybrid photocatalyst formed by CoPc immobilized on phosphorus-doped graphitic carbon

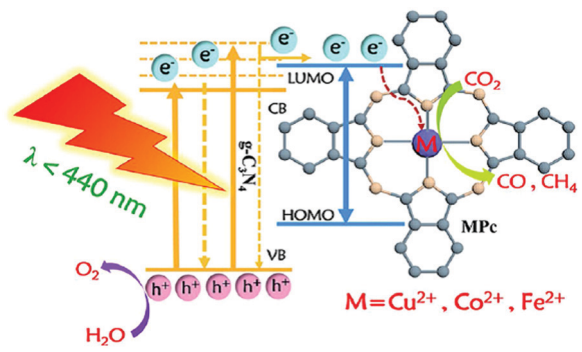

Fig. 81 HLEEs transfer process in the MPc/T-CN heterojunction. Reproduced from ref. 334, with permission from Elsevier, Copyright 2020.

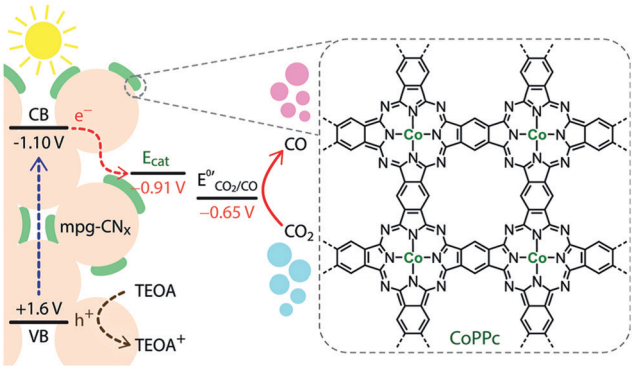

Fig. 82 mpg-CNx/CoPPc hybrid photocatalyst. Reproduced from ref. 336, with permission from John Wiley and Sons, Copyright 2019.

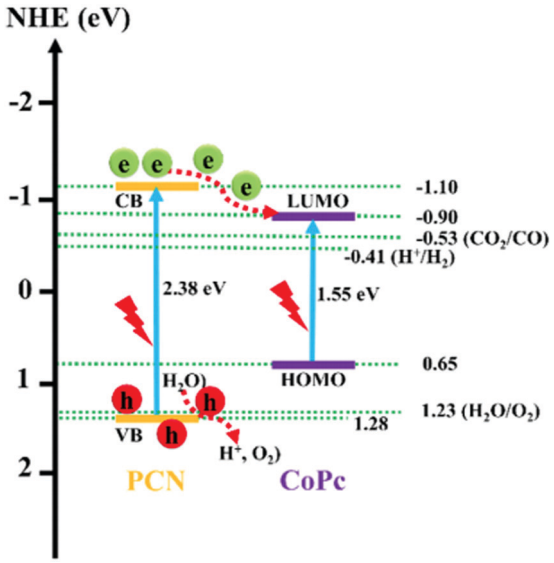

Fig. 83 Photoreduction of CO_2 with water using Co@PCN hybrid photocatalyst. Reproduced from ref. 337, with permission from Elsevier, Copyright 2021.

nitride.[337] It was found that the doping of phosphorous atoms into CN's framework enlarges the absorption spectra of g-C_3N_4 by reducing the bandgap and increasing the stability, while the incorporation of CoPc retarded charge recombination. Upon irradiation, the excited electrons at CB of PCN are transferred to the LUMO of CoPc where a CO_2 reduction reaction takes place (Fig. 83). The CoPc@P–g-C_3N_4 hybrid photocatalyst exhibited a conversion efficiency yield of 295 μmol g^{-1} for CO with the stability of up to six consecutive runs.

Lin and co-workers prepared the first example of photoelectrochemical cell CO_2 reduction with molecular catalyst driving both CO_2 reduction and H_2O oxidation using noble-metal-free materials.[338] This system is very efficient in the suppression of concurrent H_2 evolution and promoting CO generation. Light-driven CO_2 reduction was performed in a two-electrode photoelectrochemical cell (PEC) composed of a fluorinated Co_4O_4 cubane complex-modified $BiVO_4$ photoanode and a perfluorinated cobalt phthalocyanine complex-modified carbon cloth (cc) cathode. The use of hydrophobic fluorinated molecular catalyst is an efficient strategy to improve the long-term stability of the photoelectrodes in an aqueous solution. Under 1 sun AM 1.5 G illumination, simultaneous O_2 and CO evolution in a ratio of about 2 : 1 in a CO_2-saturated $NaHCO_3$ aqueous solution were achieved with high faradaic efficiency up to 87% for CO production and a remarkable solar energy conversion efficiency up to 0.44% at a cell potential of 0.8 V.

5.2 Phthalocyanines as photosensitizers in heterogeneous CO_2 reduction systems

Incorporation of Pcs as a photosensitizer onto semiconductors by means of either covalent or non-covalent interaction to form a hybrid photocatalyst is another way to improve the efficiency and selectivity of CO_2 photoreduction under visible light illumination. In this photocatalytic system, Pcs play an essential

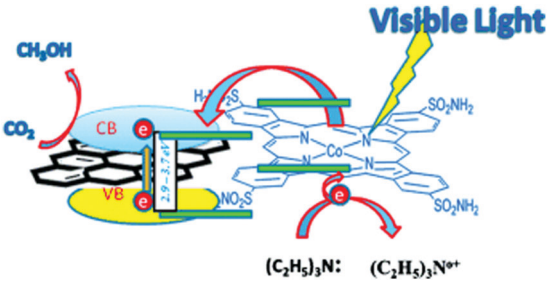

Fig. 84 Possible mechanistic pathway of CO_2 reduction by using GO-CoPc photocatalyst. Reproduced from ref. 339, with permission from John Wiley and Sons, Copyright 2014.

role as a sensitizer in harvesting visible light and promoting charge injection into the conduction band of the catalyst.

For example, a hybrid photocatalyst consisting of CoPc covalently linked to graphene oxide was reported by Kumar *et al.*[339] The photoreduction activity of GO-CoPc was tested by using TEA as SED and water as a solvent. The methanol was obtained as a major product and the conversion rate of methanol reached 78.7893 μmol g^{-1} cat h^{-1} under visible-light irradiation for 48 h. The GO-CoPc photocatalyst exhibited superior catalytic activity in comparison with the bare GO and the physical 1 : 1 mixture of GO–CoPc, methanol was obtained as a major product. The authors suggested that the covalent attachment of CoPc to GO reduces the bandgap of GO, resulting in efficient electron injection from CoPc into the conduction band of GO, which greatly increases the conversion efficiency of CO_2 with H_2O to CH_3OH (Fig. 84).

With the same motivation, Kumar *et al.* prepared a hybrid photocatalyst composed of cobalt(II) phthalocyanine tetracarboxylate (CoPc–COOH) and g-C_3N_4 for the visible light assisted reduction of CO_2 to methanol.[340] The photocatalytic activity of the hybrid photocatalyst was tested in a water/DMF system in the presence of TEA as a sacrificial agent under visible light. The hybrid photocatalyst produced a higher CH_3OH yield (12.9 mmol g^{-1}) with a conversion rate of 538.75 mmol h^{-1} g^{-1}cat. than its homogeneous counterparts, CoPc-COOH and g-C_3N_4. The better catalytic activity was found to be originated from the combination of Pc with g-C_3N_4 which potentially confer a synergetic effect such as superior charge transfer, large surface area and high CO_2 concentration due to the high binding ability of the CoPc complex with CO_2 (Fig. 85).

Recently, the same authors developed a novel hybrid photocatalyst by immobilization of CoPc onto bismuth-oxybromide (BOB).[341] Methanol was obtained as a main CO_2 reduction product during the photoreduction experiments over CoPc/BOB hybrid photocatalyst in DMF/water solution by using TEA as a sacrificial electron donor under visible light illumination. The efficiency of methanol production of up to 3485 μmol g^{-1} with a formation rate of 145.2 μmol h^{-1} g^{-1}, which is significantly higher than that of pristine CoPc and BOB photocatalysts. Once again, the higher photocatalytic activity was attributed to an efficient photo-stimulated electron transfer from CoPc to BOB, a higher concentration of CO_2 at the surface, and obtaining

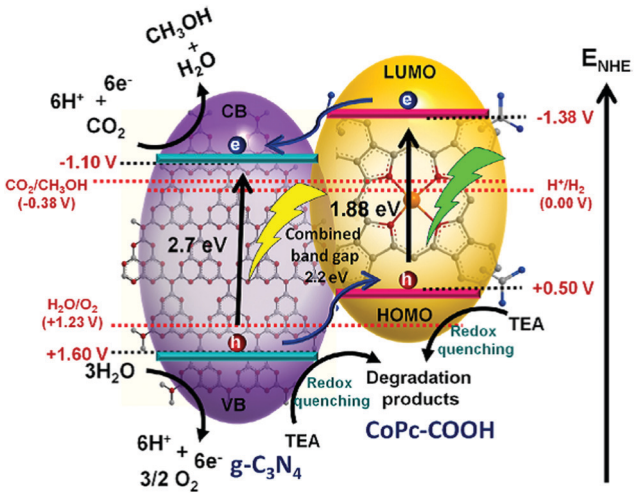

Fig. 85 Mechanism of CO_2 photoreduction by using g-C_3N_4/CoPc-COOH photocatalyst. Reproduced from ref. 340, with permission from Elsevier, Copyright 2019.

the appropriate band gap for reducing CO_2 to methanol by binding CoPc to the BOB surface.

Another type of composite, composed of tin phthalocyanine supported to mesoporous ceria (*meso*-CeO_2) was prepared and used as a photocatalyst for visible light assisted photoreduction of CO_2.[342] *meso*-CeO_2 has been inserted at the axial position of Tin(IV) phthalocyanine dichloride *via* –OH groups on the surface, resulting in a recyclable and reusable photocatalyst (Fig. 86). The photocatalytic CO_2 reduction performance of heterogeneous SnPc@CeO_2 was tested in a DMF–water–triethylamine mixture, methanol and CO were observed as photoreduction products. Compared to the *meso*-CeO_2 and homogeneous $SnPcCl_2$, SnPc@CeO_2 exhibits a higher product formation rate for methanol (97.5 μmol h^{-1} g^{-1} cat) and CO (35.0 μmol h^{-1} g^{-1} cat) thanks to the better charge injection from the excited state of the SnPc into the *meso*-CeO_2 conduction band.

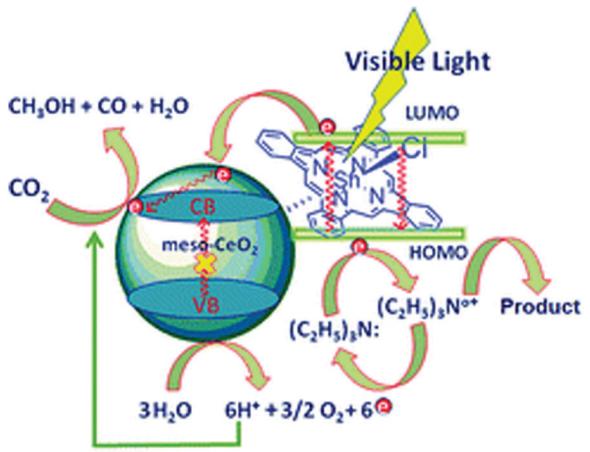

Fig. 86 Mechanism of CO_2 reduction over SnPc@CeO_2 catalyst. Reproduced from ref. 342, with permission from Royal Society of Chemistry, Copyright 2015.

6. Summary and outlook

As discussed in this review, plenty of porphyrins and phthalocyanines have been mostly employed as photo- and redox-active building blocks in photocatalytic H_2 production and CO_2 reduction schemes. The inspiration for all the above systems is derived from the natural photosynthesis, motivating scientists to prepare a vast number of artificial photosynthetic models. This review thoroughly described the role of porphyrin and phthalocyanine derivatives as photosensitizers, catalysts as well as co-catalysts and the effect of their structural modifications at the photocatalytic activity towards H_2 production and CO_2 reduction. Before analyzing the problems that most of the systems have, we can come to some conclusions. It is apparent that the homogeneous photocatalytic schemes can provide more insights into the catalytic mechanism whereas they are generally less stable compared to analogous heterogeneous systems. We can also point out that despite the numerous photocatalytic CO_2 conversion approaches, there are not many examples generating C2+ reduction products which are considerably more valuable. Moreover, from a statistical perspective, one can see that during the last years the research in CO_2 reduction is increasing more rapidly compared to the growth of H_2 production studies.

Scientists working in this field must deal with plenty of issues and challenges due to some inherent characteristics of the photocatalytic systems. Firstly, most of the systems described herein, have relatively low activity and therefore cannot compete with the present industrial methods to produce H_2 (from natural gas, oil, coal or electrolysis). To improve the activity of these schemes it is important to understand in depth the catalytic mechanism of the photocatalytic processes and identify the key factors determining the activity and selectivity. Another challenging endeavor concerns the improvement of stability of the catalytic systems and eliminate the presence of sacrificial agents. The dye sensitization on semiconductors opened the way for the development of molecular-based DSPECs and tandem cell devices based on porphyrins and phthalocyanines. These systems are one step closer to a real-world application since there is no need for sacrificial agents and they offer more stable catalysts and photosensitizers. There is also a need for low-cost materials which can be solved by focusing on the development of noble-metal free systems.

In summary, the increasing energy demands, and environmental issues caused by the over-exploitation of fossil fuels render the need for renewable, clean, and environmentally benign energy sources undoubtedly urgent. The zero-emission energy carrier, H_2 is an ideal alternative to carbon-based fuels especially when it is generated photocatalytically from water. Additionally, the photocatalytic conversion of CO_2 into chemical fuels and raw materials will both provide the CO_2 emission balance and have a significant environmental and economic impact. Therefore, the research on the photocatalytic systems discussed herein is an important challenge and has attracted plenty of scientific attention.

Abbreviation list

AA	Ascorbic acid

$AcrH_2$	Dihydroacridine
BODIPY	Boron-dipyrromethene
BPY	2,2′-Bipyridine
CA	Chloranilic acid
CB	Conduction band
COF	Covalent organic framework
CTAB	Cetyltrimethyl ammonium bromide
DSP	Dye-sensitized photocatalyst
DSPEC	Dye sensitized photoelectrochemical cell
DSSC	Dye sensitized solar cell
EDTA	Ethylenediaminetetraacetic acid
FTO	Fluorine doped tin oxide
HER	Hydrogen evolution reaction
HLEEs	High-level-energy electrons
HNTM	Hollow nanotubes
HOMO	Highest occupied molecular orbital
LBG	*N,N′*-Bis(octadecyl)-L-Boc-glutamic diamide
LED	Light-emitting diode
LP	Liposome
LUMO	Lowest unoccupied molecular orbital
MeCN	Acetonitrile
MOF	Metal organic framework
MOPS	3-Morpholinopropane-1-sulfonic acid
MTAB	Myristyltrimethylammonium bromide
MV	Methyl viologen
NI	Naphthalimide
NIR	Near-infrared
NPs	Nanoparticles
ONCs	Organic nanocrystals
PCOF	Porphyrinic covalent organic framework
Pcs	Phthalocyanines
PMOF	Porphyrin metal organic framework
POMs	Polyoxometalates
Por	Porphyrins
PS	Photosensitizer
PVP	Polyvinylpyrrolidone
RGO	Reduced-graphene oxide
SAC	Single atom catalyst
SC	Semiconductor
SDS	Sodium dodecyl sulfate
SED	Sacrificial electron donor
TCEP	Tris-(2-carboxyethyl)phosphine
TEA	Triethylamine
TEOA	Triethanolamine
TFA	Trifluoroacetic acid
TON	Turnover number
TON	Turnover frequency
TsOH	*P*-Toluenesulfonic acid
VB	Valence band
WOR	Water oxidation reaction

Conflicts of interest

There are no conflicts to declare.

Acknowledgements

This research was funded by the General Secretariat for Research and Technology (GSRT) and Hellenic Foundation for Research and Innovation (HFRI; project code: 508). This research has been co-financed by the European Union and Greek national funds through the Regional Operational Program ''Crete 2014–2020,'' project code OPS: 5029187. Moreover, the European Commission's Seventh Framework Program (FP7/2007–2013) under grant agreement no. 229927 (FP7-REGPOT-2008-1, Project BIO-SOLENUTI) and the Special Research Account of the University of Crete are gratefully acknowledged for the financial support.

References

1 Q. Schiermeier, J. Tollefson, T. Scully, A. Witze and O. Morton, *Nature*, 2008, **454**, 816–823.
2 O. Almora, D. Baran, G. C. Bazan, C. Berger, C. I. Cabrera, K. R. Catchpole, S. Erten-Ela, F. Guo, J. Hauch, A. W.-Y. Ho-Baillie, T. J. Jacobsson, R. A.-J. Janssen, T. Kirchartz, N. Kopidakis, Y. Li, M. A. Loi, R. R. Lunt, X. Mathew, M. D. McGehee, J. Min, D. B. Mitzi, M. K. Nazeeruddin, J. Nelson, A. F. Nogueira, U. W. Paetzold, N.-G. Park, B. P. Rand, U. Rau, H. J. Snaith, E. Unger, L. Vaillant-Roca, H.-L. Yip and C. J. Brabec, *Adv. Energy Mater.*, 2021, **11**, 2002774.
3 V. Humphrey, J. Zscheischler, P. Ciais, L. Gudmundsson, S. Sitch and S. I. Seneviratne, *Nature*, 2018, **560**, 628–631.
4 A. Goeppert, M. Czaun, J. P. Jones, G. K. Surya Prakash and G. A. Olah, *Chem. Soc. Rev.*, 2014, **43**, 7995–8048.
5 N. Armaroli and V. Balzani, *ChemSusChem*, 2011, **4**, 21–36.
6 D. A.-J. Rand and R. M. Dell, *Hydrogen Energy: Challenges and Prospects*, Royal Society of Chemistry, 2008, pp. 1–300.
7 D. Gust, T. A. Moore and A. L. Moore, *Acc. Chem. Res.*, 2009, **42**, 1890–1898.
8 T. Keijer, T. Bouwens, J. Hessels and J. N.-H. Reek, *Chem. Sci.*, 2020, **12**, 50–70.
9 R. J. Cogdell, T. H.-P. Brotosudarmo, A. T. Gardiner, P. M. Sanchez and L. Cronin, *Biofuels*, 2010, **1**, 861–876.
10 H. Shen, T. Peppel, J. Strunk and Z. Sun, *Sol. RRL*, 2020, **4**, 1900546.
11 W. Luc, M. Jouny, J. Rosen and F. Jiao, *Energy Environ. Sci.*, 2018, **11**, 2928–2934.
12 Z. Sun, T. Ma, H. Tao, Q. Fan and B. Han, *Chem*, 2017, **3**, 560–587.
13 S. Garg, M. Li, A. Z. Weber, L. Ge, L. Li, V. Rudolph, G. Wang and T. E. Rufford, *J. Mater. Chem. A*, 2020, **8**, 1511–1544.
14 B. Kumar, J. P. Brian, V. Atla, S. Kumari, K. A. Bertram, R. T. White and J. M. Spurgeon, *Catal. Today*, 2016, **270**, 19–30.
15 R. Francke, B. Schille and M. Roemelt, *Chem. Rev.*, 2018, **118**, 4631–4701.
16 F. Gong, H. Zhu, Y. Zhang and Y. Li, *J. CO2 Util.*, 2018, **28**, 221–227.

17 Ž. Kovačič, B. Likozar and M. Huš, *ACS Catal.*, 2020, **10**, 14984–15007.
18 S. Xie, Q. Zhang, G. Liu and Y. Wang, *Chem. Commun.*, 2016, **52**, 35–59.
19 M. Kirch, J.-M. Lehn and J.-P. Sauvage, *Helv. Chim. Acta*, 1979, **62**, 1345–1384.
20 T. Inoue, A. Fujishima, S. Konishi and K. Honda, *Nature*, 1979, **277**, 637–638.
21 A. Fujishima and K. Honda, *Nature*, 1972, **238**, 37–38.
22 X. Chen, S. Shen, L. Guo and S. S. Mao, *Chem. Rev.*, 2010, **110**, 6503–6570.
23 W. Fan, Q. Zhang and Y. Wang, *Phys. Chem. Chem. Phys.*, 2013, **15**, 2632–2649.
24 A. Kudo and Y. Miseki, *Chem. Soc. Rev.*, 2009, **38**, 253–278.
25 B. Cecconi, N. Manfredi, T. Montini, P. Fornasiero and A. Abbotto, *Eur. J. Org. Chem.*, 2016, 5194–5215.
26 A. Hagfeldt, G. Boschloo, L. Sun, L. Kloo and H. Pettersson, *Chem. Rev.*, 2010, **110**, 6595–6663.
27 J. F. Huang, Y. Lei, T. Luo and J. M. Liu, *ChemSusChem*, 2020, **13**, 5863–5895.
28 M. Watanabe, *Sci. Technol. Adv. Mater.*, 2017, **18**, 705–723.
29 X. Zhang, T. Peng and S. Song, *J. Mater. Chem. A*, 2016, **4**, 2365–2402.
30 M. Joseph and S. Haridas, *Int. J. Hydrogen Energy*, 2020, **45**, 11954–11975.
31 S. N. Yun, N. Vlachopoulos, A. Qurashi, S. Ahmad and A. Hagfeldt, *Chem. Soc. Rev.*, 2019, **48**, 3705–3722.
32 A. B. Munoz-Garcia, I. Benesperi, G. Boschloo, J. J. Concepcion, J. H. Delcamp, E. A. Gibson, G. J. Meyer, M. Pavone, H. Pettersson, A. Hagfeldt and M. Freitag, *Chem. Soc. Rev.*, 2021, **50**, 12450–12550.
33 P. T. Xu, N. S. McCool and T. E. Mallouk, *Nano Today*, 2017, **14**, 42–58.
34 B. B. Beyene and C.-H. Hung, *Coord. Chem. Rev.*, 2020, **410**, 213234.
35 S. C. Zhang, H. N. Ye, J. L. Hua and H. Tian, *EnergyChem*, 2019, **1**, 100015.
36 M. V. Martínez-Díaz, G. De La Torre and T. Torres, *Chem. Commun.*, 2010, **46**, 7090–7108.
37 G. Bottari, O. Trukhina, M. Ince and T. Torres, *Coord. Chem. Rev.*, 2012, **256**, 2453–2477.
38 K. Ladomenou, M. Natali, E. Iengo, G. Charalampidis, F. Scandola and A. G. Coutsolelos, *Coord. Chem. Rev.*, 2015, **304-305**, 38–54.
39 J. Min Park, J. H. Lee and W. D. Jang, *Coord. Chem. Rev.*, 2020, **407**, 213157.
40 G. Bottari, G. de la Torre, D. M. Guldi and T. Torres, *Coord. Chem. Rev.*, 2021, **428**, 213605.
41 T. Lazarides, M. Delor, I. V. Sazanovich, T. M. Mc Cormick, I. Georgakaki, G. Charalambidis, J. A. Weinstein and A. G. Coutsolelos, *Chem. Commun.*, 2014, **50**, 521–523.
42 A. Panagiotopoulos, K. Ladomenou, D. Sun, V. Artero and A. G. Coutsolelos, *Dalton Trans.*, 2016, **45**, 6732–6738.
43 G. B. Bodedla, W.-Y. Wong and X. Zhu, *J. Mater. Chem. A*, 2021, **9**, 20645–20652.
44 G. Landrou, A. A. Panagiotopoulos, K. Ladomenou and A. G. Coutsolelos, *J. Porphyrins Phthalocyanines*, 2016, **20**, 534–541.
45 N. Queyriaux, E. Giannoudis, C. D. Windle, S. Roy, J. Pécaut, A. G. Coutsolelos, V. Artero and M. Chavarot-Kerlidou, *Sustainable Energy Fuels*, 2018, **2**, 553–557.
46 E. Giannoudis, E. Benazzi, J. Karlsson, G. Copley, S. Panagiotakis, G. Landrou, P. Angaridis, V. Nikolaou, C. Matthaiaki, G. Charalambidis, E. A. Gibson and A. G. Coutsolelos, *Inorg. Chem.*, 2020, **59**, 1611–1621.
47 L. Mintrop, J. Windisch, C. Gotzmann, R. Alberto, B. Probst and P. Kurz, *J. Phys. Chem. B*, 2015, **119**, 13698–13706.
48 S. Salzl, M. Ertl and G. Knör, *Phys. Chem. Chem. Phys.*, 2017, **19**, 8141–8147.
49 S. S. Nurttila, R. Becker, J. Hessels, S. Woutersen and J. N.-H. Reek, *Chem. – Eur. J.*, 2018, **24**, 16395–16406.
50 P. Lang, J. Habermehl, S. I. Troyanov, S. Rau and M. Schwalbe, *Chem. – Eur. J.*, 2018, **24**, 3225–3233.
51 J. C. Manton, C. Long, J. G. Vos and M. T. Pryce, *Dalton Trans.*, 2014, **43**, 3576–3583.
52 X. Liu, J. Zhou, M. Meng, G. Y. Zhu, Y. Tan, X. Chen, J. Wei, D. B. Kuang, Y. Y. Wu, S. Su, T. Cheng, Y. Zhou and C. Y. Liu, *Appl. Catal., B*, 2021, **286**, 119836.
53 D. N. Tritton, G. B. Bodedla, G. Tang, J. Zhao, C. S. Kwan, K. C.-F. Leung, W. Y. Wong and X. Zhu, *J. Mater. Chem. A*, 2020, **8**, 3005–3010.
54 K. Zheng, G. B. Bodedla, Y. Hou, J. Zhang, R. Liang, J. Zhao, D. Lee Phillips and X. Zhu, *J. Mater. Chem. A*, 2022, **10**, 4440–4445.
55 M. Natali, A. Luisa, E. Iengo and F. Scandola, *Chem. Commun.*, 2014, **50**, 1842–1844.
56 B. B. Beyene and C. H. Hung, *Sustainable Energy Fuels*, 2018, **2**, 2036–2043.
57 O. M. Yaghi, M. J. Kalmutzki and C. S. Diercks, *Introduction to Reticular Chemistry: Metal-Organic Frameworks and Covalent Organic Frameworks*, Wiley-VCH, Weinheim, 2019.
58 J. Otsuki, *J. Mater. Chem. A*, 2018, **6**, 6710–6753.
59 T. Keijer, T. Bouwens, J. Hessels and J. N.-H. Reek, *Chem. Sci.*, 2021, **12**, 50–70.
60 C. M. Drain, A. Varotto and I. Radivojevic, *Chem. Rev.*, 2009, **109**, 1630–1658.
61 Y. Zhong, S. Liu, J. Wang, W. Zhang, T. Tian, J. Sun and F. Bai, *APL Mater.*, 2020, **8**, 120706.
62 C. Zhang, P. Chen, H. Dong, Y. Zhen, M. Liu and W. Hu, *Adv. Mater.*, 2015, **27**, 5379–5387.
63 H. Wang, Y. Song, Z. Wang, C. J. Medforth, J. E. Miller, L. Evans, P. Li and J. A. Shelnutt, *Chem. Mater.*, 2008, **20**, 7434–7439.
64 J. Wang, Y. Zhong, L. Wang, N. Zhang, R. Cao, K. Bian, L. Alarid, R. E. Haddad, F. Bai and H. Fan, *Nano Lett.*, 2016, **16**, 6523–6528.
65 Y. Zhong, Y. Hu, J. Wang, J. Wang, X. Ren, J. Sun and F. Bai, *MRS Adv.*, 2019, **4**, 2071–2078.
66 N. Zhang, L. Wang, H. Wang, R. Cao, J. Wang, F. Bai and H. Fan, *Nano Lett.*, 2018, **18**, 560–566.
67 Y. Liu, L. Wang, H. Feng, X. Ren, J. Ji, F. Bai and H. Fan, *Nano Lett.*, 2019, **19**, 2614–2619.

68 L. J. Liu, Y. D. Lai, H. H. Li, L. T. Kang, J. J. Liu, Z. M. Cao and J. N. Yao, *J. Mater. Chem. A*, 2017, **5**, 8029–8036.
69 X. Tian, C. Lin, Z. Zhong, X. Li, X. Xu, J. Liu, L. Kang, G. Chai and J. Yao, *Cryst. Growth Des.*, 2019, **19**, 3279–3287.
70 Z. Zhang, Y. Zhu, X. Chen, H. Zhang and J. Wang, *Adv. Mater.*, 2019, **31**, 1806626.
71 J. Jing, J. Yang, Z. Zhang and Y. Zhu, *Adv. Energy Mater.*, 2021, **11**, 2101392.
72 G. Yang, C. Lin, X. Feng, T. Wang and J. Jiang, *Chem. Commun.*, 2020, **56**, 527–530.
73 Q. Zou, L. Zhang, X. Yan, A. Wang, G. Ma, J. Li, H. Möhwald and S. Mann, *Angew. Chem., Int. Ed.*, 2014, **53**, 2366–2370.
74 J. Li, A. Wang, L. Zhao, Q. Dong, M. Wang, H. Xu, X. Yan and S. Bai, *ACS Appl. Mater. Interfaces*, 2018, **10**, 28420–28427.
75 Q. Zou, M. Abbas, L. Zhao, S. Li, G. Shen and X. Yan, *J. Am. Chem. Soc.*, 2017, **139**, 1921–1927.
76 K. Liu, R. Xing, Y. Li, Q. Zou, H. Möhwald and X. Yan, *Angew. Chem., Int. Ed.*, 2016, **55**, 12503–12507.
77 K. Liu, M. Abass, Q. Zou and X. Yan, *Green Energy Environ.*, 2017, **2**, 58–63.
78 E. Nikoloudakis, K. Karikis, J. Han, C. Kokotidou, A. Charisiadis, F. Folias, A. M. Douvas, A. Mitraki, G. Charalambidis, X. Yan and A. G. Coutsolelos, *Nanoscale*, 2019, **11**, 3557–3566.
79 R. Chang, E. Nikoloudakis, Q. Zou, A. Mitraki, A. G. Coutsolelos and X. Yan, *ACS Appl. Bio Mater.*, 2020, **3**, 2–9.
80 M. Reches and E. Gazit, *Science*, 2003, **300**, 625–627.
81 N. Kol, L. Adler-Abramovich, D. Barlam, R. Z. Shneck, E. Gazit and I. Rousso, *Nano Lett.*, 2005, **5**, 1343–1346.
82 K. Karikis, A. Butkiewicz, F. Folias, G. Charalambidis, C. Kokotidou, A. Charisiadis, V. Nikolaou, E. Nikoloudakis, J. Frelek, A. Mitraki and A. G. Coutsolelos, *Nanoscale*, 2018, **10**, 1735–1741.
83 G. Charalambidis, E. Kasotakis, T. Lazarides, A. Mitraki and A. G. Coutsolelos, *Chem. – Eur. J.*, 2011, **17**, 7213–7219.
84 G. Charalambidis, E. Georgilis, M. K. Panda, C. E. Anson, A. K. Powell, S. Doyle, D. Moss, T. Jochum, P. N. Horton, S. J. Coles, M. Linares, D. Beljonne, J. V. Naubron, J. Conradt, H. Kalt, A. Mitraki, A. G. Coutsolelos and T. S. Balaban, *Nat. Commun.*, 2016, **7**, 12657.
85 K. Karikis, E. Georgilis, G. Charalambidis, A. Petrou, O. Vakuliuk, T. Chatziioannou, I. Raptaki, S. Tsovola, I. Papakyriacou, A. Mitraki, D. T. Gryko and A. G. Coutsolelos, *Chem. – Eur. J.*, 2016, **22**, 11245–11252.
86 E. Nikoloudakis, K. Karikis, M. Laurans, C. Kokotidou, A. Sole-Daura, J. J. Carbo, A. Charisiadis, G. Charalambidis, G. Izzet, A. Mitraki, A. M. Douvas, J. M. Poblet, A. Proust and A. G. Coutsolelos, *Dalton Trans.*, 2018, **47**, 6304–6313.
87 V. Nikolaou, G. Charalambidis and A. G. Coutsolelos, *Chem. Commun.*, 2021, **57**, 4055–4058.
88 E. Nikoloudakis, M. Pigiaki, M. N. Polychronaki, A. Margaritopoulou, G. Charalambidis, E. Serpetzoglou, A. Mitraki, P. A. Loukakos and A. G. Coutsolelos, *ACS Sustainable Chem. Eng.*, 2021, **9**, 7781–7791.
89 E. Giannoudis, E. Benazzi, J. Karlsson, G. Copley, S. Panagiotakis, G. Landrou, P. Angaridis, V. Nikolaou, C. Matthaiaki, G. Charalambidis, E. A. Gibson and A. G. Coutsolelos, *Inorg. Chem.*, 2020, **59**, 1611–1621.
90 E. Nikoloudakis, G. Charalambidis, M. Vasila, E. Orfanos, P. Angaridis, G. A. Spyroulias and A. G. Coutsolelos, *Polyhedron*, 2021, **208**, 115421.
91 G. B. Bodedla, L. Li, Y. Che, Y. Jiang, J. Huang, J. Zhao and X. Zhu, *Chem. Commun.*, 2018, **54**, 11614–11617.
92 G. B. Bodedla, G. Tang, J. Zhao and X. Zhu, *Sustainable Energy Fuels*, 2020, **4**, 2675–2679.
93 G. B. Bodedla, J. Huang, W. Y. Wong and X. Zhu, *ACS Appl. Nano Mater.*, 2020, **3**, 7040–7046.
94 E. R. Clark and D. M. Kurtz, Jr., *Dalton Trans.*, 2016, **45**, 630–638.
95 E. R. Clark and D. M. Kurtz, *Inorg. Chem.*, 2017, **56**, 4584–4593.
96 H. Kotani, T. Miyazaki, E. Aoki, H. Sakai, T. Hasobe and T. Kojima, *ACS Appl. Energy Mater.*, 2020, **3**, 3193–3197.
97 I. I. Alkhatib, C. Garlisi, M. Pagliaro, K. Al-Ali and G. Palmisano, *Catal. Today*, 2020, **340**, 209–224.
98 A. Fateeva, P. A. Chater, C. P. Ireland, A. A. Tahir, Y. Z. Khimyak, P. V. Wiper, J. R. Darwent and M. J. Rosseinsky, *Angew. Chem., Int. Ed.*, 2012, **51**, 7440–7444.
99 K. Sasan, Q. Lin, C. Y. Mao and P. Feng, *Chem. Commun.*, 2014, **50**, 10390–10393.
100 X. Fang, Q. Shang, Y. Wang, L. Jiao, T. Yao, Y. Li, Q. Zhang, Y. Luo and H.-L. Jiang, *Adv. Mater.*, 2018, **30**, 1705112.
101 F. Leng, H. Liu, M. Ding, Q. P. Lin and H. L. Jiang, *ACS Catal.*, 2018, **8**, 4583–4590.
102 T. He, S. Chen, B. Ni, Y. Gong, Z. Wu, L. Song, L. Gu, W. Hu and X. Wang, *Angew. Chem., Int. Ed.*, 2018, **57**, 3493–3498.
103 G. Lan, Y. Y. Zhu, S. S. Veroneau, Z. Xu, D. Micheroni and W. Lin, *J. Am. Chem. Soc.*, 2018, **140**, 5326–5329.
104 S. Li, H. M. Mei, S. L. Yao, Z. Y. Chen, Y. L. Lu, L. Zhang and C. Y. Su, *Chem. Sci.*, 2019, **10**, 10577–10585.
105 S. Yuan, T.-F. Liu, D. Feng, J. Tian, K. Wang, J. Qin, Q. Zhang, Y.-P. Chen, M. Bosch, L. Zou, S. J. Teat, S. J. Dalgarno and H.-C. Zhou, *Chem. Sci.*, 2015, **6**, 3926–3930.
106 X. Wang, X. Zhang, W. Zhou, L. Liu, J. Ye and D. Wang, *Nano Energy*, 2019, **62**, 250–258.
107 Q. Zuo, T. Liu, C. Chen, Y. Ji, X. Gong, Y. Mai and Y. Zhou, *Angew. Chem., Int. Ed.*, 2019, **58**, 10198–10203.
108 Y. Diao, N. Xu, M. Q. Li, X. Zhu and Z. Xu, *Inorg. Chem.*, 2020, **59**, 12643–12649.
109 H. Hu, Z. Wang, L. Cao, L. Zeng, C. Zhang, W. Lin and C. Wang, *Nat. Chem.*, 2021, **13**, 358–366.
110 H. Hu, L. Zeng, Z. Li, T. Zhu and C. Wang, *Chin. J. Catal.*, 2021, **42**, 1345–1351.
111 P. Jin, L. Wang, X. Ma, R. Lian, J. Huang, H. She, M. Zhang and Q. Wang, *Appl. Catal., B*, 2021, **284**, 119762.
112 C. Lin, C. Han, H. Zhang, L. Gong, Y. Gao, H. Wang, Y. Bian, R. Li and J. Jiang, *Inorg. Chem.*, 2021, **60**, 3988–3995.
113 Z. Chen, J. Wang, S. Zhang, Y. Zhang, J. Zhang, R. Li and T. Peng, *ACS Appl. Energy Mater.*, 2019, **2**, 5665–5676.

114 J. Wang, L. Xu, T. Wang, S. Chen, Z. Jiang, R. Li, Y. Zhang and T. Peng, *Adv. Funct. Mater.*, 2021, **31**, 2009819.
115 Z. Fan, K. Nomura, M. Zhu, X. Li, J. Xue, T. Majima and Y. Osakada, *Commun. Chem.*, 2019, **2**, 55.
116 R. Chen, Y. Wang, Y. Ma, A. Mal, X. Y. Gao, L. Gao, L. Qiao, X. B. Li, L. Z. Wu and C. Wang, *Nat. Commun.*, 2021, **12**, 1354.
117 K. C. Ranjeesh, L. George, V. C. Wakchaure, Goudappagouda, R. N. Devi and S. S. Babu, *Chem. Commun.*, 2019, **55**, 1627–1630.
118 K. C. Ranjeesh, L. George, A. Maibam, S. Krishnamurty and S. S. Babu, *ChemCatChem*, 2021, **13**, 1717–1721.
119 M. H.-F. Ali, G. Bengasi, K. Baba and N. D. Boscher, *ACS Appl. Energy Mater.*, 2020, **3**, 9848–9855.
120 L. Xie, J. Tian, Y. Ouyang, X. Guo, W. Zhang, U. P. Apfel, W. Zhang and R. Cao, *Angew. Chem., Int. Ed.*, 2020, **59**, 15844–15848.
121 P. Liao, Y. Hu, Z. Liang, J. Zhang, H. Yang, L. Q. He, Y. X. Tong, J. M. Liu, L. Chen and C. Y. Su, *J. Mater. Chem. A*, 2018, **6**, 3195–3201.
122 X. Zhao, X. Zhang, Y. Liang, Z. Hu and F. Huang, *Macromolecules*, 2021, **54**, 4902–4909.
123 R. X. Li, X. F. Liu, T. Liu, Y. B. Yin, Y. Zhou, S. K. Mei and J. Yan, *Electrochim. Acta*, 2017, **237**, 207–216.
124 X. F. Liu, R. X. Li, X. T. Ren, Y. B. Yin, S. K. Mei, T. Liu and J. Yan, *J. Catal.*, 2017, **348**, 314–320.
125 X. Li, K. Li, D. Wang, J. Huang, C. Zhang, Y. Du and P. Yang, *J. Porphyrins Phthalocyanines*, 2017, **21**, 179–188.
126 R. Ge, X. Li, S. Z. Kang, L. Qin and G. Li, *Appl. Catal., B*, 2016, **187**, 67–74.
127 Q. Luo, K. Zhu, S. Z. Kang, L. Qin, S. Han, G. Li and X. Li, *J. Porphyrins Phthalocyanines*, 2018, **22**, 877–885.
128 K. Zhu, Q. Luo, S. Z. Kang, L. Qin, G. Li and X. Li, *Nanoscale*, 2018, **10**, 18635–18641.
129 L. Zhang, L. Qin, S. Z. Kang, G. D. Li and X. Li, *ACS Sustainable Chem. Eng.*, 2019, **7**, 8358–8366.
130 Y. J. Yuan, D. Chen, J. Zhong, L. X. Yang, J. J. Wang, Z. T. Yu and Z. G. Zou, *J. Phys. Chem. C*, 2017, **121**, 24452–24462.
131 Q. Luo, R. Ge, S. Z. Kang, L. Qin, G. Li and X. Li, *Appl. Surf. Sci.*, 2018, **427**, 15–23.
132 S. Mei, J. Gao, Y. Zhang, J. Yang, Y. Wu, X. Wang, R. Zhao, X. Zhai, C. Hao, R. Li and J. Yan, *J. Colloid Interface Sci.*, 2017, **506**, 58–65.
133 E. S. Da Silva, N. M.-M. Moura, M. G.-P. M.-S. Neves, A. Coutinho, M. Prieto, C. G. Silva and J. L. Faria, *Appl. Catal., B*, 2018, **221**, 56–69.
134 J. Wang, Y. Zheng, T. Peng, J. Zhang and R. Li, *ACS Sustainable Chem. Eng.*, 2017, **5**, 7549–7556.
135 Y. Zheng, J. Wang, J. Zhang, T. Peng and R. Li, *Dalton Trans.*, 2017, **46**, 8219–8228.
136 J. Wang, D. Liu, Q. Liu, T. Peng, R. Li and S. Zhou, *Appl. Surf. Sci.*, 2019, **464**, 255–261.
137 L. Li, G. B. Bodedla, Z. Liu and X. Zhu, *Appl. Surf. Sci.*, 2020, **499**, 143755.
138 K. Zhu, M. Zhang, X. Feng, L. Qin, S. Z. Kang and X. Li, *Appl. Catal., B*, 2020, **268**, 118434.
139 M. Zhang, K. Zhu, L. Qin, S. Z. Kang and X. Li, *Catal. Sci. Technol.*, 2020, **10**, 1640–1649.
140 P. Zeng, Y. Zheng, S. Chen, H. Liu, R. Li and T. Peng, *New J. Chem.*, 2020, **44**, 11237–11247.
141 S. Tian, S. Chen, X. Ren, R. Cao, H. Hu and F. Bai, *Nano Res.*, 2019, **12**, 3109–3115.
142 G. Maduraiveeran, M. Sasidharan and W. Jin, *Prog. Mater. Sci.*, 2019, **106**, 100574.
143 J. Hwang, R. R. Rao, L. Giordano, Y. Katayama, Y. Yu and Y. Shao-Horn, *Science*, 2017, **358**, 751–756.
144 N.-T. Suen, S.-F. Hung, Q. Quan, N. Zhang, Y.-J. Xu and H. M. Chen, *Chem. Soc. Rev.*, 2017, **46**, 337–365.
145 D. Chen, C. Chen, Z. M. Baiyee, Z. Shao and F. Ciucci, *Chem. Rev.*, 2015, **115**, 9869–9921.
146 Y. Xue, S. Sun, Q. Wang, Z. Dong and Z. Liu, *J. Mater. Chem. A*, 2018, **6**, 10595–10626.
147 S. Martha, P. Chandra Sahoo and K. M. Parida, *RSC Adv.*, 2015, **5**, 61535–61553.
148 K. Kurimoto, T. Yamazaki, Y. Suzuri, Y. Nabetani, S. Onuki, S. Takagi, T. Shimada, H. Tachibana and H. Inoue, *Photochem. Photobiol. Sci.*, 2014, **13**, 154–156.
149 A.-M. Manke, K. Geisel, A. Fetzer and P. Kurz, *Phys. Chem. Chem. Phys.*, 2014, **16**, 12029–12042.
150 E. Koposova, X. Liu, A. Pendin, B. Thiele, G. Shumilova, Y. Ermolenko, A. Offenhäusser and Y. Mourzina, *J. Phys. Chem. C*, 2016, **120**, 13873–13890.
151 Y. Yuan, H. Lu, Z. Ji, J. Zhong, M. Ding, D. Chen, Y. Li, W. Tu, D. Cao, Z. Yu and Z. Zou, *Chem. Eng. J.*, 2015, **275**, 8–16.
152 Y. J. Yuan, J. R. Tu, Z. J. Ye, H. W. Lu, Z. G. Ji, B. Hu, Y. H. Li, D. P. Cao, Z. T. Yu and Z. G. Zou, *Dyes Pigm.*, 2015, **123**, 285–292.
153 B. Zhuang, L. Xiangqing, R. Ge, S. Kang, L. Qin and G. Li, *Appl. Catal., A*, 2017, **533**, 81–89.
154 P. Wang, M. Xi, S. Z. Kang, L. Qin, S. Han and X. Li, *Int. J. Hydrogen Energy*, 2020, **45**, 6508–6518.
155 X. Guo, X. Li, L. Qin, S. Z. Kang and G. Li, *Appl. Catal., B*, 2019, **243**, 1–9.
156 F. Kuttassery, S. Sagawa, S. Mathew, Y. Nabetani, A. Iwase, A. Kudo, H. Tachibana and H. Inoue, *ACS Appl. Energy Mater.*, 2019, **2**, 8045–8051.
157 V. Nikolaou, G. Charalambidis, K. Ladomenou, E. Nikoloudakis, C. Drivas, I. Vamvasakis, S. Panagiotakis, G. Landrou, E. Agapaki, C. Stangel, C. Henkel, J. Joseph, G. Armatas, M. Vasilopoulou, S. Kennou, D. M. Guldi and A. G. Coutsolelos, *ChemSusChem*, 2021, **14**, 961–970.
158 P. Y. Ho, M. F. Mark, Y. Wang, S. C. Yiu, W. H. Yu, C. L. Ho, D. W. McCamant, R. Eisenberg and S. Huang, *ChemSusChem*, 2018, **11**, 2517–2528.
159 P. S. Gangadhar, S. Gonuguntla, S. Madanaboina, N. Islavath, U. Pal and L. Giribabu, *J. Photochem. Photobiol., A*, 2020, **392**, 112408.
160 P. Wang, M. Xi, L. Qin, S. Z. Kang, Y. Fang and X. Li, *ACS Appl. Nano Mater.*, 2019, **2**, 7409–7420.
161 M. Xi, P. Wang, M. Zhang, L. Qin, S. Z. Kang and X. Li, *Appl. Surf. Sci.*, 2020, **529**, 147200.

162 Q. Wang, Y. Shi, Q. Ma, D. Gao, J. Zhong, J. Li, F. Wang, Y. He and R. Wang, *J. Mater. Sci.: Mater. Electron.*, 2017, **28**, 2123–2127.
163 X. Feng, Z. Liu, L. Qin, S. Z. Kang and X. Li, *Phys. Chem. Chem. Phys.*, 2020, **22**, 13528–13535.
164 L. Y. Huang, J. F. Huang, Y. Lei, S. Qin and J. M. Liu, *Catalysts*, 2020, **10**, 656.
165 M. Xi, B. Zhuang, Y. Chen, L. Qin, S. Z. Kang and X. Li, *J. Solid State Chem.*, 2021, **298**, 122103.
166 G. Mukherjee, J. Thote, H. B. Aiyappa, S. Kandambeth, S. Banerjee, K. Vanka and R. Banerjee, *Chem. Commun.*, 2017, **53**, 4461–4464.
167 V. Nikolaou, G. Charalambidis, G. Landrou, E. Nikoloudakis, A. Planchat, R. Tsalameni, K. Junghans, A. Kahnt, F. Odobel and A. G. Coutsolelos, *ACS Appl. Energy Mater.*, 2021, **4**, 10042–10049.
168 D. Khusnutdinova, A. M. Beiler, B. L. Wadsworth, S. I. Jacob and G. F. Moore, *Chem. Sci.*, 2017, **8**, 253–259.
169 A. M. Beiler, D. Khusnutdinova, B. L. Wadsworth and G. F. Moore, *Inorg. Chem.*, 2017, **56**, 12178–12185.
170 B. D. Sherman, J. J. Bergkamp, C. L. Brown, A. L. Moore, D. Gust and T. A. Moore, *Energy Environ. Sci.*, 2016, **9**, 1812–1817.
171 K. Morita, K. Takijiri, K. Sakai and H. Ozawa, *Dalton Trans.*, 2017, **46**, 15181–15185.
172 K. Morita, K. Sakai and H. Ozawa, *ACS Appl. Energy Mater.*, 2019, **2**, 987–992.
173 C. Canales, A. F. Olea, L. Gidi, R. Arce and G. Ramírez, *Electrochim. Acta*, 2017, **258**, 850–857.
174 L. Gidi, J. Honores, J. Ibarra, R. Arce, M. J. Aguirre and G. Ramírez, *New J. Chem.*, 2019, **43**, 12727–12733.
175 L. Gidi, J. Honores, J. Ibarra, R. Arce, M. J. Aguirre and G. Ramírez, *Catalysts*, 2020, **10**, 239.
176 X. Li, A. Liu, D. Chu, C. Zhang, Y. Du, J. Huang and P. Yang, *Catalysts*, 2018, **8**, 108.
177 Y. Kumar, B. Patil, A. Khaligh, S. E. Hadi, T. Uyar and D. Tuncel, *ChemCatChem*, 2019, **11**, 2994–2999.
178 X. Li, Y. Zhang, W. Wang, J. Meng, K. Li, W. Lin, Z. Peng, J. Wan and Z. Hu, *Int. J. Hydrogen Energy*, 2019, **44**, 18072–18082.
179 M. Blanco, M. Lunardon, M. Bortoli, D. Mosconi, L. Girardi, L. Orian, S. Agnoli and G. Granozzi, *J. Mater. Chem. A*, 2020, **8**, 11019–11030.
180 L. Girardi, M. Blanco, S. Agnoli, G. A. Rizzi and G. Granozzi, *Nanomaterials*, 2020, **10**, 1266.
181 Y. H. Xiao, W. Tian, S. Jin, Z. G. Gu and J. Zhang, *Small*, 2020, **16**, 2005111.
182 A. Charisiadis, E. Giannoudis, Z. Pournara, A. Kosma, V. Nikolaou, G. Charalambidis, V. Artero, M. Chavarot-Kerlidou and A. G. Coutsolelos, *Eur. J. Inorg. Chem.*, 2021, 1122–1129.
183 P. Gotico, Z. Halime and A. Aukauloo, *Dalton Trans.*, 2020, **49**, 2381–2396.
184 L. Zou, R. Sa, H. Lv, H. Zhong and R. Wang, *ChemSusChem*, 2020, **13**, 6124–6140.
185 Y. Tamaki and O. Ishitani, *ACS Catal.*, 2017, **7**, 3394–3409.
186 J. Grodkowski, D. Behar, P. Neta and P. Hambright, *J. Phys. Chem. A*, 1997, **101**, 248–254.
187 J. Bonin, M. Chaussemier, M. Robert and M. Routier, *ChemCatChem*, 2014, **6**, 3200–3207.
188 J. Bonin, M. Robert and M. Routier, *J. Am. Chem. Soc.*, 2014, **136**, 16768–16771.
189 H. Rao, J. Bonin and M. Robert, *Chem. Commun.*, 2017, **53**, 2830–2833.
190 H. Rao, J. Bonin and M. Robert, *ChemSusChem*, 2017, **10**, 4447–4450.
191 H. Rao, L. C. Schmidt, J. Bonin and M. Robert, *Nature*, 2017, **548**, 74–77.
192 H. Rao, J. Bonin and M. Robert, *J. Phys. Chem. C*, 2018, **122**, 13834–13839.
193 H. Rao, C. H. Lim, J. Bonin, G. M. Miyake and M. Robert, *J. Am. Chem. Soc.*, 2018, **140**, 17830–17834.
194 M. Kientz, G. Lowe, B. G. McCarthy, G. M. Miyake, J. Bonin and M. Robert, *ChemPhotoChem*, 2022, DOI: **10.1002/cptc.202200009**.
195 A. Dannenhoffer, H. Sai, D. Huang, B. Nagasing, B. Harutyunyan, D. J. Fairfield, T. Aytun, S. M. Chin, M. J. Bedzyk, M. Olvera De La Cruz and S. I. Stupp, *Chem. Sci.*, 2019, **10**, 5779–5786.
196 H. Yuan, B. Cheng, J. Lei, L. Jiang and Z. Han, *Nat. Commun.*, 2021, **12**, 1835.
197 G. F. Manbeck and E. Fujita, *J. Porphyrins Phthalocyanines*, 2015, **19**, 45–64.
198 A. Call, M. Cibian, K. Yamamoto, T. Nakazono, K. Yamauchi and K. Sakai, *ACS Catal.*, 2019, **9**, 4867–4874.
199 X. Zhang, M. Cibian, A. Call, K. Yamauchi and K. Sakai, *ACS Catal.*, 2019, **9**, 11263–11273.
200 X. Zhang, K. Yamauchi and K. Sakai, *ACS Catal.*, 2021, **11**, 10436–10449.
201 C. Matlachowski and M. Schwalbe, *Dalton Trans.*, 2015, **44**, 6480–6489.
202 C. D. Windle, M. W. George, R. N. Perutz, P. A. Summers, X. Z. Sun and A. C. Whitwood, *Chem. Sci.*, 2015, **6**, 6847–6864.
203 J. M. Smieja and C. P. Kubiak, *Inorg. Chem.*, 2010, **49**, 9283–9289.
204 E. E. Benson and C. P. Kubiak, *Chem. Commun.*, 2012, **48**, 7374–7376.
205 C. D. Windle, E. Pastor, A. Reynal, A. C. Whitwood, Y. Vaynzof, J. R. Durrant, R. N. Perutz and E. Reisner, *Chem. – Eur. J.*, 2015, **21**, 3746–3754.
206 C. Matlachowski, B. Braun, S. Tschierlei and M. Schwalbe, *Inorg. Chem.*, 2015, **54**, 10351–10360.
207 P. Lang, M. Pfrunder, G. Quach, B. Braun-Cula, E. G. Moore and M. Schwalbe, *Chem. – Eur. J.*, 2019, **25**, 4509–4519.
208 Y. Kuramochi, Y. Fujisawa and A. Satake, *J. Am. Chem. Soc.*, 2020, **142**, 705–709.
209 Y. Kuramochi and A. Satake, *Chem. – Eur. J.*, 2020, **26**, 16365–16373.
210 J. X. Zhang, C. Y. Hu, W. Wang, H. Wang and Z. Y. Bian, *Appl. Catal., A*, 2016, **522**, 145–151.

211 J. D. Shipp, H. Carson, S. J.-P. Spall, S. C. Parker, D. Chekulaev, N. Jones, M. Y. Mel'nikov, C. C. Robertson, A. J.-H. M. Meijer and J. A. Weinstein, *Dalton Trans.*, 2020, **49**, 4230–4243.
212 Y. Amao, *Sustainable Energy Fuels*, 2018, **2**, 1928–1950.
213 Y. Amao, *Chem. Lett.*, 2017, **46**, 780–788.
214 Y. Amao, R. Abe and S. Shiotani, *J. Photochem. Photobiol., A*, 2015, **313**, 149–153.
215 S. Ikeyama and Y. Amao, *Sustainable Energy Fuels*, 2017, **1**, 1730–1733.
216 S. Ikeyama and Y. Amao, *Photochem. Photobiol. Sci.*, 2018, **17**, 60–68.
217 F. Secundo and Y. Amao, *RSC Adv.*, 2020, **10**, 42354–42362.
218 S. Ikeyama, T. Katagiri and Y. Amao, *J. Photochem. Photobiol., A*, 2018, **358**, 362–367.
219 A. Miyaji and Y. Amao, *New J. Chem.*, 2021, **45**, 5780–5790.
220 A. Miyaji and Y. Amao, *ChemNanoMat*, 2021, **7**, 626–634.
221 A. Miyaji and Y. Amao, *New J. Chem.*, 2020, **44**, 18803–18812.
222 Y. Amao, S. Ikeyama, T. Katagiri and K. Fujita, *Faraday Discuss.*, 2017, **198**, 73–81.
223 T. Katagiri, S. Ikeyama and Y. Amao, *J. Photochem. Photobiol., A*, 2018, **358**, 368–373.
224 Y. Amao and R. Kataoka, *Catal. Today*, 2018, **307**, 243–247.
225 X. Ji, J. Wang, Y. Kang, L. Mei, Z. Su, S. Wang, G. Ma, J. Shi and S. Zhang, *ACS Catal.*, 2018, **8**, 10732–10745.
226 C. Costentin, M. Robert and J.-M. Savéant, *Chem. Soc. Rev.*, 2013, **42**, 2423–2436.
227 J.-M. Savéant, *Chem. Rev.*, 2008, **108**, 2348–2378.
228 H. Q. Xu, J. Hu, D. Wang, Z. Li, Q. Zhang, Y. Luo, S. H. Yu and H. L. Jiang, *J. Am. Chem. Soc.*, 2015, **137**, 13440–13443.
229 J. Jin, *New J. Chem.*, 2020, **44**, 15362–15368.
230 R. Hariri and S. Dehghanpour, *Appl. Organomet. Chem.*, 2021, **35**, e6422.
231 H. Zhang, J. Wei, J. Dong, G. Liu, L. Shi, P. An, G. Zhao, J. Kong, X. Wang, X. Meng, J. Zhang and J. Ye, *Angew. Chem., Int. Ed.*, 2016, **55**, 14310–14314.
232 J. Liu, Y. Z. Fan, X. Li, Z. Wei, Y. W. Xu, L. Zhang and C. Y. Su, *Appl. Catal., B*, 2018, **231**, 173–181.
233 E. X. Chen, M. Qiu, Y. F. Zhang, Y. S. Zhu, L. Y. Liu, Y. Y. Sun, X. Bu, J. Zhang and Q. Lin, *Adv. Mater.*, 2018, **30**, 1704388.
234 Y. C. Qiu, S. Yuan, X. X. Li, D. Y. Du, C. Wang, J. S. Qin, H. F. Drake, Y. Q. Lan, L. Jiang and H. C. Zhou, *J. Am. Chem. Soc.*, 2019, **141**, 13841–13848.
235 L. Wang, P. Jin, J. Huang, H. She and Q. Wang, *ACS Sustainable Chem. Eng.*, 2019, **7**, 15660–15670.
236 L. Wang, P. Jin, S. Duan, H. She, J. Huang and Q. Wang, *Sci. Bull.*, 2019, **64**, 926–933.
237 L. Y. Wu, Y. F. Mu, X. X. Guo, W. Zhang, Z. M. Zhang, M. Zhang and T. B. Lu, *Angew. Chem., Int. Ed.*, 2019, **58**, 9491–9495.
238 S. Choi, W. J. Jung, K. Park, S. Y. Kim, J. O. Baeg, C. H. Kim, H. J. Son, C. Pac and S. O. Kang, *ACS Appl. Mater. Interfaces*, 2021, **13**, 2710–2722.
239 Q. Li, Y. Luo, Y. Ding, Y. Wang, Y. Wang, H. Du, R. Yuan, J. Bao, M. Fang and Y. Wu, *Dalton Trans.*, 2019, **48**, 8678–8692.
240 N. Sadeghi, S. Sharifnia and T. O. Do, *J. Mater. Chem. A*, 2018, **6**, 18031–18035.
241 N. Sadeghi and M. Sillanpää, *Photochem. Photobiol. Sci.*, 2021, **20**, 391–399.
242 S.-S. Wang, H.-H. Huang, M. Liu, S. Yao, S. Guo, J.-W. Wang, Z.-M. Zhang and T.-B. Lu, *Inorg. Chem.*, 2020, **59**, 6301–6307.
243 Y. Fu, D. Sun, Y. Chen, R. Huang, Z. Ding, X. Fu and Z. Li, *Angew. Chem., Int. Ed.*, 2012, **51**, 3364–3367.
244 S. Chen, F. Yang, H. Gao, J. Wang, X. Chen, X. Zhang, J. Li and A. Li, *J. CO2 Util.*, 2021, **48**, 101528.
245 N. Sadeghi, S. Sharifnia and M. Sheikh Arabi, *J. CO2 Util.*, 2016, **16**, 450–457.
246 Z. B. Fang, T. T. Liu, J. Liu, S. Jin, X. P. Wu, X. Q. Gong, K. Wang, Q. Yin, T. F. Liu, R. Cao and H. C. Zhou, *J. Am. Chem. Soc.*, 2020, **142**, 12515–12523.
247 J. Xu, X. Liu, Z. Zhou and M. Xu, *Appl. Surf. Sci.*, 2020, **513**, 145801.
248 L. Ye, Y. Gao, S. Cao, H. Chen, Y. Yao, J. Hou and L. Sun, *Appl. Catal., B*, 2018, **227**, 54–60.
249 T. Ouyang, H.-H. Huang, J.-W. Wang, D.-C. Zhong and T.-B. Lu, *Angew. Chem., Int. Ed.*, 2017, **56**, 738–743.
250 L. Chen, Y. Wang, F. Yu, X. Shen and C. Duan, *J. Mater. Chem. A*, 2019, **7**, 11355–11361.
251 C. Wang, X. M. Liu, M. Zhang, Y. Geng, L. Zhao, Y. G. Li and Z. M. Su, *ACS Sustainable Chem. Eng.*, 2019, **7**, 14102–14110.
252 C. Zheng, X. Qiu, J. Han, Y. Wu and S. Liu, *ACS Appl. Mater. Interfaces*, 2019, **11**, 42243–42249.
253 W. Liu, X. Li, C. Wang, H. Pan, W. Liu, K. Wang, Q. Zeng, R. Wang and J. Jiang, *J. Am. Chem. Soc.*, 2019, **141**, 17431–17440.
254 M. Lu, J. Liu, Q. Li, M. Zhang, M. Liu, J. L. Wang, D. Q. Yuan and Y. Q. Lan, *Angew. Chem., Int. Ed.*, 2019, **58**, 12392–12397.
255 S. Wan, F. Gándara, A. Asano, H. Furukawa, A. Saeki, S. K. Dey, L. Liao, M. W. Ambrogio, Y. Y. Botros, X. Duan, S. Seki, J. F. Stoddart and O. M. Yaghi, *Chem. Mater.*, 2011, **23**, 4094–4097.
256 L. J. Wang, R. L. Wang, X. Zhang, J. L. Mu, Z. Y. Zhou and Z. M. Su, *ChemSusChem*, 2020, **13**, 2973–2980.
257 H. Lv, R. Sa, P. Li, D. Yuan, X. Wang and R. Wang, *Sci. China Chem.*, 2020, **63**, 1289–1294.
258 N. Xu, Y. Diao, X. Qin, Z. Xu, H. Ke and X. Zhu, *Dalton Trans.*, 2020, **49**, 15587–15591.
259 Y.-N. Gong, W. Zhong, Y. Li, Y. Qiu, L. Zheng, J. Jiang and H.-L. Jiang, *J. Am. Chem. Soc.*, 2020, **142**, 16723–16731.
260 H. Zhong, R. Sa, H. Lv, S. Yang, D. Yuan, X. Wang and R. Wang, *Adv. Funct. Mater.*, 2020, **30**, 2002654.
261 S. Zhang, S. Wang, L. Guo, H. Chen, B. Tan and S. Jin, *J. Mater. Chem. C*, 2019, **8**, 192–200.
262 Y. Zhang, Y. Wang, L. C. An, J. Chen, T. Zhang and Y. H. Zhang, *Mater. Chem. Front.*, 2020, **4**, 2754–2761.
263 Y. Zhang, G. L. Zhang, Y. T. Wang, Z. Ma, T. Y. Yang, T. Zhang and Y. H. Zhang, *J. Colloid Interface Sci.*, 2021, **596**, 342–351.
264 K. Li, L. Lin, T. Peng, Y. Guo, R. Li and J. Zhang, *Chem. Commun.*, 2015, **51**, 12443–12446.

265 G. Mele, C. Annese, L. D'Accolti, A. De Riccardis, C. Fusco, L. Palmisano, A. Scarlino and G. Vasapollo, *Molecules*, 2015, **20**, 396–415.
266 Y. Song, J. Li and C. Wang, *J. Mater. Res.*, 2018, **33**, 2612–2620.
267 Z. Wang, W. Zhou, X. Wang, X. Zhang, H. Chen, H. Hu, L. Liu, J. Ye and D. Wang, *Catalysts*, 2020, **10**, 654.
268 L. Wang, S. Duan, P. Jin, H. She, J. Huang, Z. Lei, T. Zhang and Q. Wang, *Appl. Catal., B*, 2018, **239**, 599–608.
269 H. Gao, J. Wang, M. Jia, F. Yang, R. S. Andriamitantsoa, X. Huang, W. Dong and G. Wang, *Chem. Eng. J.*, 2019, **374**, 684–693.
270 V. Jeyalakshmi, S. Tamilmani, R. Mahalakshmy, P. Bhyrappa, K. R. Krishnamurthy and B. Viswanathan, *J. Mol. Catal. A: Chem.*, 2016, **420**, 200–207.
271 D. I. Won, J. S. Lee, Q. Ba, Y. J. Cho, H. Y. Cheong, S. Choi, C. H. Kim, H. J. Son, C. Pac and S. O. Kang, *ACS Catal.*, 2018, **8**, 1018–1030.
272 S. Choi, C. H. Kim, J. O. Baeg, H. J. Son, C. Pac and S. O. Kang, *ACS Appl. Energy Mater.*, 2020, **3**, 11581–11596.
273 G. Zhao, H. Pang, G. Liu, P. Li, H. Liu, H. Zhang, L. Shi and J. Ye, *Appl. Catal., B*, 2017, **200**, 141–149.
274 L. Lin, C. Hou, X. Zhang, Y. Wang, Y. Chen and T. He, *Appl. Catal., B*, 2018, **221**, 312–319.
275 S. Tian, S. Chen, X. Ren, Y. Hu, H. Hu, J. Sun and F. Bai, *Nano Res.*, 2020, **13**, 2665–2672.
276 P. Li, C. Hou, X. Zhang, Y. Chen and T. He, *Appl. Surf. Sci.*, 2018, **459**, 292–299.
277 P. Li, X. Zhang, C. Hou, Y. Chen and T. He, *Appl. Catal., B*, 2018, **238**, 656–663.
278 S. Lian, M. S. Kodaimati, D. S. Dolzhnikov, R. Calzada and E. A. Weiss, *J. Am. Chem. Soc.*, 2017, **139**, 8931–8938.
279 S. Lian, M. S. Kodaimati and E. A. Weiss, *ACS Nano*, 2018, **12**, 568–575.
280 F. Arcudi, L. Đorđević, B. Nagasing, S. I. Stupp and E. A. Weiss, *J. Am. Chem. Soc.*, 2021, **143**, 18131–18138.
281 M. García, M. J. Aguirre, G. Canzi, C. P. Kubiak, M. Ohlbaum and M. Isaacs, *Electrochim. Acta*, 2014, **115**, 146–154.
282 J. Liu, H. Shi, Q. Shen, C. Guo and G. Zhao, *Green Chem.*, 2017, **19**, 5900–5910.
283 Y. Kou, S. Nakatani, G. Sunagawa, Y. Tachikawa, D. Masui, T. Shimada, S. Takagi, D. A. Tryk, Y. Nabetani, H. Tachibana and H. Inoue, *J. Catal.*, 2014, **310**, 57–66.
284 R. Nakazato, Y. Kou, D. Yamamoto, T. Shimada, T. Ishida, S. Takagi, H. Munakata, K. Kanamura, H. Tachibana and H. Inoue, *Res. Chem. Intermed.*, 2021, **47**, 269–285.
285 R. Zeng, G. Chen, C. Xiong, G. Li, Y. Zheng, J. Chen, Y. Long and S. Chen, *Appl. Surf. Sci.*, 2018, **434**, 756–762.
286 Y. Dong, R. Nie, J. Wang, X. Yu, P. Tu, J. Chen and H. Jing, *Chin. J. Catal.*, 2019, **40**, 1222–1230.
287 D. Yang, H. Yu, T. He, S. Zuo, X. Liu, H. Yang, B. Ni, H. Li, L. Gu, D. Wang and X. Wang, *Nat. Commun.*, 2019, **10**, 3844.
288 Y. Zhou, L. Zheng, D. Yang, H. Yang, Q. Lu, Q. Zhang, L. Gu and X. Wang, *Small Methods*, 2021, **5**, 2000991.
289 V. Andrei, B. Reuillard and E. Reisner, *Nat. Mater.*, 2020, **19**, 189–194.
290 J. F.-D. Brito, K. Irikura, C. M. Terzi, S. Nakagaki and M. V.-B. Zanoni, *J. CO2 Util.*, 2020, **41**, 101261.
291 J. Cheng, X. Yang, X. Xuan and J. Zhou, *Chem. Eng. J.*, 2020, **392**, 123799.
292 B. Wang, F. Yang, Y. Dong, Y. Cao, J. Wang, B. Yang, Y. Wei, W. Wan, J. Chen and H. Jing, *Chem. Eng. J.*, 2020, **396**, 125255.
293 A. Charisiadis, E. Glymenaki, A. Planchat, S. Margiola, A.-C. Lavergne-Bril, E. Nikoloudakis, V. Nikolaou, G. Charalambidis, A. G. Coutsolelos and F. Odobel, *Dyes Pigm.*, 2021, **185**, 108908.
294 J. J. Cid, J. H. Yum, S. R. Jang, M. K. Nazeeruddin, E. Martínez-Ferrero, E. Palomares, J. Ko, M. Grätzel and T. Torres, *Angew. Chem., Int. Ed.*, 2007, **46**, 8358–8362.
295 M. Urbani, M. E. Ragoussi, M. K. Nazeeruddin and T. Torres, *Coord. Chem. Rev.*, 2019, **381**, 1–64.
296 X. Zhang, L. Yu, C. Zhuang, T. Peng, R. Li and X. Li, *RSC Adv.*, 2013, **3**, 14363–14370.
297 G. Kim and W. Choi, *Appl. Catal., B*, 2010, **100**, 77–83.
298 X. Zhang, B. Peng, T. Peng, L. Yu, R. Li and J. Zhang, *J. Power Sources*, 2015, **298**, 30–37.
299 M. Fang, G. Dong, R. Wei and J. C. Ho, *Adv. Energy Mater.*, 2017, **7**, 1700559.
300 A. Tiwari, N. V. Krishna, L. Giribabu and U. Pal, *J. Phys. Chem. C*, 2018, **122**, 495–502.
301 H. S. Moon and K. Yong, *Appl. Surf. Sci.*, 2020, **530**, 147215.
302 E. Genc, A. C. Yüzer, G. Yanalak, E. Harputlu, E. Aslan, K. Ocakoglu, M. Ince and I. H. Patir, *Renewable Energy*, 2020, **162**, 1340–1346.
303 M. E. Ragoussi, J. J. Cid, J. H. Yum, G. De La Torre, D. Di Censo, M. Grätzel, M. K. Nazeeruddin and T. Torres, *Angew. Chem., Int. Ed.*, 2012, **51**, 4375–4378.
304 M. E. Ragoussi, J. H. Yum, A. K. Chandiran, M. Ince, G. de la Torre, M. Grätzel, M. K. Nazeeruddin and T. Torres, *ChemPhysChem*, 2014, **15**, 1033–1036.
305 M. Ince, R. Kuboi, T. Ince, K. Yoshimura, D. Motoyoshi, M. Sonobe, R. Kudo, S. Mori, M. Kimura and T. Torres, *Sustainable Energy Fuels*, 2021, **5**, 584–589.
306 E. Genc Acar, A. C. Yüzer, G. Kurtay, G. Yanalak, E. Harputlu, E. Aslan, K. Ocakoglu, M. Güllü, M. Ince and I. H. Patir, *ACS Appl. Energy Mater.*, 2021, **4**, 10222–10233.
307 A. C. Yüzer, E. Genc, G. Kurtay, G. Yanalak, E. Aslan, E. Harputlu, K. Ocakoglu, I. Hatay Patir and M. Ince, *Chem. Commun.*, 2021, **57**, 9196–9199.
308 C. G. Claessens, D. González-Rodríguez, M. S. Rodríguez-Morgade, A. Medina and T. Torres, *Chem. Rev.*, 2014, **114**, 2192–2277.
309 T. M. Grant, D. S. Josey, K. L. Sampson, T. Mudigonda, T. P. Bender and B. H. Lessard, *Chem. Rec.*, 2019, **19**, 1093–1112.
310 M. Ince, A. Medina, J. H. Yum, A. Yella, C. G. Claessens, M. V. Martínez-Díaz, M. Grätzel, M. K. Nazeeruddin and T. Torres, *Chem. – Eur. J.*, 2014, **20**, 2016–2021.

311 M. Urbani, F. A. Sari, M. Grätzel, M. K. Nazeeruddin, T. Torres and M. Ince, *Chem. – Asian J.*, 2016, **11**, 1223–1231.
312 A. Celil Yüzer, E. Genc, E. Harputlu, G. Yanalak, E. Aslan, K. Ocakoglu, I. Hatay Patir and M. Ince, *Dalton Trans.*, 2020, **49**, 12550–12554.
313 T. Abe, K. Fukui, Y. Kawai, K. Nagai and H. Kato, *Chem. Commun.*, 2016, **52**, 7735–7737.
314 Y. Kawai, K. Nagai and T. Abe, *RSC Adv.*, 2017, **7**, 34694–34698.
315 T. Murakami, K. Ikezoi, K. Nagai, H. Kato and T. Abe, *ChemElectroChem*, 2020, **7**, 5029–5035.
316 Y. Zheng, J. Liu, J. Liang, M. Jaroniec and S. Z. Qiao, *Energy Environ. Sci.*, 2012, **5**, 6717–6731.
317 X. Zhang, T. Peng, L. Yu, R. Li, Q. Li and Z. Li, *ACS Catal.*, 2015, **5**, 504–510.
318 X. Zhang, L. Yu, R. Li, T. Peng and X. Li, *Catal. Sci. Technol.*, 2014, **4**, 3251–3260.
319 Y. Guo, S. Song, Y. Zheng, R. Li and T. Peng, *Dalton Trans.*, 2016, **45**, 14071–14079.
320 S. Song, Y. Guo, T. Peng, J. Zhang and R. Li, *RSC Adv.*, 2016, **6**, 77366–77374.
321 P. Zeng, J. Wang, Y. Guo, R. Li, G. Mei and T. Peng, *Chem. Eng. J.*, 2019, **373**, 651–659.
322 Q. Liu, J. Wang, D. Liu, R. Li and T. Peng, *J. Power Sources*, 2018, **396**, 57–63.
323 J. Huang, Y. Wu, D. Wang, Y. Ma, Z. Yue, Y. Lu, M. Zhang, Z. Zhang and P. Yang, *ACS Appl. Mater. Interfaces*, 2015, **7**, 3732–3741.
324 D. Wang, J. Huang, X. Li, P. Yang, Y. Du, C. M. Goh and C. Lu, *J. Mater. Chem. A*, 2015, **3**, 4195–4202.
325 Y. J. Yuan, J. R. Tu, H. W. Lu, Z. T. Yu, X. X. Fan and Z. G. Zou, *Dalton Trans.*, 2016, **45**, 1359–1363.
326 L. C. Song, F. X. Luo, B. B. Liu, Z. C. Gu and H. Tan, *Organometallics*, 2016, **35**, 1399–1408.
327 R. Li, F. Zhang, D. Wang, J. Yang, M. Li, J. Zhu, X. Zhou, H. Han and C. Li, *Nat. Commun.*, 2013, **4**, 1432.
328 J. Bian, J. Feng, Z. Zhang, Z. Li, Y. Zhang, Y. Liu, S. Ali, Y. Qu, L. Bai, J. Xie, D. Tang, X. Li, F. Bai, J. Tang and L. Jing, *Angew. Chem., Int. Ed.*, 2019, **58**, 10873–10878.
329 J. Bian, J. Feng, Z. Zhang, J. Sun, M. Chu, L. Sun, X. Li, D. Tang and L. Jing, *Chem. Commun.*, 2020, **56**, 4926–4929.
330 J. Bian, L. Sun, Z. Zhang, Z. Li, M. Chu, X. Li, D. Tang and L. Jing, *ACS Sustainable Chem. Eng.*, 2021, **9**, 2400–2408.
331 H. Zheng, J. Z. Ou, M. S. Strano, R. B. Kaner, A. Mitchell and K. Kalantar-Zadeh, *Adv. Funct. Mater.*, 2011, **21**, 2175–2196.
332 B. Li, L. Q. Sun, J. Bian, N. Sun, J. W. Sun, L. Q. Chen, Z. J. Li and L. Q. Jing, *Appl. Catal., B*, 2020, **270**, 118849.
333 W. J. Ong, L. L. Tan, Y. H. Ng, S. T. Yong and S. P. Chai, *Chem. Rev.*, 2016, **116**, 7159–7329.
334 J. Sun, J. Bian, J. Li, Z. Zhang, Z. Li, Y. Qu, L. Bai, Z. D. Yang and L. Jing, *Appl. Catal., B*, 2020, **277**, 119199.
335 F. Franco, C. Rettenmaier, H. S. Jeon and B. Roldan Cuenya, *Chem. Soc. Rev.*, 2020, **49**, 6884–6946.
336 S. Roy and E. Reisner, *Angew. Chem., Int. Ed.*, 2019, **58**, 12180–12184.
337 G. Liu, Y. Wang, Y. Zhou, J. Cao, M. Yuan and H. Lv, *J. Colloid Interface Sci.*, 2021, **594**, 658–668.
338 Y. Wang, Y. Zhu, L. C. Sun and F. Li, *ACS Appl. Mater. Interfaces*, 2020, **12**, 41644–41648.
339 P. Kumar, A. Kumar, B. Sreedhar, B. Sain, S. S. Ray and S. L. Jain, *Chem. – Eur. J.*, 2014, **20**, 6154–6161.
340 A. Kumar, P. K. Prajapati, M. S. Aathira, A. Bansiwal, R. Boukherroub and S. L. Jain, *J. Colloid Interface Sci.*, 2019, **543**, 201–213.
341 P. K. Prajapati and S. L. Jain, *Dalton Trans.*, 2019, **48**, 4941–4948.
342 P. Kumar, A. Kumar, C. Joshi, R. Singh, S. Saran and S. L. Jain, *RSC Adv.*, 2015, **5**, 42414–42421.